

**GEODETIC MEASUREMENT OF TECTONIC
DEFORMATION IN CENTRAL CALIFORNIA**

by

KURT LEWIS FEIGL

**Department of Earth, Atmospheric
and Planetary Sciences**

Massachusetts Institute of Technology

1991

**GEODETIC MEASUREMENT OF TECTONIC
DEFORMATION IN CENTRAL CALIFORNIA**

by

KURT LEWIS FEIGL

**Department of Earth, Atmospheric
and Planetary Sciences**

Massachusetts Institute of Technology

1991

19981202 027

REPORT DOCUMENTATION PAGE

AFRL-SR-BL-TR-98-

ved
I-0188

Public reporting burden for this collection of information is estimated to average 1 hour per response, including the time for reviewing existing information, gathering new information, and maintaining the data needed, and completing and reviewing the collection of information. Send comments regarding this burden estimate or any other aspect of this collection of information, including suggestions for reducing this burden, to Washington Headquarters Services, Directorate for Information Operations and Reports, 1215 Jefferson Davis Highway, Suite 1204, Arlington, VA 22202-4302, and to the Office of Management and Budget, Paperwork Reduction Project (0723), Washington, DC 20503.

0723

to sources, gathering
of this collection of
Davis Highway, Suite

1. AGENCY USE ONLY (Leave Blank)		2. REPORT DATE September, 1991	3. REPORT TYPE AND DATES COVERED Final
4. TITLE AND SUBTITLE Geodetic Measurement of Tectonic Deformation in Central California			5. FUNDING NUMBERS
6. AUTHORS Kurt Lewis Feigl			
7. PERFORMING ORGANIZATION NAME(S) AND ADDRESS(ES) Massachusetts Institute of Technology			8. PERFORMING ORGANIZATION REPORT NUMBER
9. SPONSORING/MONITORING AGENCY NAME(S) AND ADDRESS(ES) AFOSR/NI 4040 Fairfax Dr, Suite 500 Arlington, VA 22203-1613			10. SPONSORING/MONITORING AGENCY REPORT NUMBER
11. SUPPLEMENTARY NOTES			
12a. DISTRIBUTION AVAILABILITY STATEMENT Approved for Public Release			12b. DISTRIBUTION CODE
13. ABSTRACT (Maximum 200 words) See Attachment			
14. SUBJECT TERMS			15. NUMBER OF PAGES
			16. PRICE CODE
17. SECURITY CLASSIFICATION OF REPORT Unclassified	18. SECURITY CLASSIFICATION OF THIS PAGE Unclassified	19. SECURITY CLASSIFICATION OF ABSTRACT Unclassified	20. LIMITATION OF ABSTRACT UL

GEODETIC MEASUREMENT OF TECTONIC DEFORMATION
IN CENTRAL CALIFORNIA

by

KURT LEWIS FEIGL
B.S. Geology and Geophysics
summa cum laude with distinction in the major
Yale University (1985)

Submitted to the Department of Earth, Atmospheric and
Planetary Sciences in partial fulfillment of the
requirements for the degree of

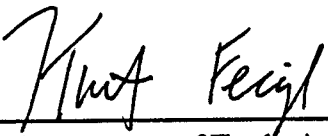
DOCTOR OF PHILOSOPHY


at the


MASSACHUSETTS INSTITUTE OF TECHNOLOGY

September, 1991

© Massachusetts Institute of Technology 1991. All rights reserved.

Signature of author 
Department of Earth, Atmospheric and Planetary Sciences
July, 1991

Certified by 
Professor Thomas H. Jordan
Department of Earth, Atmospheric and Planetary Sciences
Thesis supervisor

Accepted by 
Professor Thomas H. Jordan
Department Head

GEODETIC MEASUREMENT OF TECTONIC DEFORMATION
IN CENTRAL CALIFORNIA

by

KURT LEWIS FEIGL

Submitted to the Department of Earth, Atmospheric and
Planetary Sciences on July 18, 1991 in partial fulfillment of
the requirements for the Degree of Doctor of Philosophy

ABSTRACT

The object of this thesis is to measure directly the tectonic deformation in the Santa Maria Fold and Thrust Belt (SMFTB), northwest of Santa Barbara California. The principal measurement technique is space geodesy, using the signals transmitted by the satellites of the Global Positioning System (GPS). Beyond the introduction, the thesis contains three separate sections, concerning an improved model for drifting oscillators in the satellite and receiver, the analysis of historical surveying measurements, and finally an analysis of 5 years of GPS observations.

From March to August 1990, the microwave signals transmitted by the Block II satellites of the Global Positioning System (GPS) were dithered under a policy of "Selective Availability". The dithering appears as a $\sim 10^{-9}$ deviation of the satellite oscillator frequency, which, when accumulated over several minutes, can produce an error of ~ 100 cycles (~ 20 m) in the model for carrier beat phase. Differencing between simultaneously sampling receivers minimizes the error. If, however, the receivers do not sample simultaneously, it is necessary to model the frequency deviation, which we estimate from the phase observed at a station with a stable local oscillator. We apply such a model to data collected in March 1990 by TI4100 and MiniMac receivers sampling at times separated by 0.92 s. Applying the algorithm significantly improves the root mean square (RMS) scatter of the estimated relative position vectors. The RMS scatter from a data set including dithered satellites is similar for both simultaneously and non-simultaneously sampling receivers, a result which indicates that SA can be adequately modeled.

We have analyzed geodetic observations to resolve tectonic deformation across the SMFTB. The geodetic network forms a braced quadrilateral with ~ 40 km sides whose southwest corner is the Vandenberg very long baseline interferometry (VLBI) station. The data include (1) historical triangulation from the 1880s, 1920s and 1950s; (2)

electronic distance measurement trilateration from 1971 and 1985; and (3) GPS observations from 1986 and 1987. We combine the three different types of data to estimate two-dimensional station positions and strain rate parameters simultaneously. Using a model which constrains the relative velocity field to be linear in space and constant in time, we find significant strain rates. The maximum compressive strain is oriented $N17^{\circ}E \pm 5^{\circ}E$, and the compressive strain rate in this direction is 0.13 ± 0.03 $\mu\text{strain/yr}$. Under the assumption that the unresolved rotational component of the velocity field is zero, we estimate that the integrated rate of deformation across the basin is 7 ± 1 mm/yr oriented at $N03^{\circ}E \pm 13^{\circ}$. This vector can be decomposed into 6 ± 2 mm/yr of crustal shortening on the general structural trend of $N30^{\circ}E$ and 3 ± 1 mm/yr of right-lateral shear across this axis. On the basis of these values and earthquake focal mechanisms in the area, we infer that the deformation occurs on northwest trending folds and thrusts within the belt. These results are consistent with the rate and direction of deformation across the central California Coast Ranges inferred by balancing Pacific-North America plate motion against San Andreas slip and Basin and Range extension. They imply that the SMFTB is the primary active element in transforming motion from the Coast Ranges to the western Transverse Ranges and the Santa Barbara Channel.

We have used 5 years of GPS measurements to measure the relative velocities of five stations in the SMFTB. When considered with respect to the GPS mark nearest the Vandenberg VLBI station, the horizontal velocities of three stations are significantly different from zero at the 95% confidence level. The velocities indicate the importance of N-S compressional deformation in the area, as indicated by geologic cross sections, seismicity, earthquake focal mechanisms and borehole breakout data. The compressional components of the three most significant velocities are grossly consistent with the deformation predicted by a simple dislocation model involving two thrust faults in the SMFTB, in addition to deep slip on the San Andreas fault. The right-lateral components are larger than expected from either the fault model or the estimate from the 1879-1987 data set. This may be due to a possible systematic eastward bias in the geodetic estimation procedure, accumulation of unmodeled dextral shear, or a clockwise rotation with respect to North America.

Thesis supervisor:	Thomas H. Jordan
Title	Professor of Geophysics
Committee:	Professor Thomas A. Herring
	Dr. Robert W. King
	Dr. William H. Prescott
	Professor Leigh Royden

ACKNOWLEDGMENTS

One of the advantages of a data-driven thesis is the opportunity to work with colleagues outside the computer room. The guys of Detachment 1 of the Geodetic Survey Group at Vandenberg were always willing to show how "real surveyors" work. In particular, Sam Bangaol, C.D. Brown, Harry Harris, Jeff Kennedy, Bob Phillips, Josh Sermons, Bob Wideman, and Joe Zebrowski helped me out on numerous occasions, even though it wasn't really their job to do so.

Nor was it the job of the USGS scientists in Menlo Park to teach me about geophysics in the "real world" *i.e.*, California. Particular thanks go to Karl Gross, Michael Lisowski, David Oppenheimer, Ross Stein and Karen Wendt

My cohorts in GPS provided many hours of discussion and kilobytes of electronic mail, usually cursing programs and data formats, but occasionally discussing the Earth. They also helped bring home the data. For this, I wish to thank specifically Frank Webb, Kristine Larson, Zheng-kang Shen and Andrea Donnellan.

Danan Dong and Mark Murray were stalwart companions in the field, and patient with my naive questions about geodetic inverse problems in the lab.

Jeanne Sauber pointed out the history of geodetic measurements around Vandenberg. She also taught me to use the telephone as an advisor.

Tom Jordan showed me that good graphics and smooth prose help in the "business", as well as the scientific, side of geophysics. Rather than abandon me when he became chairman, he brought Tom Herring and Brad Hager to the sixth floor of the Green Building. He also deserves credit for mixing a mean margarita.

Yehuda Bock sharpened my skills in FORTRAN, file-naming conventions, and argumentation.

Bob King taught me about rules of thumb, and in five years of daily questions, never shooed me out of his office.

Tom Herring generously shared his software and his time. We spent many late Thursday nights in front of the computers, appreciating fresh plots and junk food.

Will Prescott taught me that suspect benchmarks are "guilty until proven innocent" and that "in this business, you want to keep everything the same".

Several geologists patiently tutored my kinematic intuition: Clark Burchfiel, Doug Clark, Jay Namson, Steve Nitchman, Burt Slemmons, and Wiki Royden.

Special thanks go to those who managed the money for my shopping and field trips: Anabela Afonso, Teresa Hernandez, Libby Kurten, Terri Macloon, Jan Sahlstrom, and Marie Sénat. Their sense of humor helped too.

My warm appreciation to all who were willing to share a meal and tell me a story.

Three Doctors Feigl have proceeded me on this path. I thank them and my brother Mark for their understanding support through the years.

Je voudrais surtout remercier Anne, pour tout.

CURRICULUM VITAE

Born January 30, 1962 in Göteborg, Sweden

HONORS

Hart Lyman Prize for Character and Achievement, Yale College, 1984

Phi Beta Kappa, 1985

Sigma Xi, 1985

Trumbull College, Yale University, Fellows' Prize, 1985

Hammer prize for presentation of senior thesis, Yale College, 1985

Belknap prize for excellence in geological studies, Yale College, 1985

NSF Graduate Fellowship, 1986-89

US Air Force Graduate Research Program Fellowship 1989-1991

EXPERIENCE

Research Assistant in geodynamics, Prof. Neil Ribe, Dept. Geology and Geophysics, Yale University, summer 1984.

Research Technician, R/V R. D. Conrad, Lamont-Doherty Geological Observatory, Columbia University, 1985-1986.

Graduate Student, MIT Dept. Earth, Atmospheric and Planetary Sciences, 1986-1991.

PUBLICATIONS

K. L. Feigl, R. W. King and T. H. Jordan, Geodetic measurement of tectonic deformation in the Santa Maria Fold and Thrust Belt, California, *J. Geophys. Res.*, 90, 2679-2699, 1990.

K. L. Feigl, R. W. King, T. A. Herring, and M. Rothacher, A scheme for reducing the effect of Selective Availability on precise GPS carrier phase measurements, *Geophys. Res. Lett.*, 18, 1289-1292, 1991.

TABLE OF CONTENTS

Abstract	2
Acknowledgments	4
Curriculum Vitae	5
Table of Contents	6

CHAPTER 1: INTRODUCTION

The San Andreas Discrepancy.....	9
Fault-normal Compression	11
Deformation in a Fold and Thrust belt.....	12
"Blind" Thrust Faults.....	13
Block Rotations	14
Development of a Geodetic Tool.....	14
Organization	15
Publications.....	17

CHAPTER 2: IMPROVEMENTS TO THE MODEL FOR CARRIER BEAT PHASE

Model for One-way Phase	19
Characterization of Oscillators.....	22
Drift of the Satellite Oscillator	24
Quadratic Polynomial Model	24
Relativistic Effects	26
Estimation of the Polynomial Coefficients.....	27
Drift of the Receiver Oscillator	30
Allan Standard Deviation of Different Types of Receivers.....	30
Automatic Calibration by the Receiver	31
Calibration of Receiver Clocks.....	33
Estimation of Receiver Clock Offset.....	33
Polynomial Model for Receiver Clock Offset	36
Epoch-by-Epoch Estimation of the Receiver Clock Offset.....	37
Polynomial Model for the Receiver Oscillator Frequency.....	37
Doubly Differenced Carrier Beat Phase	38
First Term.....	39
Second Term	39
Third Term.....	40
Fourth Term	40
Fifth Term	41
Improvements to MODEL in Version 8	41
First Term.....	41
Second Term	42
Third Term.....	44
Fourth Term	44
Fifth Term	45
Complete Expression.....	45
Shifting Time Tags For Split-sampled Observations	46
Application to Data.....	48
Correcting for the Effect of Selective Availability.....	53
Description of the Policy.....	53

Application of the Revised Model to Data in TREX 17	55
Conclusion	61

CHAPTER 3: GEODETIC MEASUREMENT OF TECTONIC DEFORMATION IN THE SANTA MARIA FOLD AND THRUST BELT, CALIFORNIA

Introduction	67
Tectonic Setting	71
The San Andreas Discrepancy	73
The Santa Maria Fold and Thrust Belt as an Active Tectonic Element	75
Data	76
Triangulation	80
Trilateration	80
GPS	81
Ties	83
Estimation of Strain Rates From Geodetic Data	84
Single Survey	84
Estimation Procedure	86
Multiple Surveys	87
Singularities in the Design Matrix	91
Derived Parameters	92
Comparison with Other Methods	98
Geodetic Results	98
Triangulation Only	102
Trilateration Only	106
Comparison With REDEAM	106
The 1927 Lompoc Earthquake	107
Discussion	108
Active Tectonics of the Santa Maria Fold and Thrust Belt	108
Implications for the San Andreas Discrepancy	112
The Santa Maria Fold and Thrust Belt as a Transition Zone	115
Deformation Rates in the Southern Coast Ranges	116
Tectonic Implications for the Western Transverse Ranges	117
Conclusions	118

CHAPTER 4: GPS MEASUREMENTS OF TECTONIC DEFORMATION IN THE FOOTPRINT OF THE VANDENBERG, CALIFORNIA VLBI STATION

Introduction	120
Motivation	120
Tectonic Setting	121
Previous Studies	124
Data	124
History of Geodetic Observations in the Network	124
Problems	137
Analysis	138
Single-day Solutions	139
Five-year Solutions	141
Results	145
Precision	145
Tie between GPS and VLBI at Vandenberg	148
Evolution of Interstation Vectors in Time	153

Velocities Relative to Vandenberg	162
Graphical Display of Deformation Fields	165
Uniform Strain over Subnetworks.....	167
Discussion	177
Robustness of the Velocity Estimates	177
Comparison with a Previous GPS estimate.....	181
Comparison with our Previous Result	183
Is the Motion Tectonic?	187
Strain Accumulation on the Locked San Andreas Fault	188
Tectonic Interpretation.....	191
Deformation in a Fold and Thrust Belt	191
Rotations.....	194
Conclusions	194

REFERENCES CITED

.....	203
-------	-----

CHAPTER 1

INTRODUCTION

...the sort of 'promissory note' type of hypotheses that so frequently function as place holders for more fully worked out theories should certainly be classified as scientific ...

Herbert Feigl [1963]

The object of this thesis is to measure directly the tectonic deformation in a corner of central California called the Santa Maria Fold and Thrust Belt (SMFTB). The area of study lies in the transition zone between the Southern Coast Ranges and the Western Transverse Ranges (Figure 3.1). It is the locus of several tectonic problems which we address with geodetic measurements.

The San Andreas Discrepancy

One of the primary motivations (and arguments for funding) this study is the "San Andreas Discrepancy". This argument is a vector balance. Starting with the vector velocity of the Pacific plate with respect to North America, we subtract vectors for the deformation observed at the plate boundary, notably slip on the San Andreas fault and extension in the Basin and Range province. If all the deformation is accounted for, the remaining vector should be zero; since it is not, we call it a discrepancy.

The word "discrepancy" first appeared in the description of the RM2 model for plate motions, where it was estimated at "about" 12 mm/yr [Minster and Jordan, 1978]. The same authors formally posed the problem as a vector balance [Minster and Jordan, 1984] and then improved their estimate of the deformation rate in the Basin and Range Province [Minster and Jordan, 1987]. The generation of a new plate motion model, NUVEL-1, yielded a smaller rate (48 mm/yr rather than 56 mm/yr) for the velocity between the North American and Pacific plates, shrinking the discrepancy [DeMets *et al.*, 1987; 1990; Jordan and Minster, 1988b]. The most recent work on the topic [Argus and Gordon, 1990; 1991] uses VLBI data and a model of simple shear to argue for a more northerly vector in the Basin and Range, shrinking the discrepancy even further, to 6 ± 3 mm/yr at N18°W (Figure 1.1). All these studies suggest that deformation is distributed across a zone extending hundreds of kilometers away from

the fault, accommodating the relative plate motion in a "broad, soft boundary" zone described by *Atwater* [1970].

Posing the problem in terms of a discrepancy can be misleading because it infers the distribution of deformation in California by measuring it elsewhere. Indeed, most of the uncertainty in the current estimates comes from the assumptions made in the Basin and Range. There, the difference between the pure extension in *Minster and Jordan's* [1987] Model B, and the pure shear model of *Argus and Gordon* [1991] is 15° in azimuth and zero mm/yr in rate. The change in azimuth alters the magnitude of the discrepancy by 2 mm/yr.

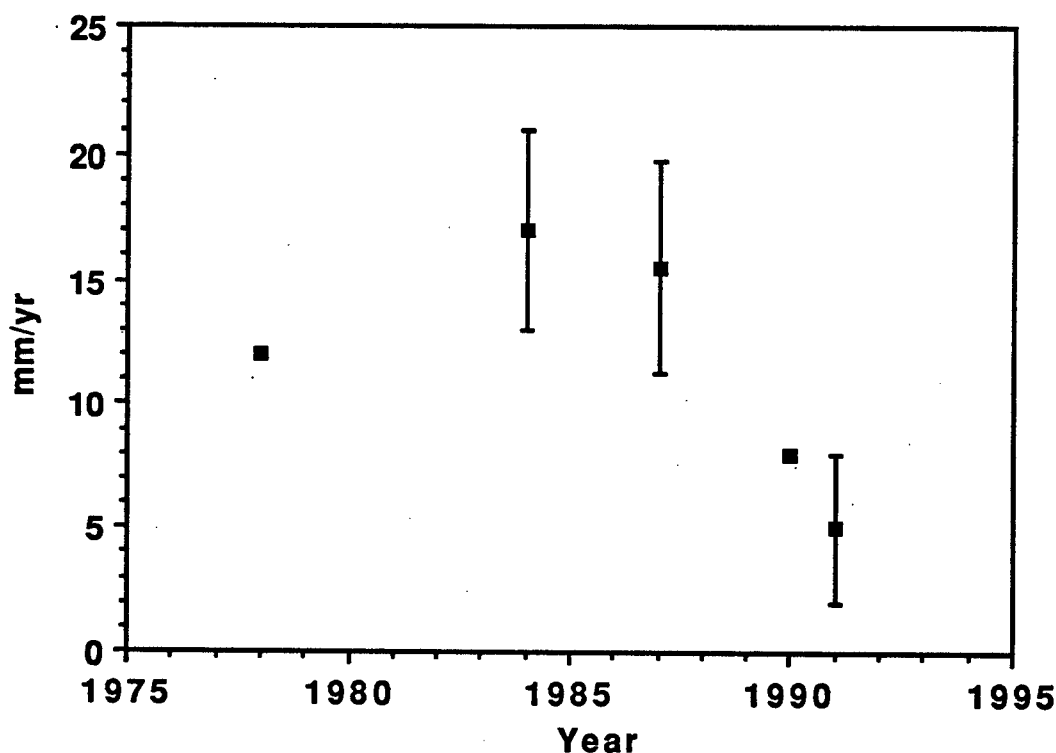


Figure 1.1. The magnitude of the "San Andreas Discrepancy" as a function of time. The estimates are from, in chronological order, *Minster and Jordan* [1978; 1984; 1987], *DeMets et al.* [1990], and *Argus and Gordon* [1991].

By announcing a discrepancy, *Minster and Jordan* have motivated many researchers to hunt for the "missing motion". Their introduction of path integrals to sum deformation [*Minster and Jordan*, 1984] has added a quantitative aspect to studies of California neotectonics [e.g. *Bird and Rosenstock*, 1984; *Weldon and Humphreys*, 1985; *Sedlock and Hamilton*, 1991]. The hunt for the discrepancy has also prompted several geodetic studies [*Sauber*, 1989; *Ward*, 1990; *Savage et al.*, 1990; *Argus and*

Gordon, 1990; 1991] all of which have "found" the missing motion somewhere onshore.

Fault-normal Compression

Deformation in California appears to be partitioned into two components: strike-slip on the San Andreas fault and compression normal to it, with very little oblique slip [Mount and Suppe, 1987]. Although the Pacific and North America plates are separated by the San Andreas fault, their relative motion does not exactly parallel the fault. The velocity of the Pacific plate with respect to North America is oriented at $N36^{\circ}W (\pm 2^{\circ})$ [DeMets *et al.*, 1990], while the San Andreas fault strikes $N41^{\circ}W (\pm 2^{\circ})$ in the northern segment between $N35.1^{\circ}$ and $N36.5^{\circ}$ [Minster and Jordan, 1984]. Compression normal to this section of the fault occurs in the southern Coast Ranges. The key observations are the orientation of fold axes [Reed and Hollister, 1936; Page, 1966], the presence of thrust faults [Crouch *et al.*, 1984], lower bounds on rates of shortening inferred from balanced cross sections [Namson and Davis, 1990], earthquake focal mechanisms [Dehlinger and Bolt, 1988], and geodetic measurements [Harris and Segall, 1987].

The difference in orientation between the relative plate motion vector and the San Andreas, and thus the importance of compression, increases to the south, as the San Andreas sweeps around the Big Bend into the western Transverse Ranges. Here the fault strikes about $N73^{\circ}W$, some 37° away from the relative plate motion vector. South of the fault, the compressional component of the deformation occurs on a N to NNE axis, as indicated by fold axes [Reed and Hollister, 1936; Jahns, 1954], balanced cross sections [Namson and Davis, 1988], and earthquake focal mechanisms [Lee *et al.*, 1979]. In this area, the geodetically estimated velocities [Eberhardt-Phillips *et al.*, 1990; Lisowski *et al.*, 1991] do not conclusively show fault-normal compression, perhaps because the "outer coordinate solution" [Prescott, 1981] used in both studies is designed to minimize it. The strain rates estimated in the off-fault part of the Los Padres network, however, show a significant compressive component oriented due North ($N01^{\circ}E \pm 2^{\circ}$) [Eberhardt-Phillips *et al.*, 1990]. Further east, the Ventura Basin is undergoing rapid (7–20 mm/yr) convergence, as indicated by geodetic measurements [Donnellan *et al.*, 1991], fault slip rates [Yeats, 1981, 1983, 1988], balanced cross sections [Yeats *et al.*, 1988], and the uplift rates of fluvial and marine terraces [Rockwell *et al.*, 1984; 1988].

Although fault-normal compression had been documented in both the southern Coast Ranges and in the western Transverse Ranges, prior to this thesis, it had not been

measured in the area between them. That area, which includes the SMFTB, is adjacent to the point where the San Andreas "turns the corner" into the Big Bend. As such, it appears to be a transition zone between the neighboring tectonic domains, a hypothesis which we confirm with measurements in Chapters 3 and 4.

Our results indicate compression normal to the San Andreas fault, corroborating the observation that the crust accommodates oblique convergence by partitioning the strain into two components: one compressive and one strike-slip. Such partitioning was first recognized in the Sunda arc by *Fitch* [1972]. It has since been suggested for New Zealand [*Walcott*, 1987a,b], New Guinea [*Abers and McCaffrey*, 1988], and western North America since the Mesozoic [*Beck*, 1983; 1986]. The mechanism to explain this observation is somewhat controversial. One popular hypothesis is that the San Andreas is "weak", that is, unable to support shear stress [*Mount and Suppe*, 1987; *Zoback et al.*, 1987]. After reviewing the occurrence of partitioning, *Molnar* [1991] argues that it is due to the orientation (essentially horizontal or vertical) of the principal stresses in the continental lithosphere, rather than to the weakness of the fault. In another model, *Sonder* [1990] suggests that the fault-normal orientation could be due to a high-density feature beneath the western Transverse Ranges as imaged with seismic tomography [*Humphreys et al.*, 1984; *Hearn and Clayton*, 1986a,b; *Humphreys and Clayton*, 1990] and confirmed by a gravity study [*Scheffels and McNutt*, 1986]. The high-density feature has been interpreted as small-scale convection, and may be responsible for much of the tectonic activity in the western Transverse Ranges [*Humphreys and Hager*, 1990].

Deformation in a Fold and Thrust belt

The compressive deformation in fold and thrust belts has been extensively studied on the geologic time scale of millions of years. Specific folds may be described using kinematic models for fault-bend folding [e.g., *Suppe*, 1983] or fault-propagation folding [e.g., *Suppe and Medeweff*, 1990]. By assuming that the thickness of the rock layers is conserved, these models allow the construction of balanced cross sections which can then be restored ("retrodeformed") to their undeformed state. Another possible assumption is that the rock particles are always displaced parallel to the underlying active fault segment [*Contreras and Suter*, 1990]. In either case, if the beds are properly dated, the amount of slip can be used to calculate rates of crustal shortening, a technique which has been recently applied in the California Coast and Transverse Ranges [*Namson and Davis*, 1988; *Davis et al.*, 1988; 1989]. In the Santa Maria Fold and Thrust Belt, two such cross sections [*Nitchman et al.*, 1990; *Namson*

and Davis, 1990] have been used to estimate rates of crustal shortening, which we compare with geodetic measurements in Chapters 3 and 4.

The mechanics of an entire fold and thrust belt have been modeled assuming that the deformation takes places at a critically tapered wedge at the verge of failure [Suppe, 1981; Davis *et al.*, 1983; Dahlen *et al.*, 1984; Dahlen, 1984; Barr and Dahlen, 1990, 1991; Barr *et al.*, 1991]. Although developed for Taiwan, these models predict that deformation rates increase toward the toe of the wedge. For the case of the SMFTB, such a model would imply higher strain rates toward the SW, a prediction which we can test using the geodetic measurements in Chapter 4.

"Blind" Thrust Faults

The 1983 Coalinga earthquake produced a magnitude $M_s = 6.5$ event without rupturing the surface [Stein and King, 1983]. Since that event, geophysicists have increasingly worried about the seismic hazard of such "blind" faults concealed beneath active folds [Yeats, 1988; Namson and Davis, 1989; Stein and Yeats, 1989]. The concern would appear to be justified in light of the $M_L = 5.9$ Whittier Narrows event, which caused \$358 million in damage without rupturing the surface [Hauksson *et al.*, 1988; Davis *et al.*, 1989; Hauksson and Jones, 1989; Lin and Stein, 1989]. In addition, the recent and damaging Loma Prieta earthquake exhibited an unexpected thrust component, suggesting the importance of folding [U.S. Geological Survey Staff, 1990].

If strain accumulates prior to such earthquakes, then geodetic measurements can bring useful constraints to bear on the problem of forecasting them [Lisowski *et al.*, 1990a]. Even if the intra-seismic deformation is not detectable, the observations made prior to a large earthquake are indispensable for measuring the coseismic displacement. Such measurements were available for the Loma Prieta event, and contributed to a model for its source mechanism [U.S. Geological Survey Staff, 1990; Lisowski *et al.*, 1990b].

The area studied in this thesis, the Santa Maria Fold and Thrust Belt, appears to be actively folding, and may be at risk for an earthquake on a blind fault [Nitchman *et al.*, 1990; Namson and Davis, 1990]. Since there do not appear to be any active faults which obviously cut Quaternary deposits in the area [Jennings, 1975; Sylvester and Darrow, 1979; Clark *et al.*, 1984; Manson, 1985], identification of the actively deforming features is difficult. It is for this reason that we have started a series of geodetic measurements with dense spatial and temporal sampling. Using the rates

estimated from these measurements, we can begin to identify which features are currently accommodating the deformation.

Block Rotations

An intriguing model for describing continental deformation consists of relatively rigid blocks moving relative to each other [e.g., *Hill, 1982; Matsu'ura et al., 1986*]. Clearly, one of the allowable motions is a rotation about a vertical axis, a scenario often invoked to describe the kinematics of deformation in California [e.g., *Luyendyk et al., 1980; 1985; Terres and Luyendyk, 1985; Kammerling and Luyendyk, 1985*]. In the Santa Ynez part of the Western Transverse Ranges, paleomagnetic declinations of $15\text{--}35^\circ$ in rocks dated to 5–20 Ma suggest minimum rotation rates of several degree/Ma, depending on the onset of deformation [*Hornafius, 1985; Hornafius et al., 1986*]. Such rates of rotation are difficult to measure directly with geological techniques unless the slip rates on the faults bounding the blocks can be estimated from displaced pairs of piercing points at several locations.

Space geodesy, however, can detect rotation with vector measurements of station position with respect to an external reference frame. Since $5^\circ/\text{Ma}$ is about $0.1 \mu\text{radian/yr}$ or one part in $10^7/\text{yr}$, rates of this order should just be resolvable in short intervals of time using current techniques. Indeed, *Sauber's* [1988] results from Very Long Baseline Interferometry (VLBI) suggest that Vandenberg and a site in Pasadena (JPL) lie on different rigid blocks, both of which appear to be rotating clockwise with respect to North America at $0.11 \pm 0.06 \mu\text{radian/yr}$ [*Jackson and Molnar, 1990*]. The vector observations in Chapter 4 permit a test of this hypothesis.

Development of a Geodetic Tool

The principal observations in this study are geodetic measurements made with signals transmitted by the satellites of the Global Positioning System (GPS). The basic technique is least-squares adjustment of geodetic parameters from carrier beat phase data, obtained by comparing the satellite signal to that of a local oscillator. The trail from raw phase data to estimates of relative station positions is a long one, strewn with important details. A complete description is beyond the scope of this study, but may be found in several guidebooks [*King et al., 1985; Wells et al., 1986; Leick, 1990*] and theses [*Remondi, 1984; Rocken 1988; Larson 1990; Murray, 1991*]

At the time I applied to graduate school, the best published GPS results were precise to 1 part in 10^6 , or 10 mm over 10 km [*Bock et al, 1985*], not precise enough for tectonic studies. A few years later, precisions of 1–2 parts in 10^8 have been achieved

for vectors several 1000 km in length [e.g., *Lichten and Bertiger*, 1989]. For tectonic studies, vectors 50 to 100 km are the most useful, and their horizontal components may be determined, over several years, with a precision of about 6 mm (see Chapter 4) allowing relative velocities to be estimated with a resolution of several mm/yr.

This improvement in precision is partially due to developments in receiver technology and the addition of satellites, but it is also a direct result of a flurry of research on techniques for analyzing the data. Much of the research concerns effects which make the difference between a centimeter and a millimeter. Because the comprehensive treatment of these developments has been undertaken elsewhere [*Leick*, 1990; *Bilham*, 1991; *Dixon et al.*, 1991; *Hager et al.*, 1991; *Murray*, 1991], I concentrate in Chapter 2 on my own contribution to improving the model for carrier beat phase.

The results in Chapter 4, however, depend critically on the contributions of others at MIT, particularly techniques for resolving integer phase ambiguities [*Dong and Bock*, 1989 and unpublished suite], generating a self-consistent reference frame [*Murray*, 1991], and estimating velocities [*Herring et al.*, 1990].

These improvements have been incorporated, with great effort, into a software package called GAMIT, for GPS Analysis at MIT [*King and Bock*, 1991]. It is a tool sufficiently precise for measuring tectonic deformation.

Organization

This thesis is about measuring deformation in the Santa Maria Fold and Thrust Belt. It is divided into three parts: improvements to the GPS technique, an estimate using pre-existing historical measurements, and a modern estimate using GPS observations.

Chapter 2 is a complete treatment of the effects of drifting oscillators on geodetic GPS measurements. The derivation was undertaken to handle the decrease, beginning in 1990, of the stability of the oscillators used during our observations in California. The receiver oscillators declined in quality when we began using lightweight Trimble 4000 SST receivers in January, 1990. The crystal oscillators in these receivers are about two orders of magnitude less stable than those in the TI4100 receivers used previously. The difference in stability required a modification in our approach for calibrating the receiver "clock".

The satellite oscillators also declined in stability. From March to August 1990, the signals transmitted by the Block II satellites were dithered under a policy of "Selective Availability" (SA). The dithering appears as a $\sim 10^{-9}$ deviation of the satellite oscillator frequency, which, when accumulated over several minutes, can produce an error of

~100 cycles (~20 m) in the model for carrier beat phase. Differencing between simultaneously sampling receivers minimizes the error. If, however, the receivers do not sample simultaneously, it is necessary to model the frequency deviation, which we estimate from the phase observed at a station with a stable local oscillator. We have developed such a model and applied it data collected in our March 1990 observations.

Chapter 3 describes an estimate of deformation in the SMFTB obtained by combining over 100 years of geodetic measurements. The geodetic network forms a braced quadrilateral with ~40 km sides whose southwest corner is the Vandenberg VLBI station. The data include (1) historical triangulation from the 1880s, 1920s and 1950s; (2) electronic distance measurement trilateration from 1971 and 1985; and (3) GPS observations from 1986 and 1987. We combine the three different types of data to estimate two-dimensional station positions and strain rate parameters simultaneously. Using a model which constrains the relative velocity field to be linear in space and constant in time, we find significant strain rates. The maximum compressive strain is oriented $N17^{\circ}E \pm 5^{\circ}E$, and the compressive strain rate in this direction is $0.13 \pm 0.03 \mu\text{strain/yr}$. Under the assumption that the unresolved rotational component of the velocity field is zero, we estimate that the integrated rate of deformation across the basin is $7 \pm 1 \text{ mm/yr}$ oriented at $N03^{\circ}E \pm 13^{\circ}$. This vector can be decomposed into $6 \pm 2 \text{ mm/yr}$ of crustal shortening on the general structural trend of $N30^{\circ}E$ and $3 \pm 1 \text{ mm/yr}$ of right-lateral shear across this axis. On the basis of these values and earthquake focal mechanisms in the area, we infer that the deformation occurs on northwest trending folds and thrusts within the belt. These results are consistent with the rate and direction of deformation across the central California Coast Ranges inferred by balancing Pacific-North America plate motion against San Andreas slip and Basin and Range extension. They imply that the Santa Maria Fold and Thrust Belt is the primary active element in transforming motion from the Coast Ranges to the western Transverse Ranges and the Santa Barbara Channel.

Chapter 4 extends the analysis of Chapter 3 by including the GPS measurements collected since 1986. The five years of GPS data can provide more information than the hundred-year data set of Chapter 3 because they produce a vector measurement which is almost ten times more precise than the 1 ppm early trilateration observations, and almost fifty times more precise than the 1-second triangulation observations. In addition, the GPS network provides more redundant observations than available in the conventional surveying network. For example, the line between Lospe and Vandenberg has been measured five times in as many years. These improvements in data quality allow us to estimate a more realistic model of deformation than the uniform

strain assumed in Chapter 3. With the GPS data, we can estimate the vector velocities of the four principal stations with respect to Vandenberg.

The stations are moving with respect to the VLBI site at Vandenberg. The velocities estimated from the GPS data are greater than 2 mm/yr for all four stations, and are significant (at the level of 95% confidence) for three stations. The components of motion at N30°E indicate compression, consistent with the tectonic interpretation presented in Chapter 3. The rate of compression is grossly consistent with the displacements predicted from a simple model of two thrust faults in the SMFTB plus deep slip on the San Andreas fault system. The right-lateral components, however, are larger than predicted by the fault model, indicative of a rotational artifact in the geodetic analysis or additional accumulation of dextral shear. In addition, the observed velocities also indicate a significant rate (81 ± 8 nanoradian/yr) of clockwise rotation.

Publications

This thesis is an assemblage of manuscripts, both published and to be submitted. Chapter 3 has been published in its entirety as *Feigl et al.* [1990]. The section of Chapter 2 describing our correction for Selective Availability has been accepted for publication in *Geophys. Res. Lett.* as *Feigl et al.* [1991]. Finally, Chapter 4 is intended for submission to *J. Geophys. Res.* with R. W. King, T. A. Herring and T. H. Jordan as coauthors.

CHAPTER 2

IMPROVEMENTS TO THE MODEL FOR CARRIER BEAT PHASE

Time travels in divers paces with divers persons.

Shakespeare, *As You Like It*, III, ii

The phase observations used in GPS measurements depend on the oscillators in the satellite and in the receiver. The observed quantity is the beat phase from a comparison of the periodic signal transmitted by the satellite with the one generated in the receiver. Although both the satellite and receiver oscillators drift, the effect of this drift can be removed by differencing the phase observations between satellites and between receivers ("double differencing"). To be completely effective, this approach should only be applied to observations of the same transmitted wavefront. This condition is approximately satisfied when all the receivers in a network sample at the same point (epoch) in time. When different types of receivers are used in the same network, however, the different sampling epochs can create serious errors, which we quantify and correct in this chapter.

For double differencing to succeed, the sampling epoch must be known absolutely to ~ 1 ms, and differentially (between epochs) to $\sim 1 \mu\text{s}$. Meeting these requirements is straightforward in most cases because we have effective polynomial models for the behavior of drifting clocks [e.g., King *et al.*, 1985]. In a few cases, however, the simple polynomial models cannot be readily applied. One such case involves receivers which reset their own clocks, creating a discontinuous series of time tags. The second case occurs when the satellite oscillator is dithered under a policy of "Selective Availability" imposed by the Department of Defense. In this chapter, we extend the polynomial models to handle these two cases.

In applying the extended clock models, we have encountered three sampling protocols which can cause minor, but surmountable, problems. *Asynchronous* sampling occurs when two receivers do not sample at the same point in time. *Irregular*

sampling occurs when one receiver does not sample at regular intervals, i.e., the period between samples varies. *Split* sampling occurs when one receiver samples different quantities (e.g., phase and pseudorange) at different times.

To quantify the error caused by different sampling protocols, we first derive an expression for undifferenced ("one-way") phase. Since this expression involves terms describing the drift of oscillators in both the satellite and in the receiver, we devote one section to the characterization of oscillators. The next two sections describe the estimation of oscillator parameters for the satellite and for the receiver. We then use these parameters in a new model for the carrier beat phase. By performing the double difference operation term by term, we quantify the error incurred by the previous model, which assumed synchronous sampling.

Finally, we apply the new model to data collected during the TREX 17 campaign in March, 1990. These observations require the new model for two reasons. First, they were collected by receivers programmed to sample at times almost 1 s apart. Second, they were collected while the signals transmitted by the satellite were dithered by Selective Availability (SA).

MODEL FOR ONE-WAY PHASE

We follow the derivation in *King et al.* [1985], but use the subscript s to denote the satellite, and r to denote the receiver. The observed quantity is the carrier beat phase ψ , formed by differencing the received phase ϕ and the phase of the local oscillator θ

$$\psi(t_r) = \phi_r(t_r) - \theta(t_r) \quad (2.1)$$

The time t_s of transmission from the satellite is related to the time of reception t_r by the propagation time (or delay) τ

$$\tau = t_r - t_s \quad (2.2)$$

The propagation time τ is composed of three terms

$$\tau = \tau_g + \tau_a + \tau_i \quad (2.3)$$

where the three terms on the right are the geometric, atmospheric and ionospheric contributions to the delay, respectively.

The geometric delay τ_g is the time (about 70 ms) for light to propagate across the distance from the satellite to the receiver in a vacuum. It is the most important term for geodetic measurements, because it contains information about the coordinates of the station. It also contains information about the orbital position of the satellite, and is

therefore calculated iteratively, as described by *King et al.* [1985, § 5.1.6] and *Rocken* [1988, § 2.3].

Our model for the geometric delay also includes station displacements due to solid Earth tides. The amplitude of the tide due to the moon's pull is about half a meter [e.g., *Stacey*, 1977]. The ETIDE subroutine in MODEL uses an extremely simple model which calculates the gravitational potential due to the sun and the moon [see *Lambeck*, 1980]. The response is then predicted with the Love number h_2 , and the the Shida number k_2 , [e.g., *Stacey*, 1977], both of which are assumed to be constant and independent of position and frequency. A more complicated model with frequency dependent h_2 and k_2 would result in modest (< 10 mm) changes in the vertical [*McCarthy*, 1989].

We do not include the effect of loading due to ocean tides, which is a vertical signal of 9.7 mm for Vandenberg, near the coast, and 2.8 mm for Owens Valley, for the M_2 tide. The O_1 and K_1 tides can each contribute about 10 mm, but not in phase with M_2 , according to *McCarthy's* [1989] calculations for VLBI sites using the technique of *Goad* [1980].

The atmospheric delay τ_a is caused by refraction in the troposphere and stratosphere and has a magnitude of about 8 ns (~ 2 m) at zenith and 27 ns (~ 8 m) at 15° elevation. We treat this effect by predicting an approximate value, and then estimating the departure from that value as an atmospheric delay parameter. The approximate value is calculated in the ATMDL subroutine of MODEL [J. L. Davis, 1987], which predicts the "wet" and "dry" components of the tropospheric delay at zenith using the model of *Saastemoinen* [1972]. For the California experiments analyzed in Chapter 4, we assume the following "typical" meteorologic conditions at sea level:

Pressure	1013.25 mb
Temperature	20.0 °C
Relative humidity	50%

The pressure at the elevation of the station is calculated by upward extrapolation assuming hydrostatic equilibrium [(2.2.8) of *Davis*, 1986] and a lapse rate (vertical temperature gradient) [*Holton*, 1979] of $-4.5^\circ\text{C}/\text{km}$. The assumed values are only approximately valid, but avoid the biases inherent in meteorologic measurements taken on the ground [e.g., *Tralli et al.*, 1988]. Since the atmospheric path length is a function of the satellite elevation angle, the zenith delay is then calculated for the satellite elevation angle according to the "CfA 2.2 mapping function" described by *Davis et al.* [1985].

Because the atmospheric delay is highly variable in time and space, we allow a deviation from the approximate value calculated by MODEL by estimating (in SOLVE) a zenith delay parameter at each station. For stations in California, this parameter is usually less than 1 ns (30 cm) in magnitude. At the moment, SOLVE assumes that the atmospheric delay parameter is constant throughout the observing session. This assumption appears to be reasonable for our 8-hour nighttime observing sessions at stations in California, but may be inadequate for longer sessions, or for the more humid conditions found in Mexico [Tralli *et al.*, 1988] or the Caribbean [Dixon *et al.*, 1991]. A more comprehensive approach [J. Genrich, program in preparation, 1991] will use a Kalman filter to estimate a stochastic atmospheric delay parameter as in the analysis of VLBI data [e.g., Herring *et al.*, 1990; Davis *et al.*, 1991].

The third term τ_i is the delay caused by propagation through the ionosphere and can range from 20 to 150 ns (6–50 m). The ionosphere is a dispersive medium, and the delay is nearly proportional to the inverse square of the frequency f

$$\tau_i = -\frac{IN_e}{f^2} + O\left(\frac{1}{f^3}\right) \quad (2.4)$$

where N_e is the areal electron density ("total electron content") along the signal path in electrons/m² [Hartmann and Leitingner, 1984]. The term I is a constant equal to $1.35 \times 10^{-7} \text{ m}^2/\text{s}$ [King *et al.*, 1985]. It is equal to h/c in the notation of Kleusberg [1986]. The term in $1/f^3$ is due to the interaction of the electrons in the ionosphere with the magnetic field (see § 7.6 of Jackson [1976] for a model). Although it is commonly neglected, this term can attain 100 ps (~30 mm) in the L1 frequency when the total electron content is extremely high [Kleusberg, 1986].

Since the electron content is a rapidly varying function of time, whose amplitude is larger near the magnetic poles and equator, handling the ionospheric delay has been the subject of several studies [Georgiadou and Kleusberg, 1988; Wild *et al.*, 1989]. The usual approach is to eliminate the $1/f^2$ ionospheric term by forming a linear combination of the L1 and L2 phase measurements. This combination is called "the ionosphere-free observable", "LC" in the GAMIT jargon [Bock *et al.*, 1986] and "L3" in the Bernese jargon [Wild *et al.*, 1989]. If only single-frequency L1 observations are available, the standard algorithm is that of Klobuchar [1987]. In any case, the approach used in GAMIT is to set $\tau_i = 0$ in MODEL, and then handle the ionospheric delay explicitly in SOLVE. At that point, the options are (1) to estimate an ionospheric delay parameter, (2) to form the ionosphere-free combination LC, or (3) both of these in the form of the "ionospheric constraint" described by Bock *et al.* [1986].

Returning to our derivation, we know that the received phase is the same as the transmitted phase at time $t_s = t_r - \tau$

$$\phi_r(t_r) = \phi_s(t_s) = \phi_s(t_r - \tau) \quad (2.5)$$

Expanding $\phi_s(t_s)$ in a Taylor series about t_r

$$\phi_r(t_r) \doteq \phi_s(t_r) - \dot{\phi}_s(t_r)\tau + \frac{1}{2}\ddot{\phi}_s(t_r)\tau^2 \quad (2.6)$$

where the negative sign results from the fact that t_s is earlier than t_r . The temporal derivatives of the transmitted phase evaluated at the time of reception t_r are

$$\begin{aligned} \phi_s(t_r) &= \phi_s(t_0) + \int_{t_0}^{t_r} f_s(t) dt \\ \dot{\phi}_s(t_r) &= f_s(t_r) \end{aligned} \quad (2.7)$$

$$\ddot{\phi}_s(t_r) = \dot{f}_s(t_r)$$

In these expressions, f_s designates the frequency of the satellite transmitter, which we are approximating by its value observed at the receiver. Substituting (2.7) into (2.6), we can rewrite expression (2.1) for the beat phase

$$\psi(t_r) = \phi_s(t_0) + \int_{t_0}^{t_r} f_s(t) dt - f_s(t_r)\tau + \frac{1}{2}\dot{f}_s(t_r)\tau^2 - \theta(t_r) \quad (2.8)$$

where phase decreases with increasing delay (range). This convention for the sign of the phase, in which the temporal derivatives of the phase and Doppler shift have the same sign, may be called the *Doppler convention*. We note that MODEL is written in the *pseudorange convention*, where the temporal derivative of the phase has the same sign as the temporal derivative of the (pseudo)range. The formula (2.8) is the basic equation of the model. After discussing the parameterization of the satellite and receiver oscillators, we shall return to this equation.

CHARACTERIZATION OF OSCILLATORS

The measurement of beat phase depends critically on the behavior of oscillators, both in the satellite and the receiver. Each of the oscillators performs two functions, acting as a frequency standard and as a clock. Used as frequency standards, oscillators

generate the wave $e^{i\phi(t)}$ transmitted by the satellite and the wave $e^{i\theta(t)}$ for the beat comparison in the receiver. Used as clocks, the oscillators generate a "tick" each time their output function crosses the zero level. A counter accumulates the number of ticks and converts it to a time tag in seconds by dividing by the ticking frequency. In the satellite, this time tag is coded into the pseudorange signal as the time of transmission. In the receiver, the time tag is recorded as the time of reception.

The stability of an oscillator is traditionally characterized by its fractional frequency stability σ_y , which is the square root of its 2-sample Allan variance [e.g., Allan, 1966; Hellwig, 1974; Vessot, 1976; Allan, 1987]. Following the lead of Herring *et al.* [1990], we call the quantity σ_y the "Allan standard deviation". To estimate it, we perform n successive measurements of the oscillator's output phase $\phi(t_i)$ and calculate the statistic

$$\sigma_y = \sqrt{\sum_{i=1}^{n-1} \frac{1}{2(n-1)} (y_{i+1} - y_i)^2} \quad (2.9)$$

where y_i is a two-point estimate of the deviation of the frequency from its nominal value f_0

$$y_i = \frac{(\phi_{i+1} - \phi_i)}{f_0(t_{i+1} - t_i)} - 1 \quad (2.10)$$

The value depends on the sampling interval between measurements. In the GAMIT software package, the Allan standard deviation σ_y is estimated for satellite oscillators by the program MAKEJ.

An alternative to the stochastic description provided by the σ_y statistic is a deterministic description in terms of a polynomial function. It is conventional to write such a polynomial expression for the offset in the time tag caused by the drifting oscillator. For example, the time tag t' assigned by an oscillator differs from the true time t by an amount Δt , which is often assumed to be a polynomial function of time

$$\Delta t = t' - t = c_0 + c_1 t + c_2 t^2 \quad (2.11)$$

In the following two sections, we will apply this model to the satellite oscillator, designating the coefficients c_i as $a^{(i)}$, and to the receiver oscillator as $b^{(i)}$. In most cases, we will estimate one set of coefficients for the entire session (typically about 8 hours).

Typical values for the Allan standard deviation σ_y and the dimensionless clock drift c_1 are given in Table 2.1. For the oscillators used in GPS, it is not easy to derive a

relation between the two quantities, because our best estimates of σ_y are made from 30 s samples, while those of c_1 cover about 8 hours ($\sim 3 \times 10^4$ s). The dominant noise process is different at the two time scales [e.g., Vessot, 1976]. The procedures for estimating these quantities from GPS data are described below.

Table 2.1 Oscillator statistics

Oscillator type	Example	Allan standard deviation $\sigma_y(30 \text{ s})$	Drift c_1 over 8 hours
Quartz crystal	Seiko wristwatch		$10^{-5} a$
Quartz crystal	Trimble 4000 SST receiver	$\sim 10^{-10}$	10^{-7}
Quartz crystal	TI 4100 receiver	3×10^{-12}	10^{-8}
Quartz crystal	TI 4100 receiver	$1 \times 10^{-11} b$	
Quartz crystal	Minimac receiver		10^{-10}
Quartz crystal	"state of the art"	$3 \times 10^{-13} c$	
Rubidium	PRN 6 in February 1991	1×10^{-12}	10^{-11}
Cesium	PRN 02 in January 1990	3×10^{-12}	10^{-12}
Dithered cesium	PRN 02 in March 1990	1×10^{-10}	10^{-9}
Hydrogen maser	CIGNET sites	$1-2 \times 10^{-14} d$	10^{-13}
Hydrogen maser	"state of the art"	$8 \times 10^{-15} c$	

Notes:

- a* Mine is good to about 30 s/month.
- b* Extrapolated from *Clynch and Coco* [1989].
- c* From *Allan* [1987].
- d* Extrapolated from *Herring et al.* [1990].

DRIFT OF THE SATELLITE OSCILLATOR

The oscillator in the satellite usually drifts with a dimensionless rate of $c_1 \sim 10^{-12}$ (Table 2.1). If it is dithered under the policy of "Selective Availability" (SA), the apparent drift can reach 2×10^{-9} . This drift effects both the satellite clock and the transmission frequency, and may be modeled with a quadratic polynomial.

Quadratic Polynomial Model

The drifting satellite clock labels the signal transmitted at true time t_s with a satellite time tag t_s' . The offset Δt_s is conventionally written as a quadratic function of time

$$\Delta t_s = t_s' - t_s = a^{(0)} + a^{(1)}(t - t_0^{(c)}) + a^{(2)}(t - t_0^{(c)})^2. \quad (2.12)$$

When SA is off, one such polynomial can provide an adequate fit over a span of up to several days and we can use the values of the coefficients $a^{(0)}$, $a^{(1)}$, $a^{(2)}$, and the reference time $t_0^{(c)}$ as transmitted by the satellite in the Navigation Message. These parameters are labelled a_{f0} , a_{f1} , a_{f2} , and t_{0c} respectively in § 20.3.3.3.3 of the Interface Control Document [Rockwell International, 1984]. When SA is on, however, we will need a new set of coefficients more frequently, at least every 30 seconds.

Expression (2.12) is sometimes written with an additional Δt_{rel} term to correct for the effects of special and general relativity [Rockwell International, 1984]. We can safely ignore this term in MODEL, for the reasons discussed below.

The time of transmission, corrected for the drift of the satellite oscillator is

$$t_s = t_r' - \Delta t_r - \tau \quad (2.13)$$

where t_r' is the receiver time tag, Δt_r is the receiver clock offset (calculated below), and τ is the theoretical delay. In the FORTRAN source code for MODEL, we write the transmission time as

$$TSEND = TOBS - RCLOCK - DELAY$$

The drifting satellite oscillator shifts the frequency of the transmitted signal and is best understood by analogy with a wristwatch. A watch which is running "fast" ticks too frequently. Similarly, the satellite keeps its time t_s' by counting zero crossings (ticks) of its oscillator. The actual frequency f_s of the oscillator is related to the "speed" of the clock by

$$f_s = \frac{dt_s'}{dt_s} f_0 \quad (2.14)$$

Since $dt_s'/dt_s = 1 + a^{(1)} + 2a^{(2)}(t - t_0^{(c)})$, we can write the actual transmission frequency as

$$f_s(t) = [1 + a^{(1)} + 2a^{(2)}(t - t_0^{(c)})] f_0 \quad (2.15)$$

This expression is equivalent to (5.6) of King *et al.* [1985], but our $a^{(1)}$ corresponds to their a and our $a^{(2)}$ to their b .

Relativistic Effects

Relativity distorts the apparent nominal frequency. A signal which is observed at the receiver to have frequency f_0 was actually transmitted with frequency f_0' . The shift in frequency is due to the effects of general and special relativity, as well as Doppler shift. The frequency shift δ [Spilker, 1980] may be written as

$$\delta = \frac{f_0}{f_0'} - 1 = \frac{U_s - U_r}{c^2} + \frac{1}{2} \left(\frac{V_r^2}{c^2} - \frac{V_s^2}{c^2} \right) + \frac{\mathbf{k}}{c} \cdot (\mathbf{V}_s - \mathbf{V}_r) \quad (2.16)$$

where U_s and U_r are the gravitational potentials of the satellite and receiver respectively, and \mathbf{V}_s and \mathbf{V}_r are their velocities in an inertial reference frame. The unit vector \mathbf{k} points from satellite to receiver. The three terms on the right side of (2.16) represent the effects of general relativity, special relativity, and Doppler, respectively.

The first term represents the "gravitational redshift" of general relativity. It arises because the satellite transmitter and the earth-bound receiver lie at different points in the Earth's gravitational potential field [e.g., Soffel, 1989]. If the GPS satellites were in a circular orbit, the shift would be constant, and approximately equal to -4.443×10^{-10} [Van Dierendonck et al., 1978]. Since the actual orbit has an eccentricity of approximately 0.02, the frequency shift varies with the 12 hour orbital period.

The second term is the frequency shift due to special relativity. The satellite and receiver travel in an inertial frame with velocities $V_s \sim 3.8$ km/s and $V_r \sim 4.3$ km/s, respectively, creating a frequency shift of order 10^{-11} , depending on the satellite's location in the orbit, and the receiver's location on the Earth.

The third term is due to Doppler shift. For a typical value of relative velocity between satellite and receiver, the frequency shift is of order 10^{-6} , four orders of magnitude times larger than the shift due to relativity. The Doppler shift is treated explicitly by the iterative calculation of the geometric delay, described above.

In practice, an average value of the relativistic frequency shift $\delta = 4.45$ is built into the satellite oscillator, which is set before launch to $f_0' = (1 - 4.55 \times 10^{-10}) \times 10.23$ MHz [Spilker, 1978]. Departures from this value occur due to the eccentricity of the satellite orbit, and lead to an offset of ~ 50 ns in the satellite clock [Van Dierendonck et al., 1978; Leick, 1990]. The relativistic satellite clock offset is indistinguishable from an offset due to a drifting oscillator, and is thus incorporated into the broadcast coefficients $a^{(0)}$, $a^{(1)}$, $a^{(2)}$ for the satellite clock offset [Van Dierendonck et al., 1978]. In any case, the effect of the offset vanishes when differenced between synchronously sampled receivers, as shown below. For this reason, we do not apply any relativistic

corrections in MODEL, although *Leick* [1990] suggests that one may be applied by the receiver.

Estimation of the Polynomial Coefficients

When Selective Availability (SA) is off, the satellite oscillator is more stable than the oscillator in a portable receiver (Table 2.1). When SA is on, the satellite oscillator appears to have an Allan standard deviation of $\sigma_y \sim 10^{-10}$. If left unmodeled, this unstable behavior can cause an important error in the asynchronous sampling case, as we shall show below. In this section, we derive a model to describe a satellite oscillator dithered by SA.

If the receiver oscillator is a stable atomic frequency standard, and the coordinates of the receiver are well known, they may be used to calibrate a dithered satellite oscillator. Specifically, we use the phase residuals from such a receiver to estimate the polynomial coefficients $a^{(1)}$ and $a^{(2)}$, corresponding to the dimensionless frequency deviation of the satellite oscillator and its drift rate in s^{-1} . The receivers in the Cooperative International GPS Network (CIGNET) provide useful data for this purpose, because many stations are equipped with extremely stable ($\sigma_y(30\text{ s}) \sim 10^{-14}$) hydrogen masers. Using data from one or more CIGNET stations, we fit at each epoch t_i a second order polynomial to the residual (observed minus calculated) beat phase $\tilde{\psi} - \bar{\psi}$ using data from three epochs centered on t_i

$$\tilde{\psi}(t_i) - \bar{\psi}(t_i) \equiv c_0 + c_1(t - t_i) + c_2(t - t_i)^2 \quad (2.17)$$

In order to obtain the most accurate estimate of frequency for times close to t_i , we would like the samples of phase to be as closely spaced as possible.

Differentiating phase to obtain an expression in frequency, we can write

$$\frac{d}{dt}(\tilde{\psi} - \bar{\psi}) = c_1 + 2c_2(t - t_i) \quad (2.18)$$

Since the local oscillator is stable, we assume that our model for it is perfect and does not contribute to the residual beat phase

$$\frac{d}{dt}(\tilde{\psi} - \bar{\psi}) = \frac{d}{dt}(\tilde{\phi}_s - \bar{\phi}_s) = \tilde{f}_s - \bar{f}_s \quad (2.19)$$

where \tilde{f}_s is an improved model of the dithered satellite frequency, and \bar{f}_s is a reference model for the satellite frequency as in (2.15). In practice, the coefficients $\bar{a}^{(1)}$ and $\bar{a}^{(2)}$ in the reference model may be obtained from the Navigation Message or determined from the observed phase over a longer segment of the data. Using the coefficients c_1

and c_2 estimated from (2.16), we can write the transmitted satellite frequency for a time near t_i as

$$\tilde{f}_s(t) = [1 + \tilde{a}^{(1)} + 2\tilde{a}^{(2)}(t - t_i)]f_0 \quad (2.20)$$

where

$$\tilde{a}^{(1)} = \frac{c_1}{f_0} + \bar{a}^{(1)} + 2(t_i - t_c)\bar{a}^{(2)} \quad (2.21)$$

$$\tilde{a}^{(2)} = \frac{c_2}{f_0} + \bar{a}^{(2)} \quad (2.22)$$

Figure 2.1 shows these quantities estimated every 30 s for two different satellites in March, 1990, one of which was dithered by SA.

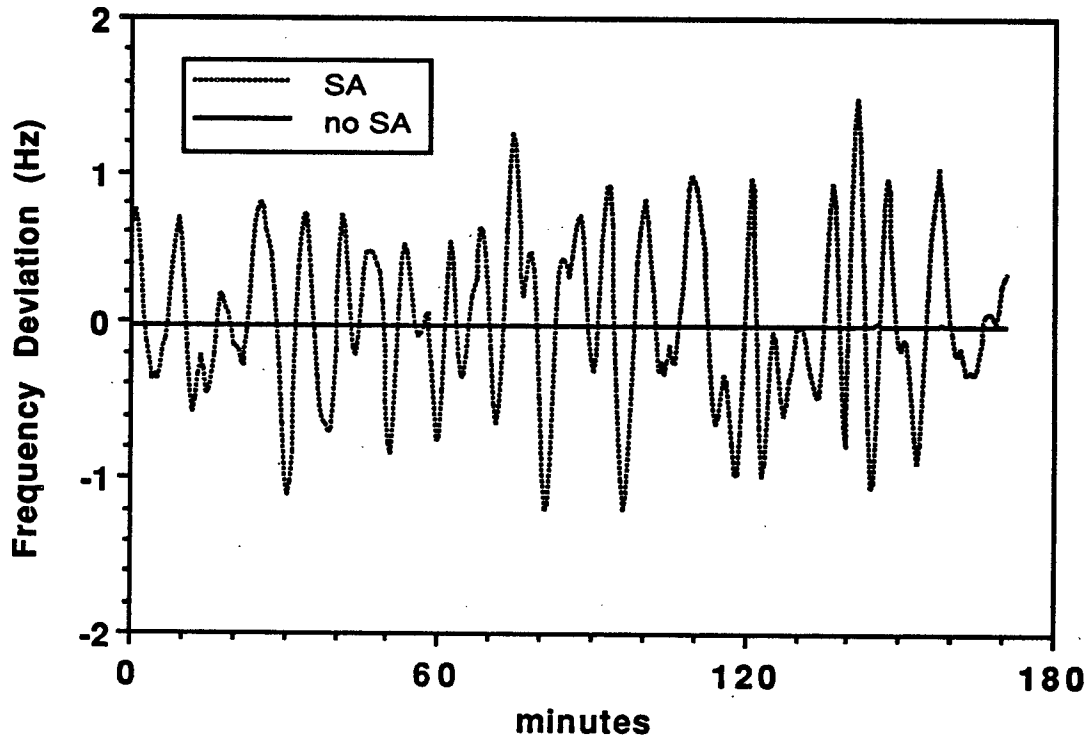


Figure 2.1. Deviation of the satellite transmission frequency from its nominal L1 value for a dithered satellite, PRN 2 (dashed line), and an undithered satellite, PRN 6 (solid line). The values are the L1 nominal frequency $f_0 = 1.57542$ GHz multiplied by the frequency deviation $\tilde{a}^{(1)}$ estimated from phase data via (2.21).

We assume that the residual (2.17) is due entirely to the dithering effect. The validity of such an assumption depends on minimizing several other sources of error.

First, we consider our model for the local oscillator to be perfect, since the hydrogen maser at one of the CIGNET stations has an Allan standard deviation $\sigma_y(30\text{ s}) \sim 10^{-14}$, about four orders of magnitude more stable than the satellite oscillator we are calibrating (Table 2.1). Second, we assume that any errors in modeling the satellite orbit and station coordinates do not contaminate our estimate of $\Delta\psi$. Since the observed Doppler shift is one part in 10^6 in frequency, the error in even a crude (10^{-6}) estimate of the orbit will effect our estimate at the level of 10^{-12} , comparable to the unmodeled variations in an undithered satellite oscillator.

We have chosen to calibrate the satellite clock in terms of frequency, rather than phase, because it could be readily incorporated into our software via the same look-up table used for the broadcast satellite clock coefficients, \bar{a}_1 and \bar{a}_2 . This approach does, however, necessitate evaluating the integral in (2.8).

The formulation in frequency allows us to incorporate calibrations estimated from other schemes. For example, *Rocken and Meertens* [1991] present two other methods for monitoring the satellite oscillator frequency. The first technique is called "Doppler-differencing" and involves forming the discrete derivative of closely sampled (every 3 s) phase observations. This derivative is the satellite frequency modified by the Doppler shift and the receiver oscillator drift rate. This method is equivalent to fitting a first order polynomial to the residual phase in our approach.

Their second technique is called "double difference monitoring". *Rocken and Meertens* [1991] difference the phase observed by two receivers sampling the phase from the same antenna, but at times separated by 0.1 s. They then difference between a dithered satellite and an undithered (Block I) satellite. Forming the discrete derivative of the phase over such a short time interval can provide a very accurate picture of the deviation of the satellite oscillator frequency, which may even be applied in real time. This technique requires two items which are not always available: an extra receiver with a programmable sample time and an undithered Block I satellite in view throughout the observing period. Unfortunately, during our observations in March of 1990, we did not have the first item; future GPS experiments are unlikely to have the second.

Yet a third approach to calibrating satellite oscillators is to re-map the observed phase to the time of transmission using a polynomial. This scheme, proposed by *Wu et al.* [1990], contrasts with ours because it estimates one such polynomial for each station. It does not apply the calibrations from stations with stable clocks to those with poor clocks. Since it requires either a frequency model or a receiver oscillator accurate to

about 1 Hz, this technique is not appropriate for our experiment, which used portable receivers with crystal oscillators.

DRIFT OF THE RECEIVER OSCILLATOR

Allan Standard Deviation of Different Types of Receivers

The crystal oscillator in the receiver typically drifts several orders of magnitude faster than the satellite oscillator (Table 2.1). We can characterize its behavior by estimating the Allan standard deviation σ_y from phase data via equation (2.9). To eliminate the effect of the satellite oscillator, we difference the observed phase between two receivers. If one of the receivers employs a stable ($\sigma_y(30\text{ s}) \sim 10^{-14}$) hydrogen maser as its oscillator, we can use it to calibrate the less stable ($\sigma_y(30\text{ s}) > 10^{-11}$) quartz oscillator in the second receiver.

We have measured the stability of the oscillators in several types of receiver (Figure 2.2). With up to 10 hours of data, sampled at 30 s, we are able to obtain reliable estimates with a sampling period of up to 3000 s. Beyond this point, the stability estimate is based on fewer than ten points and begins to break down. Different satellites yield estimates which differ slightly at longer sampling intervals, because each satellite is visible for a different time span.

The drift of the receiver oscillator affects both the epoch of the measurement (time tag) t_r' , and the frequency f_r used for the beat measurement. As for the satellite oscillator, we follow the convention of (2.11) and parameterize the drift in terms of its effect on time. The drifting oscillator shifts the time tag t_r' away from the true time of receipt t_r by an amount Δt_r

$$\Delta t_r = t_r' - t_r \quad (2.23)$$

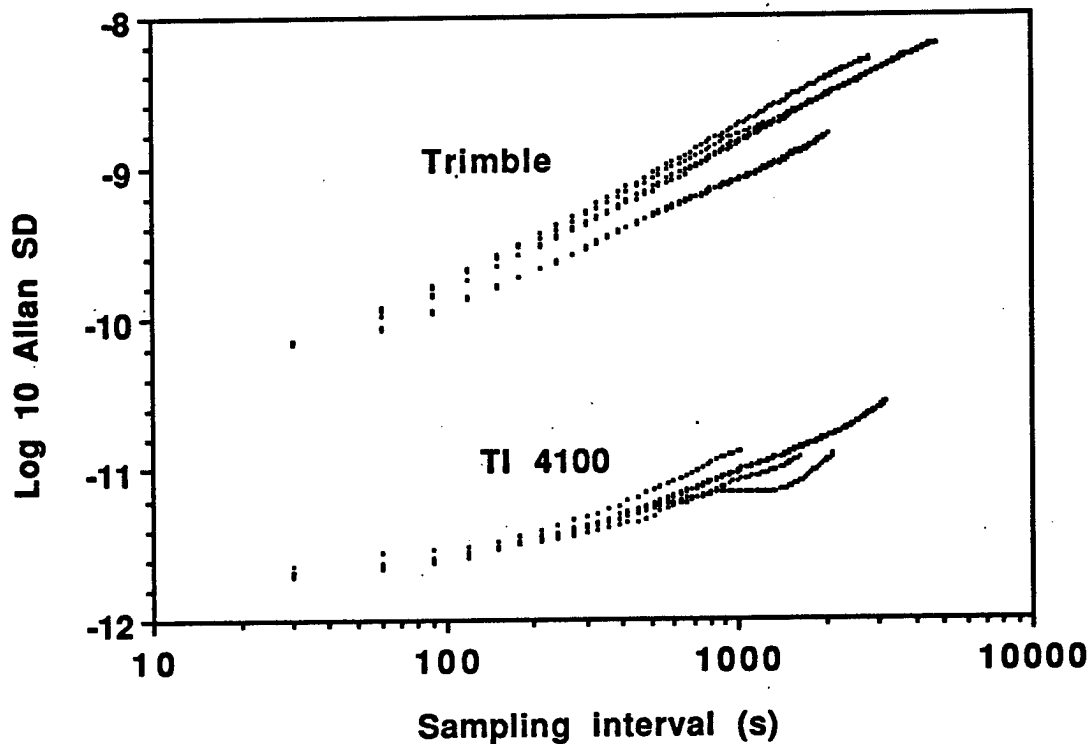


Figure 2.2. Allan standard deviation σ_y for the crystal oscillator in two types of receiver. The TI4100 is about 30 more times more stable than the Trimble 4000 SST. Each trace denotes observations of a different satellite. The estimates were performed by application of (2.9) to phase observations differenced between the field receiver at Vandenberg and one at Mojave, where the local oscillator is a hydrogen maser. The TI4100 data were collected April 1, 1989; the Trimble data on February 6, 1991.

Automatic Calibration by the Receiver

In Trimble and Ashtech receivers with inexpensive crystal oscillators, the clock drift is typically fast enough that the offset Δt_r can grow to exceed 1 ms in less than one hour (Figure 2.3). These receivers perform their own internal estimates of Δt_r based on the expression

$$\Delta t_r = \frac{\rho_1 - r}{c} + \Delta t_s \quad (2.24)$$

where r is the calculated range to the satellite, ρ_1 is the observed pseudorange and c is the speed of light. The calculated range r is just the magnitude of the vector difference between the coordinates of the station and the coordinates of the satellite. In the

receiver's internal calculation, the coordinates of the satellite are predicted from the orbital parameters included in the broadcast Navigation Message. The station coordinates are usually taken from the real-time navigational estimate, but may be constrained by the operator. When the receiver software's estimate of the offset Δt_r exceeds a threshold, the time tag is reset to reduce the offset Δt_r . In the Trimble receiver, the threshold is 1 ms, and the time tags are always reset by the same amount. The Ashtech receiver performs the same correction, but with threshold and reset values of 2 ms.

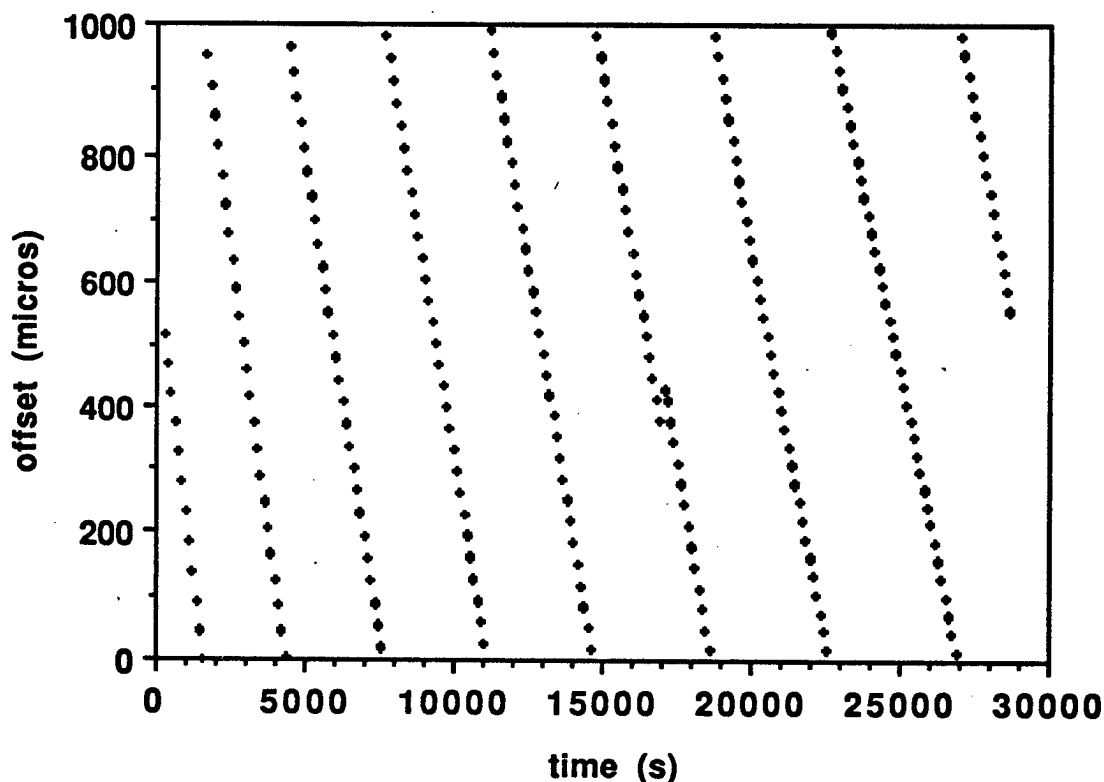


Figure 2.3. Typical clock offsets with several breaks. These data were collected by a Trimble 4000 SST receiver running version 4.11 of the NAV+SIG operating software. The receiver was located at Vandenberg (VNDN) on February 6, 1991. The offset at 17 ks is apparently due to a power failure.

When the receiver resets the time tag, it introduces a "jump" into the recorded pseudorange. The TRINEXO program [Gurtner, 1989] which translates raw Trimble data to the standard RINEX format [Gurtner *et. al.*, 1989a] detects the jumps in the pseudoranges and attempts to reverse the reset in the time tag. Certain early versions of the program performed this "recorrection" incorrectly. In this case, the receiver clock

offset Δt_r estimated from the pseudorange in the RINEX file exceeds 1 ms without resetting. In some of these files, the pseudoranges appear to be corrupted such that they cannot be used to calibrate the receiver clock offset Δt_r . To avoid this problem, we set the detection threshold for this program to 999 ms, so that no resets are ever detected.

Calibration of Receiver Clocks

The GAMIT software records the calibration of the receiver clock in K-files. Each record of a K-file contains the time of calibration and the estimated receiver clock offset Δt_r . These records may be determined in two ways. The first (and usual) method is to calculate the receiver clock offset Δt_r from the measured pseudorange and the broadcast ephemeris, using the calibration expression (2.24). This calculation may be performed in preprocessing, by the program MAKEX, or at a later stage by the program MAKEK. Both these programs call the subroutine STNCLK.

The second method involves directly measuring the clock offset Δt_r in the field by collocating two receivers. This method is used only for the Macrometer V1000 and Macrometer II receivers. Since these receivers were not used in any of our California campaigns, we will not discuss this method further.

Estimation of Receiver Clock Offset

The CLKERA subroutine estimates the polynomial coefficients from the observed clock offsets in the K-file. This routine is now robust to discontinuities ("clock breaks") in the K-file. It assumes two models for the offsets: (1) a simple first order (linear) polynomial and (2) a third order (cubic) polynomial with an arbitrary number of breaks. In the second (more robust) model, the clock offsets are assumed to be piecewise continuous, where segments of continuous data are interrupted by breaks. The rate $b^{(1)}$ acceleration $b^{(2)}$ and cubic $b^{(3)}$ term are assumed to be the same for all the segments (Figure 2.3). The breaks are detected by performing a cubic fit to the current segment. If the offset deviates by more than 10 μ s from the value predicted by the cubic fit over the current segment, then it represents a break, and thus the first point of the next segment. The model of the clock offsets is thus

$$\Delta t = b^{(0)} + b^{(1)}(t-t_0) + b^{(2)}(t-t_0)^2 + b^{(3)}(t-t_0)^3 + p_1 H(t-t_1) + p_2 H(t-t_2) \dots p_J H(t-t_J) \quad (2.25)$$

where t is the nominal time tag of reception (t_r), and a break at time t_j is described by the Heaviside step function $H(t)$ and a magnitude ("jump") p_j . The number of jumps J

may vary from zero to 20. The estimates of $b^{(0)}$, $b^{(1)}$, $b^{(2)}$, and $b^{(3)}$ are displayed for the user, who is then asked to select a parameterization: either the linear fit or the cubic fit with jumps. The appropriate estimates are then written to the S-file for later input to MODEL. The values of the jumps p_j are not retained, because they can be more accurately estimated by MODEL via an epoch-by-epoch correction, described below. Figure 2.4 shows the dimensionless frequency deviation $b^{(1)}$ estimated for several receivers. Since the value of this quantity is relatively constant from day to day, but degrades over several months, it may be a good measure of the health of the receiver.

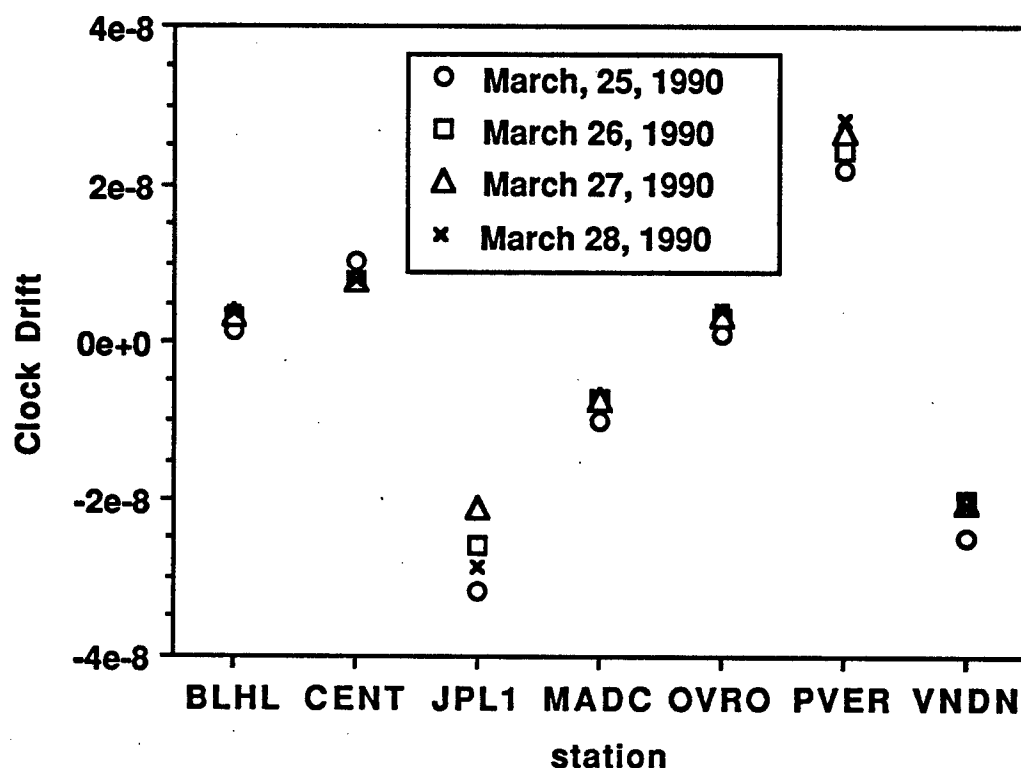


Figure 2.4a. Dimensionless clock drift $b^{(1)}$ of the local oscillators in the TI4100 receivers used in the March 1990 TREX17 campaign, where the same receiver was used for four sequential days at each station.

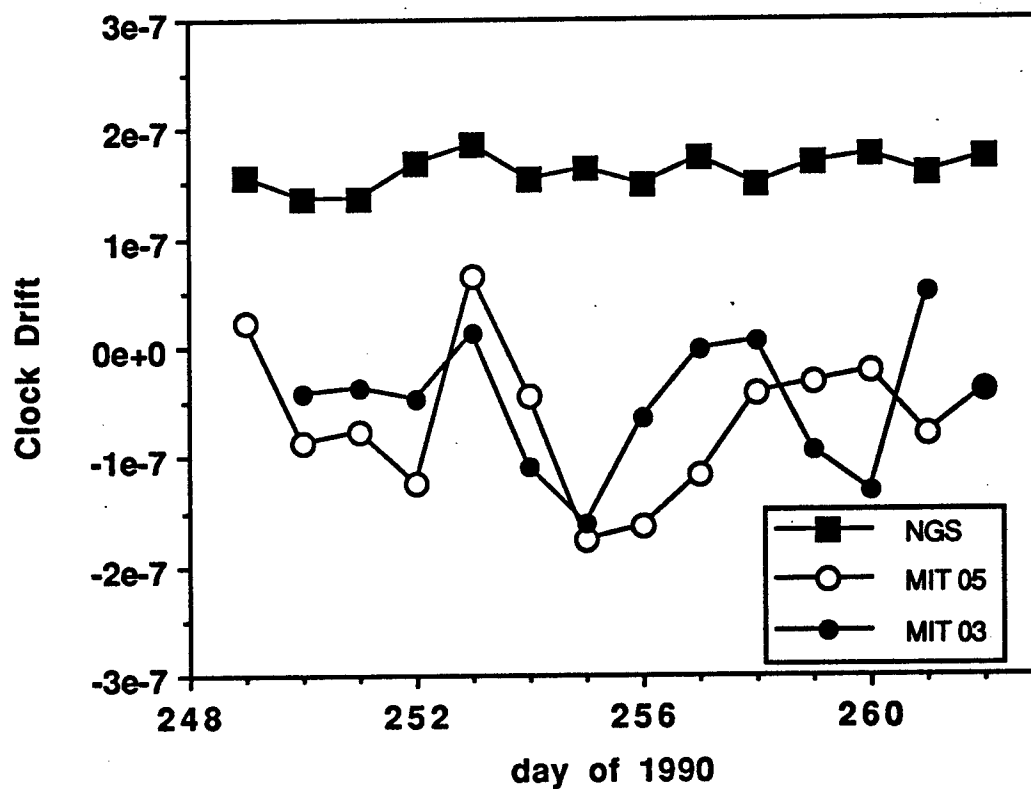


Figure 2.4b. Dimensionless clock drift $b^{(1)}$ of the local oscillators in the Trimble 4000 SST receivers used in the September, 1990 VF2 campaign. The Trimble clocks drift an order of magnitude faster than the TI4000s. Note the change in scale from the previous plot. The NGS receiver at Vandenberg operated continuously on AC power.

Polynomial Model for Receiver Clock Offset

One option for calculating the receiver clock offset Δt_r in MODEL is the polynomial expression

$$t_r' - t_r = \Delta t_r = b^{(0)} + b^{(1)}(t-t_0) + b^{(2)}(t-t_0)^2 + b^{(3)}(t-t_0)^3 \quad (2.26)$$

The coefficients $b^{(0)}$, $b^{(1)}$, and $b^{(2)}$, $b^{(3)}$ are read from the S-file as CLKEPC, CLKRAT, CLKACC and CLKCUB respectively. The first three terms correspond to q , r , and $s/2$ in the quadratic expression (5.10) of King *et al.* [1985]. (Note that the term involving q in their (5.11) should be deleted). The units for these quantities have been problematic¹, but have been rendered consistent in version 8.8 of MODEL. The clock coefficient CLKEPC is measured in seconds, CLKRAT is dimensionless, CLKACC is in s^{-1} , and CLKCUB is in s^{-2} .

Once read from the S-file by MODEL, the values of the coefficients are used to calculate the receiver clock offset Δt_r as RCLOCK.

```
TRMT0 = (JDOBS-J0)*86400.0D0 + TOBS-T0
RCLOCK = CLKEPC +
        + CLKRAT*TRMT0
        + CLKACC*TRMT0*TRMT0
        + CLKCUB*TRMT0*TRMT0*TRMT0
```

Note that this FORTRAN expression does not assume regularly sampled data, as did earlier versions. This seemingly minor improvement is important for Trimble receivers running version 3.25 of the TRM+NAV software, which sample the phase at irregular intervals. For these receivers, incorrectly assuming regular sampling commits an error at each epoch of up to 30 ns for a satellite with a rapid drift of $\alpha^{(1)} \sim 10^{-7}$.

The advantage of the cubic polynomial over a quadratic one appears to be a reduction in the RMS of the undifferenced one-way phase by a factor of two. Although this improvement is not necessary to achieve acceptable doubly differenced residuals, it can aid somewhat in detecting and repairing cycle slips.

We note that the MiniMac receivers at the CIGNET stations are programmed to perform this correction internally, so that Δt_r (RCLOCK) is zero. In practice, we set the all the clock coefficients $b^{(0)}$, $b^{(1)}$, $b^{(2)}$, and $b^{(3)}$ to zero in the S-file entries for MiniMac receivers.

¹ To avoid confusion in using old S-files, we document the modification history of the program here. Prior to version 7.11 of MODEL, the units for CLKACC were day/s², but incorrectly labeled as 1/day in S-files. Such S-files are not compatible with more recent versions of MODEL. Prior to version 8.7 of MODEL, the cubic term $b^{(3)}$ was assumed to be zero. Such S-files are compatible with more recent versions of MODEL.

Epoch-by-Epoch Estimation of the Receiver Clock Offset

The second method for modeling the receiver clock is to estimate the offset Δt_r from the observed pseudorange ρ_1 . In this technique, called "epoch-by-epoch station clock corrections", MODEL simply calculates Δt_r at each epoch using the calibration equation (2.24) in subroutine AVCLCK

$$\text{RCLOCK} = \text{PRANGT} - \text{DELAY} + \text{SVDT}$$

where PRANGT is the observed group delay (ρ/c) and SVDT is the satellite clock offset Δt_s . It is calculated by subroutine READJ using equation (2.15) and the satellite clock polynomial coefficients $a^{(0)}, a^{(1)}, a^{(2)}$ read from the J-file.

There are several measurements of RCLOCK (one for each satellite) which we average to estimate the receiver clock offset Δt_r . Since the pseudoranges may be also be corrupted by Selective Availability, the average counts the pseudoranges from the undithered Block I satellites with 100 times more weight than those from the Block II satellites. If any measurement of Δt_r lies more than 2 standard deviations from the weighted mean, it is rejected and the mean value recalculated.

Whether we use a polynomial or an epoch-by-epoch correction, the receiver clock correction Δt_r is applied in MODEL as

$$\begin{aligned} t_r &= t_r' - \Delta t_r \\ \text{TRCVR} &= \text{TOBS} - \text{RCLOCK} \end{aligned} \quad (2.27)$$

Polynomial Model for the Receiver Oscillator Frequency

The second effect of the drifting receiver oscillator is to perturb the frequency f_r of the signal used to beat against the signal received from the satellite. As with the satellite oscillator, the wristwatch analogy is valid, and the actual frequency f_r deviates from its nominal value f_0

$$f_r = \frac{dt_r'}{dt_r} f_0 \quad (2.28)$$

Taking the derivative dt_r'/dt_r of the polynomial (2.26) we can write the actual receiver frequency as

$$f_r = \left(1 + b^{(1)} + 2b^{(2)}(t-t_0) + 3b^{(3)}(t-t_0)^2 \right) f_0 \quad (2.29)$$

A possible simplification is to assume $f_r(t) = f_0$ at all times. This assumption is harmless if differences between satellites are formed (see below), but leaves large residuals dominated by the receiver clocks in the one-way phase². For this reason, we avoid the assumption, and calculate the receiver frequency f_r explicitly from (2.28). The computation is straightforward because the coefficients $b^{(1)}$ and $b^{(2)}$ are available directly from the S-file. We note, however, that in the epoch-by-epoch case, the CLKEPC coefficient $b^{(0)}$ is not used.

DOUBLY DIFFERENCED CARRIER BEAT PHASE

We now carry the complete expression for carrier beat phase through the double difference operation, which differences observations between satellites and between stations. The motivation is to quantify the errors introduced when the data are irregularly or asynchronously sampled. We can re-write the expression (2.8) for the theoretical carrier beat phase with a complete subscripted notation, where the terms are designated s and/or r if they depend on the satellite and/or receiver, respectively.

$$\psi_{sr}(t_r) = \phi_s(t_0) + \int_{t_0}^{t_r} f_s(t) dt - f_s(t_r) \tau_{sr} + \frac{1}{2} \dot{f}_s(t_r) \tau_{sr}^2 - \theta_r(t_r) \quad (2.30)$$

We now introduce an operator Δ_r to perform the difference between receiver $r = 2$ and $r = 1$ where Arabic numerals will be used index receivers. For example, the between-receiver difference of the receiver oscillator frequencies may be written as

$$\Delta_r f_r = f_2 - f_1 \quad (2.31)$$

In a strictly analogous manner, we use an operator Δ_s to perform the difference between satellite $s = II$ and satellite $s = I$, where Roman numerals will be used to index satellites. For example, the between-satellite difference of the satellite frequencies may be written as

$$\Delta_s f_s = f_{II} - f_I \quad (2.32)$$

Note that differencing between satellites with Δ_s eliminates receiver-dependent terms, while differencing between receivers with Δ_r eliminates satellite-dependent terms. Finally, we can define the double-difference operator as $\Delta_r \Delta_s$.

The motivation for this notation is to double-difference the expression (2.30) for the

² This assumption was made in version 7.1 of MODEL for the case of epoch-by-epoch clock corrections.

theoretical carrier beat phase, which we now do term by term.

First Term

The first term on the right-hand side of (2.30) is an arbitrary constant representing the satellite phase at the reference time t_0 . Since it is the same for all receivers, it vanishes when differenced between two of them

$$\Delta_s \Delta_r \phi_s(t_0) = 0 \quad (2.33)$$

Second Term

The drift of the satellite oscillator integrated from the initial epoch appears as the second term on the right hand side of (2.30). Differencing it between receivers, we find

$$\Delta_r \int_{t_0}^{t_r} f_s(t) dt = \int_{t_1}^{t_2} f_s(t) dt \quad (2.34)$$

Using equation (2.15) for the satellite oscillator frequency f_s , it is easy to evaluate the integral

$$\Delta_r \int_{t_0}^{t_r} f_s(t) dt = f_0 \left\{ (1 + a^{(1)}) (t_2 - t_1) + a^{(2)} \left[(t_2 - t_0^{(c)})^2 - (t_1 - t_0^{(c)})^2 \right] \right\} \quad (2.35)$$

Taking the double difference and assuming that the satellite clock polynomials are evaluated at the same epoch, so that $t_I^{(c)} = t_{II}^{(c)}$

$$\begin{aligned} \Delta_s \Delta_r \int_{t_0}^{t_r} \omega_s(t) dt &\doteq \omega_0 \left\{ (a_{II}^{(1)} - a_I^{(1)}) (t_2 - t_1) \right. \\ &\quad \left. + (a_{II}^{(2)} - a_I^{(2)}) \left[(t_2^2 - t_0^{(c)2}) - (t_1^2 - t_0^{(c)2}) \right] \right\} \end{aligned} \quad (2.36)$$

We can approximate to first order because the accelerations over periods of an hour are quite small ($a^{(2)} \sim 10^{-17} \text{ s}^{-1}$). With Selective Availability in operation, the acceleration term is larger ($a^{(2)} \sim 10^{-10} \text{ s}^{-1}$ over 30 s) but the reference time $t_0^{(c1)}$ is chosen to be within 1 s of the receipt time t_r . To first order, then, the double-difference of the second term of (2.30) is

$$\Delta_s \Delta_r \int_{t_0}^{t_r} f_s(t) dt \doteq f_0(a_I^{(1)} - a_I^{(1)})(t_2 - t_1) \quad (2.37)$$

This term vanishes if the two receivers sample the phase at the same time, such that $t_1 = t_2$. When they sample at different times, for example, $(t_2 - t_1) \sim 1$ s, the term can exceed 0.1 cycle. In this case, (2.37) provides a rough idea of the error caused by assuming a constant value for the satellite oscillator frequency. We shall consider the conditions under which such an assumption is valid in the section (below) on "improvements to MODEL". First we complete the term-by-term analysis of equation (2.30).

Third Term

Most of the geometric signal appears in the third term on the right side of (2.30). Its double difference is

$$\begin{aligned} \Delta_s \Delta_r f_s(t_r) &= f_0 \Delta_s \Delta_r [1 + a_s^{(1)} + 2a_s^{(2)}(t - t_0^{(c)})] \tau_{sr} \\ &= f_0 [\Delta_s \Delta_r \tau_{sr} + \Delta_s \Delta_r a_s^{(1)} \tau_{sr} + 2\Delta_s \Delta_r a_s^{(2)} \tau_{sr} (t - t_0^{(c)})] \\ &\sim (10^9 \text{ Hz}) [(10^{-2} \text{ s}) + (10^{-11})(10^{-2} \text{ s}) + (10^{-17} \text{ s}^{-1})(10^4 \text{ s})(10^{-2} \text{ s})] \\ &\sim 10^7 + 10^{-4} + 10^{-6} \text{ cycles} \end{aligned} \quad (2.38)$$

It is thus safe to approximate

$$\Delta_s \Delta_r f_s(t_r) \doteq f_0(\tau_{I11} - \tau_{I12} - \tau_{I1} + \tau_{I2}) \quad (2.39)$$

Fourth Term

The second order (in Δt) term from the Taylor series appears in the fourth term on the right-hand side of (2.30). After double-differencing, it is

$$\begin{aligned} \Delta_s \Delta_r \dot{f}_s(t_s) \tau_{rs}^2 &= \Delta_s \Delta_r f_0 a_s^{(2)} \tau_{sr}^2 \\ &= f_0 \Delta_s (a_s^{(2)} \tau_{s2}^2 - a_s^{(2)} \tau_{s1}^2) \\ &= f_0 (a_{I1}^{(2)} \tau_{I2}^2 - a_{I1}^{(2)} \tau_{I1}^2 - a_{I2}^{(2)} \tau_{I2}^2 + a_{I2}^{(2)} \tau_{I1}^2) \end{aligned} \quad (2.40)$$

Each of these terms are negligibly small, for example

$$f_0 a_{11}^{(2)} \tau_{12}^2 \sim (10^9 \text{ Hz}) (10^{-17} \text{ s}^{-1}) (10^{-2} \text{ s})^2 \sim (10^{-12} \text{ cycles}) \quad (2.41)$$

Fifth Term

The total phase of the receiver oscillator (final term in (2.30)) vanishes in the between-satellite difference

$$\Delta_s \Delta_r \theta_r(t_r) = 0 \quad (2.42)$$

This expression assumes that the receiver samples all of its channels at the same time t_r without multiplexing. This assumption is true of the Minimac, Trimble and Rogue receivers. It appears to be also valid for the TI4100, although it does multiplex channels.

Having estimated the magnitude of the five terms in our model, we are now ready to describe the implementation of the complete model in the software.

IMPROVEMENTS TO MODEL IN VERSION 8

To properly model asynchronously sampled data, we must correctly incorporate the effect of the drifting satellite oscillator on the transmission frequency f_s . Previously, we assumed f_s to be constant, but now we express f_s as a second-order polynomial. In this section, we explicitly calculate an improved expression for the carrier beat phase (2.30) using the quadratic satellite clock model (2.17). As before, we proceed term by term.

First Term

The first term in (2.30), representing the satellite phase at the reference epoch t_0 , will vanish in the between-station difference, so we may safely assume

$$\phi_s(t_0) = 0 \quad (2.43)$$

To be completely explicit about this assumption, we code it as

$$\begin{aligned} \text{TRM1}(1) &= 0.0\text{d}0 \\ \text{TRM1}(2) &= 0.0\text{d}0 \end{aligned}$$

for the L1 and L2 frequencies respectively.

Second Term

The second term in (2.30) calculates the effect of the drifting satellite oscillator. We abandon the assumption of constant frequency $f_s(t) = f_0$ in favor of integrating the actual frequency f_s from (2.15)

$$\int_{t_0}^{t_r} f_s(t) dt = f_0 \int_{t_0}^{t_r} [1 + a^{(1)} + 2 a^{(2)}(t - t_0^{(c)})] dt \quad (2.44)$$

If Selective Availability is not in effect, then the satellite clock terms $a^{(1)}$ and $a^{(2)}$ may be assumed constant over a single 8-hour session, and the integral may be evaluated analytically. Changing variables to $t^* = t - t_0^{(c)}$ leads to

$$\int_{t_0}^{t_r} f_s(t) dt = f_0 \int_{t_0 - t_0^{(c)}}^{t_r - t_0^{(c)}} [1 + a^{(1)} + 2 a^{(2)} t^*] dt^* \quad (2.45)$$

and finally to the desired expression for integrated drift of the satellite oscillator

$$\int_{t_0}^{t_r} f_s(t) dt = f_0 \left\{ (1 + a^{(1)})(t_r - t_0) + a^{(2)} \left[(t_r - t_0^{(c)})^2 - (t_0 - t_0^{(c)})^2 \right] \right\} \quad (2.46)$$

When Selective Availability is on, however, the satellite frequency standards are dithered such that the terms $a^{(1)}$ and $a^{(2)}$ vary rapidly with time. In this case, it is necessary to perform the integral numerically. Using the trapezoidal rule, we obtain an expression for the integral term in the n th measurement, received at time t_r

$$\begin{aligned} \int_{t_0}^{t_r} f_s(t) dt &\doteq (t_r - t_0) f_0 + \sum_{i=2}^n \frac{\tilde{f}_i + \tilde{f}_{i-1}}{2} (t_i - t_{i-1}) \\ &\quad + (t_r - t_n) [\tilde{a}_n^{(1)} + 2 (t_r - t_n) \tilde{a}_n^{(2)}] f_0 \end{aligned} \quad (2.47)$$

where t_n is the nominal time tag nearest the actual time of reception t_r , and \tilde{f}_i denotes the frequency deviation (2.20) evaluated at t_i , such that $\tilde{f}_i = \tilde{f}_s(t_i) - f_0$.

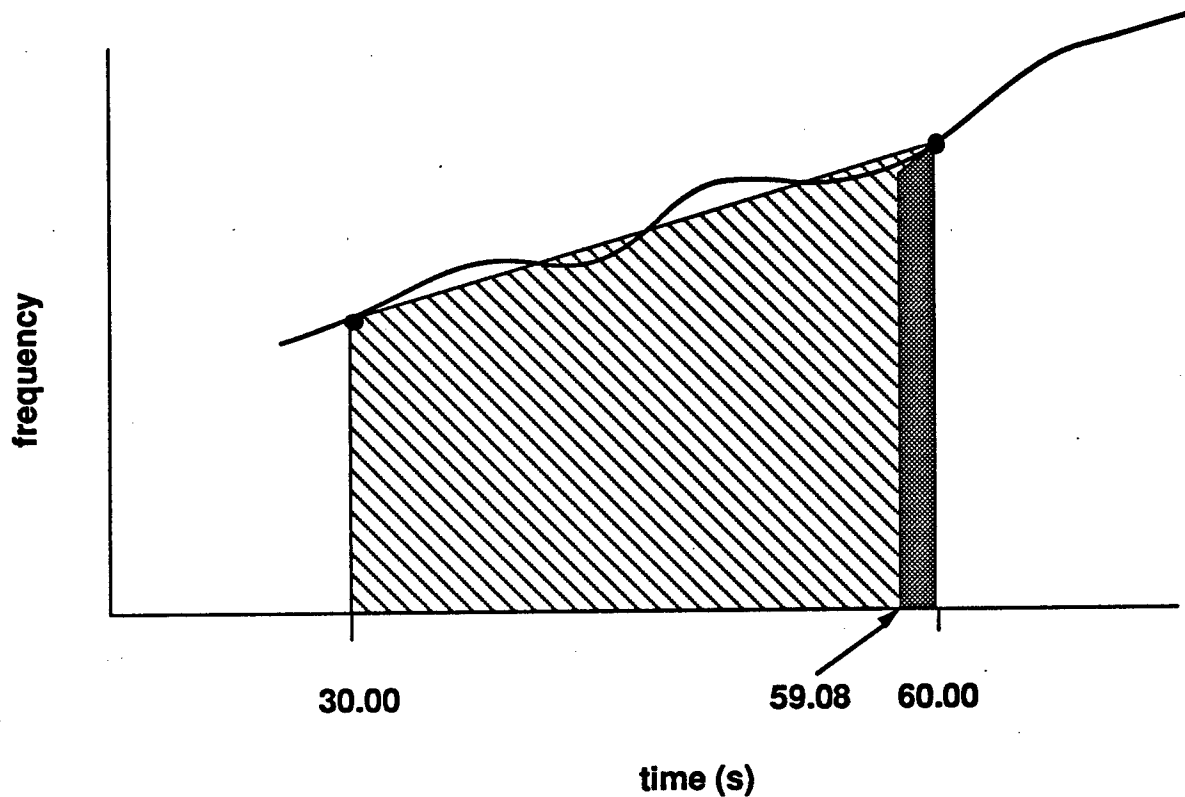


Figure 2.5. Scheme used for integrating the satellite oscillator frequency in (2.47). The curve is the actual frequency, approximated by the linear coefficients $\tilde{\alpha}^{(1)}$ and $\tilde{\alpha}^{(2)}$ as estimated at times t_i designated by dots. The TI4100 receiver samples at 59.08 s. The small shaded area represents the part of the integrated satellite frequency not eliminated by double-differencing.

The three parts of the integral in (2.47) are worth considering separately. The large first term in $f_0(t_r - t_0)$ will cancel with an identical expression in the fifth term for the receiver phase $\theta_r(t_r)$. The second term represents the accumulated phase between the (regularly spaced) nominal time tags and vanishes in the double difference. This term is shown schematically as the large (~30 s) piece of the integral in Figure 2.5. The third term, represented by the small (shaded) piece in Figure 2.5, is the only one to remain in the doubly differenced phase observations. Although the second term is eliminated in

the double difference, we include it in our model calculations to reduce the size of the one-way residual phases, which aids greatly in correcting cycle slips.

In the FORTRAN expression for the integral, the satellite clock terms SVC RAT, SVCACC, JDC+TC are $a^{(1)}$, $a^{(2)}$, and $t_0^{(c)}$ respectively, as read by READJ from a table in the J-file. The SUM2 term is the first two terms of the integral in (2.47), while PHSCOR is the third term.

Third Term

The contribution of the geometric delay to the phase becomes

$$-f_s(t_r)\tau = -f_0 \left(1 + a^{(1)} + 2a^{(2)}(t - t_0^{(c)}) \right) \tau \quad (2.48)$$

which is coded as

```
TRMTC = TIMDIF(JDRCVR, TRCVR, JDC, TC)
TRM3(1) = -FREQL1 * (1.0D0 + SVC RAT + 2.0D0*SVCACC*TRMTC)
          * (DELAY(1, ICHAN) + ATDEL(ICHAN))
TRM3(2) = -FREQL2 * (1.0D0 + SVC RAT + 2.0D0*SVCACC*TRMTC)
          * (DELAY(2, ICHAN) + ATDEL(ICHAN))
```

for the L1 and L2 frequencies, respectively. The TIMDIF functions performs the subtraction $t - t_0$ on the time tags written in Julian day and second of day.

Fourth Term

The fourth term in (2.30) becomes

$$\frac{1}{2} \ddot{f}_s(t_r) \tau^2 = a^{(2)} f_0 \tau^2 \quad (2.49)$$

The magnitude of this term is small

$$\begin{aligned} a^{(2)} f_0 \tau^2 &\sim (10^{-17} \text{s}^{-1})(10^9 \text{Hz})(10^{-2} \text{s})^2 \\ &\sim 10^{-12} \text{ cycle} \end{aligned} \quad (2.50)$$

We may safely neglect it in the code

```
TRM4(1) = 0.0D0
TRM4(2) = 0.0D0
```

for the L1 and L2 frequencies, respectively.

Fifth Term

The fifth term of (2.30) denotes the phase of the receiver oscillator. We write it as the integral of the cubic polynomial for the receiver frequency (2.29)

$$\theta(t_r) = f_0(t_r - t_0) + f_0 \left[b^{(1)}(t_r - t_0) + b^{(2)}(t_r - t_0)^2 + b^{(3)}(t_r - t_0)^3 \right] \quad (2.51)$$

After cancelling $f_0(t_r - t_0)$ with the same term in the second term (2.47) we code this as

```
TRMT0 = TIMDIF(JDRCVR, TRCVR, JD0, T0)
FDEV = CLKRAT*TRMT0
      + CLKACC*TRMT0*TRMT0
      + CLKCUB*TRMT0*TRMT0*TRMT0
TRM5(1) = -FREQL1 * FDEV
TRM5(2) = -FREQL2 * FDEV
```

for the L1 and L2 frequencies, respectively. The negative sign is included because the phase θ of the local oscillator is subtracted from the received phase ϕ_r in (2.1).

Complete Expression

Summing all five terms of (2.30), we write the expression for modeled carrier beat phase as

```
PHASE1 = TRM1(1) + TRM2(1) + TRM3(1) + TRM4(1) + TRM5(1)
PHASE2 = TRM1(2) + TRM2(2) + TRM3(2) + TRM4(2) + TRM5(2)
```

Finally, for consistency with the convention for observed phase used in RINEX files [Gurtner *et al.*, 1989a], we convert the expression from the Doppler sign convention to the pseudorange convention

```
PHASE1 = -PHASE1
PHASE2 = -PHASE2
```

The expression for the pseudorange must also incorporate the actual transmission frequency so that the "wide-lane combination" is consistent [Blewitt, 1989; 1990]. The difference between the observed and calculated pseudorange, in cycles, is

```
TRMTC = TIMDIF(JDRCVR, TRCVR, JDC, TC)
OMC(3, ICHAN) = FREQL1*(1.0d0 + SVC RAT + 2.0d0*SVCACC*TRMTC)
               *OBS(3, ICHAN) / (VLIGHT*1.D3) - PHASE1
OMC(4, ICHAN) = FREQL2*(1.0d0 + SVC RAT + 2.0d0*SVCACC*TRMTC)
               *OBS(4, ICHAN) / (VLIGHT*1.D3) - PHASE2
```

This expression completes the derivation of version 8 of MODEL, which we apply to data in a later section.

SHIFTING TIME TAGS FOR SPLIT-SAMPLED OBSERVATIONS

In the above discussion, we have assumed that all quantities observed by the receiver are sampled at the same time. This assumption is not valid on several occasions in the TREX campaigns. The "ROM" software used in older TI4100 receivers samples the L1 and L2 carrier phases at 1.02 and 0.98 s before the integer minute, but the P1 and P2 pseudoranges at 1.00 s before the integer minute. There is thus a separation of 20 ms between the sampling times of the different quantities. This split introduces a slope into the "wide-lane" combination of L1, L2, P1 and P2 [Dong and Bock, 1989; Blewitt, 1989, 1990]. Properly constructed, this combination is constant in the absence of cycle-slips, making it useful for editing data and for resolving integer ambiguities. Removing the incorrect slope, then, is important for successful analysis of data from these receivers.

In this section, we re-derive an expression for the "wide-lane" combination and show how it is effected when the four quantities in the combination are not sampled at the same time. We then present a simple procedure to "shift" the pseudorange measurements to the same time tag as the phase measurement.

The four quantities sampled by the receiver are the phase ϕ_1 at the L1 carrier frequency, the phase ϕ_2 at the L2 carrier frequency, the group delay ρ_1 (pseudorange) of the P code modulated on the L1 carrier, and the group delay ρ_2 (pseudorange) of the P code modulated on the L2 carrier. All four signals are delayed by propagating through the ionosphere, a dispersive medium, as described above. The apparent change in path length is proportional to the square of the wavelength λ , and affects phase delay and group delay with opposite signs. For simplicity, we write the increase in path length as $\lambda^2 I$, where I depends on the electron density of the ionosphere at any given time, as shown in equation (2.4). We also continue to use the Doppler convention for phase so that the temporal derivatives of the phase and range have opposite sign. Ignoring all sources of error except the ionosphere, we write a simple expression for the two phases in cycles according to (22) and (23) of Dong and Bock [1989]

$$\phi_1 = \lambda_1 I - \frac{1}{\lambda_1} r + n_1 \quad (2.52)$$

$$\phi_2 = \lambda_2 I - \frac{1}{\lambda_2} r + n_2 \quad (2.53)$$

where r denotes the range (distance) between the satellite and receiver. The terms n_1 and n_2 denote the integer ambiguities ("biases") in cycles. The analogous expressions for the pseudoranges may be written in meters according to equation (1) of *Blewitt* [1989]

$$\rho_1 = r + \lambda_1^2 I \quad (2.54)$$

$$\rho_2 = r + \lambda_2^2 I \quad (2.55)$$

The temporal derivatives of the phase may be written as

$$\dot{\phi}_1 = \lambda_1 \dot{I} - \frac{1}{\lambda_1} \dot{r} \quad (2.56)$$

$$\dot{\phi}_2 = \lambda_2 \dot{I} - \frac{1}{\lambda_2} \dot{r} \quad (2.57)$$

where the dot indicates differentiation in time. These quantities are recorded by the receiver. By combining them, it is possible to obtain an expression for the derivative of the ionospheric term

$$\dot{I} = \frac{\lambda_1 \dot{\phi}_1 - \lambda_2 \dot{\phi}_2}{\lambda_1^2 - \lambda_2^2} \quad (2.58)$$

Similarly, the range rate is

$$\dot{r} = \frac{\lambda_1^{-1} \dot{\phi}_1 - \lambda_2^{-1} \dot{\phi}_2}{\lambda_2^{-2} - \lambda_1^{-2}} \quad (2.59)$$

These two terms permit us to calculate the derivatives of the pseudoranges, two quantities which are not recorded by the receiver

$$\dot{\rho}_1 = \dot{r} + \lambda_1^2 \dot{I} \quad (2.60)$$

$$\dot{\rho}_2 = \dot{r} + \lambda_2^2 \dot{I} \quad (2.61)$$

Finally, we can predict the pseudoranges at time $t + \delta t$ by using Taylor expansions about t

$$\rho_1(t + \delta t) \doteq \rho_1(t) + \dot{\rho}_1 \delta t \quad (2.62)$$

$$\rho_2(t + \delta t) \doteq \rho_2(t) + \dot{\rho}_2 \delta t \quad (2.63)$$

where all the quantities on the right side are derived from observations recorded by the receiver. This correction is performed in the preprocessing program MAKEX.

The motive for the correction is to ensure that the wide lane combination is correct. It is defined as the difference between the two ambiguities [Dong and Bock, 1989; Blewitt, 1989]

$$n_2 - n_1 = \phi_2 - \phi_1 + \frac{\lambda_1 - \lambda_2}{\lambda_1 + \lambda_2} \left(\frac{\rho_1}{\lambda_1} + \frac{\rho_2}{\lambda_2} \right) \quad (2.64)$$

Neglecting to apply the correction produces an error of

$$\delta(n_2 - n_1) = \frac{\lambda_1 - \lambda_2}{\lambda_1 + \lambda_2} \left(\frac{\delta t \dot{\rho}_1}{\lambda_1} + \frac{\delta t \dot{\rho}_2}{\lambda_2} \right) \quad (2.65)$$

In the case of the TI4100 ROM software, the offset δt between the phase time tag and the pseudorange time tag is 80 ms, which can cause an error of about 50 m in the wide lane combination for typical values of the derivatives.

APPLICATION TO DATA

The improvements described above are designed to ensure that the observed quantities may be correctly combined in linear combinations (e.g. "wide lane", or double-differences) even if they are not sampled at the same time. In the above derivation, we have generalized the model to account for asynchronous, irregular, and split sampling.

The occurrence of these situations may be determined for a given set of receivers from Table 2.2, which shows the sampling times of various receiver-software combinations. In the course of five years of collecting data in California, several different types of receivers and software versions have been used, leading to several special situations.

TABLE 2.2. Receiver Sampling Times

Receiver	Software	Time of sample, seconds after 00:00.0 GPST
TI 4100	GESAR version 1.1–1.9	–0.92
TI 4100	ROM (L1 and L2 phase)	–1.08 and –0.92
TI 4100	ROM (P1 and P2 pseudorange)	0.0
Macrometer II		5.0 ^a
MiniMac	MMAT version 1.49 and earlier	+5.001 ^a
MiniMac	MMAT version 1.61 and later	0.0 ^b
Rogue	version 2.30 before late 1990	6.0–8.0 ^a
Rogue	version 2.30 after late 1990	0.0
Trimble 4000 SST	SIG + NAV version 3.25	0.0 ± 0.256 ^d
Trimble 4000 SST	SIG + NAV version 4.1 and higher	0.0 ^c
Trimble 4000 SLD		0.0 ± 0.256 ^d
Ashtech	early 1989 versions	0.0 ± 0.256 ^d
Ashtech	version 5F and 6A	0.0

Notes:

- ^a Sampling schedule on UTC rather than GPST
- ^b Programmable, but the default value of 0 will sample at 0:00.0 UTC.
- ^c adjustable in increments of 1 ms
- ^d Sampled at the multiple of 256 ms nearest 00:00.0 GPST

We now perform a simple, first-order calculation to assess the effect of deviations in the satellite frequency f_s . We assume (only for this assessment) that the satellite phase is linear $\phi_s(t) = \phi_0 + f_s t$. To minimize the effects of the satellite clock, we difference the carrier beat phase between receivers which sample at times separated by an amount Δt . To first order in Δt , the difference in phase observed by the two receivers is $(\Delta t - \Delta \tau)f_s$, where $\Delta \tau$ is the difference in propagation delay to the two receivers. If our model of the satellite f_s is in error by an amount δf_s , then the differenced phase will be in error by

$$\delta(\Delta_r \phi_s) \sim \delta f_s (\Delta t - \Delta \tau) \quad (2.66)$$

where the operator Δ_r differences between receivers 2 and 1.

As a rule of thumb, expression (2.66) implies that the error is proportional to both the frequency deviation and the difference in transmission times between the two sampled wavefronts. The error can be eliminated by differencing between receivers, but only if the receivers sample the same transmitted wavefront. In practice, this situation is rarely achieved, because the receivers are not programmed to compensate for differences in the propagation time of the wave from satellite to receiver. When the time offset $\Delta t - \Delta \tau$ is 10 ms, the phase error reaches 0.01 cycles (2 mm) for a frequency deviation of 1 Hz. This corresponds to the maximum propagation delay difference for two stations separated by ~3000 km.

If the two receivers are programmed to measure phase at times different by much greater than 10 ms, then the error introduced by the frequency deviation becomes significant. For example, the Minimac (and most other receivers) record phase at the integer minute, while the TI4100 receiver records 0.92 seconds earlier. In this case, if the satellite oscillator frequency is dithered by 1 Hz, then differencing the phase between the two types of receiver produces an unacceptably large error of order 1 cycle (~200 mm).

A worse, but rarer case occurred during the 1988 GOTEX campaign, when TI4100 receivers operating under GESAR 1.5 sampled the phase 59.08 seconds after the integer GPST second, while Minimac receivers operating under version 1.49 sampled at the integer UTC second. Since UTC-GPST was then 5 seconds, the offset $t_1 - t_2$ reached 5.92 s in magnitude, creating an error of 0.9 cycles for a rapidly drifting oscillator with $a^{(1)} \sim 10^{-11}$. Since this error is nearly constant, it may not be evident in the phase residuals. It would, however, render the constant part of the doubly-differenced phase a non-integer value, preventing the correct resolution of ambiguities.

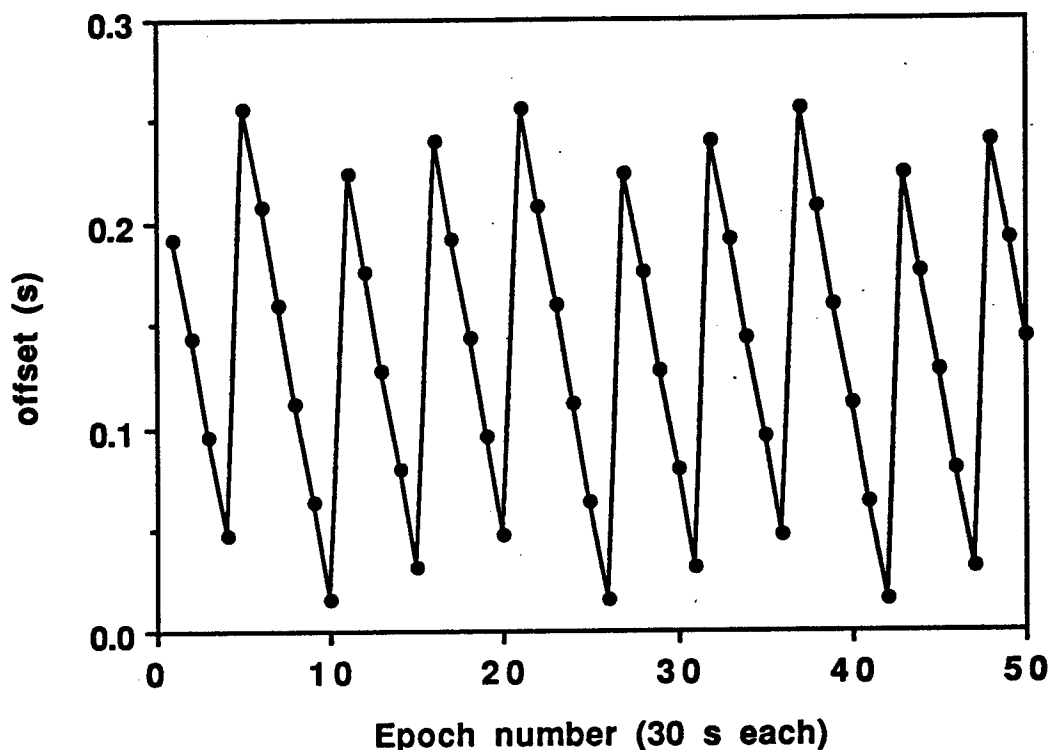


Figure 2.6. Difference between Trimble and Minimac time tags as a function of epoch number, in an example of irregular sampling. Under SIG+NAV version 3.25, the Trimble receiver samples every 256 ms, and records the sample nearest the specified epoch, in this case, every 30 seconds.

An early version of the Trimble software (SIG+NAV version 3.25) samples every 256 ms, but records only at the point closest to the integer minute. When combined with data from a receiver sampling at the integer GPST minute, the difference in time tags ($t_2 - t_1$) can vary by up to 256 ms in a characteristic 5- or 6-point sawtooth function (Figure 2.6). If we incorrectly assume regular sampling (as we did in version 7 of MODEL), the sawtooth signal appears in the doubly differenced phase residuals (Figure 2.7). Using version 8 of MODEL eliminates the sawtooth signature by explicitly calculating the time tag and correctly modeling the drift of the satellite oscillator (Figure 2.8).

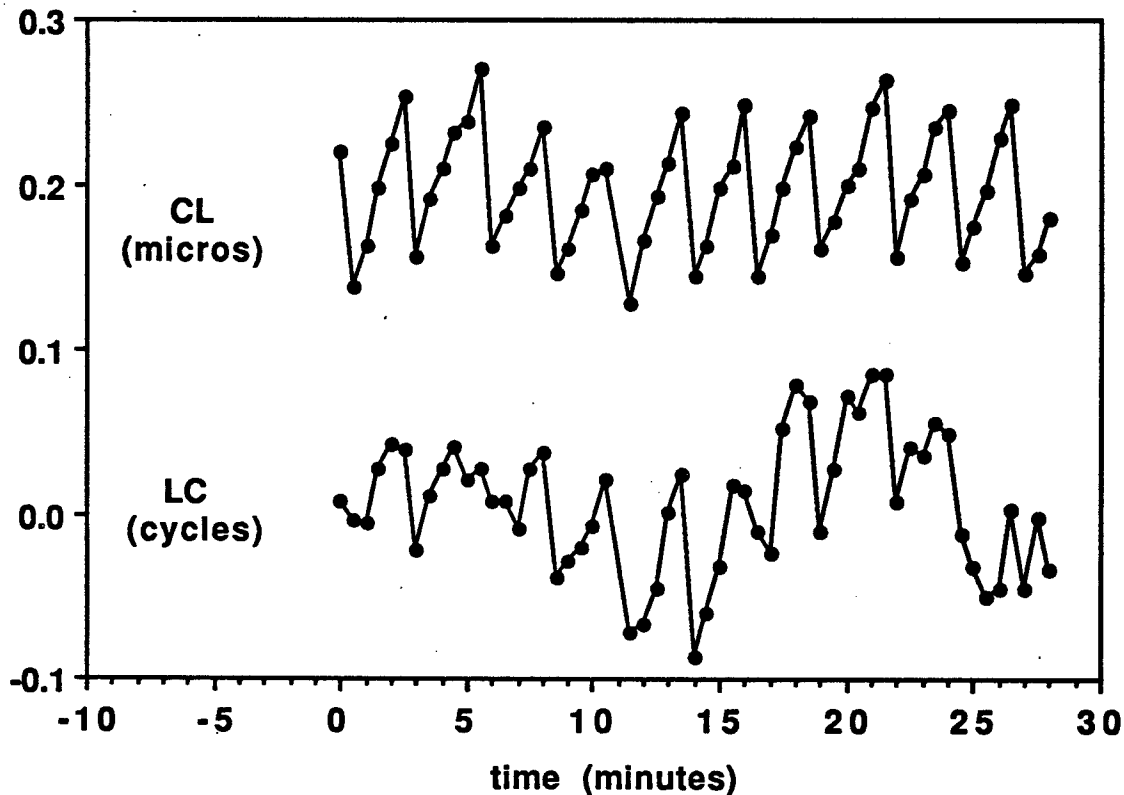


Figure 2.7. Doubly-differenced, post-fit residuals of irregularly sampled data. The upper trace (CL) represents the epoch-by-epoch estimate of the receiver clock offset Δt_r . The lower trace (LC) represents the ionosphere-free combination of the L1 and L2 phases. The sawtooth pattern in CL appears in the LC residual because the old version (7) of MODEL incorrectly assumed that the data were regularly sampled. The stations are VNDN, which observed using a Trimble 4000 SDT receiver running SIG and NAV version 3.25, and MOJM, which used a Minimac receiver running software version 1.61. The satellites are PRN 12 and PRN 3. A second-order polynomial has been removed. The data were collected February 1, 1990.

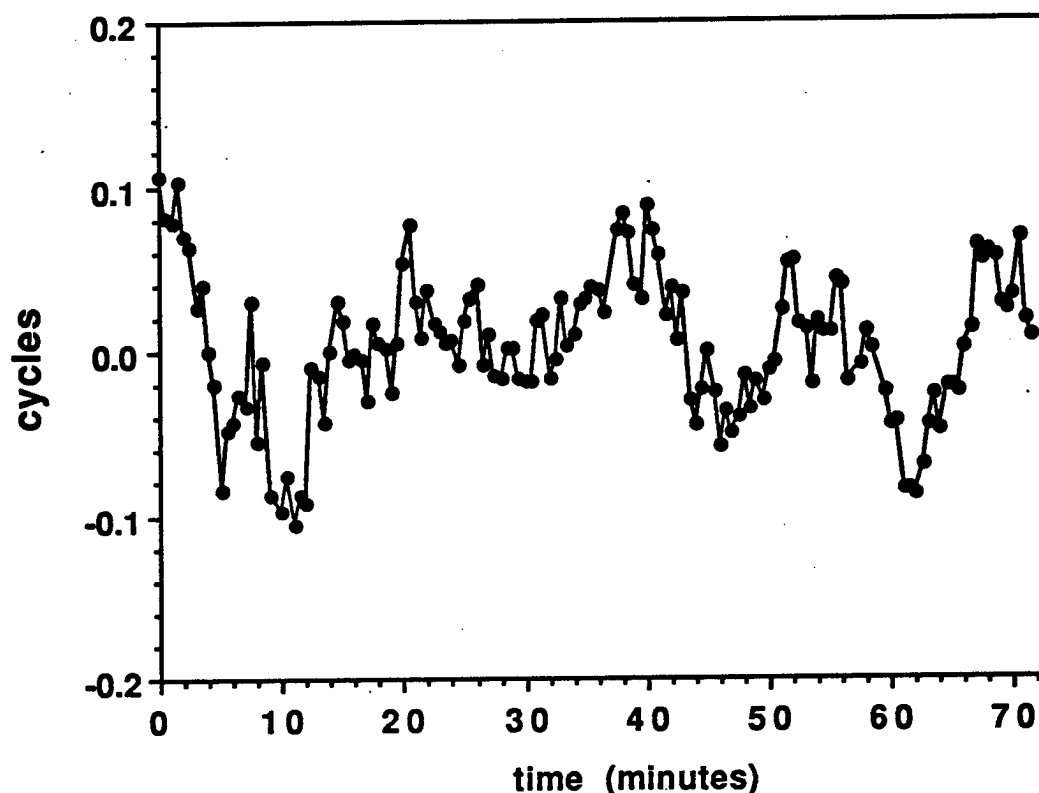


Figure 2.8. Doubly-differenced, post-fit L1 residuals of irregularly sampled data. The observations are the same as in Figure 2.7, but they have been modelled with MODEL version 8 which is valid for irregularly sampled data. Note the absence of the sawtooth seen in Figure 2.7.

CORRECTING FOR THE EFFECT OF SELECTIVE AVAILABILITY

Description of the Policy

The signals transmitted by the satellites of the Global Positioning System (GPS) have been degraded under the U.S. Defense Department's policy of "Selective Availability" (SA). The policy is designed to maintain 100 m accuracy 95% of the time to satisfy civilian navigational requirements. Applied only to the Block II satellites, SA degrades the quality of three types of data: the broadcast orbital information, the pseudorange time tag, and the satellite oscillator frequency. Altering the broadcast orbital elements does not pose a serious problem for precise geodetic applications because these quantities can be estimated from differential phase measurements. Similarly, the degraded pseudorange time tag is not troublesome because it is used only

to estimate the offset between the receiver clocks, where an accuracy of one microsecond (300 m) is sufficient for millimeter accuracy in estimating relative station positions. Dithering the frequency of the satellite oscillator can be more serious because it directly effects the phase measurements used for geodesy by interferometry. Correcting the effect of the dithering is the subject of this section.

When SA is on, the satellite oscillator appears to be about 100 times noisier than when SA is off (Figures 2.1 and 2.9). The deviations in frequency alter all the transmitted signals in the same manner because they are all derived from the same 10.23 MHz oscillator. For example, the transmitted L1 frequency can depart from the nominal value of 1.57542 GHz by several Hz, producing an error of order 10 m in the range from satellite to receiver. The error can be eliminated by differencing between receivers, but only if all the receivers in the network sample the signals simultaneously. If, instead, the receivers do not sample simultaneously, it becomes necessary to treat the dithering explicitly by modeling the deviations in the transmitted carrier frequency.

We have not been able to locate a specific description of the governmental policy. One description was presented verbally by Lt. Col. Jules G. McNeff of the US Air Force, who is Military Assistant to the Assistant Secretary of Defense for Command, Control, Communications and Intelligence at the Pentagon [McNeff, 1990]. He reiterated the official position on GPS, pointing out that it was designed for "force enhancement requirements". He noted that the policy on dithering has not changed since its inception and contains three main objectives: (1) to protect the military utility of GPS Precise Positioning Service (PPS), (2) to protect the algorithms used, and (3) to make useful/acceptable service for positioning and timing available for civilian use. He referred the audience to the Federal Radionavigation Plan [U.S. Dept. Trans., 1990], which is completely vague. The only sentences pertaining to SA are the two on page 3-37:

As soon as satellites are added to the operational constellation and have passed specific tests, the Master Control Station will turn on Selective Availability (SA). SA is a method to control the availability of the system's full capabilities.

It appears that the frequency was dithered on Block II satellites beginning in late March, 1990. The dithering was discontinued between August, 1990 and July 1, 1991 to expedite US military operations in the Middle East. Of the data analyzed for this thesis, only those collected in the TREX17 and TREX18 campaigns in March, 1990 were collected under the dithering imposed by Selective Availability.

Application of the Revised Model to Data in TREX 17

We have applied our algorithm to a network observed in California from March 25 to 28, 1990, using a subset of ten stations which sampled every 30 s for 7.5 hours per day for four sequential days. Of the ten stations, three were the CIGNET MiniMac receivers at Mojave, California, Richmond, Florida, and Westford, Massachusetts. These receivers used hydrogen masers as their local oscillators and sampled the phase on integer seconds. An additional tracking station using a TI4100 receiver was operated by the Pacific Geoscience Center at Sydney, British Columbia. The remaining six receivers were TI4100 receivers at field sites in California with interstation distances from 100 to 400 km.

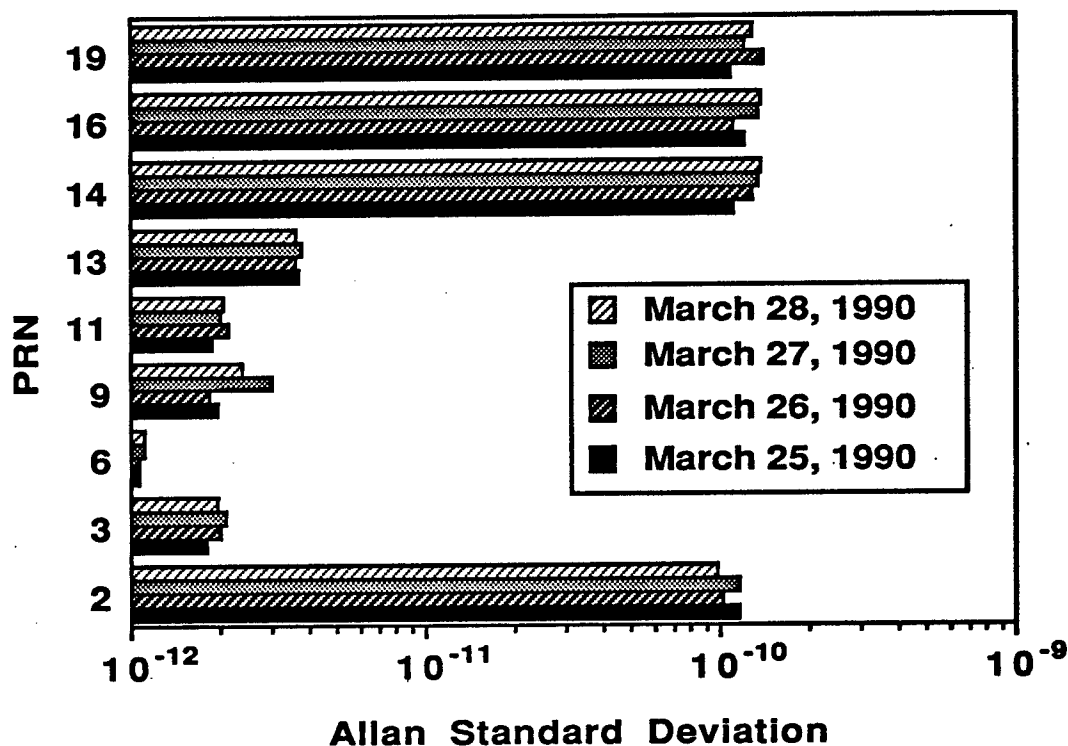


Figure 2.9. Apparent Allan standard deviation $\sigma_y(30 \text{ s})$ for the TREX17 experiment in March 1990. The satellites numbered PRN 3, 6, 9 and 11 are undithered Block I satellites. Those numbered 2, 13, 14, 16 and 19 are Block II satellites dithered by Selective Availability. The level of dithering appears to be fairly constant between satellites and over the four days of observation.

Using the phase data sampled every 30 s at the CIGNET sites equipped with hydrogen masers, we have determined the satellite frequency deviation by estimating

the coefficients \tilde{a}_1 and \tilde{a}_2 . A comparison of these estimates from different stations suggests that they are precise to better than 0.5 % of their magnitude, i.e. about 5 mHz for the L1 frequency. A typical plot of the estimated frequency deviation is shown in Figure 2.1.

The level of dithering, as measured by the Allan standard deviation $\sigma_y(30 \text{ s})$ appears to be fairly constant across the four days observed in March, 1990, and between the Block II satellites (Figure 2.9). The amplitude of the deviations is between 1 and 2 Hz in the L1 frequency, consistent with those estimated by *Rocken and Meertens* [1990]. The characteristic repeat time of about 5 minutes is typical and appears in all the dithered observations we have examined. It is not, however, the true period of a regular oscillation. We estimated the spectral content of the signal using the method of "maximum entropy" [Press *et al.*, 1987]. The lack of a sharp spectral peak in Figure 2.10 precludes the idea of removing the dithering by filtering in the frequency domain.

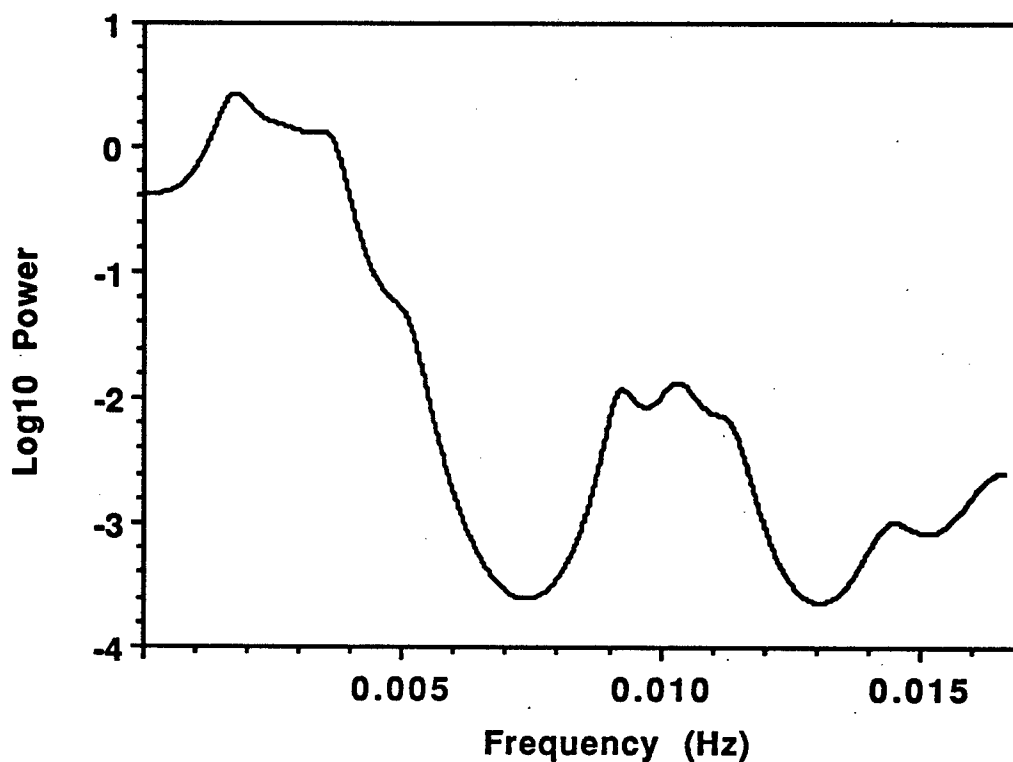


Figure 2.10. Spectrum of the deviation in the oscillator frequency of PRN 02 on March 28, 1990, while Selective Availability was on. The peaks are at periods of approximately 500 s and 100 s. The spectrum was estimated by maximum entropy from the derivative of phase observed at Westford.

We applied our new model (2.30) to the phase, taking as an example the residual (observed minus calculated) phase $\tilde{\psi} - \bar{\psi}$ for a dithered satellite (PRN 2) as received at Mojave. Figure 2.11 compares the phase residuals from two models using different sets of values for the frequency deviation coefficients a_1 and a_2 . Using the broadcast values \bar{a}_1 and \bar{a}_2 to calculate the phase $\bar{\psi}$, we find residuals with an RMS scatter of ~ 50 cycles (dashed line in Figure 2.11). If we instead use our estimates \tilde{a}_1 and \tilde{a}_2 , the RMS scatter is reduced to ~ 1 cycle (solid line in Figure 2.11), a value of the same order as for an undithered satellite. This reduction in the residual phase is important for detecting and correcting cycle slips in the data, even though most of the unmodeled SA signature vanishes when differenced between receivers. The remaining signature is the one we correct, namely that due to satellite frequency variations between the transmission times of the wavefronts sampled by the two different receivers.

The improved model also improves the doubly differenced residuals. Figure 2.12 shows phase residuals differenced between two receivers sampling at times separated by 0.92 seconds. The broadcast values $\bar{a}^{(1)}$ and $\bar{a}^{(2)}$ produce residuals with unacceptably large scatter (RMS ~ 0.58 cycle). The magnitude of this term is of the same order as predicted by the rule of thumb (2.66). It is less than the observation of *Rocken and Meertens* [1990], who report errors of 0.04 cm for each millisecond of separation between sampling times. In the present case, they would predict about 1.7 cycle of modeling error. Our estimated frequency deviations $\tilde{a}^{(1)}$ and $\tilde{a}^{(2)}$ reduce the RMS scatter to ~ 0.10 cycle, a value of the same order as for undithered satellites. Some signature remains, however, possibly because the 30 second sampling interval at the CIGNET is too coarse to generate accurate estimates of $\tilde{a}^{(1)}$ and $\tilde{a}^{(2)}$.

We then analyzed the data from all the stations using doubly differenced phase (differencing not only between stations, but also between satellites to cancel the effects of variations in the receiver oscillators). The effect of the improved model is shown in Figure 2.12 for two receivers sampling at times separated by 0.92 seconds. The broadcast values \bar{a}_1 and \bar{a}_2 produce residuals with unacceptably large scatter (RMS ~ 0.58 cycle). Our estimated frequency deviations \tilde{a}_1 and \tilde{a}_2 reduce the RMS scatter to ~ 0.10 cycle, a value of the same order as for undithered satellites. A small high frequency signature remains, but we cannot distinguish any residual SA from other effects, such as signal multipathing.

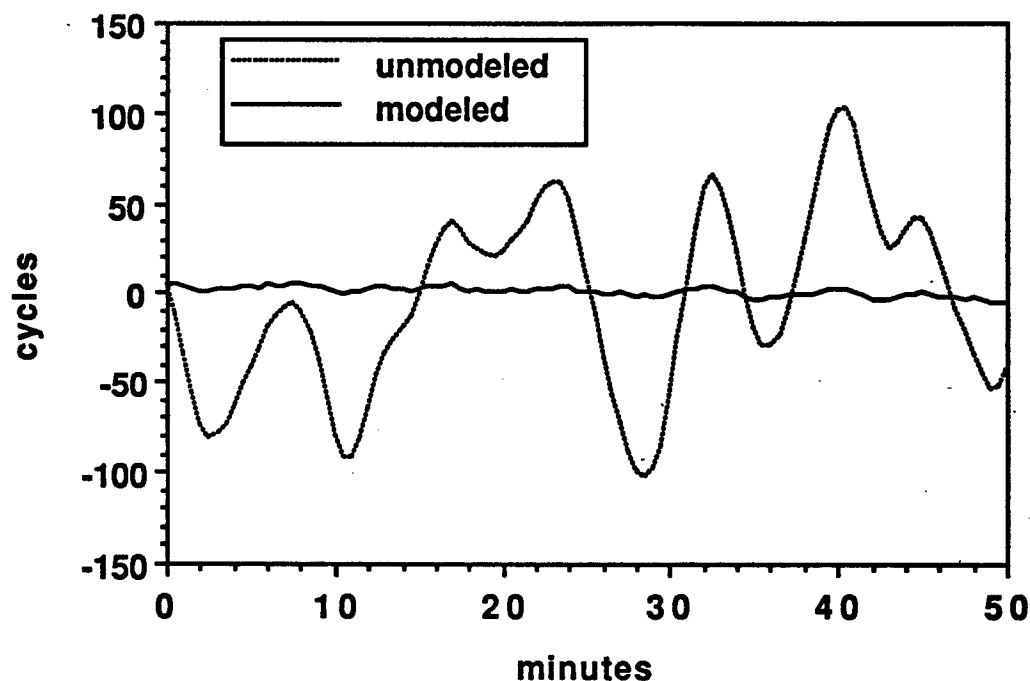


Figure 2.11. Undifferenced L1 phase residuals for a dithered satellite (PRN 2). The dashed line shows results obtained using the broadcast values $\bar{\alpha}^{(1)}$ and $\bar{\alpha}^{(2)}$ to model the satellite oscillator frequency. The solid line represents residuals obtained using values $\tilde{\alpha}^{(1)}$ and $\tilde{\alpha}^{(2)}$ estimated from the CIGNET stations via (2.21) and (2.22).

A direct test of our technique would compare our calibrated phase with the phase observed by a receiver capable of decoding the dithering. Since we did not have access to such receivers, we instead performed two indirect tests which compare the results from dithered and undithered satellites. The basis for comparison is the precision of station coordinates estimated in our test network. These tests can only place an upper bound on the impact of SA because over 75% of the observations in our experiment came from Block I satellites without dithered oscillators.

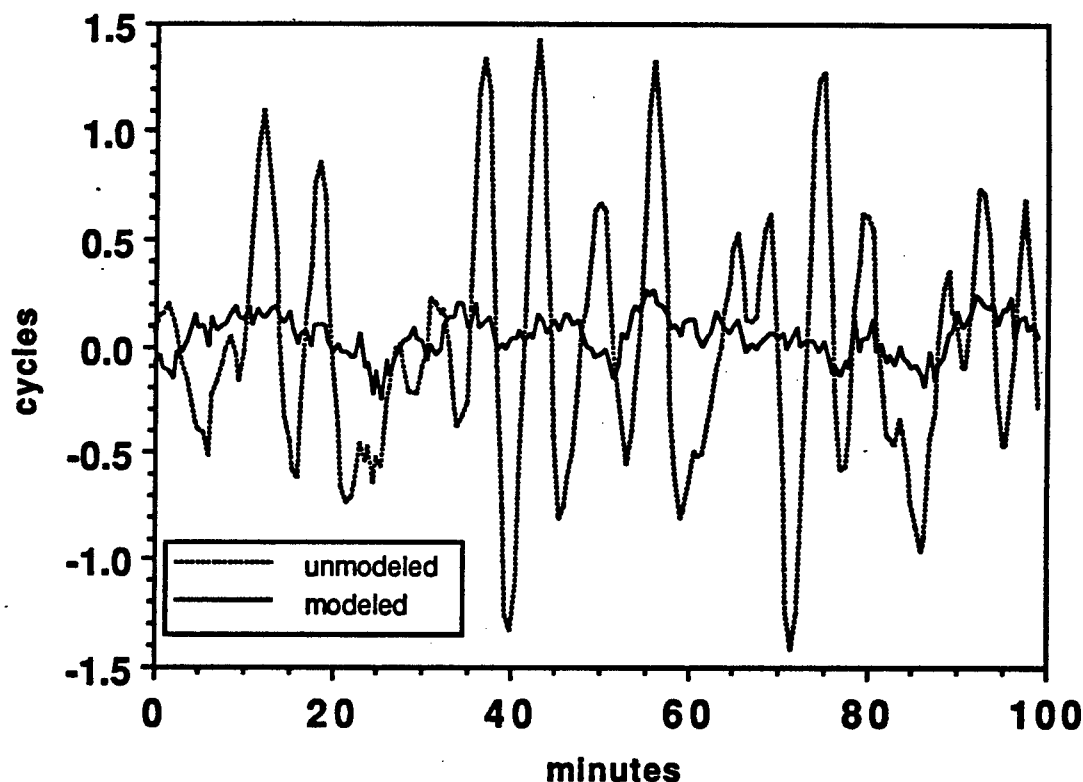


Figure 2.12. Doubly-differenced residuals. Dashed and solid lines as in Figure 2.11. The curves shown are residual (observed minus calculated) phase after removal of a second-order polynomial. The effect of the ionosphere has been removed by forming a linear combination of the L1 and L2 phase. The signals were transmitted by a dithered satellite (PRN 14) and an undithered one (PRN 03) on March 28, 1990. They were sampled asynchronously by a TI 4100 receiver at Black Hill and a MiniMac receiver at Mojave, at times separated by 0.92 s. The baseline is 358 km long.

Both tests evaluated the scatter in the estimated vector components over the four sequential days of observation. On each day, we estimated the three coordinates of each station except Mojave, which was held fixed. The orbital parameters were also held fixed to values estimated previously from the same data set by fixing the coordinates of Mojave, Westford and Richmond for the four-day period.

In the first test, we compared our results with and without correcting for SA. We estimated relative position vectors without the SA correction by using the broadcast coefficients \bar{a}_1 and \bar{a}_2 . The maximum scatter for the vectors in California was 6 mm, 22 mm, and 32 mm in the north, east, and vertical components respectively (Figure 2.13). For all three components, the maximum value occurred on a vector between two

receivers sampling at times 0.92 s apart. Modeling SA with the estimated values \tilde{a}_1 and \tilde{a}_2 lowered the maximum scatter to 4 mm, 12 mm, and 19 mm in the north, east, and vertical components respectively, all of which occurred on a vector between two simultaneously sampling receivers (Figure 2.14). The improvements are all significant at the 95% confidence interval, using an F-test, indicating that our technique reduces the effect of dithering when the receivers are almost 1 second out of synchronization.

In the second test, we evaluated the effect of dithered satellites by applying the SA model to two subsets of the data. The first subset contained only undithered satellites, and the second added four dithered satellites, increasing the number of doubly differenced observations by 20% and improving the geometry. The maximum scatter in the north component is the same in both cases (4 mm), but improved from 19 mm to 12 mm in the east component and from 26 mm to 19 mm in the vertical when the dithered satellites were included (Figures 2.14 and 2.15).

The improvement gained by adding the four dithered satellites was not as great as expected, however, given the change in the formal standard deviation of the estimates. In the east component, this deviation from the expected improvement is significant with a 95% confidence interval. This result might possibly indicate that our SA calibration is imperfect. However, a strong indicator that the deviation from the expected improvement is not due to SA is that a similar F-statistic is generated for vectors estimated from both simultaneously and non-simultaneously sampled data. If any SA signature were left unmodeled, the rule of thumb (2.66) would predict different values of the F-statistic for the two sampling offsets. We therefore conclude that we have adequately modelled SA in our experiment.

The SA correction allowed us to resolve the integer phase ambiguities, which was not possible without the correction. The maximum scatters in the final estimates, after SA correction and ambiguity resolution, were 8 mm in the north component, 14 mm in the east component, and 21 mm in the vertical (Figure 2.16).

Although effective in this experiment, our calibration technique does have several requirements which might limit its application to other experiments. It requires a receiver oscillator which is more stable than the level of dithering imposed on the satellite. This receiver must observe the satellites over the same time span as the other receivers in the network. In practice, this means that the calibration technique may only be applied to networks within several thousand kilometers of a CIGNET station. In addition, the calibrating receiver must sample frequently enough to allow accurate estimates of the coefficients \tilde{a}_1 and \tilde{a}_2 . For the levels of SA observed in our experiment, the 30 s sampling interval at the CIGNET sites appears to be adequate, but

more frequent sampling may be necessary if the level of SA dithering is raised. Finally, the calibration technique requires good (1 part in 10^7) models for the receivers' positions and the satellites' orbits.

CONCLUSION

Driven mostly by the need to retain high accuracy in spite of Selective Availability, we have improved our model for the carrier beat phase. Our software now accepts observations with general time tags and correctly handles asynchronous, irregular, and split sampling. It can also model observations collected by receivers with unstable clocks. It eliminates an error which occurred in previous models when treating irregularly sampled data. More importantly, it reduces the effect of dithering under the policy of SA.

For precise determinations of relative position, the principal effect of SA is to alter the frequency of the carrier signal transmitted by the satellite at the level of 10^{-9} . When two receivers sample the phase simultaneously, this effect nearly vanishes when the phase is differenced between them. In the case of non-simultaneous sampling, however, the effect becomes an important source of error, which we can reduce by calibrating the transmission frequency with a stable receiver oscillator. The calibrated satellite frequency, when used to model the carrier beat phase, permits the use of otherwise unusable receiver combinations. We have successfully applied our technique to a test network with ten receivers, of which three sampled at times 0.92 s away from the others. In this case, we were able to estimate relative position vectors whose precisions are as good as those obtained in the absence of SA.

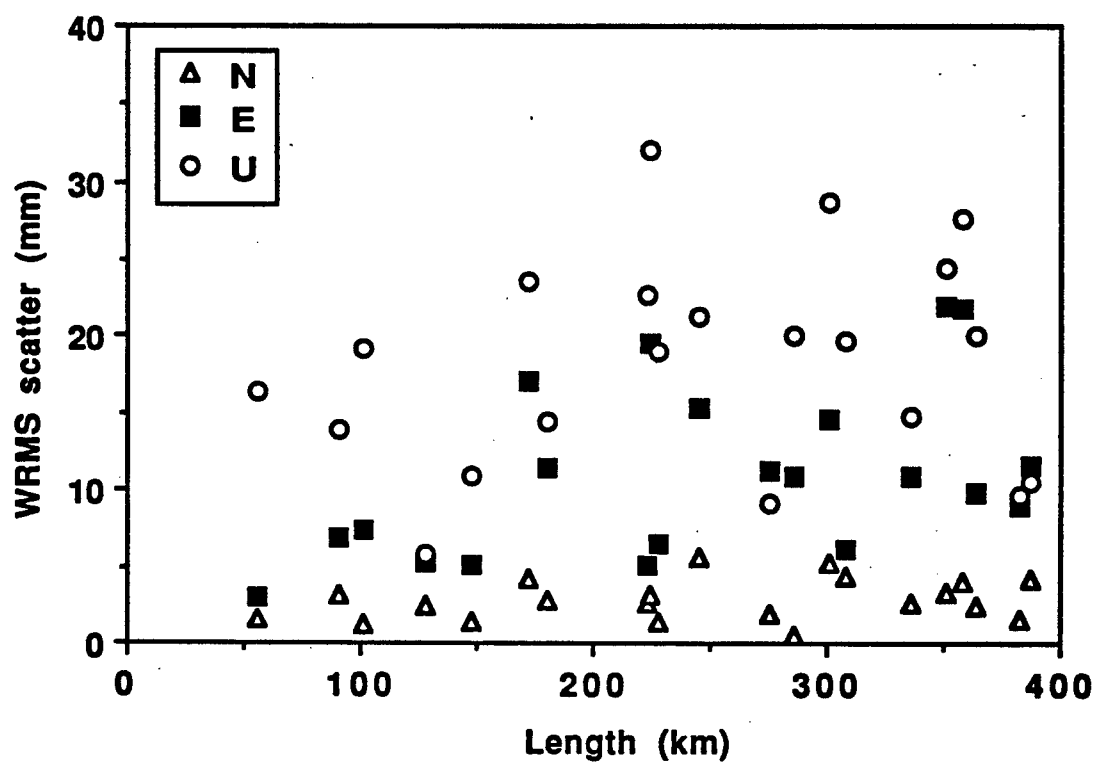


Figure 2.13. Scatter of vector components north (triangles), east (squares) and up (circles) using data from all available satellites and using the broadcast values of the clock polynomial coefficients. The high values are the 6 asynchronously sampled vectors.

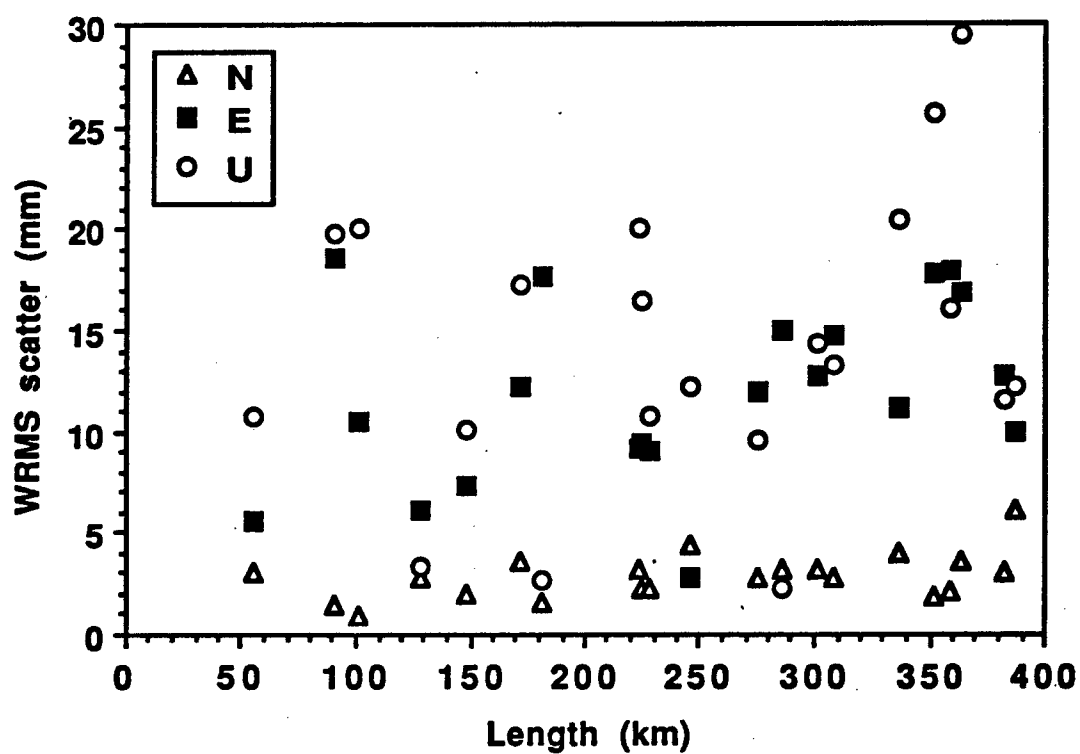


Figure 2.14. Scatter of vector components using only data from undithered satellites. Triangles denote the north component, squares denote the east component, and circles denote the vertical component. The data set includes 6 asynchronously sampled vectors and 15 synchronously sampled vectors. Note the change in scale from the previous figure.

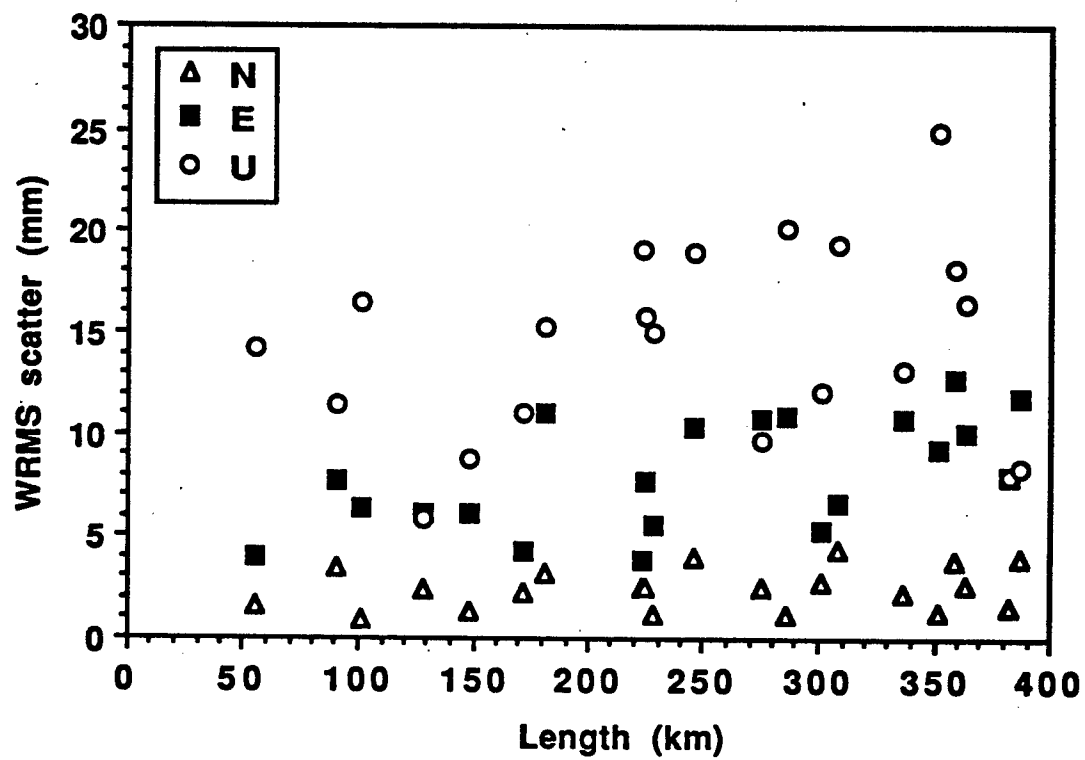


Figure 2.15. Scatter of vector components using data from all available satellites. Triangles denote the north component, squares denote the east component, and circles denote the vertical component. The data set includes 6 asynchronously sampled vectors and 15 synchronously sampled vectors.

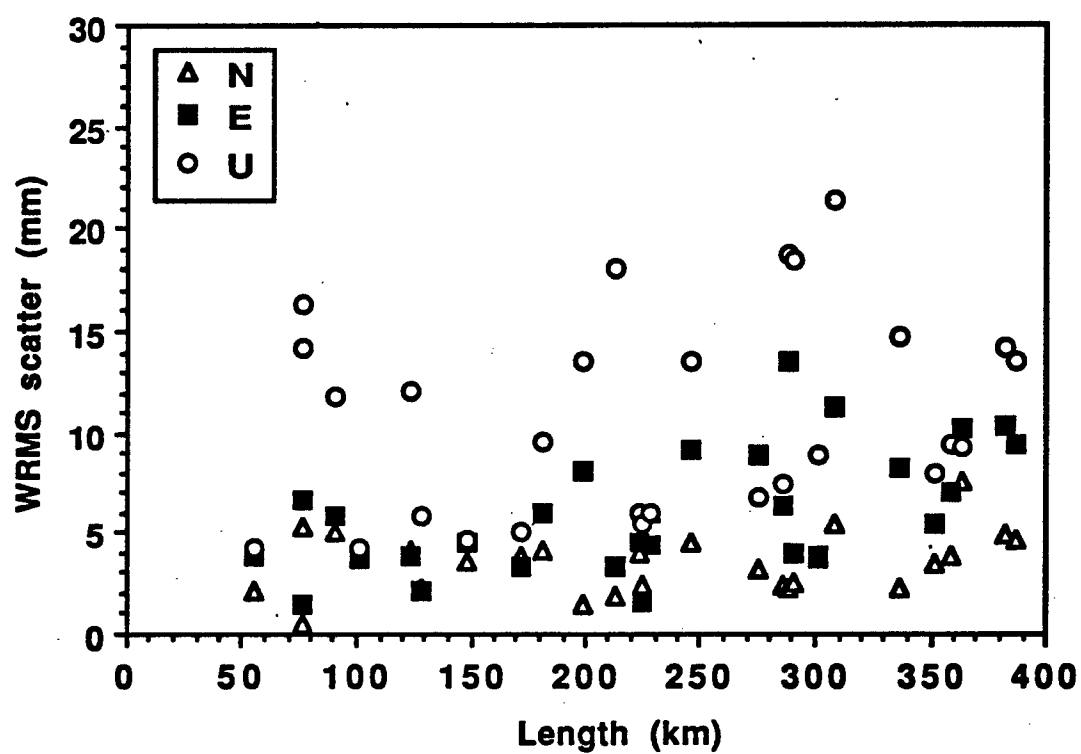


Figure 2.16. Scatter of vector components using only all satellites, after correction for SA and ambiguity resolution. Triangles denote the north component, squares denote the east component, and circles denote the vertical component.

CHAPTER 3

GEODETIC MEASUREMENT OF TECTONIC DEFORMATION IN THE SANTA MARIA FOLD AND THRUST BELT, CALIFORNIA

Fortunately, a method was devised at the office of the Coast and Geodetic Survey which makes it possible to adjust a triangulation net over large areas with a relatively small amount of effort. A dozen or more mathematicians were able to work simultaneously on the western net, and in 15 months the readjustment was complete....

William Bowie [1928]

INTRODUCTION

The active deformation of the western United States is not adequately described by a model of two rigid plates separated by the San Andreas fault. Instead, the relative motion between the Pacific and North American plates is accommodated in a "wide, soft boundary" which extends east and west of the fault, as suggested by *Atwater* [1970]. The Santa Maria Fold and Thrust Belt of coastal California is part of this broad zone (Figure 3.1), and the present-day deformation within it is the subject of this paper.

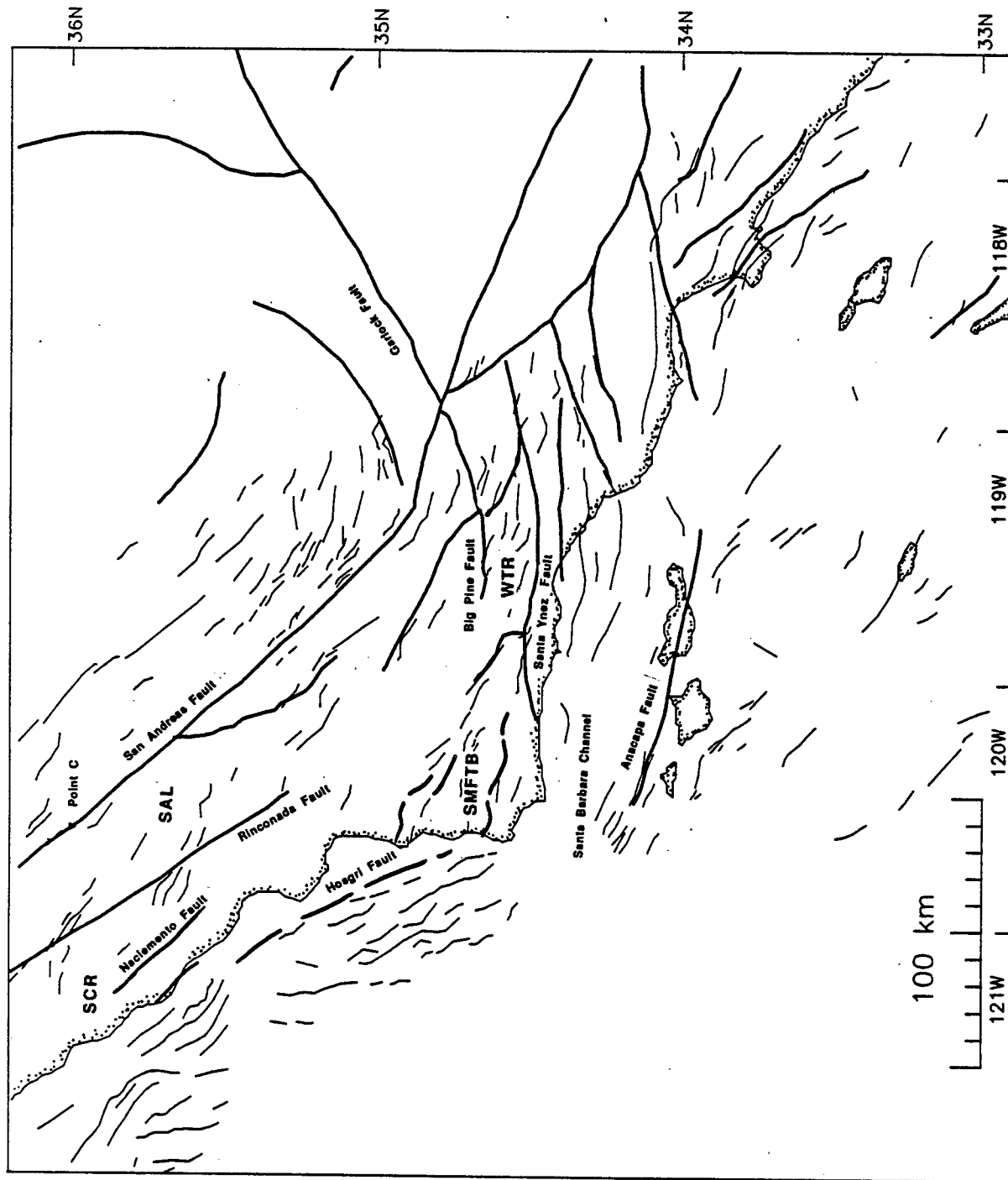


Figure 3.1. (a) Generalized map of California showing traces of major faults (thick lines) and Neogene fold axes from *Stein and Yeats* [1989] (thin lines). The tectonic domains include the Santa Maria Fold and Thrust Belt (SMFTB), the southern Coast Ranges (SCR), the western Transverse Ranges (WTR), and the Salinian Block (SAL).

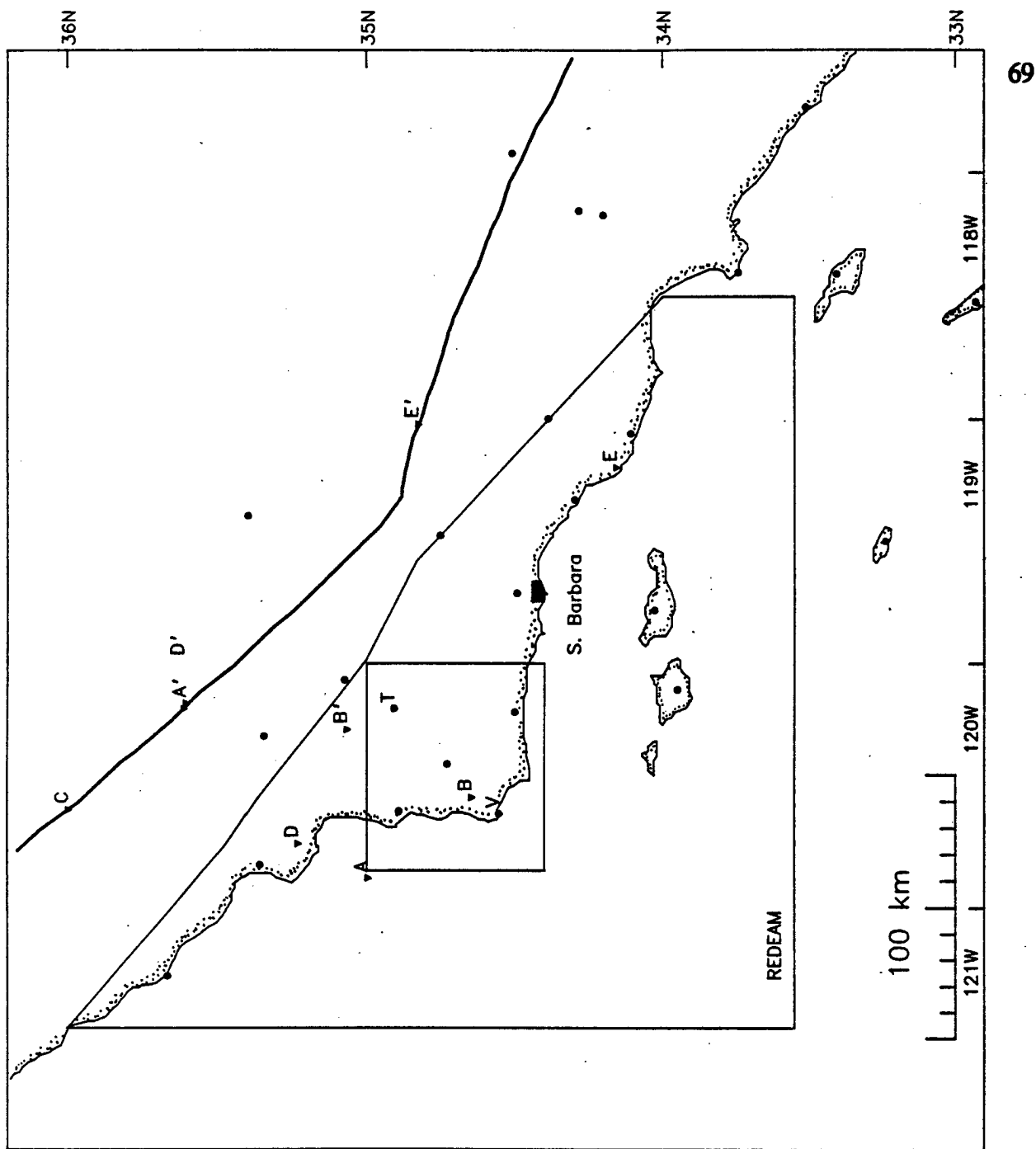


Figure 3.1(b) Key map showing GPS stations (circles), the area detailed in Figure 2 (small rectangle) and the REDEAM Bakersfield region, district I (large quadrilateral). Points V and T are geodetic stations at Vandenberg (VNDN) and Tepusquet Peak (TEPW), respectively. Points A, A', B and B' (triangles) are the endpoints of balanced cross sections of *Namson and Davis* [1990]. Point C is the fiducial point in the San Andreas fault employed by *Minster and Jordan* [1984; 1987]. Points D and D' are within the geodetic network of *King et al.* [1987] and *Harris and Segall* [1987]. Points E and E' are the end points of the cross section of *Namson and Davis* [1988b].

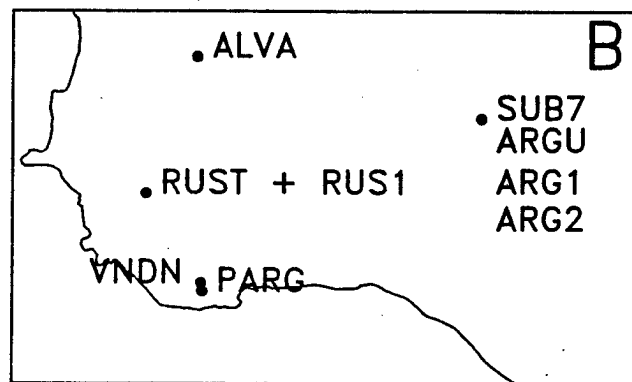
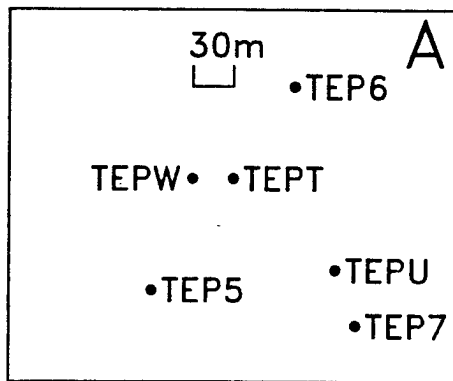
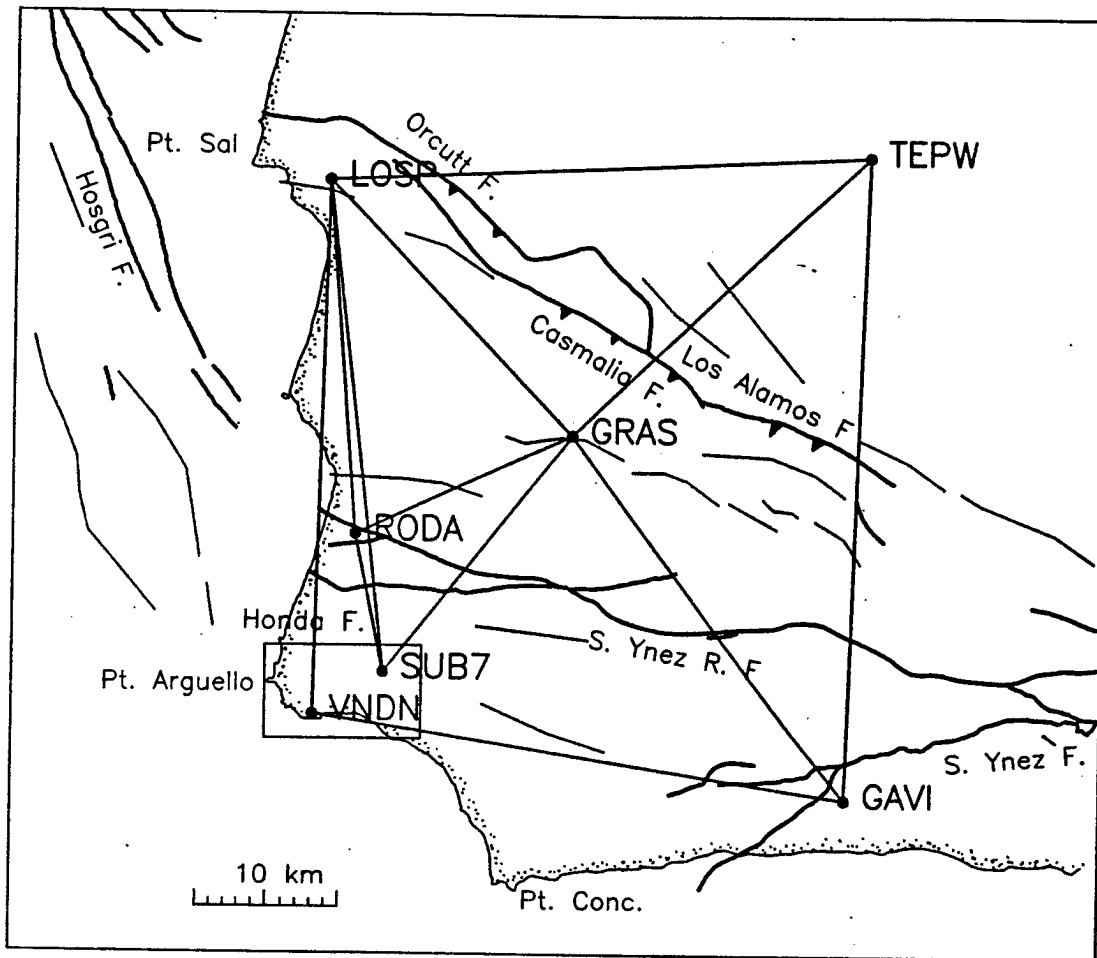


Figure 3.2. Tectonic map of the SMFTB with a skeleton of the geodetic network. Traces of faults (heavy lines) are from *Hall* [1982]. Fold axes (thin lines) are from *Stein and Yeats* [1989]. Insets A and B show the ties at TEPW and VNDN respectively.

Tectonic Setting

For simplicity, we distinguish four tectonic domains, shown in Figure 3.1. (1) The Salinian block as defined by *Dibblee* [1977] is bounded by the Rinconada, Big Pine, and San Andreas faults. (2) The southern Coast Ranges include the Santa Lucia mountains and the coastal belt province of *Dehlinger and Bolt* [1988]. (3) The Santa Maria Fold and Thrust Belt (SMFTB) is the triangular region bounded by the Santa Lucia and San Rafael mountains on the northeast and by the Santa Ynez range front on the south [*Nitchman*, 1988; *Nitchman et al.*, 1989]. (4) The western Transverse Ranges are roughly bounded on the north by the Santa Ynez and Santa Ynez River faults and on the south by the Anacapa-Santa Monica fault, which cuts the Channel Islands [*Yerkes and Lee*, 1979]. The western Transverse Ranges and the SMFTB overlap, so that defining a sharp boundary between them is not possible. The geodetic network shown in Figure 3.2 spans this boundary and measures deformation between and within the SMFTB and the western Transverse Ranges.

The SMFTB is a late Pliocene-Quaternary feature which does not completely coincide with the Santa Maria Basin, a Miocene pull-apart. During the Miocene, right-lateral strike slip dominated the tectonics of central California, offsetting Franciscan outcrops 80–95 km [*Hall*, 1978, 1981]. The Hosgri fault was active during this time, as was the Santa Ynez River fault (mapped by *Hall* [1978] as the Lompoc-Solvang fault). This fault was given its current name by *Sylvester and Darrow* [1979], who described it as left-lateral. It has been modeled as the boundary between the Santa Maria Basin and the western Transverse Ranges by *Up De Graff and Luyendyk* [1989] and appears to have accommodated the simple shear inferred from significant clockwise paleomagnetic rotations in the Neogene [*Luyendyk et al.*, 1980, 1985; *Hornafius*, 1985; *Hornafius et al.*, 1986].

The strike-slip regime ended about 3–5 m.y. ago, probably in response to a reorientation of the relative motions of the Pacific and North American plates [*Cox and Engebretson*, 1985; *Harbert and Cox*, 1989]. Since then, compressive tectonics have become more important [*Page*, 1966, 1981; *Crouch et al.*, 1984; *Namson and Davis*, 1990; *Nitchman et al.*, 1989] and many of the Miocene faults, such as the Lion's Head, Orcutt Frontal, and Santa Maria River faults [*Hall*, 1978] have ceased to be active [*Manson*, 1985].

It is clear that the SMFTB is currently tectonically active. The area has experienced several earthquakes of magnitude 5 or greater [*Pacific Gas and Electric Company*, 1988, hereinafter referred to as PG&E]. In 1915, an event on the Los

Alamos fault shook the area with Rossi-Forrel intensity VII, collapsing several chimneys, but not rupturing the Earth's surface [Beal, 1915]. The 1927 Lompoc event released energy with Rossi-Forrel intensity IX, sufficient to shift a house on its foundations, throw a railroad bridge out of line, and cause a tsunami [Byerly, 1930]. The other characteristics of this earthquake are the subject of some controversy, however. Estimates of the surface wave magnitude (M_s) vary from 7.3 [Gawthrop, 1978b] to 7.0 (PG&E). Similarly, the moment magnitude has been estimated at 7.3 [Hanks, 1979] to 6.6 (PG&E). The offshore epicenter appears to be determined with an uncertainty of at least 10 km [Byerly, 1930; Gawthrop, 1978b; Hanks, 1979; PG&E]. The focal mechanism for the event has been inferred to be reverse slip, with a NE striking axis of compression (PG&E). Finally, in 1980, an event with magnitude 5.0 ruptured off Point Sal, apparently on the Hosgri fault [Cockerham and Eaton, 1982; Eaton, 1984]. The focal mechanisms for these events, as well as other smaller events in the SMFTB, indicate stresses with principal compressive axes oriented NE-SW [Eaton, 1984; Hill et al., 1989; Gawthrop, 1975, 1978a; PG&E]. Not all the events are associated with known faults which cut the surface, suggesting that they may be occurring on "blind thrust" faults hidden within folds [Stein and Yeats, 1989].

Geodetic estimates also suggest active deformation in the area. Savage and Prescott [1978] inverted triangulation data from 1876 through 1956 to find significant shear strain rates of $\sim 0.2 \mu\text{rad/yr}$ across the SMFTB. As part of the REDEAM project, Snay et al. [1987] inverted a large historical geodetic data set to estimate an average shear strain rate of about $0.2 \mu\text{rad/yr}$ for a large district (outlined in Figure 3.1) which includes the SMFTB.

The importance of NE-SW compression in the SMFTB has been recognized by several geologic studies. The bending of the strikes of Neogene fold axes from NW in the southern Coast Ranges to almost due west in the western Transverse Ranges suggests compression normal to these azimuths [Page, 1966, 1981]. The same trends apply to offshore structures and onshore thrust faults [Crouch et al., 1984], as well as geologic structures observed in Landsat images [Matz and Slemmons, 1987] and in the field (E. Vittori et al., unpublished manuscript, 1989). A balanced cross section across the SMFTB between points B and B' (Figure 3.1) suggests crustal shortening at the rate of about 2 mm/yr [Namson and Davis, 1990]. These observations imply that the SMFTB is a zone of currently active deformation with northeast-directed shortening accommodated by WNW striking reverse and thrust faults and folds

(Figure 3.2) [Namson and Davis, 1990; Stein and Yeats, 1989; Nitchman et al., 1989].

The San Andreas Discrepancy

Several studies [Minster and Jordan, 1978, 1984, 1987; Bird and Rosenstock, 1984; Weldon and Humphreys, 1986; Jordan and Minster, 1988b] have recognized that the estimate of the slip rate on the San Andreas fault does not fully account for the relative velocity predicted by global models of plate motion. Dubbed the "San Andreas discrepancy," this missing motion is partitioned between extension in the Basin and Range province and deformation taking place along the California coast.

The rate of deformation for central and coastal California can be estimated by balancing Pacific-North America plate motions against San Andreas slip and Basin and Range extension, as described by the vector equation of Minster and Jordan [1984],

$$\mathbf{v}_{PC} = \mathbf{v}_{PN} - \mathbf{v}_{SA} - \mathbf{v}_{CN} \quad (3.1)$$

The vector \mathbf{v}_{PC} is the Pacific plate velocity in a reference frame grounded just west of a fiducial point C which they define to be on the San Andreas fault at the latitude of 36°N. Thus this (vector) velocity represents the integral of the (tensor) deformation rate field across the California continental margin west of point C. According to (3.1), the sum of this velocity, the San Andreas slip rate (\mathbf{v}_{SA}) and the rate of deformation east of point C (\mathbf{v}_{CN}), must equal the Pacific-North America plate motion (\mathbf{v}_{PN}). In this paper, we compare the values of \mathbf{v}_{PC} predicted from (3.1) with an estimate inferred from geodetic estimates along the California margin.

TABLE 3.1. Relative Velocities

Velocity	Rate, mm/yr	Azimuth	Source
\mathbf{v}_{PN} Pacific-North American Plates	48 ± 1	$N36^\circ W \pm 2^\circ$	DeMets et al. [1989]
\mathbf{v}_{SA} San Andreas Fault slip	34 ± 3	$N41^\circ W \pm 2^\circ$	Minster & Jordan [1984]
\mathbf{v}_{CN} Basin and Range model C	10 ± 2	$N56^\circ W \pm 10^\circ$	Minster & Jordan [1987]
\mathbf{v}_{PC} Pacific Plate to point C	8 ± 3	$N17^\circ E \pm 24^\circ$	equation (3.1)

In our calculations, we use the values listed in Table 3.1 for the relative velocities in (3.1). We take the vector \mathbf{v}_{PN} to be the Pacific-North America plate velocity

calculated at point C from the NUVEL-1 plate motion model [DeMets *et al.*, 1989]. The vector v_{SA} is taken to be the estimate of slip between two points on opposite sides of the San Andreas at point C as synthesized by *Minster and Jordan* [1984] from geologic [e.g., *Sieh and Jahns*, 1984] and geodetic [e.g., *Savage and Burford*, 1973] observations. Finally, v_{CN} is taken to be the motion of the Sierra Nevada-Great Valley block with respect to stable North America, obtained from the model C of *Minster and Jordan* [1987], who estimate Basin and Range extension from very long baseline interferometry (VLBI) and geologic data. This model assumes that the Sierra Nevada-Great Valley just east of point C is rigid. As discussed by *Minster and Jordan* [1984, 1987], this assumption is not strictly correct because the area just east of the San Andreas appears to be undergoing fault-normal compression, evident in the thrust mechanism of the 1983 Coalinga earthquake [Hartzell and Heaton, 1983], geologic cross sections of the San Joaquin Valley [Namson and Davis, 1988a] and geodetic measurements [Harris and Segall, 1987]. Thus equation (3.1) lumps a small amount deformation east of the San Andreas into v_{PC} , lengthening it by about 1–2 mm/yr.

The calculation of v_{PC} in Table 3.1 predicts 8 ± 3 mm/yr oriented at $N17^\circ E \pm 24^\circ$ for the area west of the San Andreas, in good agreement with the previously published value of about 9 mm/yr oriented nearly due north estimated by *DeMets et al.* [1987]. Both of these results are especially dependent on the extension direction in the Basin and Range which enters equation (3.1) as the azimuth of the v_{CN} vector. This quantity can be estimated by several methods, as described by *Minster and Jordan* [1987]. Using geology alone (their model A), the estimated azimuth of v_{CN} is $N64^\circ W \pm 10^\circ$; using VLBI data alone (model B), it is $N48^\circ W \pm 17^\circ$; and using both geology and VLBI data (model C, employed here), it is $N56^\circ W \pm 10^\circ$. Based on a more extensive set of VLBI data, *Argus and Gordon* [1988] argue for a more northerly azimuth and correspondingly smaller rate for v_{PC} than is given in Table 3.1.

To measure this deformation, we partition v_{PC} into three terms

$$v_{PC} = v_{PV} + v_{VT} + v_{TC} \quad (3.2)$$

Each of these vectors represents the integrated rate of deformation between two points on the path linking the Pacific plate with point C. The v_{PV} term includes deformation between the stable part of the Pacific plate and the Vandenberg VLBI station (VNDN) at the SW corner of the SMFTB (Figure 3.1). The v_{VT} term represents the relative motion between VNDN and Tepusquet Peak (points V and T in Figure 3.1), a path spanning the SMFTB. Finally, the v_{TC} term represents the motion of Tepusquet Peak with respect to a point just west of C on the San Andreas.

Since VLBI estimates of the velocity of VNDN relative to a reference frame fixed on North America [Clark *et al.*, 1987; Sauber, 1988] are close to the value predicted for the Pacific plate by the NUVEL-1 global plate motion model [DeMets *et al.*, 1989], we infer that v_{PV} is small or zero. Although there is the possibility of compressive deformation offshore on the Santa Lucia Banks or on the "Queenie Structure" (PG&E), the implication of the VLBI measurements is that most of the deformation west of the San Andreas is accommodated inboard of VNDN.

The vector v_{TC} measures deformation in the Salinian block, which, in light of the relative rigidity of this domain [Dibblee, 1977], is likely to be small; hence the deformation rate within the SMFTB measured by v_{VT} probably accounts for most of v_{PC} . Local geodetic measurements of v_{VT} can thus contribute to refining models of the San Andreas discrepancy.

The Santa Maria Fold and Thrust Belt as an Active Tectonic Element

In this paper, we use geodetic measurements to estimate what fraction of the deformation predicted by the vector balance is actually being accommodated within the SMFTB. How is the strike-slip component of the motion in the southern Coast Ranges transferred into the compression observed in the western Transverse Ranges and the Santa Barbara Channel? The answer has implications for the amount of motion on the San Gregorio-Hosgri fault system, which is not well constrained geologically and has not been directly measured geodetically. In particular, the behavior of the southern section of the Hosgri fault, near Point Sal, is uncertain.

We consider three competing hypotheses. The first is that the Hosgri fault is not active in the neotectonic deformation of coastal California. Recent seismicity on the Hosgri fault is low compared to the Santa Barbara Channel, for example [Tuttle, 1985; Lee *et al.*, 1979], and the fault trace terminates off Point Conception [Steritz and Luyendyk, 1986]. This hypothesis implies that the deformation west of the San Andreas consists of fault-normal compression [Harris and Segall, 1987] and right-lateral shear distributed on minor faults in the Coast Ranges.

The second hypothesis is that the Hosgri fault is indeed active but transfers its motion to the Santa Barbara Channel via offshore deformation so that the zone of active tectonics "wraps around" Points Arguello and Conception, as suggested by Bird and Rosenstock [1984]. This hypothesis is already in doubt because VNDN appears to ride nearly on the Pacific plate, making the offshore deformation measured by v_{PV} fairly small, as discussed by Sauber [1988].

The third hypothesis, and the one we advocate here, also states that the Hosgri is active but that the right-lateral motion along the Hosgri fault system and the compression across the southern Coast Ranges are transformed into the Santa Barbara Channel by faults and folds which cut across the "corner" formed by the SMFTB, as suggested by *Crouch et al.* [1984] and *Humphreys and Weldon* [1989].

The aim of this study is to quantify the active deformation in the Santa Maria Fold and Thrust Belt. To measure strain rates and test the hypothesis that they are significant, we have examined geodetic observations taken over the last 100 years from a geodetic network spanning the SMFTB. To resolve strain rates of 0.1–0.2 $\mu\text{strain/yr}$, it is necessary to combine consistently three different types of geodetic data: triangulation, trilateration, and relative-position vectors obtained by tracking satellites of the Global Positioning System (GPS).

DATA

The geodetic network consists of four principal stations (TEPU, GAVI, LOSP and VNDN) in the form of a braced quadrilateral with ~ 40 km sides. Figure 3.2 shows the network in its tectonic setting. The names and abbreviations of the stations are listed in Table 3.2. The network has been surveyed to the best available standards of the time on eight different occasions ("epochs") since 1876, as shown in Figure 3.3. The geodetic data include three types of observations: triangulation, trilateration, and GPS, as summarized in Table 3.3. The data sets are named according to their temporal midpoint; for example, the 1876–1883 observations are designated 1879.

TABLE 3.2. Stations Used

ID	Name	QID ^a	QSN ^b	1879	1910	1924	1956	1959	1971	1986	1987
ALVA	ALVADO 1933	341204	1002							•	
ARGU	ARGUELLO 1875	341204	1004	•	•	•					
ARG1	ARGUELLO 1 1942 ^c	341204	1004				•				
ARG2	ARGUELLO 2 1959	341204	1004					•	•	•	
GAVI	GAVIOTA 1873	341201	1005	•	•	•	•	•	•		•
GRAS	GRASSY USGS 1959	341201	1032				•	•	•	•	
LOSP	LOSPE 1875	341204	1021	•	•	•	•	•	•	•	•
PARG	POINT ARGUELLO	341204	1028							•	
RODA	RODA 1959	341204	1081						•	•	•
RUST	RUSTAD 1874	341204	1038								
RUS1	RUSTAD RM1	-	-							•	
SUB7	SUB USATOPOCOM 1970 ^d	341204	1084						•	•	
TEPU	TEPUSQUET 1875	342101	1013	•	•	•	•	•	•		
TEP7	TEPUSQUET RM 7	341201	1013A						•		•
TEPT	TEPUSQUET TEMPORARY	-	-								•
TEPW	TEPUSQUET WITNESS	-	-								•
VNDN	VLBI STA 7223 RM 1 1983 DET 1 GSS	-	-							•	•

Notes

- ^aNGS quadrant identification.
- ^bNGS quadrant station number.
- ^cStamped ARGUELLO 1924 but reset after hill was leveled in 1942.
- ^dDesignated SUB TPC 1971 in REDEAM data set.

TABLE 3.3. Summary of Observations

Survey	Duration ^a	Directions	Distances	Azimuths (Constraints)	Total
1879	1875–1883	12		1	13
1910		5			5
1924		63			63
1956		34	2 ^b		36
1959		7			7
1971	1985–1987	17	78		95
1986		31	42		73
1987	1986–1987	6 ^c	4 ^c	1	11
Total	1879–1987	175	126	2	303

Notes

^a Surveys are designated in the text by the year of their temporal midpoint.

^b Taped distances at TEPU.

^c Derived from GPS vectors.

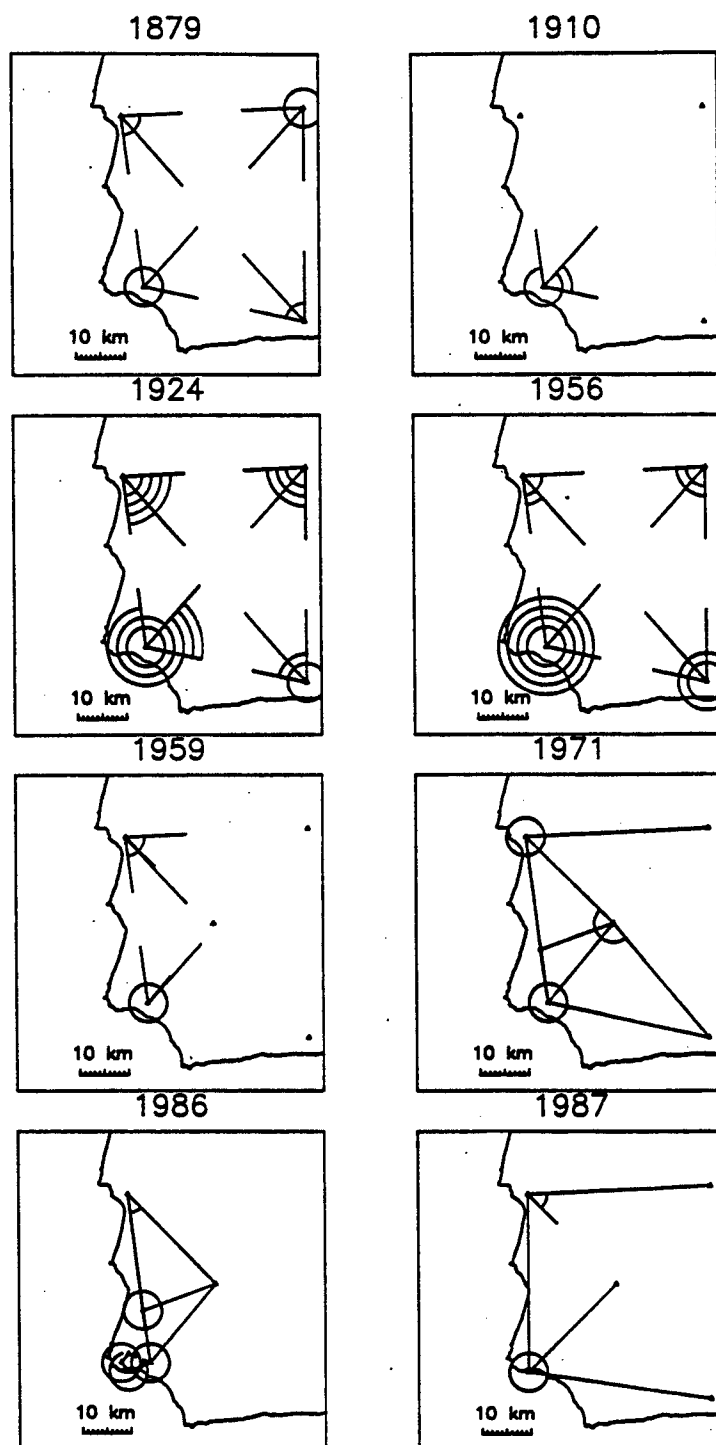


Figure 3.3. Geodetic observations in the SMFTB network at the eight epochs analyzed in this study. Lines completely connecting a pair of stations represent distance measurements. Lines partially connecting a pair of stations represent triangulation measurements with the connecting arcs indicating the observed angles. Short-distance tie measurements are not shown. The 1987 panel shows the six directions and four angles derived from the 11 GPS vectors in Table 3.4.

Triangulation

Triangulation was performed in surveys centered on 1879, 1910, 1924, 1956, and 1959. The measurements are reported in direction lists, where each direction represents the mean of n positions of a theodolite. Classically, the value of n determines the order of the survey and the conventional standard error assigned to the measurement. For the observations analyzed here, the standard error of the mean is typically 0.7 arc sec. The direction lists from the 1880s give the probable errors (0.6745σ) of single observations as 1.4 to 2.0 arc sec. For these directions, 7–20 positions were taken, suggesting that the standard error of the mean is smaller by a factor of \sqrt{n} , or about 0.5–1.0 arc sec, consistent with modern first-order standards, where $n = 16$ and $\sigma/\sqrt{n} = 0.7$ arc sec. The small 1910 survey is presumably of the same quality. Each direction taken in 1924 represents the average of 16 positions and the average deviation of the positions from their mean is about 2 arc sec [Bowie, 1928]. By Peter's formula [Bomford, 1980], this implies a standard error of the mean about 0.6 arc sec, consistent with first-order standards. The 1956 and 1959 surveys were performed to first-order specifications and observed directions with standard errors of 0.7 arc sec. We therefore assign a standard error of 0.7 arc sec ($\sim 3 \mu\text{rad}$) to all the direction observations analyzed in this study.

Savage and Prescott [1978] used direction lists that are a subset of the 1879–1956 data set analyzed here. The complete direction lists, with the exception of the 1959 survey, are a subset of the REDEAM data set [Snay *et al.*, 1987] obtained from the National Geodetic Survey (NGS).

Trilateration

A first-order trilateration and triangulation survey was performed in 1971 as part of the West Coast Precise Traverse. The distances were observed by electronic distance measurement (EDM) using Geodolite and Geodimeter instruments, and meteorologic measurements were taken at the endpoints [Smith, 1974]. Similar observations were performed with Geodimeter and Rangemaster instruments from 1985 to 1987 by the Defense Mapping Agency (DMA). Measurements of this type are assigned standard deviations

$$\sigma_{\text{EDM}} = \sqrt{a^2 + (bR)^2} \quad (3.3)$$

where R denotes the length of the line, and a and b are constants. The DMA (H. Harris, personal communication, 1988), Smith [1974], King *et al.* [1987], and

Gergen [1975] set the proportional part b to 10^{-6} while choosing $a = 5, 6, 10$, and 15 mm, respectively. We use the conservative value of $a = 15$ mm. Typical values of σ_{EDM} for observations in the SMFTB network are 35-50 mm, sufficient to cover the effects of atmospheric refraction discussed by *Savage* [1975].

GPS

GPS measurements were performed in 1986 and 1987 by several universities and government agencies as part of a 5-year investigation of deformation in central and southern California [*Agnew et al.*, 1987]. The data for the SMFTB network were analyzed by us and others at the Massachusetts Institute of Technology (MIT) using the GAMIT software described by *Bock et al.* [1986] and *Dong and Bock* [1989]. The VNDN-GAVI and VNDN-LOSP vectors were measured in separate campaigns on 3 and 5 days, respectively, as part of a network including up to 15 stations in California and three to five "fiducial" stations in North America. Analyses of the larger data set suggest that the standard deviations for the horizontal components of the vectors are 5-10 mm from a single day's measurement [*Murray et al.*, 1988]. This is consistent with the uncertainties suggested by analyses of similar networks at the Jet Propulsion Laboratory (JPL) [*Blewitt*, 1989], NGS [*Strange*, 1987], and U.S. Geologic Survey (USGS) [*Davis et al.*, 1989]. The baselines from VNDN to GRAS and TEPW were measured on 2 days in a third campaign using a much poorer fiducial network. The day-to-day scatter of these measurements and comparison with similar solutions suggest that the uncertainties for the horizontal components are 15-20 mm.

To estimate the internal consistency of the GPS measurements, we performed a network adjustment of the six vectors listed in Table 3.4. These measurements span a period of 9 months, which we treat as a single epoch. Our *a posteriori* estimate of the variance factor $\tilde{\nu}^2$ (derived below) indicates that the uncertainties of the adjusted vectors should be scaled by a factor of $\tilde{\nu} = 2.6$, a value which reflects the differences in fiducial network control between the different GPS solutions. We used the results of this adjustment of the GPS vectors to calculate an independent set of four interstation distances and three interstation angles (final panel of Figure 3.3) and their standard deviations, which we then combined with the historical data. The scaled standard deviations are 10-35 mm for the distances, and 0.1-0.2 arc sec (0.5-1.0 μrad) for the angles.

TABLE 3.4. GPS Vectors Estimated by the GAMIT Software

From To		Date	X, m	σ_X , m	Y, m	σ_Y , m	Z, m	σ_Z , m	L, m	σ_L , m
GRAS	TEPW	Oct. 1, 1987	23435.327	0.019	-1120.278	0.015	16698.417	0.010	28797.686	0.014
VNDN	GAVI	Jan. 3 1987	31016.267	0.009	-22865.262	0.013	-4565.977	0.010	38803.056	0.005
VNDN	GAVI	Jan. 4, 1987	31016.244	0.010	-22865.257	0.014	-4565.962	0.012	38803.033	0.006
VNDN	GAVI	Jan. 5, 1987	31016.246	0.009	-22865.274	0.013	-4565.965	0.011	38803.045	0.005
VNDN	GRAS	Oct. 1, 1987	21403.741	0.016	-183.170	0.014	16103.053	0.014	26785.481	0.011
VNDN	GRAS	Oct. 2, 1987	21403.717	0.020	-183.143	0.017	16103.052	0.012	26785.461	0.013
VNDN	LOSP	Dec. 16, 1986	11450.314	0.009	17552.420	0.013	31041.699	0.011	37453.761	0.003
VNDN	LOSP	Dec. 17, 1986	11450.316	0.008	17552.392	0.012	31041.727	0.010	37453.772	0.003
VNDN	LOSP	Dec. 18, 1986	11450.333	0.008	17552.416	0.012	31041.711	0.009	37453.775	0.003
VNDN	LOSP	Dec. 19, 1986	11450.322	0.008	17552.409	0.012	31041.721	0.010	37453.777	0.003
VNDN	LOSP	Dec. 20, 1986	11450.319	0.009	17552.423	0.013	31041.708	0.010	37453.771	0.003
VNDN	TEPW	Oct. 1, 1987	44839.067	0.022	-1303.449	0.020	32801.470	0.011	55571.372	0.017

Ties

Bench marks at the NE and SW corners of the network were destroyed and replaced at some time in their history, degrading the data set and complicating our analysis. According to the NGS recovery notes, the original ARGU station on Tranquillon Peak near Point Arguello was established in 1875 and used for surveys in 1875 and 1924. The mark was a copper bolt in a piece of rough stone on a concrete foundation, resting partly on solid ledge and partly on ground. In 1924 the copper bolt was replaced by a brass disk. Four check measurements (two angles and two distances) were made to surrounding reference marks in 1875 and 1933; three differed by about 10 mm, but one direction differed by 64 arc min (~ 39 mm). Given the uncertainties of these third-order check measurements, we believe the replacement is reliable for resolving motions of the order of 5 mm/yr.

In 1942 the original 1875 ARGU mark was destroyed by military construction, and the same disk (!), stamped "ARGUELLO 1924", was reset in a new location by the U.S. Engineer Office, 4th District Region. We have found no record of any geodetic connection between the two locations of this disk. To avoid confusion, we name the 1942 placement ARG1. The 1956 survey used ARG1, but in 1958 a new building was constructed on the station, destroying ARG1. Another mark, ARG2, was set on top of the building and used for the 1959 survey. There are no observations connecting ARG2 to ARG1. In 1971, SUB7 was installed as a convenient alternative to ARG2. Observations tying SUB7 to ARG2 were performed, and SUB7 continues to be used for EDM measurements. However, its poor sky visibility renders SUB7 unusable for space geodesy, and VNDN has been used instead for VLBI and GPS surveys in the 1980s (Figure 3.2*b*). Measurements performed since 1959 using ARG2, SUB7, or VNDN can be related with uncertainties of less than 15 mm in length using local surveys to ALVA, RUST, RUS1 and PARG, but these measurements cannot be connected to triangulation performed prior to 1942. There are, however, two surveys involving ARGU (in 1875–1883 and 1924), and three to the modern group (in 1959, 1971, and 1987), so that strain rates can be estimated in both intervals (Table 3.2).

The situation in the NE corner of the network is simpler, as shown in Figure 3.2*a*. The mark at TEPU was deemed unstable prior to the 1971 survey, and a reference mark, TEP7, was used in its place. Although this mark still exists, it cannot be occupied using GPS due to the presence of structures causing signal multipathing. However, GPS observations were made in 1987 from the witness post (TEPW)

simultaneously with another temporary mark (TEPT), and an EDM was used to tie both GPS stations to TEP7 with uncertainties of the order of 15 mm (D. D. Jackson, personal communication, 1987).

ESTIMATION OF STRAIN RATES FROM GEODETIC DATA

The data are heterogeneous, but if properly combined, they are useful for measuring tectonic deformation. The problem is to estimate the station positions as a function of time, and thus the strain field, from data collected during several surveys conducted at different times and at different sets of stations. To perform the estimation, we use the DYNAP program written by *Drew and Snay* [1987]. The algorithm is based on the method of simultaneous adjustment proposed by *Bibby* [1982], and described by *Snay et al.* [1983], *Snay* [1986], and *Drew and Snay* [1989]. In the following discussion, we follow their development but use a general notation which displays the singularities explicitly and suggests the connection to other estimation techniques. Understanding these issues is useful for correctly interpreting the geodetic results in their tectonic context.

Single Survey

Before considering the full time-dependent problem, we first treat a single epoch survey. The data consist of N observations of angles, distances, and vectors between M stations, whose static positions are to be estimated. We specify the coordinates of the m th station by $\mathbf{x}^{(m)}$ and linearize the problem about an approximate preliminary estimate $\xi^{(m)}$ of the coordinates. In general, these vectors each have three components, but in the case where only horizontal geodetic observations are available, only two components can be determined. For simplicity, but without loss of generality, we consider the two-dimensional case. The total number of station coordinates to be estimated is thus $2M$, and we concatenate them into a single model vector

$$\mathbf{X} = \begin{bmatrix} \mathbf{x}^{(1)} \\ \mathbf{x}^{(2)} \\ \vdots \\ \mathbf{x}^{(M)} \end{bmatrix} \quad (3.4)$$

Similarly, the initial estimates of the station coordinates $\xi^{(m)}$ can be concatenated into another vector Ξ of dimension $2M$. The N interstation distances, angles, and vectors

form an observation vector \bar{S} which is a function of the network coordinates, $\bar{S} = F(X)$. Expanding F in a Taylor series about $X = \Xi$ yields the linearized model equation

$$\delta\bar{S} = F(\Xi + \delta X) - F(\Xi) = A\delta X \quad (3.5)$$

Hence $\delta\bar{S}$ is the difference between the observation vector calculated from the true station positions and that calculated from their initial estimates, correct to first order in the postadjustment vector δX . In most geodetic applications, including this one, the errors associated with the first-order approximation are completely negligible. The A term is the $N \times 2M$ design matrix containing the partial derivatives evaluated at Ξ . In rows of A corresponding to distance or GPS observations, there are direction cosines linking pairs of stations; for angular observations, each row links a triplet of stations. Since the data are all relative measurements, the columns of A are not linearly independent, and A is not full rank. The rank deficiency is the datum defect (usually $d \geq 2$) and depends on the type of observations available, as shown in Table 3.5.

TABLE 3.5. Rank Deficiency d and Minimal Constraints

Epochs	Directions	Distances	Azimuths	d	Constrained	Undetermined
1	•	•	•	2	origin	$x_0^{(0)}$
1	•	•		3	above + 1 azimuth	above + orientation
1	•			4	above + 1 distance	above + scale
> 1	•	•	•	4	origin	$x_0^{(0)}$
					origin velocity	$u^{(0)}$
> 1	•	•		6	above + 2 azimuths	above + \dot{w}
> 1	•			8	above + 2 distances	above + $\dot{\epsilon}$

The well-posed two-dimensional single-epoch problem requires observations and/or constraints sufficient to determine four parameters: (1) origin latitude, (2) origin longitude, (3) scale, and (4) orientation [Caspary, 1987]. In practice, the problem is rendered nonsingular by "fixing" the latitude and longitude of a reference station and, depending on the availability of data, the azimuth and/or distance between two stations. Other equivalent techniques for handling the singularity include "inner constraints" or generalized inverses [e.g., Welsch, 1979].

Information on scale comes from distance observations, either EDM or GPS. For example, the 1879 data set cannot determine a scale parameter because no distances were observed between the stations of interest. In our single-epoch analysis of these data, we imposed a scale by fixing the LOSP-GAVI distance at a value calculated from the REDEAM station positions. Similarly, information on orientation, if available, would come from repeated measurements of astronomic azimuths or GPS vectors involving stations in a larger reference network. The surveys analyzed here lack such data however, leaving the orientation of the network underdetermined. In our single-epoch treatment of these observations, we fix the LOSP-GAVI azimuth to the value calculated from the REDEAM station positions. This constraint brings the design matrix to full rank and poses the minimally-constrained problem, as shown in Table 3.5.

Once the rank deficiency of A is removed, an estimate of δX can be obtained by the standard weighted least squares procedure described below. A refined estimate of X is then formed by adding δX to the initial estimate Ξ , and the procedure is iterated to convergence.

Estimation Procedure

We assume that the residuals can be described by a stochastic process δS with mean $\langle \delta S \rangle = \delta \bar{S}$ and a variance matrix $V_S = \langle (\delta S - \delta \bar{S})(\delta S - \delta \bar{S})^T \rangle$ which is the product $V_S = \nu^2 \hat{V}_S$ of a known diagonal matrix \hat{V}_S and an unknown variance factor ν^2 to be estimated from the data. The problem is to minimize with respect to δX the squared norm of the scaled error process

$$\hat{r} = \delta \hat{S} - \hat{A} \delta X \quad (3.6)$$

where the carat indicates normalization by the "standard deviation matrix" $\hat{V}_S^{1/2}$

$$\begin{aligned} \delta \hat{S} &\equiv \hat{V}_S^{-1/2} \delta S \\ \hat{A} &\equiv \hat{V}_S^{-1/2} A \end{aligned} \quad (3.7)$$

The improvements $\delta \tilde{X}$ to the parameters can then be estimated by

$$\delta \tilde{X} = \hat{A}^\dagger \delta \hat{S} \quad (3.8)$$

where \hat{A}^\dagger is the pseudoinverse of \hat{A} . In the case where A has been rendered full rank, the generalized inverse is equivalent to the classical least squares estimator

$$\hat{\mathbf{A}}^\dagger = [\hat{\mathbf{A}}^T \hat{\mathbf{A}}]^{-1} \hat{\mathbf{A}}^T \quad (3.9)$$

The particular estimate of $\delta\tilde{\mathbf{X}}$ available to the observer is $\delta\tilde{\mathbf{X}}^O$ obtained by substituting the observed values \mathbf{S}^O of the data vector \mathbf{S} into equation (3.8). It represents one realization of a normally distributed stochastic process whose mean is $\delta\mathbf{X}$ and normalized variance matrix is $\hat{\mathbf{V}}_{\mathbf{X}} = (\hat{\mathbf{A}}^T \hat{\mathbf{A}})^{-1}$. The variance factor v^2 can be estimated *a posteriori* from the sample variance

$$\bar{v}^2 = \frac{|\delta\hat{\mathbf{S}}^O - \hat{\mathbf{A}}\delta\tilde{\mathbf{X}}^O|^2}{N - 2M} \quad (3.10)$$

This quantity is called the "variance of unit weight" by geodesists and has an expected value of unity if $\hat{\mathbf{V}}_{\mathbf{S}}$ is correctly scaled. We multiply the numerical value of this factor obtained from (3.10) by $\hat{\mathbf{V}}_{\mathbf{X}}$ to calculate the uncertainty of the estimate $\delta\tilde{\mathbf{X}}$.

Multiple Surveys

We now consider several surveys conducted at P distinct times (epochs) $\{t_p; p = 1, 2, \dots, P\}$. The data at the p th epoch consist of N_p observations \mathbf{S}_p of interstation angles, distances, and vectors. Collectively, the surveys form a data vector \mathbf{S} composed of the P subvectors $\{\mathbf{S}_p; p = 1, 2, \dots, P\}$ for a total of $N = \sum_1^P N_p$ observations involving M stations. As in the single-epoch problem, we treat the 2-dimensional case.

We specify our preliminary estimate of the coordinates of the m th station as a 2-vector $\xi^{(m)}$. These estimates for the M stations are only approximate, and need not be consistently valid at any single time. To express the time-dependent motion of the stations, we allow a different set of station coordinates at each epoch by writing the coordinates of the m th station at time t_p as $\mathbf{x}_p^{(m)}$. It is convenient to define a temporal origin t_0 , at which time the coordinates of the m th station are $\mathbf{x}_0^{(m)}$. In the DYNAP algorithm, the choice of t_0 is arbitrary, but in Prescott's [1976] technique, choosing t_0 to be at the temporal centroid permits an elegant simplification. We also designate a spatial origin, whose coordinates at t_0 are $\mathbf{x}_0^{(0)}$, and denote the coordinates relative to it with a capital delta

$$\Delta\mathbf{x}_0^{(m)} = \mathbf{x}_p^{(m)} - \mathbf{x}_0^{(0)} \quad (3.11)$$

Again, the choice of the origin $\mathbf{x}_0^{(0)}$ is arbitrary in the DYNAP algorithm, but other algorithms set it at the spatial centroid of the network. For example, in the "inner constraint" solution of Prescott [1981], this centroid remains fixed. The advantage of

the centroid is also apparent in the analogous problem of locating earthquake hypocenters, for which *Jordan and Sverdrup* [1981] have developed a method based on the "hypocentroidal decomposition theorem."

After choosing a spatial origin and an origin time, we can write the relative position of the m th station at time t_p as

$$\Delta \mathbf{x}_p^{(m)} = \Delta \mathbf{x}_0^{(m)} + (t_p - t_0) \mathbf{u}^{(m)} \quad (3.12)$$

where $\mathbf{u}^{(m)}$ is the velocity of the m th station, which we assume constant in time. As a simple parameterization of the velocity field, we describe $\mathbf{u}^{(m)}$ in terms of its gradient $L_{ij} = \partial u_i / \partial x_j$ [Malvern, 1969], evaluated at t_0 and $\mathbf{x}_0^{(0)}$. Adopting a uniform strain model [e.g., *Drew and Snay*, 1989], we assume \mathbf{L} to be constant in time and space and write the velocity of the m th station as

$$\mathbf{u}^{(m)} = \mathbf{u}^{(0)} + \mathbf{L} (\mathbf{x}_0^{(m)} - \mathbf{x}_0^{(0)}) \quad (3.13)$$

where $\mathbf{u}^{(0)}$ is the velocity of the origin. Because \mathbf{L} is not necessarily symmetric, the motion can include an arbitrary rigid body rotation about the origin. To make this rotation explicit, we write

$$\mathbf{L} = \dot{\mathbf{E}} + \dot{\mathbf{W}} \quad (3.14)$$

where $\dot{\mathbf{E}}$ is the strain rate tensor, and $\dot{\mathbf{W}}$ is the rotation rate tensor

$$\begin{aligned} \dot{\mathbf{E}} &\equiv \frac{1}{2} (\mathbf{L} + \mathbf{L}^T) \\ \dot{\mathbf{W}} &\equiv \frac{1}{2} (\mathbf{L} - \mathbf{L}^T) \end{aligned} \quad (3.15)$$

For the purpose of calculating differential quantities, we can approximate the positions of the stations relative to the origin by their initial estimates

$$\Delta \xi^{(m)} = \xi^{(m)} - \xi^{(0)} \quad (3.16)$$

For further notational simplicity, we rewrite the irrotational and rotational components of the velocity of the m th station with respect to the (moving) origin as

$$\begin{aligned} \dot{\mathbf{E}} \Delta \xi^{(m)} &= \mathbf{C}_m \dot{\mathbf{e}} \\ \dot{\mathbf{W}} \Delta \xi^{(m)} &= \mathbf{D}_m \dot{\mathbf{w}} \end{aligned} \quad (3.17)$$

where

$$\dot{\mathbf{e}} \equiv \begin{bmatrix} \dot{E}_{11} \\ \dot{E}_{22} \\ \dot{E}_{12} \end{bmatrix}; \quad \dot{\mathbf{w}} \equiv \dot{W}_{12} \quad (3.18)$$

and

$$\mathbf{C}_m \equiv \begin{bmatrix} \Delta \xi_1^{(m)} & 0 & \Delta \xi_2^{(m)} \\ 0 & \Delta \xi_2^{(m)} & \Delta \xi_1^{(m)} \end{bmatrix} \quad (3.19)$$

$$\mathbf{D}_m \equiv \begin{bmatrix} \Delta \xi_2^{(m)} \\ -\Delta \xi_1^{(m)} \end{bmatrix}$$

The improvement to the position vector of the m th station at time t_p is thus

$$\delta \mathbf{x}_p^{(m)} = \delta \Delta \mathbf{x}_0^{(m)} + \delta \mathbf{x}_0^{(0)} + (t_p - t_0) [\mathbf{u}^{(0)} + \mathbf{C}_m \dot{\mathbf{e}} + \mathbf{D}_m \dot{\mathbf{w}}] \quad (3.20)$$

The first two terms on the right side of equation (3.20) describe the improvements to the values at t_0 of the m th station's origin-relative position and the origin, respectively. The final term in equation (3.20) gives the displacement of the m th station in the time from t_0 to t_p .

To combine the M stations, we use a $kM \times k$ "copy" operator:

$$\mathbf{K}_k \equiv \begin{bmatrix} \mathbf{I}_k \\ \mathbf{I}_k \\ \vdots \\ \mathbf{I}_k \end{bmatrix} \quad (M \text{ partitions}) \quad (3.21)$$

where \mathbf{I}_k is the $k \times k$ identity matrix. It allows writing the improvements to the coordinates of all the stations at t_p as a concatenation of equation (3.20) over $m = 1, 2, \dots, M$

$$\begin{aligned} \delta \mathbf{X}_p &= \delta \Delta \mathbf{X}_0 + \mathbf{K}_2 \delta \mathbf{x}_0^{(0)} \\ &+ (t_p - t_0) [\mathbf{K}_2 \mathbf{u}^{(0)} + \mathbf{C} \mathbf{K}_3 \dot{\mathbf{e}} + \mathbf{D} \mathbf{K}_1 \dot{\mathbf{w}}] \end{aligned} \quad (3.22)$$

where $\delta \mathbf{X}_p$ and $\delta \Delta \mathbf{X}_0$ are the $2M$ -component vectors composed of the subvectors $\{\delta \mathbf{x}_p^{(m)}; m = 1, 2, \dots, M\}$ and $\{\delta \Delta \mathbf{x}_0^{(m)}; m = 1, 2, \dots, M\}$, respectively. The \mathbf{C} and \mathbf{D} matrices are simple block diagonal concatenations

$$\mathbf{C} \equiv \begin{bmatrix} \mathbf{C}_1 & & & \\ & \mathbf{C}_2 & & \\ & & \ddots & \\ & & & \mathbf{C}_M \end{bmatrix} \quad (3.23)$$

and

$$\mathbf{D} \equiv \begin{bmatrix} \mathbf{D}_1 & & & \\ & \mathbf{D}_2 & & \\ & & \ddots & \\ & & & \mathbf{D}_M \end{bmatrix} \quad (3.24)$$

At the p th epoch, the design matrix is \mathbf{A}_p . Its rows are a subset of the rows of \mathbf{A}_0 , which includes the partial derivatives of all Q possible interstation angles, distances, and vectors with respect to all $2M$ station coordinates. In practice, of course, not all these quantities are actually measured, so we write $\mathbf{A}_p = \mathbf{B}_p \mathbf{A}_0$, where \mathbf{B}_p is an $N_p \times Q$ matrix whose $(n, 2q)$ th entry is 1 if the n th observation involves the q th station and 0 otherwise. The normalized error vector for the p th epoch is thus

$$\hat{\mathbf{r}}_p = \Delta \hat{\mathbf{S}}_p - \hat{\mathbf{B}}_p \mathbf{A}_0 \delta \mathbf{X}_p \quad (3.25)$$

By substituting equation (3.22) for $\Delta \mathbf{X}_p$ we show the error vector in a form which separates the different types of parameters

$$\hat{\mathbf{r}}_p = \Delta \mathbf{S}_p - \hat{\mathbf{B}}_p \mathbf{A}_0 \begin{bmatrix} \mathbf{I}_{2M} & \mathbf{K}_2 & (t_p - t_0) \mathbf{K}_2 & (t_p - t_0) \mathbf{D} \mathbf{K}_1 & (t_p - t_0) \mathbf{C} \mathbf{K}_3 \end{bmatrix} \begin{bmatrix} \delta \Delta \mathbf{X}_0 \\ \delta \mathbf{x}_0^{(0)} \\ \mathbf{u}^{(0)} \\ \dot{\mathbf{w}} \\ \dot{\mathbf{e}} \end{bmatrix} \quad (3.26)$$

For P epochs, the problem becomes the concatenation of P versions of equation (3.26). Defining $\hat{\mathcal{A}}$ as the design matrix for the P -epoch problem, we find that it separates into two blocks, corresponding to the deformation parameters of interest $\dot{\mathbf{e}}$ and the other parameters \mathbf{y} .

$$\hat{\mathbf{r}} = \Delta \hat{\mathbf{S}} - \hat{\mathcal{A}} \begin{bmatrix} \mathbf{y} \\ \dot{\mathbf{e}} \end{bmatrix} = \Delta \hat{\mathbf{S}} - [\hat{\mathbf{G}} \ \hat{\mathbf{H}}] \begin{bmatrix} \mathbf{y} \\ \dot{\mathbf{e}} \end{bmatrix} \quad (3.27)$$

Here the vector \mathbf{y} contains the "nuisance" parameters [Jordan and Sverdrup, 1981].

$$\mathbf{y} \equiv \begin{bmatrix} \delta \Delta \mathbf{X}_0 \\ \delta \mathbf{x}_0^{(0)} \\ \mathbf{u}^{(0)} \\ \dot{\mathbf{w}} \end{bmatrix} \quad (3.28)$$

whose coefficients are given by the $N \times (2M + 5)$ matrix

$$\hat{\mathbf{G}} = \begin{bmatrix} \hat{\mathbf{B}}_1 \mathbf{A}_0 \mathbf{I}_{2M} & \hat{\mathbf{B}}_1 \mathbf{A}_0 \mathbf{K}_2 & (t_1 - t_0) \hat{\mathbf{B}}_1 \mathbf{A}_0 \mathbf{K}_2 & (t_1 - t_0) \hat{\mathbf{B}}_1 \mathbf{A}_0 \mathbf{D} \mathbf{K}_1 \\ \hat{\mathbf{B}}_2 \mathbf{A}_0 \mathbf{I}_{2M} & \hat{\mathbf{B}}_2 \mathbf{A}_0 \mathbf{K}_2 & (t_2 - t_0) \hat{\mathbf{B}}_2 \mathbf{A}_0 \mathbf{K}_2 & (t_2 - t_0) \hat{\mathbf{B}}_2 \mathbf{A}_0 \mathbf{D} \mathbf{K}_1 \\ \vdots & \vdots & \vdots & \vdots \\ \hat{\mathbf{B}}_P \mathbf{A}_0 \mathbf{I}_{2M} & \hat{\mathbf{B}}_P \mathbf{A}_0 \mathbf{K}_2 & (t_P - t_0) \hat{\mathbf{B}}_P \mathbf{A}_0 \mathbf{K}_2 & (t_P - t_0) \hat{\mathbf{B}}_P \mathbf{A}_0 \mathbf{D} \mathbf{K}_1 \end{bmatrix} \quad (3.29)$$

The coefficients of the strain rate parameters of interest form an $N \times 3$ matrix

$$\hat{\mathbf{H}} = \begin{bmatrix} (t_1 - t_0) \hat{\mathbf{B}}_1 \mathbf{A}_0 \mathbf{C} \mathbf{K}_3 \\ (t_2 - t_0) \hat{\mathbf{B}}_2 \mathbf{A}_0 \mathbf{C} \mathbf{K}_3 \\ \vdots \\ (t_P - t_0) \hat{\mathbf{B}}_P \mathbf{A}_0 \mathbf{C} \mathbf{K}_3 \end{bmatrix} \quad (3.30)$$

Singularities in the Design Matrix

As in the single-epoch problem, the complete design matrix $\hat{\mathbf{A}}$ is rank deficient. In our case, with distance measurements at two distinct epochs, the rank deficiency d is 6, leaving the rigid-body motion of the network (described by $\mathbf{x}_0^{(0)}$, $\mathbf{u}^{(0)}$, and $\dot{\mathbf{w}}$) completely undetermined. To solve the multiple-epoch problem using DYNAP, we set these parameters to zero by supplementing the data with constraints. For example, the origin $\mathbf{x}_0^{(0)}$ is specified by fixing one station as a reference station; holding it fixed for all time sets $\mathbf{u}^{(0)} = 0$. In our adjustments, we choose LOSP as the reference station because it is observed at every epoch. The choice, however, is arbitrary and does not affect the estimates of the strain rates. The rotation rate $\dot{\mathbf{w}}$ is constrained by fixing the azimuth between two stations at t_1 and t_P . We choose to fix the azimuth from LOSP to GAVI, but again, the choice is arbitrary.

An alternative to imposing these constraints is the "denuisancing" algorithm of *Jordan and Sverdrup* [1981]. By using projection operators, it avoids the difficulty of adding information (e.g., azimuths) to remove the singularities and then ignoring the estimates determined solely by that information (e.g., the rotation rate $\dot{\mathbf{w}}$). We do not

use this algorithm, however, because *Drew and Snay* [1987, 1989] have already written and tested an adequate program. Their DYNAP code is a straightforward approach to the problem, which, with a proper understanding of the singularities described above, is easy to use. The form of $\hat{\mathcal{A}}$ exhibited in equation (3.27) ensures that the estimates of the resolvable strain rates are immune to errors in the constraints, a result we can confirm numerically with sensitivity tests. For different choices and weightings of the constraints in the minimal set listed in Table 3.5, the DYNAP estimates of the strain rates do not change significantly.

The design matrix $\hat{\mathcal{A}}$ is also the key to combining different types of data. As described by *Drew and Snay* [1989], the design matrix maps triangulation observations from a coordinate system which is local at the standpoint station into a global coordinate system. This transformation requires knowledge of the local gravity field to correct triangulation measurements for the deflection of the vertical and to convert orthometric heights (from leveling) to ellipsoidal heights. Local deflection of the vertical can distort triangulation measurements at the level of 1 arc second, or approximately one standard deviation [*Bomford*, 1980]. Because the ellipsoidal heights are held fixed in our two-dimensional adjustment, our estimates of the strain rate parameters are sensitive to differences in station elevation, particularly for steeply inclined baselines. Since the network is located on Vandenberg Air Force Base and is frequently surveyed by the DMA, we were able to obtain reliable values for the deflection of the vertical (± 1 arc sec) and the ellipsoidal heights (± 10 cm) at all stations (R. Phillips, personal communication, 1988).

Derived Parameters

Although the DYNAP algorithm expresses the velocity field in terms of its gradient \mathbf{L} , there are other possible parameterizations which are more easily compared with geophysical observations. For the two-dimensional case, equation (3.14) can be written in components as

$$\mathbf{L} = \begin{bmatrix} \dot{E}_{11} & \dot{E}_{12} \\ \dot{E}_{12} & \dot{E}_{22} \end{bmatrix} + \begin{bmatrix} 0 & \dot{\omega} \\ -\dot{\omega} & 0 \end{bmatrix} \quad (3.31)$$

This decomposition is useful when the rotation rate $\dot{\omega}$ is undetermined due to the absence of orientation observations, e.g., astronomic azimuths or GPS vectors to a larger-scale reference frame. The strain rate $\dot{\mathbf{E}}$ can be represented in the coordinate

system defined by the principal strain axes by decomposing it into its eigenvalues $\dot{\epsilon}_i$ and its eigenvectors \hat{e}_i

$$\dot{\mathbf{E}} = \sum_{i=1}^2 \dot{\epsilon}_i \hat{e}_i \hat{e}_i^T \quad (3.32)$$

By convention, extension is positive, $\dot{\epsilon}_1 > \dot{\epsilon}_2$ and θ is measured clockwise from north (x_2 axis) to the principal axis \hat{e}_2 . As shown in Figure 3.4, the eigenvectors are

$$\hat{e}_1 = \begin{bmatrix} \cos \theta \\ -\sin \theta \end{bmatrix} \quad \hat{e}_2 = \begin{bmatrix} \sin \theta \\ \cos \theta \end{bmatrix} \quad (3.33)$$

The azimuth θ is the orientation of the maximum compressive strain rate $\dot{\epsilon}_2$ and coincides with the projection of the seismologist's compressive (P) axis onto the surface of the Earth. Since the eigenvalues $\dot{\epsilon}_i$ can be written as

$$\dot{\epsilon}_i = \hat{e}_i^T \dot{\mathbf{E}} \hat{e}_i \quad (3.34)$$

the magnitudes of the strain rates in the directions of the principal axes are

$$\begin{aligned} \dot{\epsilon}_1 &= \dot{E}_{11} \cos^2 \theta + \dot{E}_{22} \sin^2 \theta - 2\dot{E}_{12} \sin \theta \cos \theta \\ \dot{\epsilon}_2 &= \dot{E}_{11} \sin^2 \theta + \dot{E}_{22} \cos^2 \theta + 2\dot{E}_{12} \sin \theta \cos \theta \end{aligned} \quad (3.35)$$

The four quantities $\{\dot{\epsilon}_1, \dot{\epsilon}_2, \theta, \dot{\omega}\}$ define the "eigenvalue parameterization" of the two-dimensional velocity field.

A third parameterization can be written in terms of two engineering shear rates, a dilatation rate, and a rotation rate. By convention [Prescott *et al.*, 1979; Savage, 1983], the angular shear rates are defined as:

$$\begin{aligned} \dot{\gamma}_1 &= \dot{E}_{11} - \dot{E}_{22} \\ \dot{\gamma}_2 &= 2\dot{E}_{12} \end{aligned} \quad (3.36)$$

As shown in Figure 3.5, the shear parameter $\dot{\gamma}_2$ measures the decrease in the right angle between a ray pointed north and one pointed east. This decrease can be attributed to either right-lateral shear across a vertical fault striking due east or to left-lateral shear across a fault striking north. Similarly, $\dot{\gamma}_1$ measures the increase in the right angle between rays pointing NW and NE, due to right-lateral shear on a fault striking N45°W or left-lateral shear on a fault striking N45°E. In the absence of distance observations, it is not possible to resolve the ambiguity inherent in these two

parameters. *Prescott's* [1976] extension of *Frank's* [1966] method uses $\dot{\gamma}_1$ and $\dot{\gamma}_2$ to parameterize triangulation adjustments. The rate of areal dilatation is

$$\bar{\dot{\epsilon}} = \dot{\epsilon}_1 + \dot{\epsilon}_2 \quad (3.37)$$

The "engineering parameterization" is thus defined by $\{\dot{\gamma}_1, \dot{\gamma}_2, \bar{\dot{\epsilon}}, \dot{\omega}\}$ and is most useful in surveys involving triangulation observations only, when $\bar{\dot{\epsilon}}$ and $\dot{\omega}$ are undetermined.

It is important to remember that all three parameterizations (engineering, eigenvalue, and gradient) are completely equivalent descriptions of the same (constant-gradient) velocity field. The gradient parameterization is useful for calculations, but is rarely completely determined. The eigenvalue and engineering parameterizations are both useful because they separate the rotational component $\dot{\omega}$, which is typically poorly determined or completely undetermined. If measurements involving an external reference frame are not available or used, $\dot{\omega}$ is determined only by the azimuthal constraints, not the data, and is not meaningful. The other parameters in the engineering and principal parameterizations are immune to errors in the azimuthal data or constraints.

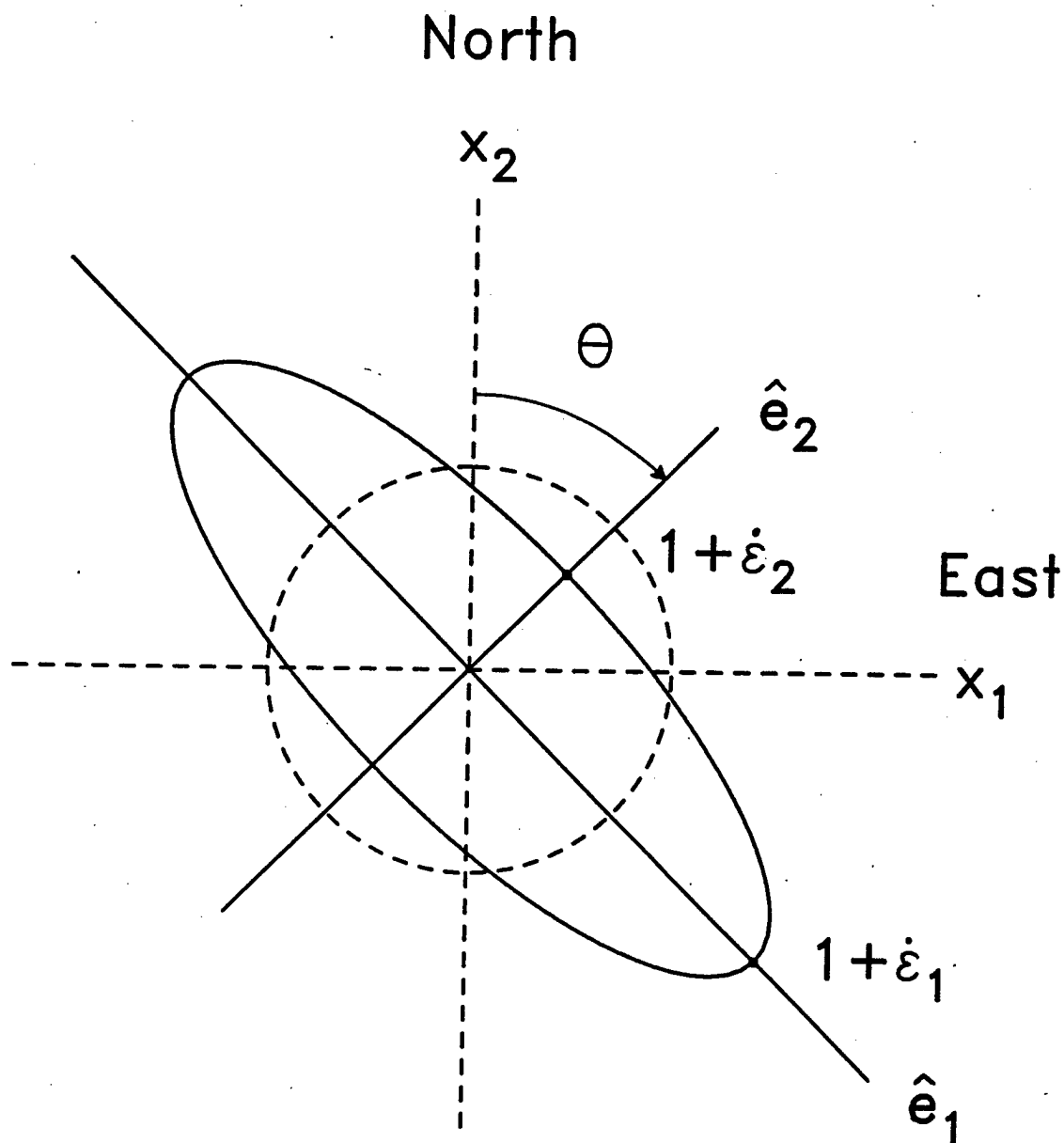


Figure 3.4. The eigenvalue parameterization. The unit circle deforms to the ellipse. The principal axes (eigenvectors) of the strain rate tensor $\dot{\mathbf{E}}$ are denoted by \hat{e}_1 and \hat{e}_2 . The strain rates in these directions are the eigenvalues $\dot{\epsilon}_1$ and $\dot{\epsilon}_2$. By convention, extension is positive, $\dot{\epsilon}_1 > \dot{\epsilon}_2$, and θ is measured clockwise from north (x_2 axis) to the principal axis \hat{e}_2 .

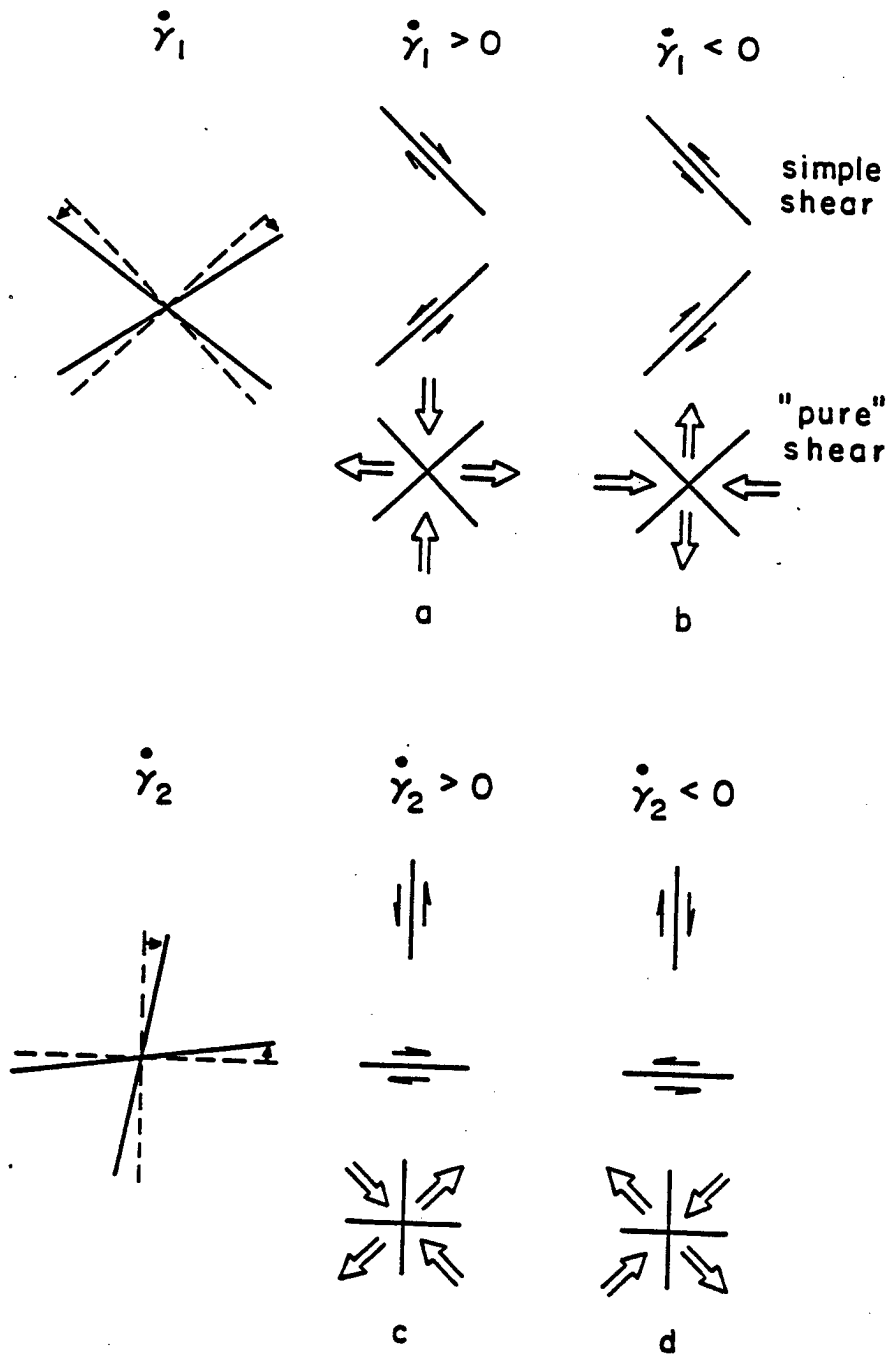


Figure 3.5. The engineering parameters $\dot{\gamma}_1$ and $\dot{\gamma}_2$ used to describe angular shear. The $\dot{\gamma}_1$ component is equal to the rate of increase in the (initially) right angle formed by the solid lines and measures shear in three different cases (top to bottom): (1) simple shear across a fault striking NW, (2) simple shear across a fault striking NE, and (3) N-S pure shear. The $\dot{\gamma}_2$ component is equal equal to the rate of increase in the (initially) right angle formed by the solid lines and measures shear in three different cases (top to bottom): (1) simple shear across a plane striking N, (2) simple shear across a plane striking E, or (3) NE-SW pure shear. (a) $\dot{\gamma}_1 > 0$, (b) $\dot{\gamma}_1 < 0$, (c) $\dot{\gamma}_2 > 0$, (d) $\dot{\gamma}_2 < 0$.

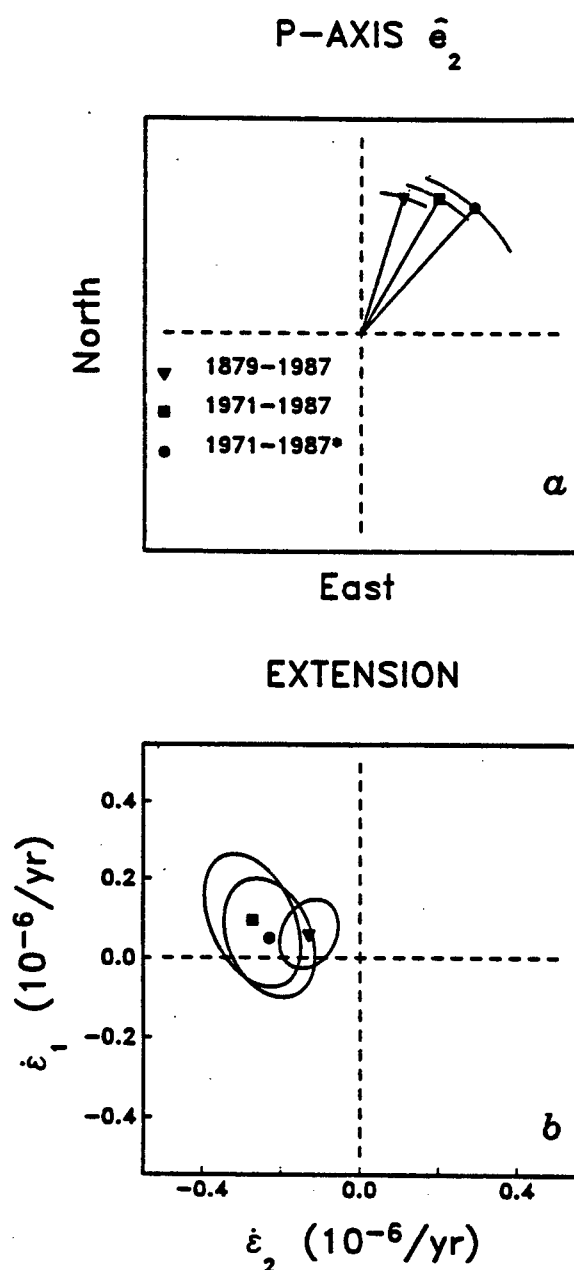


Figure 3.6. Eigenvalue parameterization of strain rates estimated from three different data sets: the complete 1879-1987 data set (triangles), the 1971-1987 trilateration subset (squares), and the 1971-1987 trilateration subset edited to favor the null hypothesis as described in the text (circles). (a) Orientation θ of the principal compressive strain axis \hat{e}_2 . The lengths of the vectors are arbitrary and the arcs denote 95% confidence intervals for θ . (b) Strain rate eigenvalues $\dot{\epsilon}_1$ and $\dot{\epsilon}_2$ in the coordinate frame of the eigenvectors \hat{e}_1 and \hat{e}_2 . Ellipses represent 95% confidence scaled by the *a posteriori* estimate of the variance factor \tilde{v}^2 .

Comparison with Other Methods

The form of equation (3.13) acts as a constraint on the velocity field. In particular, the velocity gradients must be constant in time and space, and the velocity of the origin is set to zero in the DYNAP algorithm. Although the completely general problem of station motion involves estimating a position vector and a velocity at each station, this approach would tend to map observation errors into velocities unless many repeated observations were available. In our case, assuming uniform strain through equation (3.13) reduces the number of parameters needed to describe the velocities of M stations from $2M$ to only the four components of L . The trade-off, of course, is that this assumption averages strain rate over the network as a whole.

An alternative is to use techniques developed for a "homogeneous" network, i.e., one where the same observations are exactly repeated at several different epochs. For triangulation surveys, *Prescott* [1976] extends *Frank's* [1966] method to calculate the two angular shear rate parameters $\dot{\gamma}_1$ and $\dot{\gamma}_2$ for an assumed uniform strain field from changes in angles. For trilateration surveys, *Prescott* [1981] and *Segall and Matthews* [1988] estimate individual station velocities (but not positions) from changes in repeated measurements of line lengths. These three approaches all require exactly repeated observations and are thus ill-suited to the eight different surveys of the SMFTB network. Distances and angles which are not observed at more than one epoch do not contribute to the determination of the strain rate parameters. For example, when station marks are destroyed and replaced, these homogeneous network techniques cannot be used directly, even if "ties" are available. In contrast, the DYNAP algorithm, by simultaneously estimating station coordinates and strain rate parameters, permits us to use all the available data.

GEODETIC RESULTS

Our complete solution includes all the observations from 1876 through 1987 shown in Table 3.3. These data are sufficient to determine the three independent components of the strain rate tensor \dot{E} , but not the rotation rate $\dot{\omega}$. The estimates expressed in the eigenvalue parameterization are displayed with their 95% confidence ellipses in Figure 3.6. In the text and Table 3.6, however, we present estimates with their uncertainties (± 1 standard deviation) scaled by \tilde{v} . The most significant strain rate parameter is $\dot{\epsilon}_2 = -0.13 \pm 0.03 \mu\text{strain/yr}$, which indicates compressive strain parallel to the second eigenvector, \hat{e}_2 , oriented at $\theta = N17^\circ E \pm 5^\circ$. Together, these values indicate significant N-NE compression. In the perpendicular \hat{e}_1 direction, the

estimated strain rate is $\dot{\epsilon}_1 = 0.06 \pm 0.04 \mu\text{strain/yr}$. This value has less than half the magnitude of $\dot{\epsilon}_2$ and is only marginally different from zero, suggesting that W–NW extension is relatively unimportant.

The estimates of the angular shear rates are shown in Figure 3.7. We find $\dot{\gamma}_1 = 0.16 \pm 0.04 \mu\text{rad/yr}$, which is compatible with any of the three dilatation-free fields shown in Figure 3.5a: (1) right-lateral simple shear on NW trending faults, (2) left-lateral simple shear on NE trending faults or (3) pure shear compression directed N–S. In the simple shear cases 1 and 2, surface features undergo a net rotation, while in the pure shear case 3, they experience no net rotation. The second component $\dot{\gamma}_2$ is $-0.15 \pm 0.03 \mu\text{rad/yr}$, compatible with any of the three possibilities shown in Figure 3.5d: (1) right-lateral simple shear on north striking faults, (2) left-lateral simple shear on west striking faults, or (3) pure shear due to NE–SW compression.

Superimposed on the shearing component of the strain field is a dilatation, which we estimate to be $\bar{\epsilon} = -0.07 \pm 0.05 \mu\text{strain/yr}$. The negative value indicates areal contraction (compression), which is significant at the 91% confidence level in a one-sided test.

We calculate the velocity v_{VT} of VNDN relative to TEPW by integrating the strain rate $\dot{\mathbf{E}}$ along the NE line between them to find $7 \pm 1 \text{ mm/yr}$ directed $\text{N}03^\circ\text{E} \pm 13^\circ$ (Figure 3.8). By integrating the symmetric tensor $\dot{\mathbf{E}}$, we have assumed that the unresolved rotation $\dot{\omega}$ is zero. Of course, the geodetic data alone do not justify the no-rotation assumption. The effect of a clockwise rotation on the VNDN–TEPW relative velocity would be to move the estimate northwestward along a line perpendicular the VNDN–TEPW azimuth.

To verify the strain rates estimated from the complete data set, we analyzed two different subsets of the data: angles only and distances only. These analyses permit the estimation of strain rates without the potential pitfalls of combining heterogeneous data.

TABLE 3.6. Estimated Strain Rates

TABLE 3.6. Estimated Strain Rates

Years	$\tilde{\nu}^2$	$\dot{\gamma}_1$, 0.1 $\mu\text{rad/yr}$	$\dot{\gamma}_2$, 0.1 $\mu\text{rad/yr}$	$\dot{\epsilon}$, 0.1 $\mu\text{strain/yr}$	θ	$\dot{\epsilon}_1$, 0.1 $\mu\text{strain/yr}$	$\dot{\epsilon}_2$, 0.1 $\mu\text{strain/yr}$
1879-1987	1.44	1.6 ± 0.4	-1.1 ± 0.3	-0.7 ± 0.5	$\text{N}17^\circ\text{E} \pm 05^\circ$	0.6 ± 0.4	-1.3 ± 0.3
1971-1987	1.20	1.9 ± 1.0	-3.2 ± 0.8	-1.8 ± 0.7	$\text{N}30^\circ\text{E} \pm 07^\circ$	0.9 ± 0.7	-2.7 ± 0.5
1971-1987 ^a	0.98	0.3 ± 1.0	-2.8 ± 0.8	-1.8 ± 0.7	$\text{N}42^\circ\text{E} \pm 10^\circ$	0.5 ± 0.6	-2.3 ± 0.5
1879-1924	2.11	-0.1 ± 1.3	-1.7 ± 0.9	-1.7 ± 1.1	$\text{N}46^\circ\text{E} \pm 23^\circ$		

Notes:

^a Edited data set

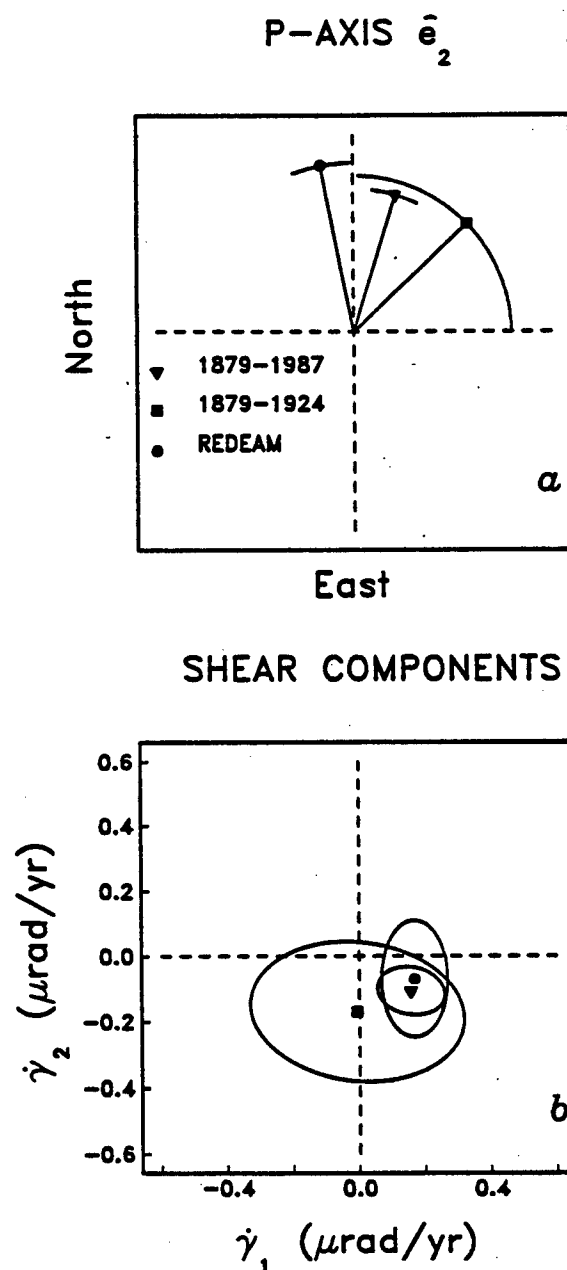


Figure 3.7. Engineering parameterization of strain rates estimated from three different data sets: the complete 1879-1987 data set (triangles), the 1897-1924 triangulation subset (squares), and the results from the REDEAM Bakersfield region, district 6 as determined by *Snay et al.* [1987] (circles). (a) Orientation θ of the principal compressive strain axis \hat{e}_2 as in Figure 3.6a. (b) Engineering shear parameters $\dot{\gamma}_1$ and $\dot{\gamma}_2$. Ellipses represent 95% confidence scaled by the *a posteriori* estimate of the variance factor \tilde{v}^2 .

Triangulation Only

The first subset includes only the triangulation measurements taken in 1879 and repeated in 1924. The network of this data subset consists of four stations forming a braced quadrilateral: TEPU, GAVI, LOSP and ARGU. It is the same network analyzed by *Savage and Prescott* [1978], but more observations from 1924 exist in the REDEAM data set than were available to them. Their limited data set includes only one or two measurements of each direction in 1924 while the REDEAM data set contains two or three measurements (Table 3.3).

We first used the small 1879–1924 data set of *Savage and Prescott* [1978] to compare the DYNAP technique with *Prescott's* [1976] technique. In the DYNAP solution, we eliminated the $d = 4$ rank deficiency by constraining the distance and azimuth of the LOSP–GAVI vector (Table 3.5). The two different techniques yield estimates which differ by less than $0.1 \mu\text{rad/yr}$, a small fraction of the uncertainties. As an additional test, we compared the estimates from the large REDEAM 1879–1924 data set with those from the subset of *Savage and Prescott* [1978]. The estimates from the two different data sets differ slightly, but agree to within their uncertainties. Finally, our DYNAP estimates from the complete data set agree with the published values of *Savage and Prescott* [1978] to within their uncertainties.

Our results from the large 1879–1924 REDEAM triangulation data subset are shown in Figures 3.7 and 3.9. The second shear component $\dot{\gamma}_2$ is negative, although not significant at the 95% confidence level, and is in qualitative agreement with the estimate from the complete data set. A graphical representation of the 1879–1924 triangulation observations is shown in Figure 3.9. For each angle α , we estimate a time derivative $d\alpha/dt$, which we normalize by $\sin\alpha$ and plot as a function of azimuth. As shown by *Snay* [1986], the uniform strain field described by equation (3.13) implies that this quantity varies sinusoidally with azimuth:

$$\frac{1}{\sin\alpha} \frac{d\alpha}{dt} = [\dot{\gamma}_1 \cos 2\bar{\theta} - \dot{\gamma}_2 \sin 2\bar{\theta}] \quad (3.38)$$

where $\bar{\theta}$ is the azimuth which bisects the angle. The crests of the sine wave occur at azimuths $\bar{\theta}$ and $\bar{\theta} + 180^\circ$. Of the 12 angles shown in Figure 3.9, only eight are independent. For example, the two rapidly decreasing angles near $\bar{\theta} = 300^\circ$ are both derived from observations of the GAVI–ARGU direction. We compare the angular data with two models: the strain rates estimated from the completed data set, and those from the 1879–1924 triangulation observations. The data are qualitatively consistent with both of the modeled curves, but they are also consistent with zero

strain. This is also illustrated in Figure 3.7, where the 95% confidence ellipse for $\dot{\gamma}_1$ and $\dot{\gamma}_2$ estimated from the 1879–1924 triangulation data includes both the estimate from the complete data set and the point $(\dot{\gamma}_1, \dot{\gamma}_2) = 0$.

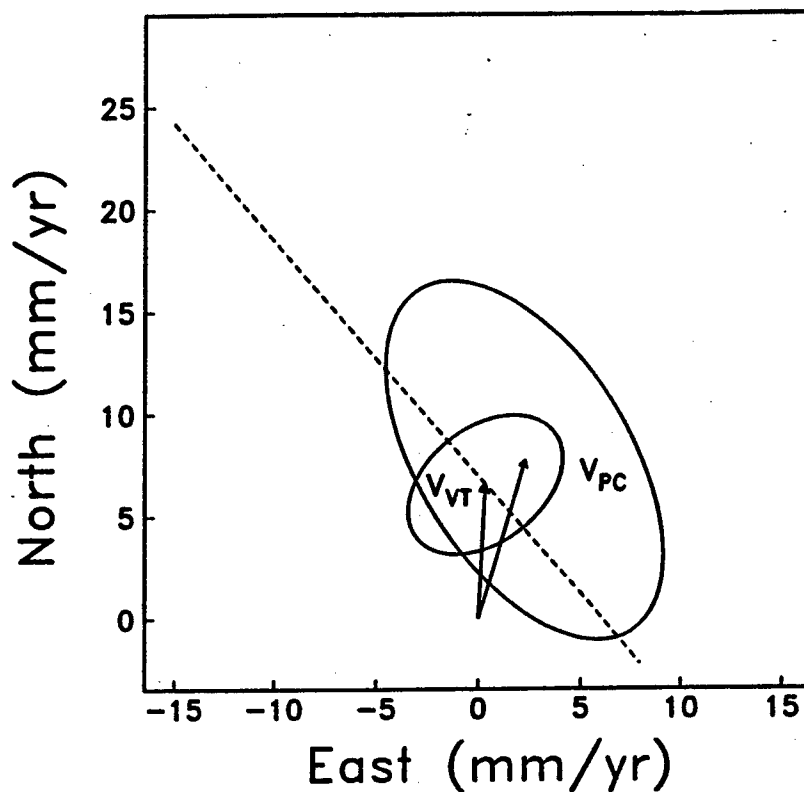


Figure 3.8. Observed and predicted relative velocities. The velocity v_{VT} of VNDN relative to TEPW is the line integral of the strain rate $\dot{\mathbf{E}}$ estimated from the complete data set under the assumption of zero rotation. A clockwise rotation would move the estimated vector to the left along the dashed line perpendicular to the VNDN-TEPW azimuth. The "discrepancy vector" (v_{PC}) is calculated from equation (3.1) with the values in Table 3.1. The ellipses delimit the regions of 95% confidence.

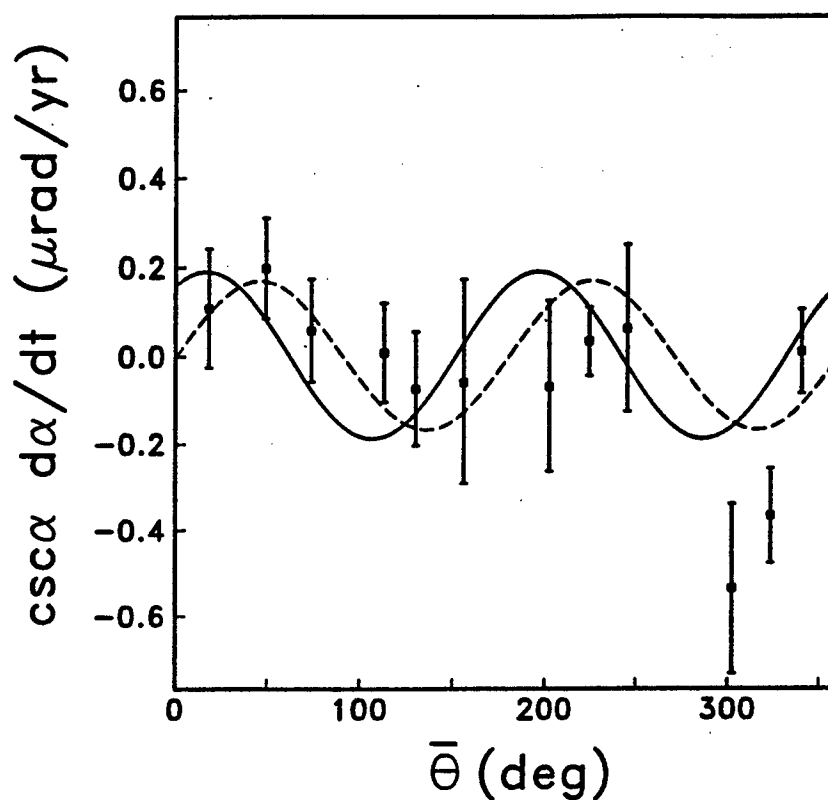


Figure 3.9. Normalized angular rate of change $\text{csc}\alpha \frac{\partial\alpha}{\partial t}$ as a function of bisector azimuth $\bar{\theta}$, measured clockwise from north. The curves are calculated according to equation (3.38) using the values of the angular shear rate parameters $\dot{\gamma}_1$ and $\dot{\gamma}_2$ estimated from the complete 1879-1987 data set (solid line) and the 1879-1924 triangulation subset (dashed line). Only angles repeated at two epochs separated by more than 10 years are shown. Error bars indicate one standard deviation.

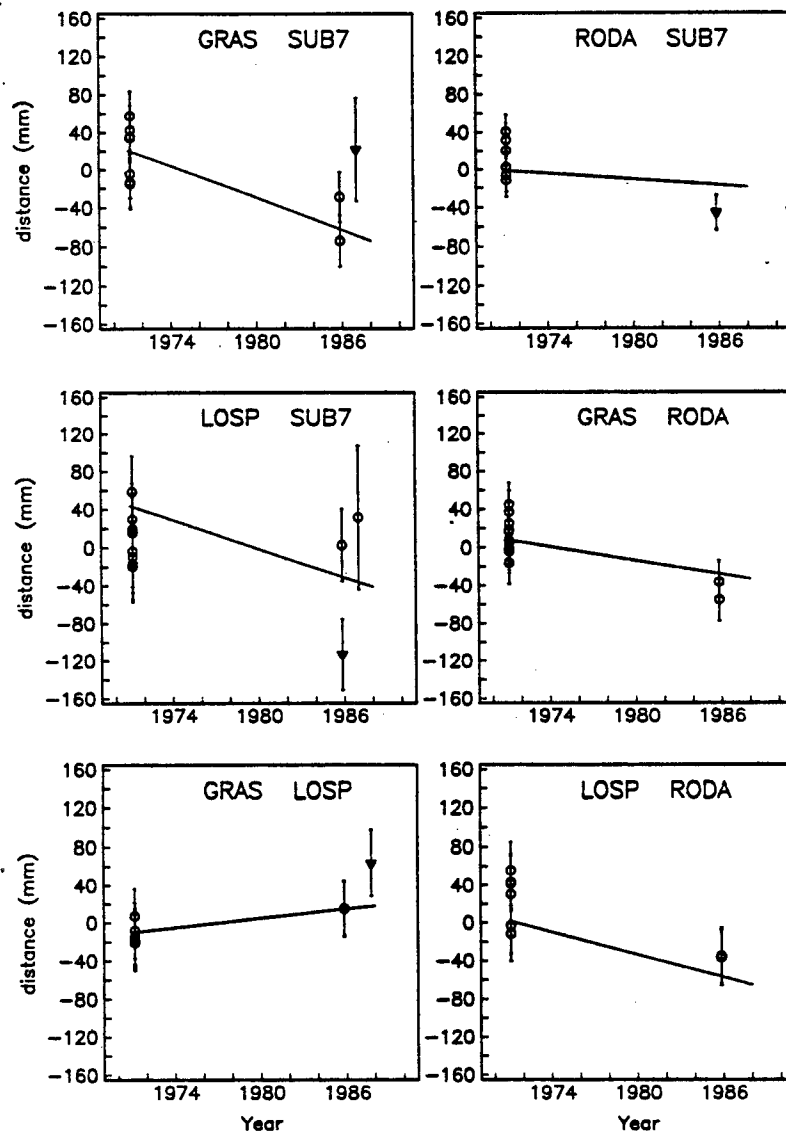


Figure 3.10. Interstation distances as a function of time. The sloped lines represent the rate of change predicted by the uniform strain model estimated from the complete 1879-1987 data set. The distances are shown after subtracting a nominal mean length and the error bars indicate one standard deviation for a single observation. Triangles denote suspect data points, three of which were edited in a separate adjustment, as described in the text.

Trilateration Only

Distance observations were made with EDM in 1971 and exactly repeated in 1985 between stations RODA, GRAS, SUB7, and LOSP (Figure 3.3). By combining the GPS vectors in Table 4 with a local tie between SUB7 and VNDN, we can calculate the distances between SUB7, LOSP, and GRAS for the 1987 epoch. Together, these observations form a data set of six lines whose lengths were measured in 1971, 1985, and 1987. As shown in Figure 10, five out of six of these lines are shortening. These data, when inverted with DYNAP, yield estimates which are consistent with the results from the complete data set, although $\dot{\epsilon}_1$ is slightly higher and θ more easterly (Figure 3.6).

To verify the robustness of these estimates, we performed a second analysis in which we altered the weights of the three suspect measurements shown with triangles in Figure 3.10. We changed the weights of these data points to force the estimates of strain to favor the null hypothesis of zero strain: (1) we doubled the standard deviation assigned to the 1986 EDM measurement of the short RODA–SUB7 line, to account for a possible underestimate of the instrument bias in the 1986 survey; (2) we omitted the 1987 GRAS–LOSP vector, constructed from the two GPS vectors, VNDN–LOSP and VNDN–GRAS, which were measured in different surveys using different fiducial networks; and (3) we omitted the short 1986 EDM measurement of LOSP–SUB7, marked as suspect by the DMA. To favor the null hypothesis of zero strain, we did not delete or reweight a fourth suspect measurement, the 1987 GRAS–SUB7 distance constructed from a combination of a GPS vector and local ties. Despite these modifications, the edited data set yields estimates of strain rates which are significantly different from zero at the 95% confidence level and consistent with the estimates from the complete data set (Figure 3.6 and Table 3.6).

Comparison With REDEAM

As a further check, we compared our results with those of the REDEAM project [Snay *et al.*, 1987], an inversion of a large historical data set which includes the first four epochs of this study, through 1971. Snay *et al.* [1987] estimate the average strain rates over districts roughly four times the size of the SMFTB quadrilateral. Their region 6 (Bakersfield), district I, includes all the stations in our network, as well as several hundred others. For this district, outlined in Figure 3.1, they found maximum dextral shear oriented $N56^\circ W \pm 5^\circ$. Assuming uniaxial strain, this value implies that

the compressional axis \hat{e}_2 is oriented $N11^\circ W \pm 5^\circ$, significantly different from our result of $N17^\circ E \pm 5^\circ$ (Figure 3.7).

There are two possible reasons for the difference. The first is that the different-sized networks are sampling different strain fields. The REDEAM inversion averages strain over a large area including several different tectonic regions. For example, the REDEAM district combines the SMFTB area with the active Ventura Basin, where *Donnellan et al.* [1988] have observed 30 ± 5 mm/yr of north-south compression.

Another possible reason for the disagreement between our results and the REDEAM model is the existence of some spurious observations in the large data set analyzed by *Snay et al.* [1987]. It appears that observations made in the 1880s, but published in 1929, were entered as 1929 observations. Since the same observations were already entered with their correct (1880s) dates, the spurious 1929 observations would tend to erase the effect of any strain in the pre-seismic period and over-emphasize the coseismic strain.

The 1927 Lompoc Earthquake

We investigated the possible geodetic signal of displacement due to the 1927 Lompoc earthquake which, for a magnitude 7.3 event [*Hanks, 1979*] could be of the order of 1 m on the fault. *Savage and Prescott* [1978] estimated the coseismic signal by dividing the triangulation data into a preseismic (1879–1924) interval and a coseismic and postseismic (1924–1956) interval. They then estimated $\dot{\gamma}_1$ and $\dot{\gamma}_2$ for each interval and attributed the marginally significant change in $\dot{\gamma}_1$ to the earthquake.

There are two reasons to believe that *Savage and Prescott's* [1978] determination of the coseismic strain is an overestimate. First, they were not aware that ARGU was moved to ARG1 in 1942 without changing the name of the mark. Their estimates of $\dot{\gamma}_1$ and $\dot{\gamma}_2$ for 1924–1956 are contaminated by the reset, not the earthquake. Second, the earthquake has been relocated. *Savage and Prescott* [1978] used *Gawthrop's* [1978b] epicenter, less than 10 km from the geodetic network, in their dislocation model for co-seismic displacement. *Hanks* [1979] and PG&E however, relocate the earthquake farther south, almost 30 km from the network. Using a simple model of a double couple at a point in an infinite elastic medium [*Aki and Richards, 1980*], we would expect displacements in the geodetic network of less than 10 mm, an order of magnitude smaller than the triangulation uncertainties.

DISCUSSION

Active Tectonics of the Santa Maria Fold and Thrust Belt

Our geodetic results indicate significant rates of deformation in the Santa Maria Fold and Thrust Belt. We have measured compression occurring along a N–NE axis at a rate of $0.13 \pm 0.03 \mu\text{strain/yr}$. The rate of angular shear is described by $\dot{\gamma}_1$ and $\dot{\gamma}_2$, which we estimate to be significantly positive and negative, respectively. Due to the lack of orientation information we cannot estimate the rotation rate $\dot{\omega}$, however. We are thus unable to distinguish between simple shear and pure shear on the basis of the geodetic estimates alone. The dilatation-free part of the strain field may be accommodated in any of the three mechanisms shown (from top to bottom) in Figures 3.5a and 3.5d: (1) dextral simple shear on faults trending north to NW, (2) sinistral simple shear on faults trending west to SW, or (3) irrotational pure shear directed north to NE. In the absence of an estimate of $\dot{\omega}$, we must employ geologic evidence to interpret the strain field, because each of these three mechanisms has a different tectonic expression.

Our geodetic estimate of the orientation of the principal compressive axis (θ) is $N17^\circ E \pm 5^\circ$, consistent with geologic indicators. This axis is nearly perpendicular to the Neogene fold axes plotted by Page [1966, 1981]. In a more quantitative analysis, Matz and Slemmons [1987] have examined the azimuthal distribution of compressive features in the Santa Maria Basin expressed in Landsat images. They find that fold axes and fault scarps there have an average orientation of $N50^\circ W \pm 20^\circ$, indicative of compression perpendicular to that direction ($N40^\circ E \pm 20^\circ$). E. Vittori et al. (unpublished manuscript, 1989) have performed a similar analysis of field geologic data: jointing, normal faults, and layering for the Santa Maria Valley and the San Luis Obispo area to the north. The azimuthal distributions of Pliocene and Quaternary layers and normal fault strikes both show a peak at about $N60^\circ W$, indicative of compression oriented $N30^\circ E$. Similarly, their jointing data cluster around $N33^\circ E$ (σ_1) and $N71^\circ W$ (σ_2). The absence of faults striking west to SW (evident in Figure 3.2) argues against left-lateral simple shear on faults striking in this direction.

The orientation of the principal axis of compression estimated from the geodetic data also agrees with the principal stress directions inferred from earthquake focal mechanisms determined in the SMFTB [Gawthrop 1975, 1978a; Eaton, 1984; Hill et al., 1989]. In these mechanisms, the compressive (P) axis is generally oriented NE–SW, and the null (B) axis NW–SE (Figure 3.11), consistent with the three

geodetically determined parameters θ , $\dot{\epsilon}_1$, and $\dot{\epsilon}_2$ shown in Figure 3.6. The orientation of compression given by θ is NE–SW, the strain in this direction is compressive ($\dot{\epsilon}_2 < 0$), and the NW–SE extension is negligible, ($\dot{\epsilon}_1 \approx 0$).

The rate of deformation estimated from the geodetic data is also consistent with geologic observations of deformation over the last several million years. For comparison, we can estimate a (scalar) rate of crustal shortening from the (vector) relative velocity v_{VT} by projecting it onto a line perpendicular to the strike of local structure. In the SMFTB, such a line connects points B and B' in Figure 3.1 and trends N30°E, essentially normal to the compressive features. The rate of crustal shortening along this line (the magnitude of the N30°E component of v_{VT}) is 6 ± 2 mm/yr, a result which is not strongly dependent on the assumption of no rotation. A geologic cross section along the same B–B' line yields a rate of shortening of 2.3–4.6 mm/yr [Namson and Davis, 1990]. Although evaluating its uncertainty is difficult, the geologic estimate provides at least qualitative confirmation that compression is actively occurring.

The amount of right-lateral shear occurring perpendicular to the B–B' line is the N60°W component of v_{VT} , which we estimate to be 3 ± 1 mm/yr. This estimate assumes, for lack of better information, that the unknown rotation rate $\dot{\omega}$ is zero. If, for example, the clockwise rotations of the order of 5°/m.y. proposed by Hornafius [1985] for the last 5 m.y. are currently active, then the right-lateral strike-slip component of v_{VT} would increase by about 5 mm/yr, moving the relative velocity vector northwestward on the dashed line in Figure 3.8. Conversely, a counterclockwise rotation would decrease our estimate of the strike-slip component. Since most models of Neogene rotation around the SMFTB suggest that the sense of rotation is clockwise [Luyendyk et al., 1980, 1985; Hornafius, 1985; Hornafius et al., 1986], our estimate of the strike-slip component probably represents a lower bound.

Using the focal mechanisms to estimate the amount of shear also requires additional assumptions, because the small strike-slip component of the focal mechanisms is ambiguous. In most of the focal mechanisms shown in Figure 3.11, one of the two fault planes strikes NW, but the solutions do not determine which one is actually the principal fault plane. In light of the abundance of NW striking faults in the area (Figure 3.2), it is reasonable to choose planes striking in this direction as the principal fault planes. To the degree that this inference is correct, we can identify the minor strike-slip component of these mechanisms as right-lateral.

Although the assumption of no net rotation allows us to make a qualitative argument for substantial amounts of right-lateral shear or strike-slip in the SMFTB,

quantification of the amount of right-lateral slip occurring as oblique slip on NW trending faults will require future GPS observations at multiple epochs to measure the rotation rate $\dot{\omega}$ with respect to a well-determined external reference frame.

The compression evident in the estimate of $\dot{\epsilon}_2$ and in the thrusting mechanisms, however, does not depend strongly on the assumption of no rotation, is statistically significant, and represents substantial tectonic deformation. We infer that N-NE compressive deformation is being accommodated on NW trending folds or thrust faults, such as the Los Alamos, Baseline, North Baseline, Orcutt, and Casmalia, which may also undergo some right-lateral oblique slip. With the exception of the Los Alamos fault [Guptill *et al.*, 1981], these faults do not appear to cut the surface. They are thus blind or incipient thrusts, probably associated with fault-propagation folding, as suggested by Namson and Davis [1990] and Nitchman *et al.* [1989]. This model is also favored by the association of earthquake hypocenters with the folds shown in Figure 3.2 [Stein and Yeats, 1989].

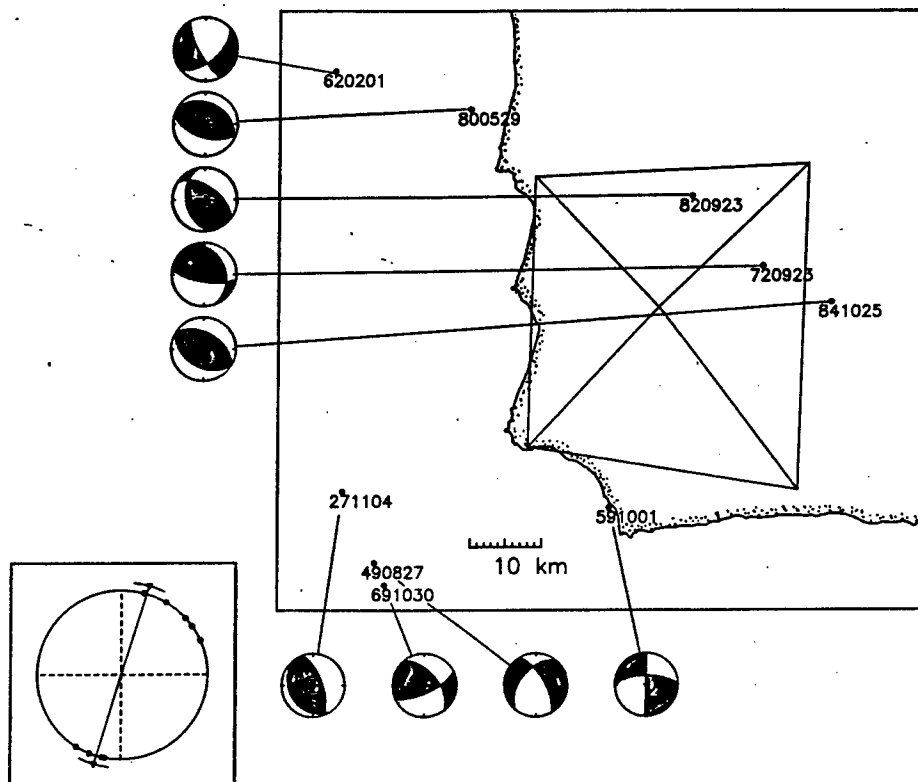


Figure 3.11. Earthquake focal mechanisms. The inset shows orientation of the horizontal projection of their P axes (circles) and the principal compressive axis \hat{e}_2 estimated from the complete 1879-1987 geodetic data set (line connecting the two triangles). The mechanisms (labelled with their dates) are from *Gawthrop* [1975, 1978a], *Lee et al.* [1979], *Eaton* [1984], and *Hill et al.* [1989] and project first arrivals onto the lower hemisphere and shade the quadrants of compressional arrivals.

Implications for the San Andreas Discrepancy

We have measured the amount of active deformation in the SMFTB; to put it in a larger context, we compare it with the values predicted by regional kinematic models. As discussed in the introduction, the amount of deformation west of the San Andreas is described by v_{PC} , which represents the velocity of the Pacific plate relative to a coordinate frame grounded just west of point C. In Figure 3.12, we compare two estimates of v_{PC} , one obtained from the continental-scale vector balance of equation (3.1), and a second that makes use of our geodetic results. The latter sums the deformation along a path connecting a point on the stable Pacific plate to the west side of point C. The path comes onshore at VNDN, crosses the SMFTB to TEPW, and proceeds across the Salinian block to point C. As described by equation (3.2), this integral can be broken into three pieces.

The first part, v_{PV} , measures the velocity of the Pacific plate with respect to VNDN. We can evaluate this term by comparing two estimates of the velocity of the Vandenberg VLBI site with respect to stable North America: the 49 ± 1 mm/yr at $N38^\circ W \pm 2^\circ$ predicted by the NUVEL-1 model of global plate motions [DeMets *et al.*, 1989], and the 46 ± 3 mm/yr at $N41^\circ W \pm 6^\circ$ observed by VLBI [Sauber, 1988]. Their difference is a vector with a rate of 4 ± 4 mm/yr at an azimuth of $N03^\circ E \pm 57^\circ$. We note that this value is insignificantly different from zero, consistent with the hypothesis that VNDN is fairly well anchored on the Pacific plate. However, it is also consistent with the possibility that some additional deformation may be occurring offshore, perhaps as far out as the Santa Lucia Banks, at a rate of several millimeters per year [Crouch *et al.*, 1984].

The second term, v_{VT} , represents the integrated rate of deformation within the SMFTB, which the geodetic data constrain to be 7 ± 1 mm/yr directed $N03^\circ E \pm 13^\circ$. As discussed earlier, this estimate assumes no rotation. It partitions into about equal amounts of compression and right-lateral shear. Since the estimates of v_{VT} and v_{PC} agree at the 95% confidence level (Figure 3.8), we infer that most of the deformation along this path is occurring within the Santa Maria Fold and Thrust Belt.

The third part, v_{TC} , measures deformation across the Salinian Block. The relative rigidity of this domain [Dibblee, 1977] suggests that the amount of deformation is not likely to be large, although the actual rate is not well determined, due to the absence of geodetic data. A path from Tepusquet Peak (point T in Figure 3.1), at $N45^\circ E$ to the San Andreas crosses several features. In the Sierra Madre mountains, the Rinconada fault and an inferred NW extension of the Ozena fault are probably not

active because they are cut by the active Big Pine fault farther to the SE [Dibblee, 1977]. There is no indication of activity on the La Panza fault in the range of the same name; e.g., it is not marked as active on the Quaternary map of Jennings [1975]. In the Caliente Range, the Whiterock and Morales thrust faults appear to have accommodated about 2 and 7 km of offset in the last 3 m.y. [Davis *et al.*, 1988]. Since these faults dip at about 45° , a simple (but perhaps naive) average suggests a rate of order 2 mm/yr at about $N45^\circ E$. If we assume that there is no deformation between two points on the same section of the San Andreas, then the total amount of deformation between points T and C is roughly 2 ± 1 mm/yr at $N45^\circ E \pm 16^\circ$.

The direct estimate of v_{PC} obtained from (3.2) using the three estimates just described is 12 ± 5 mm/yr at $N09^\circ E \pm 20^\circ$. Figure 12 compares it with the closure estimate of 8 ± 3 mm/yr at $N17^\circ E \pm 24^\circ$ derived from (3.1) using the estimates of Table 3.1. As previously noted, the latter includes 1–2 mm/yr of fault-normal compression east of the San Andreas, whereas the former does not. The direct estimate is larger than the closure estimate, although the two are not significantly different at the 95% confidence level.

If the direct estimate of v_{PC} is fed back into (3.1), and the values given in Table 3.1 are used for v_{PN} and v_{SA} , then we obtain $v_{CN} = 8 \pm 5$ mm/yr at $N83^\circ W \pm 39^\circ$. This value is qualitatively different from, but statistically consistent with, the rate and azimuth of Basin and Range extension estimated from the VLBI data (9 ± 4 mm/yr at $N48^\circ W \pm 17^\circ$) according to Minster and Jordan's [1987] model B. Clearly, more remains to be learned about the San Andreas discrepancy through continued space geodetic observations.

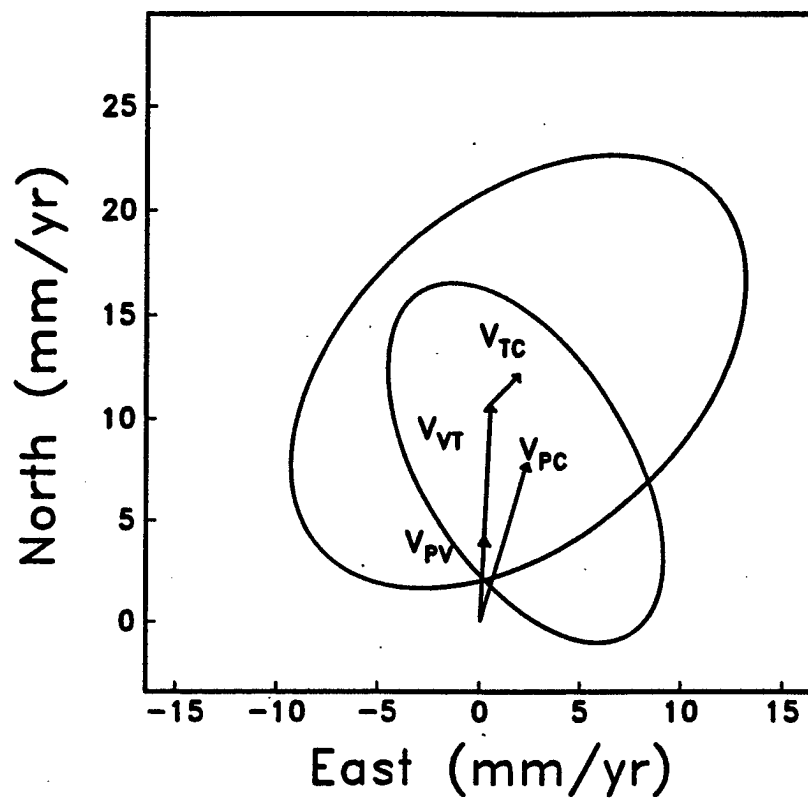


Figure 3.12. Two estimates of the integrated rate of deformation in coastal California. The shorter vector (v_{PC}) is estimated from the regional vector balance of equation (3.1) as in Figure 3.8. The other vector represents a local estimate from equation (3.2), which sums deformation offshore of Vandenberg (v_{PV}), within the SMFTB (v_{VT}), and between the SMFTB and the San Andreas (v_{TC}).

The Santa Maria Fold and Thrust Belt as a Transition Zone

Our local measurement of v_{VT} implies that a significant fraction of the deformation west of the San Andreas is occurring within the Santa Maria Fold and Thrust Belt. This observation can be used to constrain kinematic models of deformation in the adjacent tectonic domains, particularly the southern Coast Ranges which abut the SMFTB to the north and the western Transverse Ranges which join it to the south and east. Our results are consistent with the notion that the SMFTB acts as a transition zone in the modes of folding and faulting taking place in these two domains.

On a southward traverse of the southern California margin, the local structures trend in a sweeping arc from the NW striking features subparallel to the San Andreas in the Coast Ranges, to the WNW strikes in the SMFTB, to the west striking trends in the Transverse Ranges (Figure 3.13). Projecting the integrated deformation rate expressed by v_{PC} onto these local structures results in about equal amounts of right-lateral shear and fault-normal compression in the southern Coast Ranges. The right-lateral component decreases across the SMFTB and essentially vanishes in the eastern part of the Santa Barbara Channel, where the deformation appears to be accommodated primarily by N-S compression (Figure 3.13).

The transition is evident in earthquake focal mechanisms. In the Coast Ranges west of the Nacimiento fault, the average P axis orientation is $N26^\circ E \pm 18^\circ$ [Dehlinger and Bolt, 1988], somewhat more easterly than the N-NE orientation observed for the P axes of the events in the SMFTB (Figure 3.11). The available focal mechanisms tend to belong to one of two separate populations: either thrusting normal to the San Andreas, or right-lateral strike-slip events on planes striking parallel to it [Dehlinger and Bolt, 1988; PG&E]. This dichotomy has been explained by the hypothesis that deformation in a transpressive regime "decouples" into strike-slip and compression along separate faults [e.g., Fitch, 1972; Mount and Suppe, 1987; Namson and Davis, 1988a]. In the western Transverse Ranges, the azimuthal distribution of P axes exhibits two maxima, one at due north, the other at about $N50^\circ E$, which bracket the normal to the San Andreas fault trace at $N24^\circ E$ [Lee et al., 1979; Yerkes and Lee, 1979]. It appears that the P -axes are closer to due north in the area west of $119.5^\circ W$ near the city of Santa Barbara and closer to NE in the area east of this longitude.

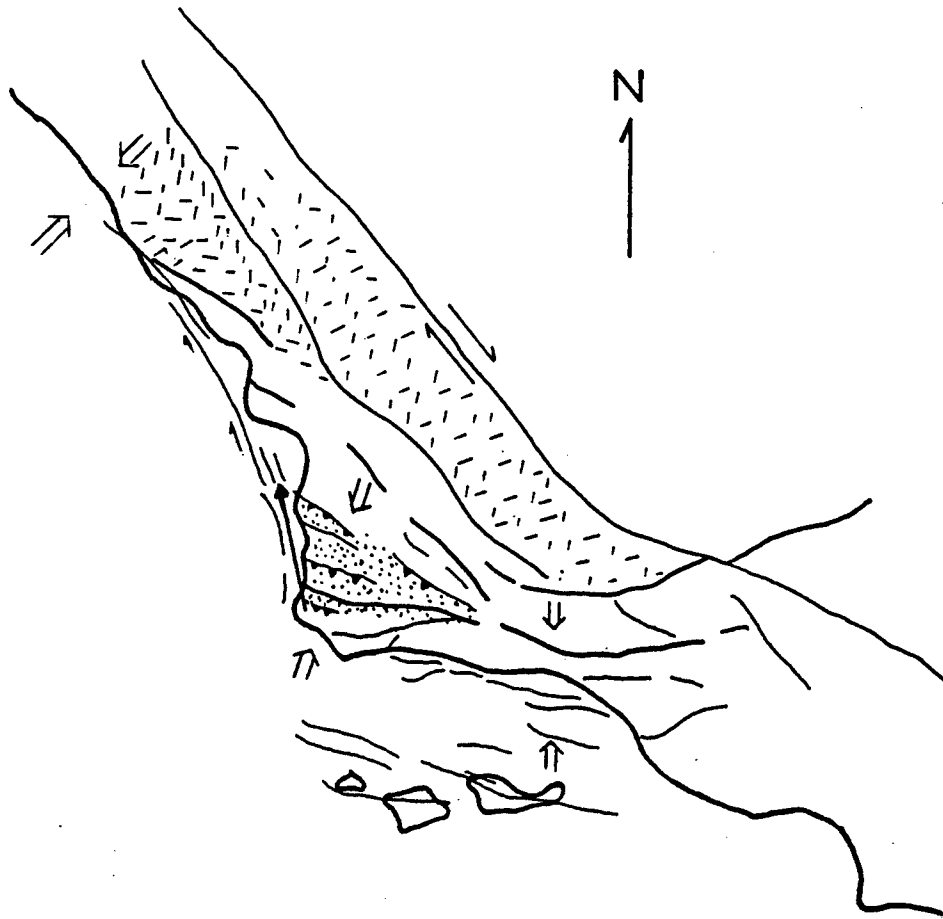


Figure 3.13. Schematic sketch of active tectonic deformation of southern California. The thin arrow is our local estimate of velocity v_{VT} of VNDN with respect to TEPW. The NW motion of the Pacific plate relative to North America is expressed as N-S compression (hollow arrows) in the western Transverse Ranges, NE-SW compression and right-lateral simple shear in the southern Coast Ranges and a combination of both in the transitional Santa Maria Fold and Thrust Belt.

Deformation Rates in the Southern Coast Ranges

If our estimate of v_{PC} is accurate, then it should agree with the deformation observed along path integrals across the California margin northwest and southeast of the SMFTB. In the southern Coast Ranges, a geologic rate of 6.7–13.4 mm/yr for fault-normal compression has been estimated by *Namson and Davis* [1990] from a balanced cross section between point A west of the Hosgri and point A' on the San Andreas (Figure 3.1). This is compatible with a rate of 9 ± 5 mm/yr obtained by

projecting our direct estimate of v_{PC} perpendicular to the $N41^\circ W$ strike of the San Andreas. In the latter, 6 mm/yr comes from the geodetic estimate of v_{VT} and 3 mm/yr from the less certain estimates of v_{PV} and v_{TC} .

Projecting v_{PC} parallel to the San Andreas yields a right-lateral displacement rate of 8 ± 3 mm/yr, of which 5 ± 1 is attributable to v_{VT} . One possibility is that the motion is taken up by strike-slip displacements concentrated on the Hosgri fault system. Alternatively, it could be accommodated as shear distributed over a broader zone comprising more than one fault. The offshore location of the Hosgri fault system makes it difficult to test these alternatives, although some information regarding the onshore deformation is provided by a USGS-operated geodetic network at the latitude of San Luis Obispo [King *et al.*, 1987]. Harris and Segall [1987] used observations from this network primarily to investigate transient deformation associated with the locked segment of San Andreas, but also estimated a uniform strain field for stations more than 30 km away, beyond the influence of transient effects. Integrating this secular strain field between point D, onshore near San Luis Obispo, and point D' on the San Andreas (Figure 3.1) yields 5 ± 2 mm/yr of fault-normal compression and 4 ± 2 mm/yr of right-lateral strike slip. It is thus marginally possible that onshore distributed shear could account for the right-lateral component inferred from our estimates of v_{VT} and v_{PC} . However, although the Coast Range geodetic network does not extend offshore and does not span the Hosgri fault, a portion of the motion measured by Harris and Segall [1987] might be due to transient strain accumulated on the offshore faults. In any case, the data are consistent with previous studies that suggest that the Hosgri is an active right-lateral fault [Gawthrop, 1978a; Minster and Jordan, 1984].

Tectonic Implications for the Western Transverse Ranges and the Santa Barbara Channel

The deformation in the SMFTB appears to transform into compression in the western Transverse Ranges, where most of the structures strike E-W. When projected onto this strike, our estimates of v_{VT} and v_{PC} from the SMFTB imply 7 ± 1 and 12 ± 4 mm/yr of N-S shortening, respectively. The amount of strike slip is not significant, only 0 ± 2 and 2 ± 5 mm/yr, respectively. Because these estimates apply to a path going proceeding due south from the San Andreas, across the western Transverse Ranges, and into the Santa Barbara Channel, they should be compared to the sum of onshore and offshore deformation.

For the onshore portion, through the Ventura Basin, *Namson and Davis* [1988b] estimate ~ 14 mm/yr of shortening from a balanced cross section between points E and E' in Figure 3.1. An estimate twice this magnitude has been obtained from geodetic observations in the Ventura Basin by *Donnellan et al.* [1988], but this may be due to local effects, such as oil extraction.

In the Santa Barbara Channel, significant N-S compression appears to be occurring at approximately 10 mm/yr based on a comparison of GPS measurements with triangulation (S. Larsen, D. Agnew and B. Hager, Strain accumulation in the Santa Barbara Channel: 1971-1987, manuscript in preparation, 1989) and historical trilateration [Webb, 1989]. The decrease in seismicity toward the west end of the channel [e.g., *Stein and Yeats*, 1989] suggests that deformation moves onshore into the SMFTB.

For the total deformation south of the San Andreas, across both the Channel and the western Transverse Ranges, *Yeats* [1981, 1983] estimates 18-23 mm/yr of N-S compression. Using these results and observations from individual structures [e.g., *Yeats*, 1988; *Rockwell et al.*, 1988], E. D. Humphreys (personal communication, 1989) obtain a vector of about 10-27 mm/yr at $N0^\circ \pm 20^\circ$ by a formal path integral. These rates are higher than the amount of shortening implied by the N-S component of v_{VT} , but the lower bound of the latter estimate is in reasonable agreement with our value for v_{PC} .

CONCLUSIONS

The rate of deformation in the Santa Maria Fold and Thrust Belt is significant. The principal axis of compression \hat{e}_2 is oriented at $\theta = N17^\circ E \pm 5^\circ$, and the principal strain rate $\dot{\epsilon}_2$ is -0.13 ± 0.03 μ strain/yr, indicating compression directed N-NE across the SMFTB. Under the assumption of zero rotation, we estimate the integrated rate of deformation across the belt to be 7 ± 2 mm/yr at $N03^\circ W \pm 13^\circ$. This vector can be decomposed into 6 ± 2 mm/yr of crustal shortening on the structural trend of $N30^\circ E$ plus 3 ± 1 mm/yr of right-lateral shear across this axis. The rate of shear, but not the shortening, is dependent on the assumption of no rotation. These geodetic estimates are consistent with structural orientations, earthquake focal mechanisms, geologic cross sections and kinematic models in this region of central California. Taken together, these pieces of evidence suggest that significant deformation is occurring as NE-SW compression on NW trending thrust faults and folds, with an unknown amount of right-lateral shear. Our estimate accounts for a significant fraction of the

San Andreas discrepancy and appears to be compatible with the kinematics of two neighboring tectonic domains, the Coast Ranges to the northwest and the Transverse Ranges to the southeast. We infer that the Santa Maria Fold and Thrust Belt acts as a transition zone in transforming motion from one to the other. Additional GPS observations planned for the next several years will allow us to estimate the rate of rotation and thus quantify the amount of strike-slip, to increase the spatial extent and resolution of the networks, and ultimately, to refine the tectonic model.

CHAPTER 4

GPS MEASUREMENTS OF TECTONIC DEFORMATION IN THE FOOTPRINT OF THE VANDENBERG, CALIFORNIA VLBI STATION

*Je plie, et ne romps pas.
(I bend and do not break)*

Jean de la Fontaine [1688]

INTRODUCTION

Motivation

The principal motivation for this study has been described by *Jordan and Minster [1988a]*:

... baseline measurements in geologically complicated zones of deformation are useful only to the extent that the endpoints can be fixed in a local kinematical frame that includes major crustal blocks. For this purpose, the establishment of local geodetic networks around major VLBI and SLR sites in active areas should receive high priority.

The Vandenberg VLBI site meets these criteria. It is major, having been a principal site in observation campaigns in North America. Before the mobile antenna ("MV1") was removed in mid 1990, it had been observed over 150 times since its installation in late 1983.

It lies in a tectonically active area. The VLBI site at Vandenberg is located at the extreme western end of the Transverse Ranges. As discussed in Chapter 3 and below, this area is at the edge of the Santa Maria Fold and Thrust Belt (SMFTB), a transition zone between the Santa Barbara Channel and the Southern Coast Ranges (Figure 4.1).

The monument is not in bedrock, but is rather a concrete pad in soil and Quaternary marine terrace deposits. This crumbly material is at least 2 m thick and overlies the competent, but fractured Monterey Shale below (drilling performed on September 16, 1990). The depth of the concrete, and whether it penetrates the Monterey Shale, has been difficult to determine because the field notes taken during the installation can no longer be found at NASA [S. DiNardo (JPL) and D. Allenby (GSFC) personal communication, 1990]. A contractor involved in the installation [V. Nelson, Bendix, personal communication, 1991] recalls that the concrete pad extends to about 2.6 m depth, penetrating the Monterey shale. The benchmark disk is attached to a rod which passes through the concrete and then about 2 m into the shale. Unless the alluvium is sliding seaward down the sloping terrace platform, this arrangement should be stable. Indeed, the VLBI measurements suggest that the mark is stable to better than one centimeter.

Tectonic Setting

We have presented an extensive discussion of the tectonic setting in Chapter 3. In this section, we briefly summarize that discussion and consider additional information gathered since the time of that study.

How is the compression in the onshore SMFTB related to the deformation in the offshore Santa Maria Basin? A high-resolution seismic survey in 1986 begins to answer this question. Performed as an extension of the Long Term Seismic Risk Project for the Diablo Canyon Power Plant by Pacific Gas and Electric (PG&E), the EDGE (not an acronym) survey recorded several reflection profiles off the coast near Point Sal. One of the main goals was to image the Hosgri Fault Zone. One of the principle offshore compressive features is the Queenie Structure, extensively studied by *Clark et al.* [1991]. It is an oil-bearing anticline which formed in the late Neogene. Despite the presence of the anticline and some ongoing seismicity, those authors claim that the current rate of deformation is less than 0.005 mm/yr.

In San Luis Obispo Bay, landward of the Hosgri fault system, the RU-3 profile reveals a synclinal fold involving the most recent stratigraphic units [*McIntosh et al.*, 1991]. Based on this and other evidence, *McIntosh et al.* [1991] infer "renewed convergence accompanied by probable strike-slip (transpression) from the mid-Pliocene to the present". On the other hand, *Meltzer and Levander* [1991] interpret the same lines to indicate relatively minor (1-3 km) shortening in the Neogene in the offshore Santa Maria Basin, and argue for convergence in the onshore part of the Basin.

The Casmalia range appears to be actively folding, based on recent mapping by D.G. Clark, ["Late Quaternary tectonic deformation in the Casmalia Range, Coastal South-Central California", manuscript in preparation, 1990]. His analysis of Quaternary marine terraces near Point Sal suggests uplift rates of 0.1–0.2 mm/yr.

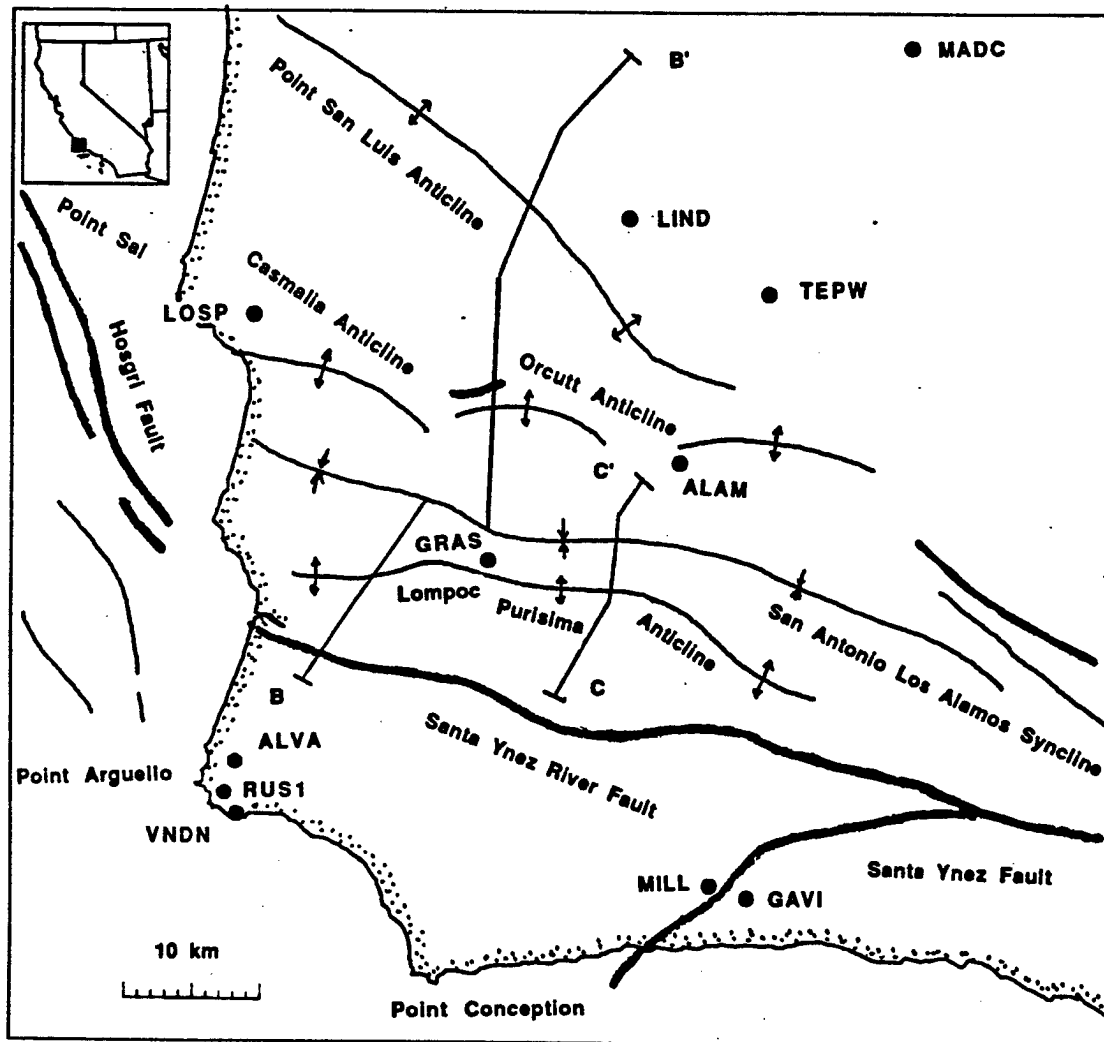


Figure 4.1. Tectonic map of the Santa Maria Fold and Thrust Belt (SMFTB). The dark black dots denote GPS stations, labelled with the 4-character codes defined in Table 4.1. Traces of faults (thick lines) are from *Hall* [1982]. Fold axes (thin lines) are from *Stein and Yeats* [1989] and *Namson and Davis* [1990]. The straight lines connecting points B-B' and C-C' are the transects used for balanced cross-sections by *Namson and Davis* [1990]. The scale and area of the map are preserved in subsequent figures.

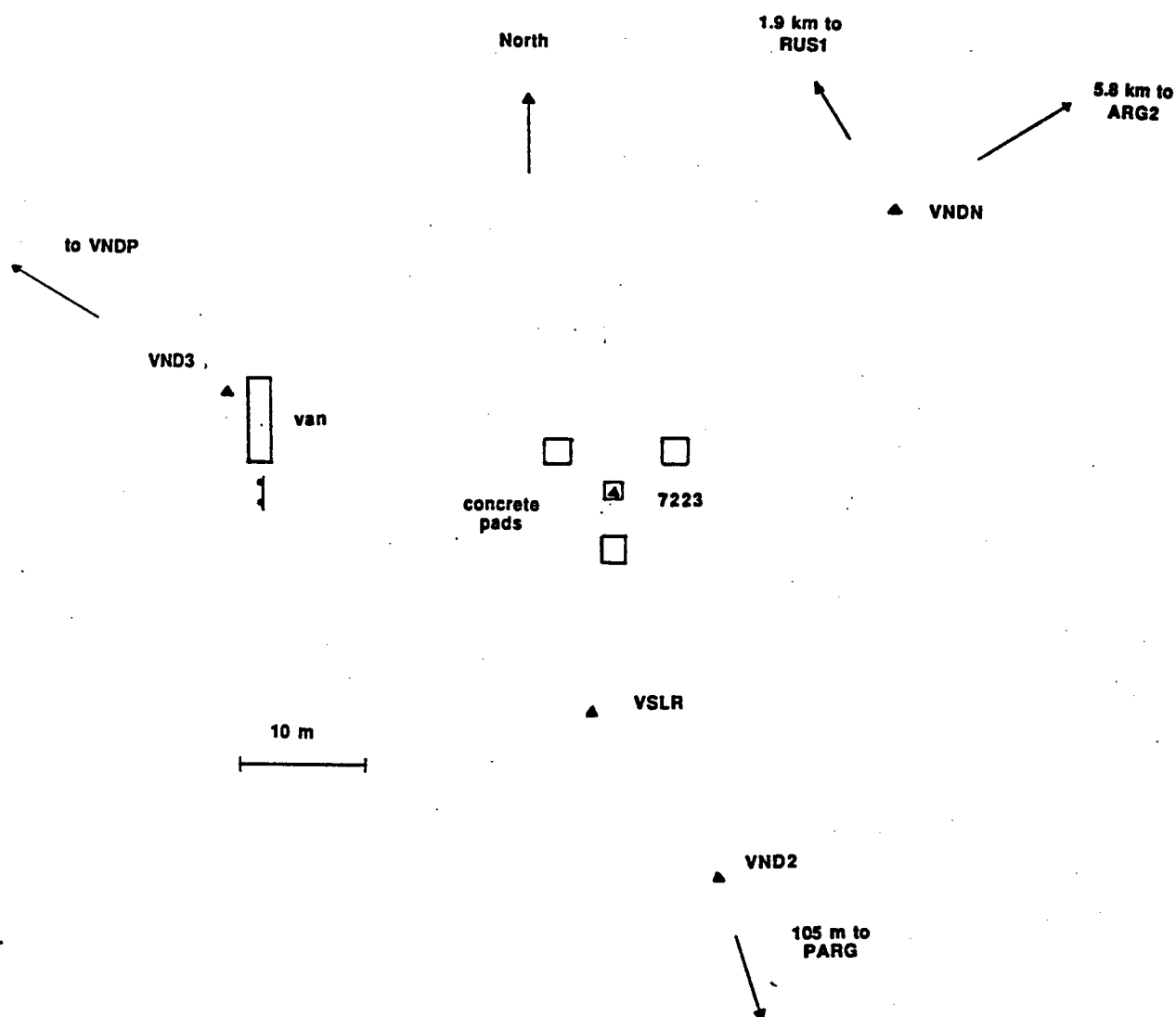


Figure 4.2. Map of benchmarks near the VLBI monument at Vandenberg. The site codes are defined in Table 4.1. Redrawn from the VLBI site catalog [*Crustal Dynamics Project Staff*, 1988]. The 7223 mark is used for VLBI observations, while the VNDN mark is used for GPS. Note that the VSLR mark has been destroyed, and that the permanent GPS receiver at VNDP has not yet been installed. The storage van in place in early 1991 obstructs the view from 7223 to VND3.

Previous Studies

In our previous paper [Feigl *et al.*, 1990] we combined historical geodetic observations from 1879 through 1985 with a single set of GPS observations taken in 1986 and 1987 to measure the deformation in the SMFTB. Assuming uniform strain and no net rotation, we found the integrated rate of deformation, expressed as the velocity of VNDN with respect to TEPW, to be 7 ± 1 mm/yr oriented at $N03^\circ E \pm 13^\circ$. This vector can be decomposed into 6 ± 2 mm/yr of crustal shortening on the structural trend of $N30^\circ E$ plus 3 ± 1 mm/yr of right-lateral shear across this axis. Since the rate of shear, but not the shortening, is dependent on the assumption of no rotation, our principal result is the magnitude of compression.

The compression appears to be accommodated on actively deforming folds underlain by thrust faults, as suggested by Namson and Davis [1990]. In this chapter, we present measurements of the deformation based on GPS data collected between 1986 and 1991. The high precision and vector quality of these measurements permit us to obtain a higher resolution map of the velocity field than is possible with the older scalar data.

DATA

History of Geodetic Observations in the Network

The local network at Vandenberg has become known as a "footprint" around the VLBI site. The network shown in Figure 4.1 includes stations at three length scales: ~30 m, ~3 km and ~30 km away from the VLBI site. The complete names of the stations are given in Table 4.1, but we will refer to them by the 4-character codes defined there. Their coordinates are given in Table 4.2. At the short ~30 m scale, the VLBI monument has three reference marks (VNDN, VND2 and VND3) surveyed with terrestrial techniques in 1983 (Figure 4.2). If properly surveyed to the VLBI monument, the reference marks could replace it if it were disturbed. At the medium scale, there are two stations (RUS1 and ALVA) within 5 km of the VLBI monument, which, when resurveyed, should detect any seaward sliding of the alluvium on the underlying terrace. At the large ~30 km scale, LOSP, GRAS, GAVI, and MADC have been surveyed with GPS at least three times between 1986 and 1991. The stations at LOSP and MADC are part of a network [Agnew *et al.*, 1987] measured on a yearly basis by a consortium including Scripps, Caltech, UCLA and MIT (dubbed "SCUM" by Larson [1990]).

The history of measurements in the Vandenberg Footprint is a complicated patchwork of surveys performed for other purposes (Figure 3.3). The initial triangulation was part of a coastal survey performed in the last century and repeated in the 1920s [Bowie, 1924; 1928]. The military developed an interest when Camp Cook was established in the 1930s. When the area became Vandenberg Air Force Base in 1959, the aiming of missiles required a good knowledge of the gravity field. Trilateration was added in 1971 and continues to be performed on an irregular basis by the Geodetic Survey Group of the Defense Mapping Agency (DMA). These data, and the tectonic deformation we infer from them, have been described in Chapter 3.

The first GPS measurement at Vandenberg was performed in June 1986, when VNDN was occupied [Dixon *et al.*, 1990]. Since then, the SCUM consortium has performed quasi-yearly GPS measurements from VNDN to stations over 50 km away. These observations constitute the Transverse Range EXperiments (TREX) and have been numbered sequentially in Table 4.3. See Murray [1991] for a more complete description of the TREX data. On two occasions, the operations of this experiment have been extended to include stations in the Vandenberg footprint. In the Fall of 1987, we were able to measure from VNDN to GRAS and TEPW before the Whittier Narrows earthquake of October 1 [Hauksson *et al.*, 1988] interrupted the experiment. In 1989, we managed to occupy VNDN, GRAS and GAVI on three days of April Fools' weekend.

Observations in the Vandenberg footprint network began in earnest with the VF1 campaign in January 1990, our first with the new Trimble 4000 SST receivers (Table 4.4). At that time, the antennas were sensitive to static electricity and the available memory was only sufficient to record about 14 hours of data. Since we conducted the experiment with only a single operator (KLF), he had to visit each receiver every day. As a result, we successfully collected only 23 station-days of data. In September, 1990, we were able to perform a more successful campaign (VF2), and add several more stations to the network (Table 4.5).

The mark at VNDN is also included in several other GPS networks. It has been occupied by the U.S. Geological Survey at least twice per year since 1986 with a site at Mojave and at Palos Verdes. Many of the occupations are included in our analysis, but the complete data set has been reduced by Davis *et al.* [1989] and Larson [1990]. In addition, VNDN was occupied as a tracking station following the 1989 Loma Prieta earthquake [Lisowski *et al.*, 1990]. It has been included in measurements across the Santa Barbara Channel scheduled for June 3-6, 1991 [K. Larson, personal communication, 1991] and a 5 km footprint network surveyed in June, 1991 by Bendix

for the NASA Crustal Dynamics Project [*Bell*, 1991; V. Nelson, personal communication]. The VLBI mark (7223) has been included in a network established by the California Department of Transportation (Caltrans) although that organization designates the mark as "VAND" [Y. Bock, personal communication, 1991]. In late 1991, we plan to install a permanent GPS receiver at Vandenberg as part of the Permanent Geodetic GPS Array (PGGA) in Southern California developed by investigators at JPL, MIT, and Scripps [*Bock and Shimada*, 1989].

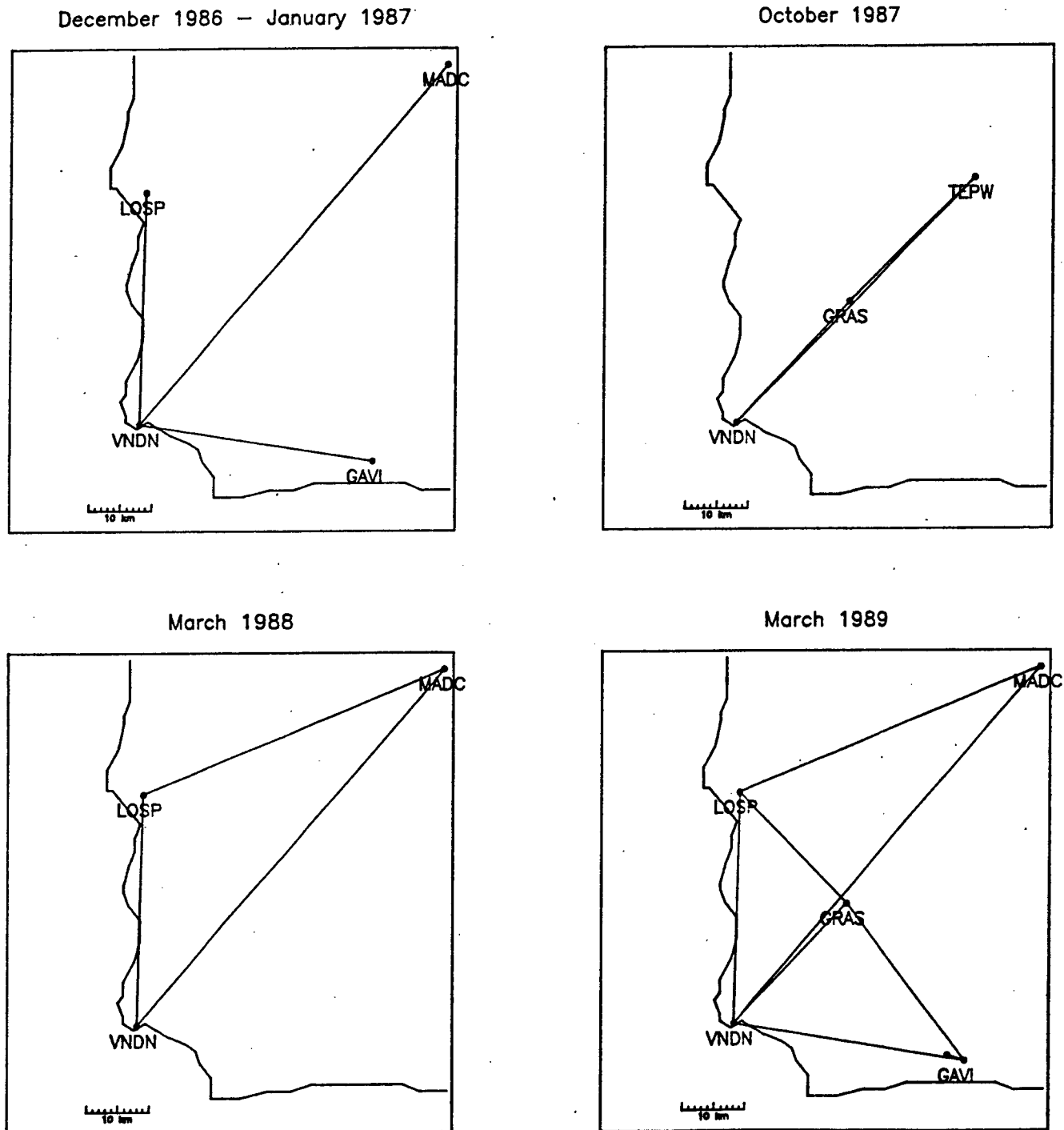
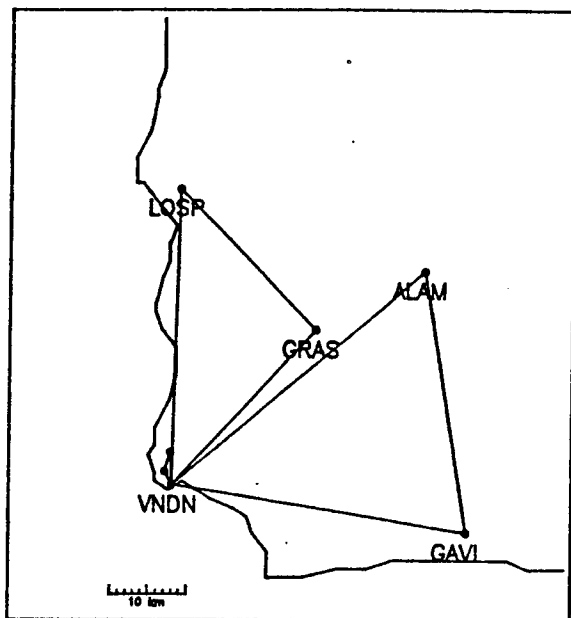
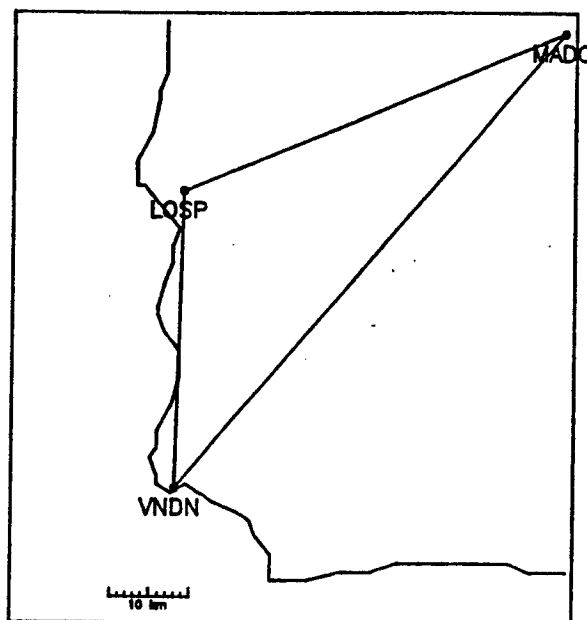


Figure 4.3 GPS network through time. Lines connect stations which were occupied on the same day, but of course, other vectors can be calculated by closure.

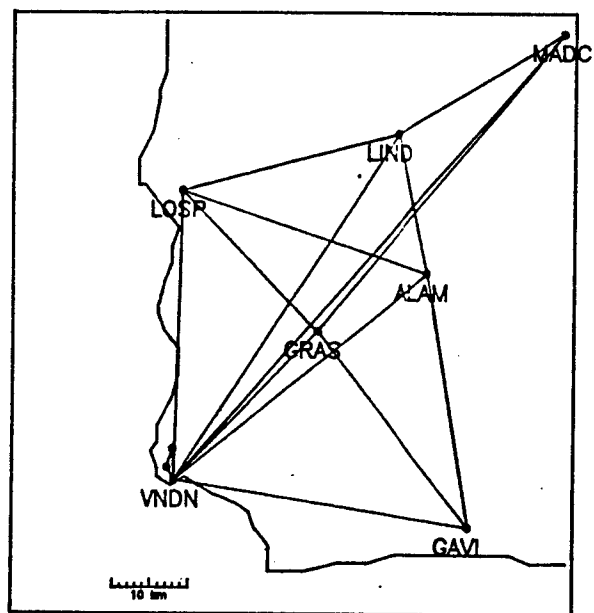
February 1990



March 1990



September 1990



February 1991

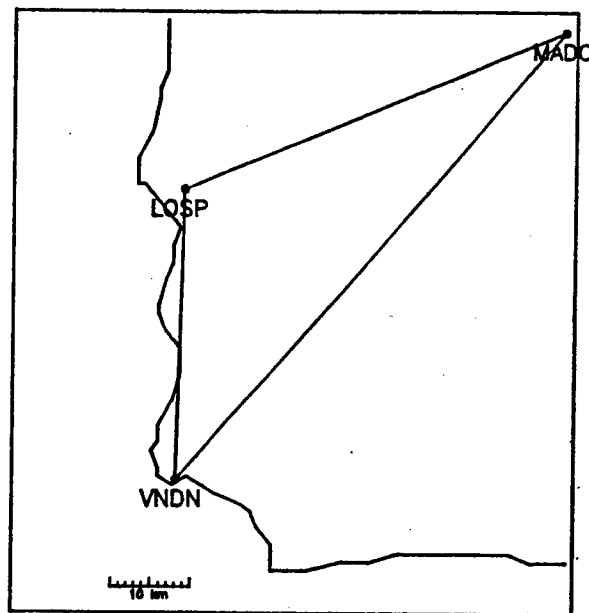


Figure 4.3 continued.

Table 4.1. Stations in the Vandenberg Footprint

ID	Name	QID ^a	QSN ^b	DMA ^c
3ARG	ARG 1933 ^j	341204	1003	
7223	VLBI STA 7223	—	—	
ALAM	ALAMO 1925 ^k	341201	1001	
ALVA	ALVADO 1933	341204	1002	
ARG1	ARGUELLO 1 1942 ^d	341204	1004	
ARG2	ARGUELLO 2 1959	341204	1004	
ARGU	ARGUELLO 1875	341204	1004	
GAVI	GAVIOTA 1873	341201	1005	
GRAS	GRASSY USGS 1959	341201	1032	11362
LIND	375 203 7h LINDA 1955	—	^g	
LOSP	LOSPE 1875	341204	1021	51258
MADC	MADRE ECC 1980		^f	
PARG	POINT ARGUELLO 1874-1933 ⁱ	341204	1028	
RODA	RODA 1959	341204	1081	
RUS1	RUSTAD RM1	—	—	
RUST	RUSTAD 1874	341204	1038	
SUB7	SUB USATOPOCOM 1970 ^e	341204	1084	11787
SYNZ	SANTA YNEZ 11917 1990 GSG DET 1			11917
TEP7	TEPUSQUET RM 7	341201	1013A	
TEPT	TEPUSQUET TEMPORARY	—	—	
TEPU	TEPUSQUET 1875	342101	1013	
TEPW	TEPUSQUET WITNESS	—	—	
VNDP	VANDENBERG PGGA ^m			
VINA	VINA 1933	341204	1052	
VND2	VLBI STA 7223 RM 2 1983 DET 1 GSS			
VND3	VLBI STA 7223 RM 3 1983 DET 1 GSS			
VNDN	VLBI STA 7223 RM 1 1983 DET 1 GSS	—	^h	11651
VSLR	TLRS STA 7880 ^l			

Notes:

- ^a NGS quadrant identification.
- ^b NGS quadrant station number.
- ^c DMA Doppler station number.
- ^d Stamped ARGUELLO 1924 but reset after hill was leveled in 1942.
- ^e Designated SUB TPC 1971 in REDEAM data set.
- ^f Part of USGS Carrizo Plain trilateration network.
- ^g USGS mark.
- ^h Reference mark for VLBI site with NASA CDP¹ monument number 7223
- ⁱ Despite its name, this site is not actually on Point Arguello.
- ^j This site is actually on Point Arguello.
- ^k Not to be confused with ALAMOS 1933 in the DMA network.
- ^l Destroyed in 1989.
- ^m To be installed late 1991.

Table 4.2 Coordinates for GPS Stations

ID	Latitude <i>dd°mm'ss.sssss"</i>	Longitude <i>dd°mm'ss.sssss"</i>	Height, m
7223	34 33 21.89187	-120 36 59.10426	-12.3187
ALAM	34 47 54.60549	-120 15 24.47175	457.1624
ALVA	34 35 33.66438	-120 37 1.08797	293.9618
GAVI	34 30 6.51940	-120 11 55.65255	713.3459
GRAS	34 43 50.04168	-120 24 50.63702	331.1302
LOSP	34 53 37.47310	-120 36 22.27312	463.0934
MADC	35 4 32.23261	-120 4 1.66022	958.0447
PARG	34 33 17.73558	-120 36 57.55453	-13.0652
SYNZ	34 31 49.96289	-119 59 9.19153	1217.8618
TEPT	34 54 35.34540	-120 11 11.54485	952.5544
TEPW	34 54 35.99808	-120 11 12.27832	953.1967
VND2	34 33 20.98833	-120 36 58.81151	-12.7389
VNDN	34 33 22.55376	-120 36 58.30540	-11.5327

Notes:

Coordinates for epoch 1991.11 in the SV5 system [M. H. Murray, personal communication, 1990] expressed on the NAD83 ellipsoid with semimajor axis $a = 63718137$ m and inverse flattening $1/f = 298.257222101$ [e.g., *Leick*, 1990]. The differences in position from the WGS84 ellipsoid, with the same semimajor axis but $1/f = 298.257223563$ [DMA, 1987] is submillimeter. No transformation between SV5 and WGS84 has been applied. The transformation, when formally estimated from the GOTEX experiment, is expected to produce coordinate shifts of less than 1 m [P. J. Morgan and R. W. King, manuscript in preparation, 1991].

Table 4.3. Observations conducted during SCUM occupations of TREX sites

Date	Year	Day of year	TREX number	VNDN	LOSP	MADC	GRAS	GAVI or MILL	Tracking or ACMPRIWY
June 17	1986	167	(0)a						
June 18	1986	168	(0)a	•					
June 19	1986	169	(0)a	•					
June 20	1986	170	(0)a	•					
Dec. 16	1986	350	1	•	•				P T
Dec. 17	1986	351	1	•	•				P T
Dec. 18	1986	352	1	•	•				T
Dec. 19	1986	353	1	•	•				P
Dec. 20	1986	354	(1)	•	•				
Dec. 29	1986	363	2	•	•	•			A P
Dec. 30	1986	364	2	•	•	•			AC P TW
Dec. 31	1986	365	2	•	b	•			AC P W
Jan. 1	1987	001	2	•	b	•			AC P W
Jan. 2	1987	002	2	•	b	•			AC P W
Jan. 3	1987	003	3	•				•	AC P W
Jan. 4	1987	004	3	•				•	AC P W
Jan. 5	1987	005	3	•				•	AC P W
Jan. 6	1987	006	3	—				*	AC P W
Jan. 7	1987	007	3	•				*	AC P
May 24	1987	144	7	•					M TWY
May 25	1987	145	7	•					M TWY
May 26	1987	146	7	•					TW
May 27	1987	147	7	•					M TWY
May 28	1987	148	7	•					M TW
Sep. 22	1987	265	8	•					CMP WY
Sep. 23	1987	266	8	•					CMP WY
Sep. 24	1987	267	8	•					CMP WY
Sep. 25	1987	268	8	•					CMP WY
Sep. 26	1987	269	8	•					CMP WY

Tracking Stations:

A Algonquin
P Platteville, CO
W Westford, MA

C Churchill, Manitoba
R Richmond, FA
Y Yellowknife, NWT

M Mojave, CA
T Austin, TX

Table 4.3 (continued)

Date	Year	Day of year	TREX number	VNDN	LOSP	MADC	GRAS	GAVI or MILL	Tracking ACMPRIWY
Sep. 28	1987	271	(9)	•					
Sep. 29	1987	272	(9)	•					
Oct. 1	1987	274	10	•			•		M W
Oct. 2	1987	275	10	•			•		M WY
Oct. 3	1987	276	(10)	•					M WY
Oct. 4	1987	277	(10)	•					M WY
Mar. 15	1988	075	11	•	•	•			AC PR WY
Mar. 16	1988	076	11	—	•	•			ACMPR WY
Mar. 17	1988	077	11	•	•	•			ACMP WY
Mar. 18	1988	078	11	•	•	•			ACMPR W
Mar. 28	1989	087	14	•	•	•			M
Mar. 29	1989	088	14	•	•	•			M Y
Mar. 30	1989	089	14	•	•	•			M Y
Mar. 31	1989	090	14	•	•	•			M Y
Apr. 1	1989	091	15	•	•			•	M R WY
Apr. 2	1989	092	15	•	•			•	M R W
Apr. 3	1989	093	15	•	•			•	M R W
Mar. 25	1990	084	17	•	•				A M R W
Mar. 26	1990	085	17	•	•				A M R W
Mar. 27	1990	086	17	•	•				A M R W
Mar. 28	1990	087	17	•	•				A M R W
Mar. 29	1990	088	(18)	—	•	—			A MPR WY
Mar. 30	1990	089	(18)	•	•	•			A MPR WY
Mar. 31	1990	090	(18)	•	•	•			A MPR WY
Apr. 1	1990	091	(18)	•	•	•			A MPR WY
Feb. 7	1991	038	20	•	•	•			M R W
Feb. 8	1991	039	20	•	•	•			M R W
Feb. 9	1991	040	20	•	•	•			M R W
Feb. 10	1991	041	20	•	•	•			M R W

Notes:

- a* Data collected by investigators from Caltech, JPL, NGS and Scripps.
- b* Data corrupted by local radio interference.
- Less than half the scenario contains usable data.
- * MILL was used as an alternative to GAVI, when GAVI was inaccessible in wet weather.
- () Not analyzed in this study.

Table 4.4. GPS observations at Vandenberg AFB February, 1990

Date, 1990	Day of Year	MIT01 Trimble ^a	MIT02 Trimble ^a	MIT04 Trimble ^a	Tracking stations KMRW
Jan. 31	031	VNDN ^b	RUS1 ^b		KMRW
Feb. 2	032	VNDN	RUS1	ALVA	KMRW
Feb. 3	033	VNDN	LOSP	GRAS	KMRW
Feb. 4	034		LOSP		KMRW
Feb. 5	035	VNDN	LOSP	GRAS ^b	K RW
Feb. 6	036				KMRW
Feb. 7	037	VNDN			KMRW
Feb. 8	038	VNDN	SYNZ	ALAM	KMRW
Feb. 9	039	VNDN		ALAM	KMRW
Feb. 10	040	VNDN		GAVI	KMRW
Feb. 11	040	VNDN		GAVI	KMRW

Notes:

Scenarios ran from 00:00-14:00 UTC, advancing 4 minutes earlier each day.

K Kokee Park, Hawaii TI 4100 receiver running CORE v. 1.4

M Mojave, California, Minimax 2816 AT receiver running version 1.61 software.

R Richmond, Florida Minimax 2816 AT receiver running version 1.61 software.

W Westford, Massachusetts Minimax 2816 AT receiver running version 1.61 software.

^a Trimble 4000 SST receiver running version 3.25 of the SIG+NAV software.

^b Only 5 hours of data collected.

Table 4.5. GPS observations At Vandenberg AFB September, 1990

Date, 1990	Day of Year	NGS Trimble ^e	MIT05 Trimble ^e	MIT03 Trimble ^e	CIGNET Minimac ^f MRW
Sept. 5	248	inventory	inventory	inventory	
Sept. 6	249	VNDN ^a	RUS1		MRW
Sept. 7	250	VNDN ^a	RUS1	ALVA	MRW
Sept. 8	251	VNDN ^a	GRAS ^b	ALVA	MRW
Sept. 9	252	VNDN ^a	GRAS	LOSP	MRW
Sept. 10	253	VNDN ^a	ALAM	LOSP	MR ^d
Sept. 11	254	VNDN	ALAM	LIND	MRW
Sept. 12	255	VNDN	LOSP	LIND	MRW
Sept. 13	256	VNDN	LOSP	GRAS	MRW
Sept. 14	257	VNDN ^c	GAVI	GRAS	MRW
Sept. 15	258	VNDN ^c	GAVI	ALAM	MRW
Sept. 16	259	VNDN ^c	LIND	ALAM	MRW
Sept. 17	260	VNDN ^c	LIND	MADC	MRW
Sept. 18	261	VNDN	GRAS	MADC	MRW
Sept. 19	262	VNDN	GRAS	pack	MRW
Sept. 20	263	pack	pack		

Notes:

Scenarios ran from 11:30-21:30 UTC, advancing 4 minutes earlier each day.

^a 4 mm horizontal offset occurred during this period, probably September 6

^b Receiver was inadvertently programmed to stop tracking below 15° elevation

^c Cow tipped over antenna during this period, apparently after end of scenario on September 17.

^d Minimac BE file available from PGGA; no R-file

^e Trimble 4000 SST receivers running SIG+NAV version 4.11 software.

^f Minimac 2816 AT receivers running version 1.61 software.

M Mojave, California

R Richmond, Florida

W Westford, Massachusetts

Table 4.6. Tally of vectors observed in the Vandenberg Footprint

	1971	1983- 1985	1986	1987	1988	1989	1990	1990	1990	1991
VNDN-GRAS				274 275			033 (034) 035		251 252 256 257 261 262	
VNDN-LOSP			350 351 352 353 354 363 (364) (365)	(001) (002)	075 076 077	087 088 091 092 093	033 (034) 035	084 085 086 087 088 090 091	252 253 255 256	038 039 040 041
VNDN-GAVI				001 002 003 004		091 092 093?	040 041		257 258	++
VNDN-RUS1		EDM					031 032		249 250	+
VNDN-ALVA							032		250 251	+
VNDN-ALAM							038 039		253 254 258 259	
VNDN-LIND									254 255 259 260	
VNDN-MADC			363 364 365	001 002	075 076	087 088 089 090	(084) 085 086 (087) (088) 089 090 091		260 261	038 039 040 041
VNDN-7223		EDM								037 +
VNDN-VINA										+
VNDN-VND2		EDM					088 ^a 089 ^a 090 ^a 091 ^a			037 +

Table 4.6 continued.

	1971	1985	1986	1987	1988	1989	1990	1990	1990	1991
GRAS-LOSP	EDM		EDM				033 (034) 035		252 256	
GRAS-ALVA			EDM						251	
GRAS-GAVI	EDM					091 092 093			257	
LOSP-ALAM									253	
LOSP-LIND									255	
LOSP-MADC			363 364 (365)	(001) (002)						038 039 040 041
ALVA-RUS1			EDM				032		250	+
ALAM-LIND									254 259	

Notes:

Only direct observations are listed. Additional vectors can be calculated by closure.

Listing is by day of year.

() Unrecoverable problem.

+ Observations planned for June, 1991 by NASA CDP [L. Bell, personal communication]

++ Observations planned as part of Santa Barbara Channel Experiment June 3 through 6, 1991 [K. Larson, personal communication].

^a Mixed receiver types with offset time tags under Selective Availability.

Problems

Over the five years of this study, we have encountered a number of problems in collecting the data. We document them here to avoid repeating them.

Radio interference apparently corrupted some of the data collected at LOSP for three days in December, 1986 and January 1987. The symptom is many (> 20 /hour) cycle slips or data outages in all channels. Discussions with Tony Jordan, the Frequency Manager at Vandenberg Air Force Base, did not uncover the source of the interference. Because GPS receivers are used in many Air Force vehicles, the Air Force attempts to keep the L band clear. Since the problem has not recurred since 1987, we suspect a radar antenna was in use then for a relatively rare operation, such as a missile launch.

The jamming frequency may have been a multiple of one of the frequencies used by GPS, as at Devil's Peak on January 3, 1987. There, the receiver was located within 3 m of an antenna transmitting at 102.3–103.1 MHz, very nearly a multiple of the P-code frequency of 10.23 MHz. In this case, the signal-to-noise ratio for the L2 channel was about 10 times lower than usual. The problem ceased when the transmitter was turned off.

At station TEPW, we could not collect any data in 1989 due to the construction of a microwave antenna within 4 m of the benchmark since the 1987 observations. The receiver could not establish lock on more than one satellite because the microwave antenna tower blocked half the sky. The microwave transmission also prevented reception because the receiver could not establish lock, even when the operator (D. Dong) moved it to a point with a clear view of the sky.

We have successfully left receivers to operate unattended on Vandenberg Air Force Base. On two occasions, however, the tripod at VNDN was found lying on the ground after the observing scenario. Local observations of animal behavior suggested that a grazing cow had used the antenna ground plane as a scratching post. Fortunately, the antenna was disturbed only after the last GPS observation had been made. Subsequently, we placed pipes on the ground in a triangle around the antenna to inhibit the cows. Although no cow attacked the antenna while we were using this procedure, we cannot infer the absolute efficacy of the protective triangle. More robust protection, in the form of a barbed wire fence, is planned for the permanent GPS antenna at Vandenberg.

The most frequent cause of data loss has been power failures. The TI4100 receiver draws about 170 W at 24 V, necessitating the use of two heavy duty (> 60 Amp-hour) marine batteries for a 7.5 hour observation scenario. Old or incompletely charged

batteries have failed on several occasions. The Trimble 4000 SST draws less power: 8 W according to the owner's manual, 10–12 W in practice. The lower power consumption easily allows two 10-hour observing scenarios to be made with a single marine 50 A-hour battery. The health of a battery is difficult to evaluate in the field. We have found the voltage under a 100 A load to be a good indicator. A brand-new, fully charged battery will deliver over 11.5 V, an older battery between 10 V and 11 V, but batteries reading below 10 V have failed in the field, and should be retired from service. We note that a battery in almost any state of health will read over 12 V when measured without a load.

ANALYSIS

Our approach to data analysis has two steps: single-day solutions for station positions and the five-year solution for station velocities. For the first step, we use the GAMIT software package [King and Bock, 1991] to estimate station coordinates, atmospheric parameters, orbital elements, and phase ambiguities from doubly differenced phase data. For the second step, we use a Kalman filter program called GLOBK [Herring, 1991] to combine the adjustments and covariance matrices from the 69 single-day GAMIT solutions. The GLOBK program can estimate station velocities, Earth orientation parameters, and other global parameters pertaining to the whole 5-year data span.

This two-step process has two advantages. First, it allows us to handle the data easily. The single-day solution condenses the information in the large (~1 Mbyte/station/day) data set into a compact file containing the adjustments and their covariance matrix. This information is then passed as input to GLOBK, which permits allows us to perform different solutions (e.g., with different orbital constraints) quickly and easily.

The second advantage of our approach is that it affords a rigorous solution to the problem of an inhomogeneous fiducial network, where the set of stations changes from day to day and year to year. Since the choice of fiducial (constrained) stations determines the frame to which the estimated vectors are referenced, a naive comparison of a vector estimated on two days with different fiducial networks can lead to an inaccurate estimate of its rate of change. The magnitude of the inconsistency depends on the spatial scale of the fiducial network and the accuracy of the fiducial coordinates. The effect of the shifting geometry in the fiducial network may be minimized by imposing the constraints on the fiducial coordinates in a consistent manner. GLOBK

does this by imposing the constraints globally across the five year data span. This approach has the advantage of simplifying the treatment of unconstrained tracking stations which have been observed only a few times, e.g, Austin, Texas.

Single-day Solutions

To obtain adjustments and covariance matrices suitable for the global analysis, we use the GAMIT software to perform a sequence of six least-squares solutions using the phase data from each day of observations. The first four of these solutions are performed with realistic constraints to resolve correctly the integer ambiguities in phase. The fifth and sixth solutions employ very loose constraints (1 part per million) to generate adjustments and covariance matrices for later input to GLOBK.

Resolution of the ambiguities is accomplished in four steps, each estimating a subset of the geodetic and ambiguity ("bias") parameters from different combinations of the doubly-differenced phase data:

- (1) All parameters are estimated using the "LC" combination of the L1 and L2 phases. This combination is designed to eliminate the dispersive effects of the ionosphere, and is therefore called "ionosphere-free" [see equation (36) of *Bock et al.*, 1986].

- (2) With the geodetic parameters held fixed at the values obtained in step (1), the wide-lane (L2-L1) biases are estimated and, if possible, constrained to integer values. This operation employs the L1 and L2 phases under an ionospheric constraint and, if pseudorange data are available, the wide-lane combination.

- (3) With the wide-lane biases held fixed at the values obtained in step (2), the narrow-lane (L1) biases are estimated, along with all the geodetic parameters, from the LC data.

- (4) With the resolved values of both the wide-lane and narrow-lane biases held fixed to the integer values obtained in step (3), the geodetic parameters are estimated from the LC data.

The algorithms used to resolve ambiguities are those of *Schaffrin and Bock* [1988] and *Dong and Bock* [1989], except that the values of the geodetic parameters estimated in step (1) are retained in step (2) [D. Dong and R. King, personal communication, 1990]. The four step procedure allows us to resolve almost all (> 90%) of the ambiguities in most experiments.

The next two solutions produce the estimates and covariance matrices for later input into second (global) stage of our analysis. They are performed with constraints which are sufficiently loose (1 part per million) to avoid biasing the estimates.

(5) We perform a solution with the LC combination as in step (1), but with loose constraints on the geodetic parameters. The bias parameters are free to assume real values.

(6) The "bias-fixed" solution of step (4), with the resolved phase ambiguities constrained to integer values, is repeated with loose constraints on the geodetic parameters.

For all of the single-day GAMIT solutions, we compute the theoretical phase according to the model described in Chapter 2, based on that presented in *King et al.*, [1985]. To eliminate the effects of receiver and satellite clocks, we employ the standard technique of "double differencing" which differences the phase between stations and receivers via a linear operator [e.g., equations (19) through (21) of *Bock et al.*, 1986]. For a more detailed description of the models for calculating station positions, satellite orbits, and Earth orientation, see *Murray* [1991]. Atmospheric effects are treated by estimating the deviation, at zenith, from the atmospheric model described in Chapter 2. One such atmospheric delay parameter is estimated at each site on each day.

To achieve the accuracy of 1 part in 10^7 needed for successful resolution of phase ambiguities requires an orbital accuracy of better than 10 m [e.g., *Lichten*, 1989]. We describe the orbit of each satellite in terms of eight parameters: three for the position (X, Y, Z) of the satellite in inertial space, three for its velocity ($\dot{X}, \dot{Y}, \dot{Z}$), and two for non-gravitational forces. One of the non-gravitational parameters represents the effect of direct solar radiation pressure, the other, anomalous accelerations along the solar panel or Y-axis of the spacecraft [e.g., *Fliegel et al.*, 1985]. Although we have the capability to estimate a third non-gravitational parameter along the Earth-pointing Z-axis of the spacecraft, our experience suggests that it does not improve the precision of the estimated interstation vectors.

We use one set of eight parameters to describe the satellite orbits for each campaign, typically four or five days. This length of time seems to be a good compromise between short and long arcs. Short (8-hr) arcs tend to be weakly determined because observing for less than one complete period (approximately 12 hours) does not resolve well the semi-major axis of the elliptical orbit. On the other hand, long (> 1 week) arcs allow the unmodeled effects of non-gravitational forces to accumulate [*Schutz et al.*, 1990; *Lichten*, 1990b]. In the case of the February and September 1990 experiments, which each lasted two weeks, we break the orbits into two arcs, each spanning one week.

In estimating the orbits, we have found that the precision depends on the spatial extent of the fiducial network. During campaigns where the fiducial coverage was

limited (as in December, 1986), our estimates of the orbital parameters are less certain than when many stations throughout the globe tracked the satellites (as in February, 1991). The importance of the spatial extent of the fiducial network has been documented for the early (1987-1989) years of GPS experiments in California [Larson, 1990] and for a network in South America [Freymuller and Kellogg, 1990].

In our single-day solutions, we use *a priori* coordinates determined from a judicious combination of VLBI and SLR solutions, the SV5 system, described by Murray *et al.* [1990], and later developed into the SV6 system [Murray, 1991]. The coordinates are assigned *a priori* uncertainties of 10 mm at several fiducial stations when estimating orbits. In practice, we choose Vandenberg (VNDN), California, and the CIGNET stations at Westford, Massachusetts, and Richmond, Florida when they are available. When the data from one or more of these stations are unavailable or unusable (38 of 69 days), we constrain the coordinates of one or more of the following sites in the SV5 system: Platteville, Colorado, Kokee Park, Hawaii, or Mojave, California.

Detecting and removing cycle slips in the phase data is performed with a combination of automatic and interactive editing programs. For data from TI4100 receivers, the automatic editor can use the "wide-lane" combination [Blewitt, 1990] to repair about 80% of the cycle slips in most cases. For data from the "codeless" Trimble and Minimac receivers, however, the editor has only linear combinations of phase data to examine. In this case, we have to remove the small (< 10 cycles) slips using an interactive data editor. Manual editing is also required to handle the noise imposed by Selective Availability, rapidly drifting receiver oscillators, or large gaps.

Five-year Solutions

We combine the single-day solutions to perform a global estimate over five years using the GLOBK program. This program is a Kalman filter as described by Herring *et al.* [1990] and Herring [1991]. Its input consists of the adjustments and covariance matrices from the loosely-constrained GAMIT solutions. Using the GLOBK program, we estimate station coordinates, station velocities, orbital elements, and earth orientation parameters according to the list in Table 4.7. In this estimation, we apply several constraints which we discuss in detail here.

As for the single-day solutions, we define a reference frame by constraining the coordinates of three stations to their coordinates in the SV5 system [Murray *et al.*, 1990]. The *a priori* velocities of these three stations are derived from a VLBI solution provided in Table 4.8 [T. Herring, personal communication, 1991]. The velocities are referred to a frame in which the velocity of the stable part of the North American plate is

zero. The station most often observed (63 of 69 days) is Vandenberg (VNDN), which we constrain to 10 mm in position and 1 mm/yr in velocity. The other two constrained sites are the CIGNET stations at Westford and Richmond.

The CIGNET station at Mojave, CA, has had three different antennas between 1986 and 1991. The initial antenna was a TI4100, which was changed to a FRPA on February 15, 1988, and finally replaced with a Minimac on July 19, 1988. Although we have tied the three antennas together with offsets estimated from local surveys [CSTG, 1989], our solution still yields a ~50 mm vertical discrepancy between measurements separated by a change in antenna. Rather than investigate the offset, we allow the coordinates of Mojave to vary stochastically (50 mm over 1 day), preventing the unknown ties there from corrupting the rest of the solution.

All the other stations are left effectively unconstrained. Their *a priori* coordinates are assigned an uncertainty of 10 m, and their velocities 1 m/yr. The only exception is for stations observed for less than 18 months, whose velocities were not allowed to vary from their *a priori* values.

The orbital parameters were constrained only loosely. The *a priori* values of the eight orbital parameters were assigned large uncertainties, corresponding to 500 m in X, Y, and Z, as shown in Table 4.6. The elements are allowed to vary stochastically according to a random walk which permits perturbations of 10 m from one day to the next. This level of constraint is fairly loose and almost uncouples one day's orbit from the next. A daily perturbation of 10 m is 10 to 100 times larger than the level we expect for most satellites [Herring and Dong, 1991]. It helps avoid the effect of unmodeled non-gravitational forces on the satellite, especially when the satellite is "eclipsed", spending part of its orbit in the Earth's shadow [Lichten, 1990b]. Since most of the satellites were eclipsed at some time during the 4.2-year data span, we are obliged to apply the loose 10 m constraint across the entire span. A more realistic constraint would be variable, about 10 m when the satellite is eclipsed, and 0.1 m when it is not. Since our software does not yet allow such variable constraints, we will consider how tightening the constraint effects the velocity estimates below.

The solution just described is the one we use to estimate station velocities. To estimate the precision of that solution, we perform a "back solution" as described by Herring *et al.* [1990] with the same constraints on the orbits but allowing the station coordinates to vary stochastically, rather than with a constant velocity. This technique permits a comparison of single-day solutions by producing an estimate of each station's position on each day of observation.

Table 4.7. Parameters estimated in the 5-year global solution.

Parameters	number	<i>A priori</i> uncertainty	Markov perturbation ^a
3 station coordinates ^b	3 × 12	1 m	0
3 components of station velocity ^b	3 × 12	1 m/yr	0
3 station coordinates ^c	3 × 37	1 m	0
3 components of station velocity ^c	0	0	0
3 coordinates of Mojave ^d	3	1 m	50 mm
3 components of Mojave's velocity ^{d,e}	3	1 mm/yr	0
3 coordinates of Vandenberg, Richmond, and Westford	3 × 3	10 mm	0
3 components of velocity of Vandenberg, Richmond, and Westford ^e	3 × 3	1 mm/yr	0
UT1	1	100 mas	1 mas
Polar Motion X, Y	2	100 mas	1 mas
Satellite X, Y, Z	3 × 14	500 m	10 m
Satellite \dot{X} , \dot{Y} , \dot{Z}	3 × 14	50 mm/s	1 mm/s
Satellite radiation pressure	1 × 14	1000%	10%
Satellite Y-bias	1 × 14	1000%	10%
Total	322		

Notes:

- a* The standard deviation of the *a priori* constraint on the differences between two values in a random walk separated by one day. As described in *Herring et al.* [1990], it is $\sqrt{(\Phi_r \Delta t)}$, where Φ_r is the power spectral density (PSD) of the white noise driving the random walk, and Δt is the time difference, taken here to be one day.
- b* For stations observed more than 1.5 years.
- c* For stations observed less than 1.5 years.
- d* To handle the unknown offset when the antenna was moved in 1988 and 1989.
- e* *A priori* estimates of velocities from the VLBI solution for data between 1980.5 and 1990.0 given in Table 4.8 [T. Herring, personal communication, 1991].

Table 4.8. *A priori* velocities

code	name	North, mm/yr	East, mm/yr	Up, mm/yr
7223	Vandenberg	35.7	-27.2	4.5
ALAM	Alamo	35.8	-27.1	4.5
ALGO	Algonquin	-3.5	-1.9	9.0
ALVA	Alvado	35.7	-27.2	4.5
AUST	Austin	0.0	0.0	0.0
FTOR	Fort Ord	32.7	-28.5	21.3
GAVI	Gaviota	35.8	-27.0	4.3
GRAS	Grassy	35.7	-27.1	4.5
JPL1	JPL	20.7	-24.4	5.1
KOKE	Kokee Park	56.4	-57.9	1.9
LIND	Linda	35.8	-27.1	4.6
LOSP	Lospe	35.7	-27.2	4.7
MADC	Madre	35.8	-27.0	4.6
MILL	Miller	35.8	-27.1	4.3
MOJA	Mojave	6.5	-1.8	2.9
ONSA	Onsala	-8.9	16.6	-7.3
OVRO	Owens Valley	7.1	-4.1	3.8
PLAT	Platteville	1.4	-1.0	1.5
PVER	Palos Verdes	26.2	-25.4	3.9
RICH	Richmond	1.1	-1.0	7.1
RUS1	Rustad	35.7	-27.2	4.5
SYNZ	Santa Ynez	35.9	-27.0	4.3
TEPW	Tepusquet	35.8	-27.0	4.5
VND2	Vandenberg	35.7	-27.2	4.5
VNDN	Vandenberg	35.7	-27.2	4.5
WETT	Wetzell	-10.0	19.6	-12.5
WSFD	Westford	0.2	-0.6	2.7
YKNF	Yellowknife	-0.5	6.2	54.5

For stations at VLBI sites, the velocities are taken from a VLBI solution for data between 1980.5 and 1990.0 [T. Herring, personal communication, 1991]. Stations in the Vandenberg network are assigned the same velocity (reckoned in X, Y, Z) as the Vandenberg VLBI site (7223).

RESULTS

Precision

The scatter in the stochastic station coordinates in the back solution provides a good measure of the precision of the estimated velocities. At each epoch, we calculate the vector between each pair of stations. The scatter of these values indicates the "repeatability" of our measurements. To evaluate the long-term scatter, we include only those vectors observed more than ten times in a span of over 1.5 years and calculate the weighted root mean square (WRMS) deviations from a straight line. The long-term WRMS scatters for the vectors in the complete network, including the tracking stations over 1000 km from California, are shown in a histogram in Figure 4.4. For the short (< 80 km) vectors connecting the five primary stations in the SFMTB network, the long-term WRMS deviations are shown as function of baseline length in Figure 4.5. The average WRMS values are 6 mm in the north component, 6 mm in the east, 5 mm in length, and 19 mm in height.

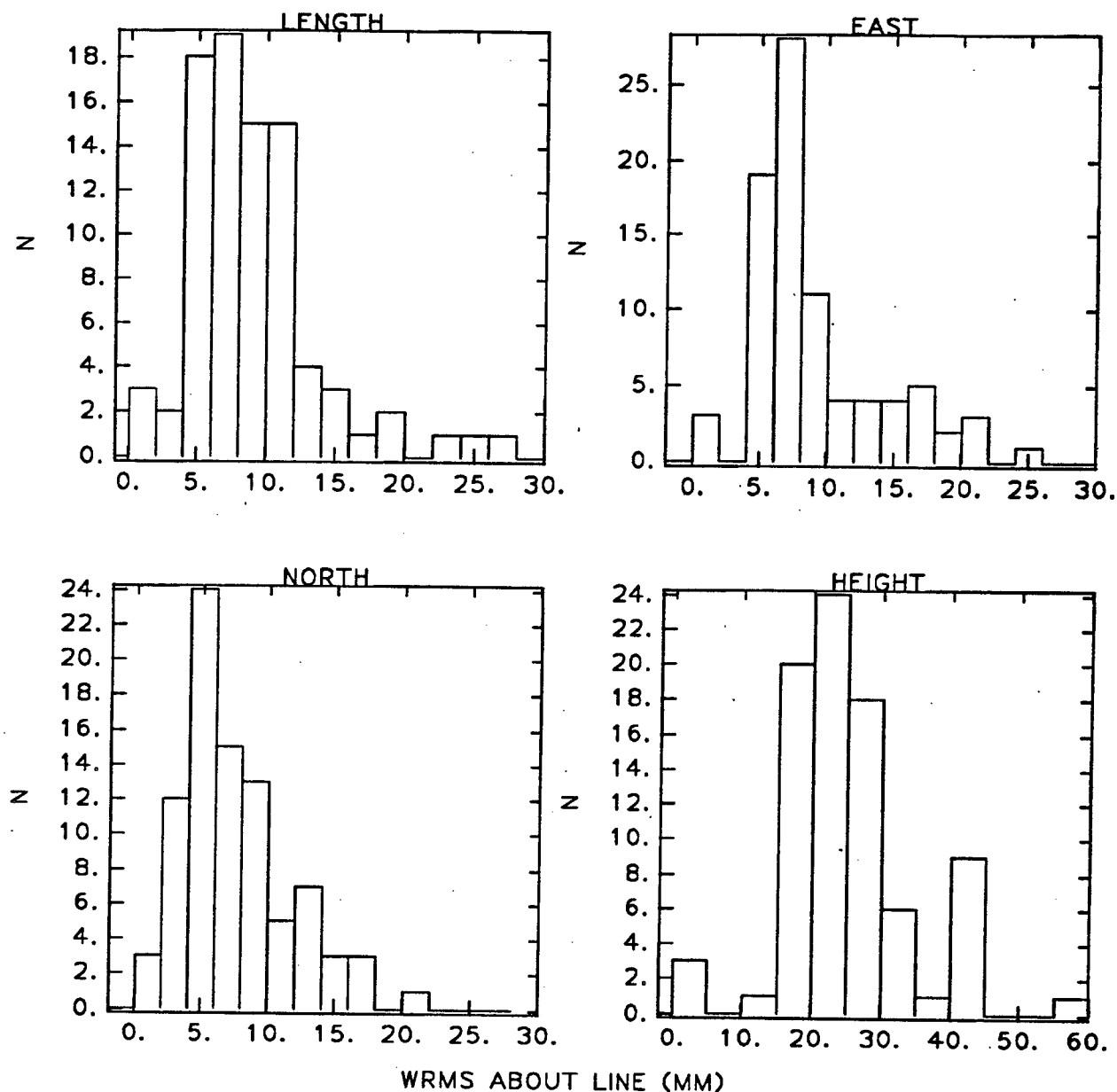


Figure 4.4. Histograms of the scatter in estimated interstation vectors. The scatter is the weighted root mean square (WRMS) deviation of the stochastic estimates from a straight line. The north, east and height components, as well as the length, of the vectors are each plotted separately. The population of vectors includes only those vectors observed more than 10 times over a span of longer than 1.5 years. The skewing to the right occurs because the population includes long (> 1000 km) lines to distant tracking stations.

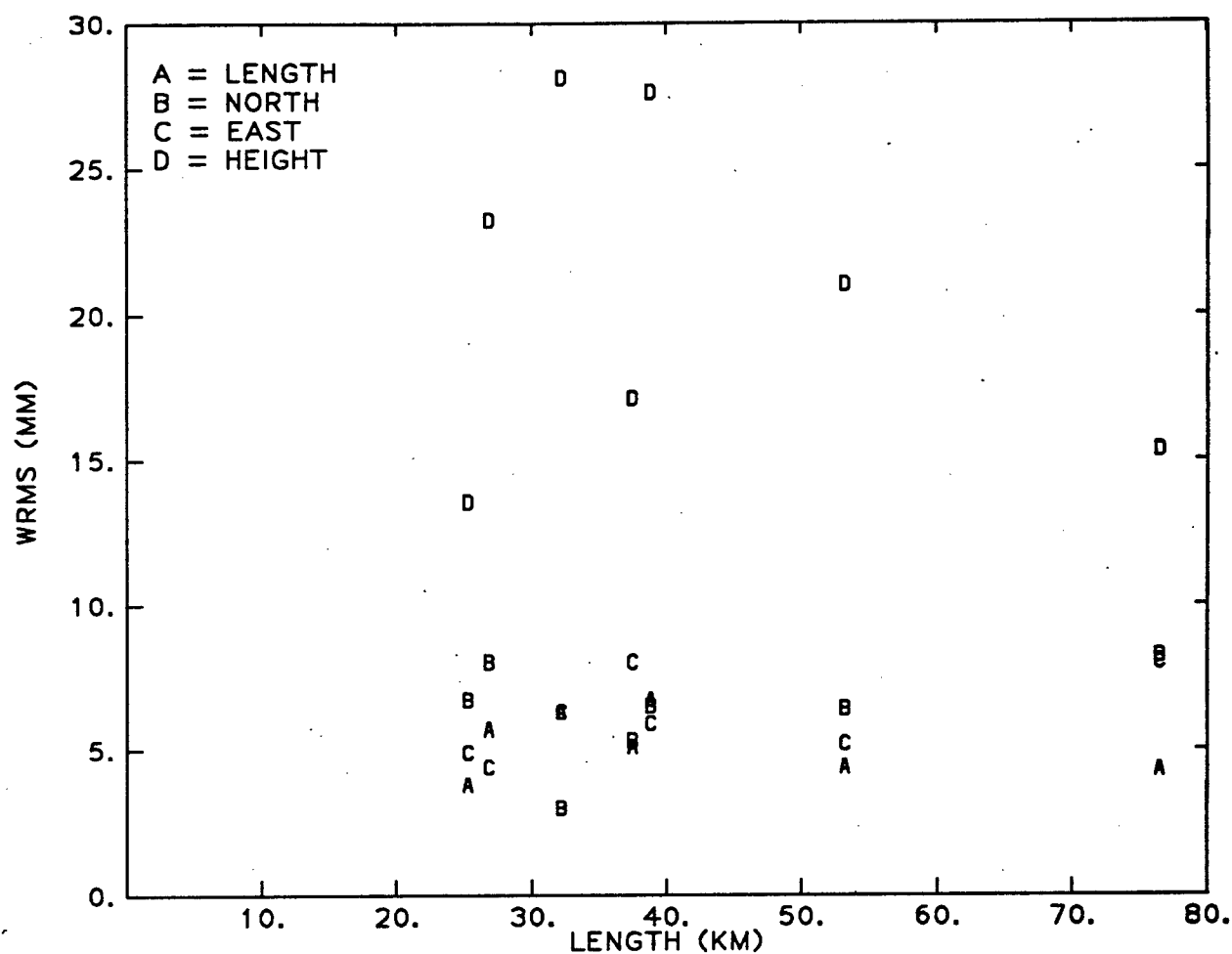


Figure 4.5. Long-term scatter of estimated components for 7 primary interstation vectors in the SFMTB network. For each component, the scatter is expressed as a weighted root mean square (WRMS) deviation from a linear fit to the estimated values. Only vectors observed more than 10 times over a span of longer than 1.5 years are included.

Tie between GPS and VLBI at Vandenberg

At Vandenberg, the VLBI monument (7223) is not the same as the VNDN monument used for GPS observations, which is a reference mark (Table 4.1, Figure 4.2). Both marks were installed during the construction of the VLBI facility in 1983. The tie between them has been measured on only two occasions.

During the period from August 1983 through May 1984, the Defense Mapping Agency (DMA) surveyed the VLBI monument with respect to its three reference marks, as well as to RUS1 and PARG, using trilateration, triangulation and leveling [Harris, 1984]. The data from this survey were adjusted to yield a set of coordinates, which were in turn used to calculate the differential coordinates given in the VLBI site catalog [Crustal Dynamics Project Staff, 1988; V. Nelson, personal communication, 1991].

In March 1990, while the TREX18 campaign operated Trimbles at VNDN and other sites, a TI4100 receiver was placed on the second reference mark, VND2. In principle, this 4-day occupation should provide a strong (1 mm) measurement of the 50 m vector between VNDN and VND2. In practice, however, the measurement is probably only accurate to 5 mm because mixing receivers introduces two additional sources of error. The combination of heterogeneous antennas may introduce an offset due to the different phase centers [Rocken and Meertens, 1989; Gurtner *et al.*, 1989b]. Secondly, the two different receivers sampled the phase at times separated by up to 1.236 s, an amount sufficiently large that the effect of Selective Availability does not vanish when differenced between receivers [Feigl *et al.*, 1991 and Chapter 2]. Because of these problems and the omission of the VLBI monument (7223), we have not pursued a high-accuracy estimate of the VNDN-VND2 vector from these observations.

After the removal of the 9 m "mobile" VLBI antenna in the summer of 1990, it was once again feasible to survey the VLBI monument to the GPS monument. We occupied the GPS site (VNDN), the VLBI mark (7223) and the second reference mark (VND2) on February 6, 1991 using Trimble 4000 SST GPS receivers. An additional survey involving VNDN, 7223, ARG3, VND2 and VINA was performed in June, 1991 by the NASA Crustal Dynamics Project [V. Nelson, personal communication, 1991].

The vectors estimated from the February 1991 survey are compared to the CDP ties in Table 4.9. The differences between the two surveys are up to 2.5 times larger than their uncertainties, even for the EDM measured lengths. Moreover, the 1991 lengths are all shorter than those measured in 1983 (Figures 4.6 and 4.7). We have attempted

to uncover the source of the discrepancies, but have been unable to distinguish between three possibilities: human error, instrumental error, or site motion.

A blunder in setting up and measuring the antenna during the 1991 GPS measurement is unlikely. The operator (KLF) was experienced, rested, and worked during the day under fine weather conditions. The tribrachs had been calibrated the same day and verified with a plumb bob. The DMA surveyor working in 1983 was certainly capable of setting up an instrument to better than 1 cm [B. Wideman, VAFB geodesist, personal communication, 1991]. An error in locating the instrument at a single station is unlikely in light of the geometry in Figure 4.7.

Could the concrete pad surrounding 7223 have shifted? In January, 1991, we found tire tracks on the pad, suggesting that the crane or the trailer used to remove the 9 m VLBI antenna drove over the monument. There were no cracks between the concrete and the surrounding gravel, however. The asphalt gasket between the rod capped by the benchmark and the surrounding concrete was also undisturbed. If the monument shifted between surveys, the geometry in Figure 4.7 would suggest that 7223 moved about 15 mm to the east. Such a movement would not explain the shortening of the VNDN-VND2 distance by 19 mm, or about four times the EDM uncertainty. These arguments suggest that a shift of greater than 10 mm in 7223 alone is unlikely.

One of the EDM measurements (VND2-7223) was "reweighted" in the DMA adjustment by assigning it an uncertainty of 15 mm rather than the standard 5 mm. This was apparently done because the EDM measurement disagreed with the angle measurements. We note that only one measurement of the distance was made, although the usual first-order practice calls for four measurements, two in each direction [V. Nelson, personal communication, 1991].

The most likely possibility is that the HP3080A instrument was miscalibrated and provided readings which were too long by a constant amount of 10–20 mm. Such a miscalibration is possible due to a poorly focused lens within the instrument. The surveyors at Vandenberg recollect uncovering such a miscalibration in the mid 1980s, but do not remember the sign of the error [H. Harris, VAFB geodesist, personal communication, 1988].

The vertical components of the vectors are also different in the two surveys. The VND2-VNDN line shows the largest discrepancy, 145 mm, which is considerably larger than the uncertainties in the measurements. The 1984 survey determined the relative geoidal heights of the stations by measuring vertical angles, a technique with an uncertainty of about 5 seconds of arc [Gergen, 1975], or about 1 mm over 50 m. The ellipsoidal height differences estimated from GPS are arguably better than 5 mm over

lines less than 50 m long. The vertical displacements satisfy closure around the triangle shown in Figure 4.7. Starting at 7223 and proceeding counterclockwise around the triangle, the vertical changes between the 1984 and 1991 surveys are +60 mm, -145 mm and +84 mm, for a closure sum of -1 mm. Such closure is consistent with slumping, but only if VNDN is sinking at 10.5 mm/yr with respect to 7223, while VND2 is rising at 7.5 mm/yr with respect to 7223. Such rapid movement in opposite directions seems unlikely for closely spaced monuments in alluvium.

If the discrepancies are due to errors in the 1984 survey, they may remain buried forever. On the other hand, the 1991 results will be tested by additional EDM and GPS observations made by the Bendix Survey crew during the NASA 5-km footprint survey in June, 1991 [V. Nelson, personal communication, 1991]. We consider this discrepancy to be illustrative of the need for frequent (at least yearly) surveys between important monuments and their reference marks.

Table 4.9 Ties at VNDN

vector	source	N, m	σ_N mm	E, m	σ_E mm	U, m	σ_U mm	L, m	σ_L mm
7223 to VND2	GPS	-27.843	1.5	7.463	1.5	-0.336	3.3	28.827	1.5
	CDP	-27.826		7.459		-0.420		28.811	
	EDM							28.851	5.
7223 to VNDN	GPS	20.401	1.5	20.368	1.5	0.718	3.3	28.837	1.5
	CDP	20.417		20.378		0.778		28.857	
	EDM							28.856	5.
VND2 to VNDN	GPS	48.244	1.5	12.905	1.2	1.053	3.3	49.951	1.5
	CDP	48.243		12.919		1.198		49.963	
	EDM							49.970	5.

Notes:

- GPS Estimated from an L1 only solution from GPS data collected February 6, 1991. The standard deviations σ_i are the formal uncertainty multiplied by a factor of 3 to reflect typical scatter.
- CDP As printed in *Crustal Dynamics Staff* [1989]. The VND2-to-VNDN vector was obtained by subtraction.
- EDM Mark to mark distance measured by the DMA Geodetic Survey Squadron at Vandenberg AFB with an HP3808A instrument on August 8, 1983. The measurements were originally assigned a "weight code" of 105 or 1 ppm + 5 mm, although the 7223-VND2 measurement was "reweighted" to 215 (2 ppm + 15 mm) in the DMA's adjustment, apparently because of its large misfit in the adjustment.

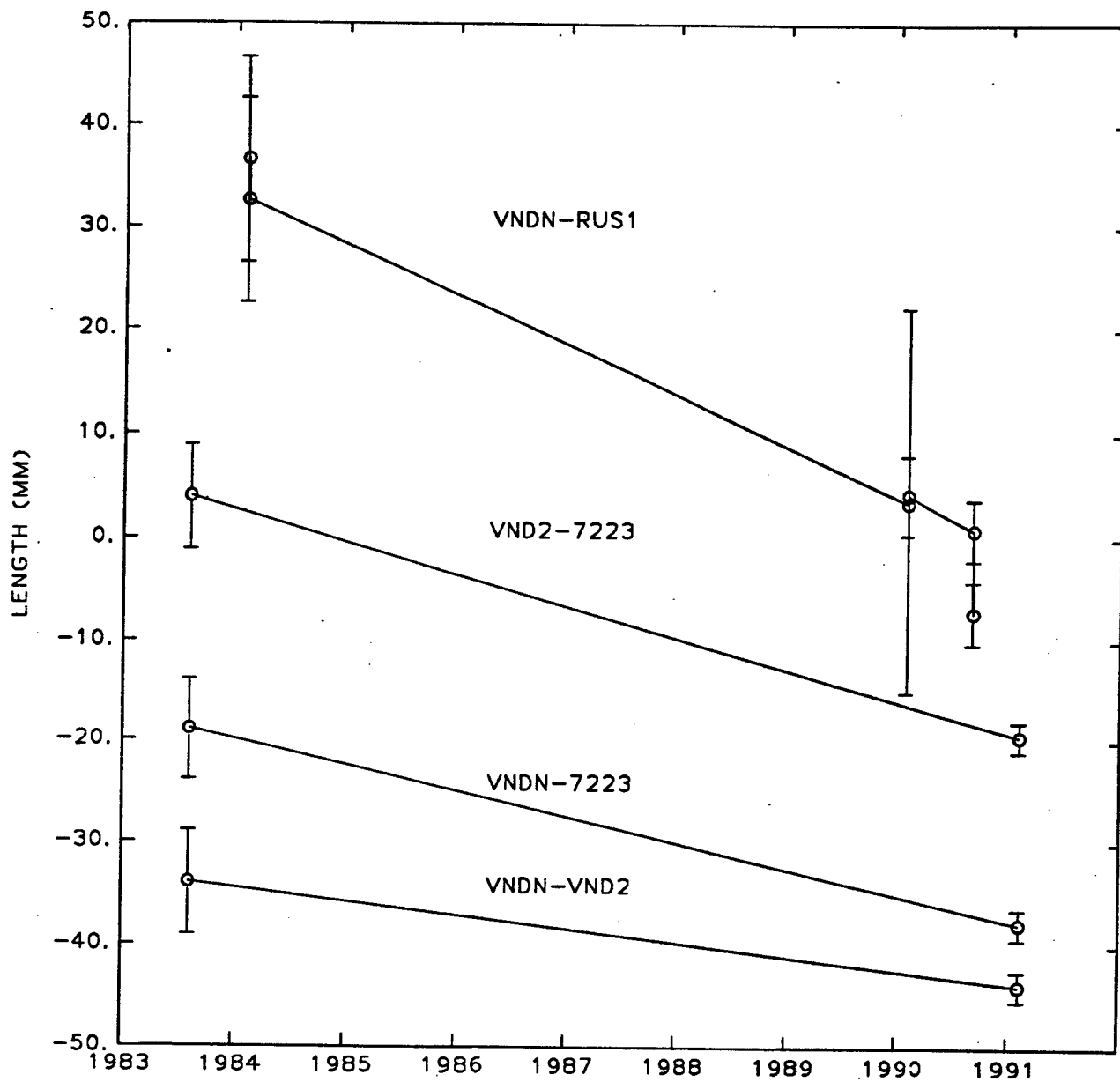


Figure 4.6. Interstation distance as a function of time several short lines near VNDN. The points prior to 1986 are EDM measurements performed by the Defense Mapping Agency. The points after 1987 are L1 estimates from individual day solutions from SOLVE. Error bars denote one standard deviation. The lines connecting the points are meant to guide the eye and do not represent a fit to the data.

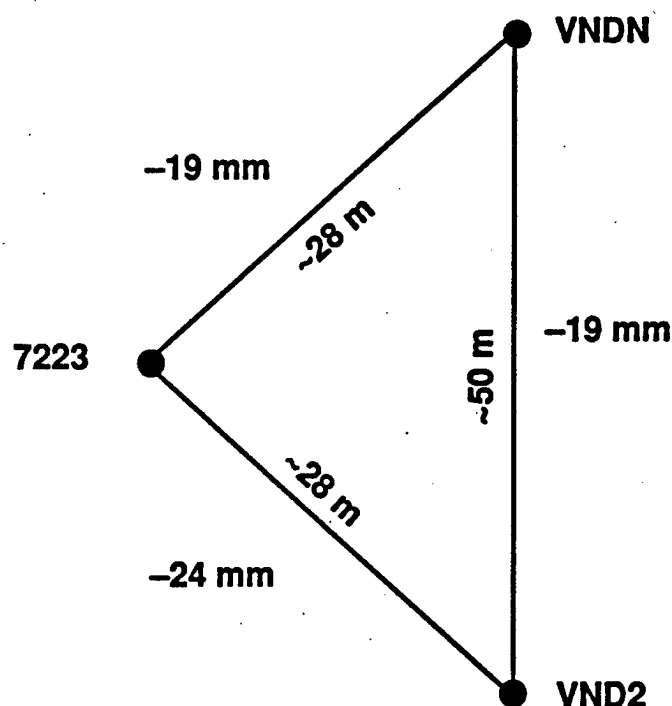


Figure 4.7. Sketch of the lines connecting the Vandenberg VLBI site to its two of its reference marks. The lines were measured with an HP3808A trilateration instrument on August 8, 1983 and with GPS on February 6, 1991. The change between the two surveys is given in millimeters.

Evolution of Interstation Vectors in Time

We use the stochastic estimates of station positions from the "back solution" to evaluate the evolution of the interstation vectors in time. They provide a visual display of the consistency of our observations from one year to the next, and of the consistency of the observations with the estimated velocities. We have plotted the vectors connecting each of the four principal stations (MADC, GAVI, GRAS and LOSP) with VNDN in Figure 4.8.

Several points are worth noting. The determination of the LOSP-VNDN vector on January 2, 1987 is extremely weak and is not shown in Figure 4.8c. Its standard deviation in the single-day solution is over 100 mm in all three components, and also lies over 100 mm away from the three other observations of the vector made that year. The cause of the problem is apparently radio interference from the nearby radar antennas on Vandenberg Air Force Base. The interference was sufficiently strong on December 31, 1986, January 1 and 2, 1987 to reduce the phase data in quality and quantity.

The scatter of the VF1 and VF2 measurements taken in February and September, 1990, are larger than for the other (TREX) experiments. The larger scatter may be due to the difference in the fiducial networks used in the two sets of experiments. In the VF1 and VF2 networks, we used a small fiducial network, consisting of only three or four stations (Tables 4.4 and 4.5), while the fiducial network used for the TREX experiments has more stations covering a large fraction of the globe.

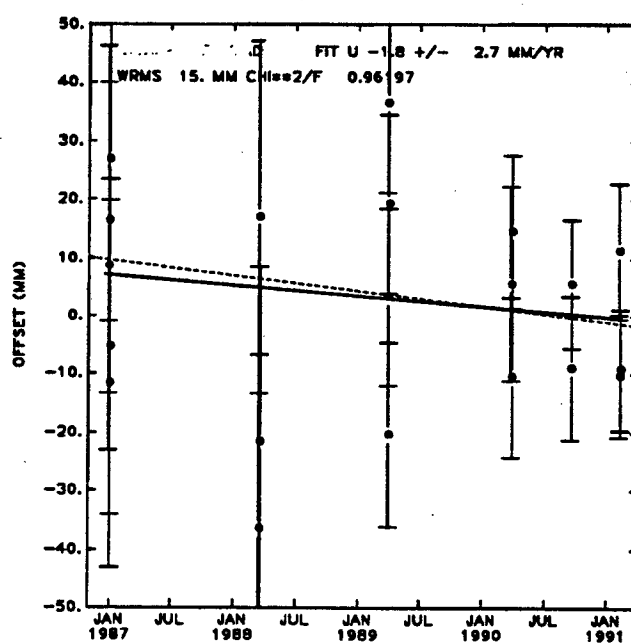
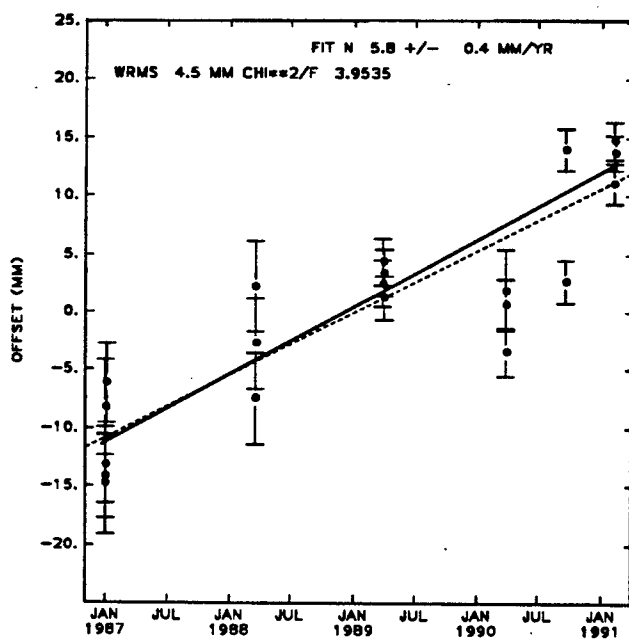
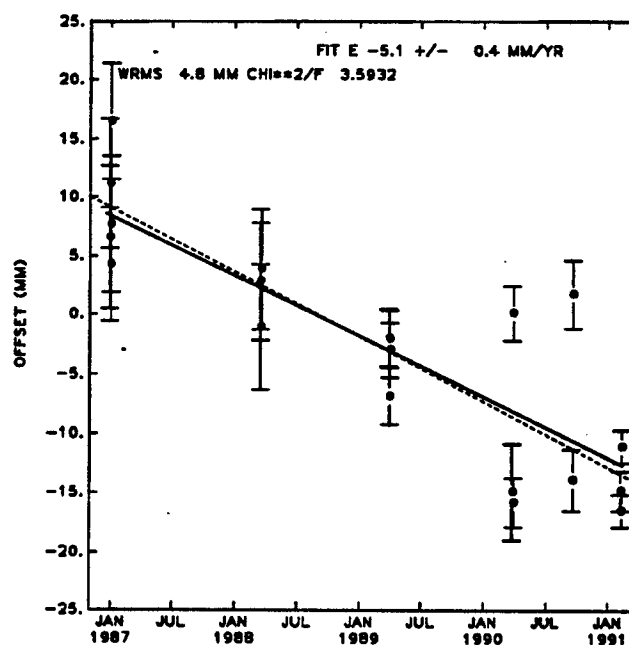
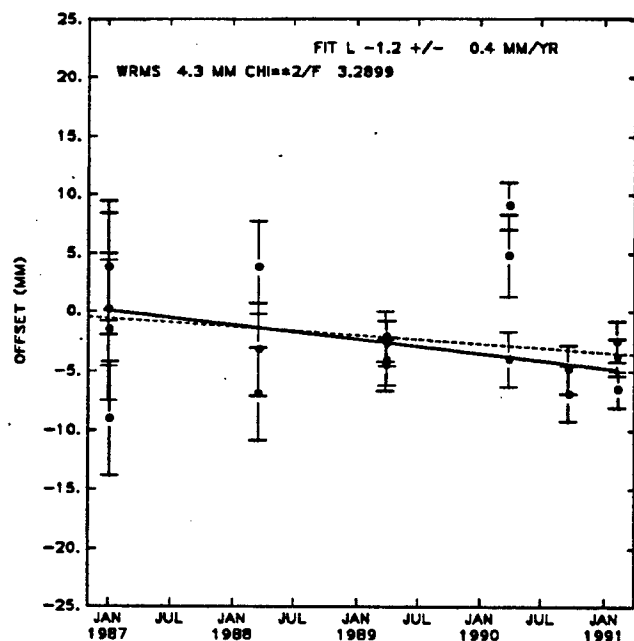
In the set of measurements connecting MADC and Owens Valley to VNDN (Figures 4.8a and 4.8f), the points from February, 1990 fit the linear trend less well than the other measurements. This may also be due to inhomogenities in the fiducial network. The three clusters of points in Figure 4.8a before 1990 come from a network including Churchill, but in February, 1990, Churchill was not observed.

It is interesting to note that the vertical velocities (with respect to VNDN) of all the stations with except GRAS were insignificantly different from zero at 95% confidence. GRAS is estimated to be rising with respect to VNDN at 15.5 ± 5.6 mm/yr.

There exist two EDM observations of the 40 km line between GRAS and LOSP, which we compare to the GPS measurements of line length in Figure 4.8e. Although the rate of change in length estimated from the GPS data is opposite in sign from that estimated from the EDM data, neither one is significantly different from zero at 95% confidence.

We have four other lines on which we can compare the EDM and GPS measurements (Figure 4.6). The first three are the short (< 50 m) ties at VNDN; the fourth is a 2 km line between RUS1 and VNDN. As discussed above, the length differences between the 1983 EDM and the 1990 GPS measurements are over 10 mm, several times the standard deviation of either measurement, possibly due to a miscalibrated EDM.

Figure 4.8a. The vector VNDN-MADC as a function of time. The north (N), east (E) and height (H) components, as well as the length (L), of the vector are shown. The distance between the two stations is 76 km. The circles are the values estimated from a Kalman "back" solution, in which the adjustments to the station coordinates are allowed to vary as a random walk. The solid lines represent the velocities estimated in a "forward" solution in which the station positions vary linearly with time. The slope of this line is given as the FIT, with its unscaled 1- σ uncertainty. The dashed lines are the the best-fitting line to the stochastic values plotted as circles. The weighted root mean square (WRMS) deviation and χ^2/f (CHI**2) statistics are calculated for the fit shown by the dashed line. One outlier with uncertainties greater than 20 mm is not shown.



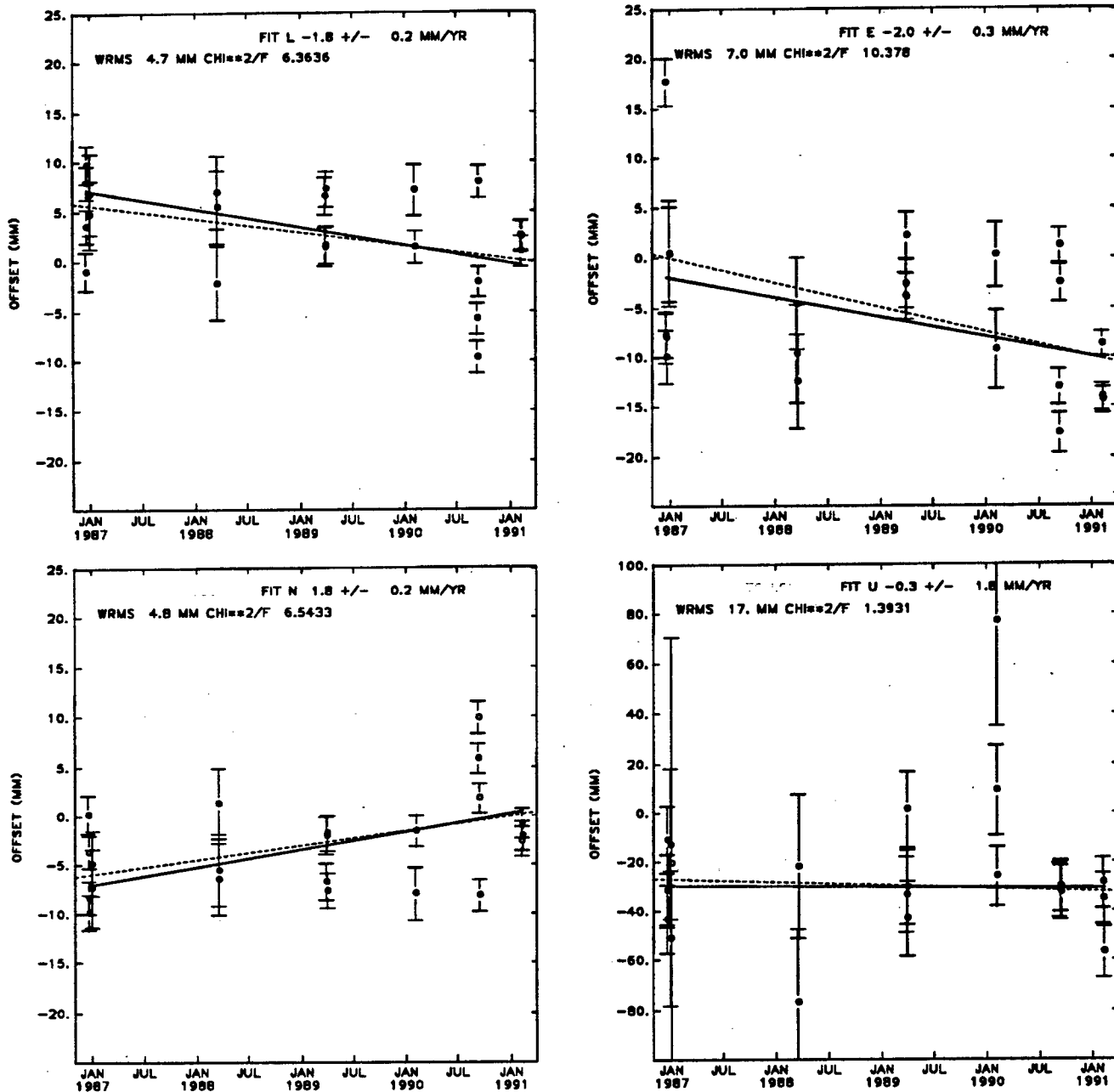


Figure 4.8b. The vector VNDN-LOSP as a function of time, plotted as in Figure 4.8a. Two outliers are not shown. One is the measurement of January 2, 1987 and lies over 150 mm off the line in length, probably because of problems with radio interference. The other is consistent with the data shown, but has large (> 10 mm) uncertainties. The distance between the two stations is 37 km.

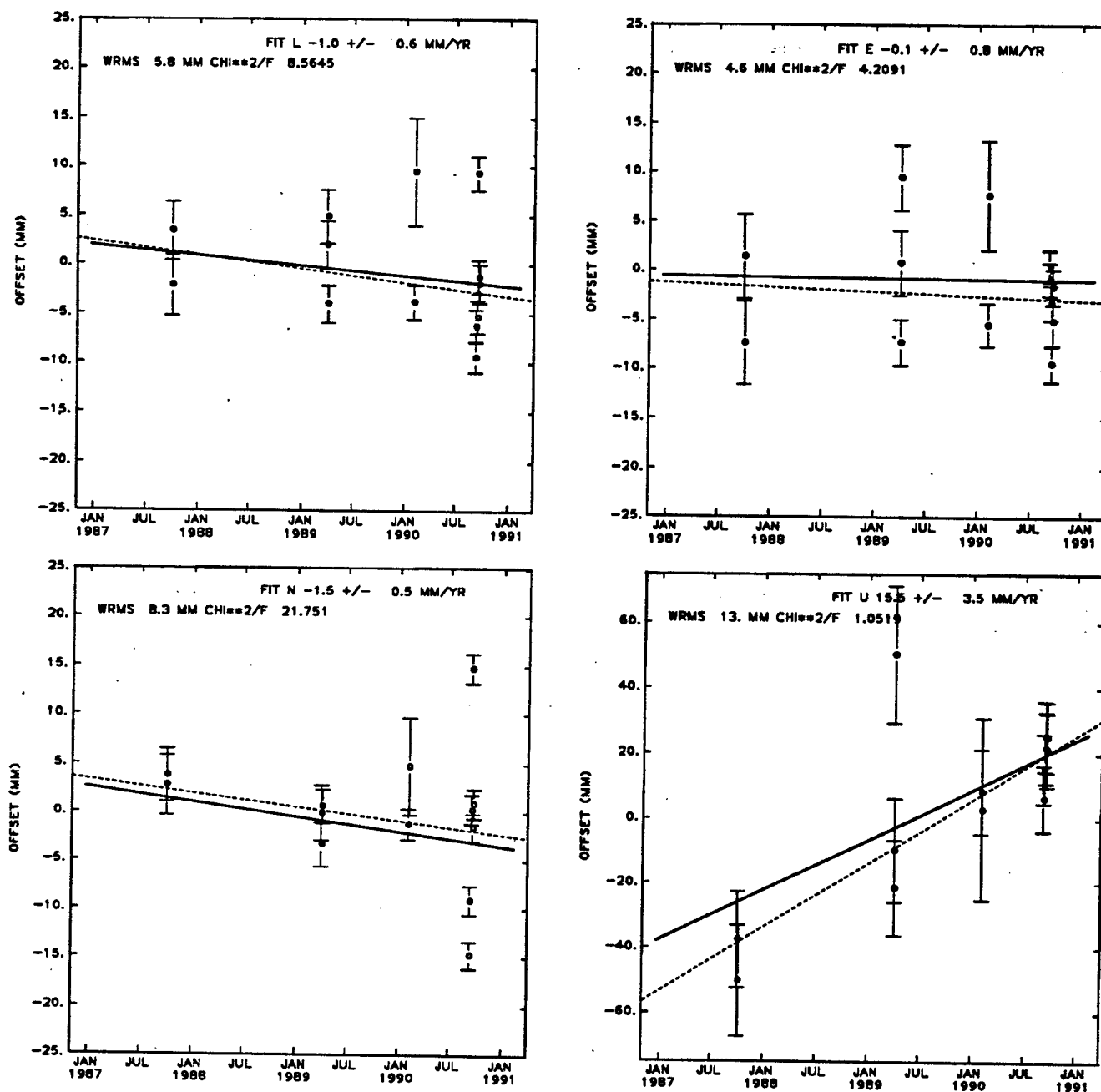


Figure 4.8c. The vector GRAS-VNDN as a function of time, plotted as in Figure 4.8a. The distance between the two stations is 27 km.

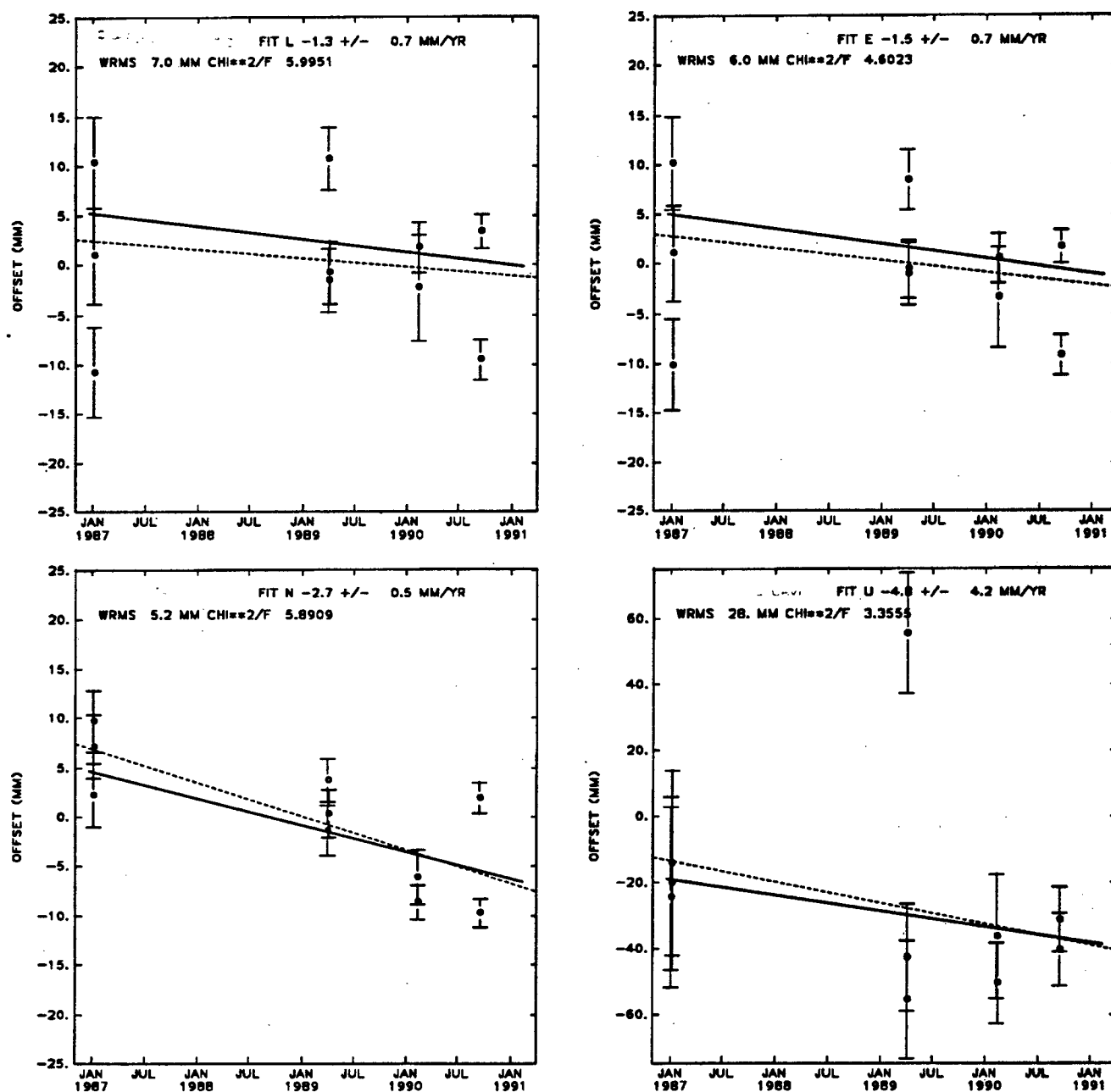


Figure 4.8d. The vector GAVI-VNDN as a function of time, plotted as in Figure 4.8a. The distance between the two stations is 39 km.

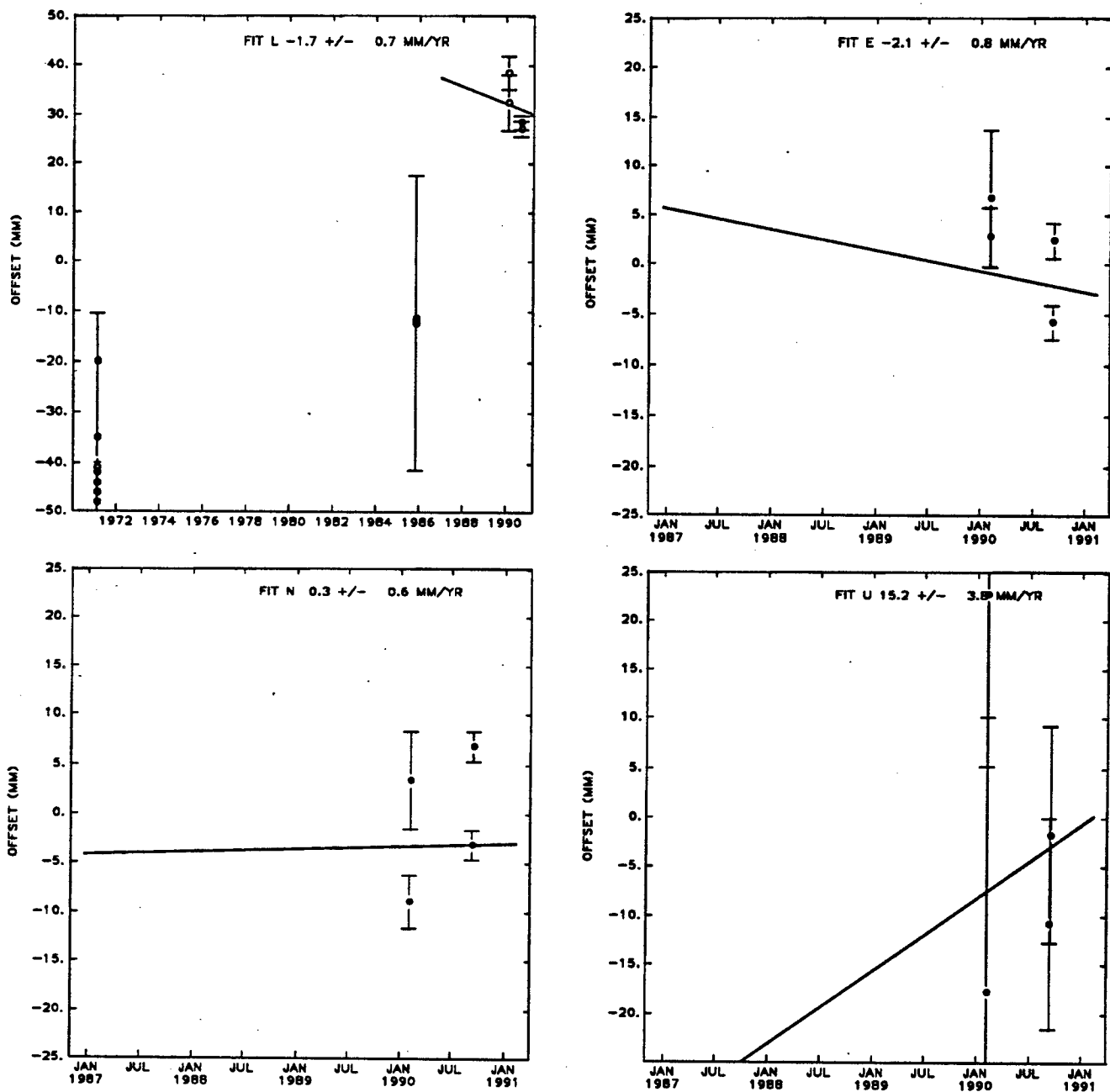


Figure 4.8e. The vector GRAS-LOSP as a function of time, plotted as in Figure 4.8a. The distance between the two stations is 25 km. Note that the time scale for the plot of length has been expanded to include the 1971 and 1985 EDM measurements.

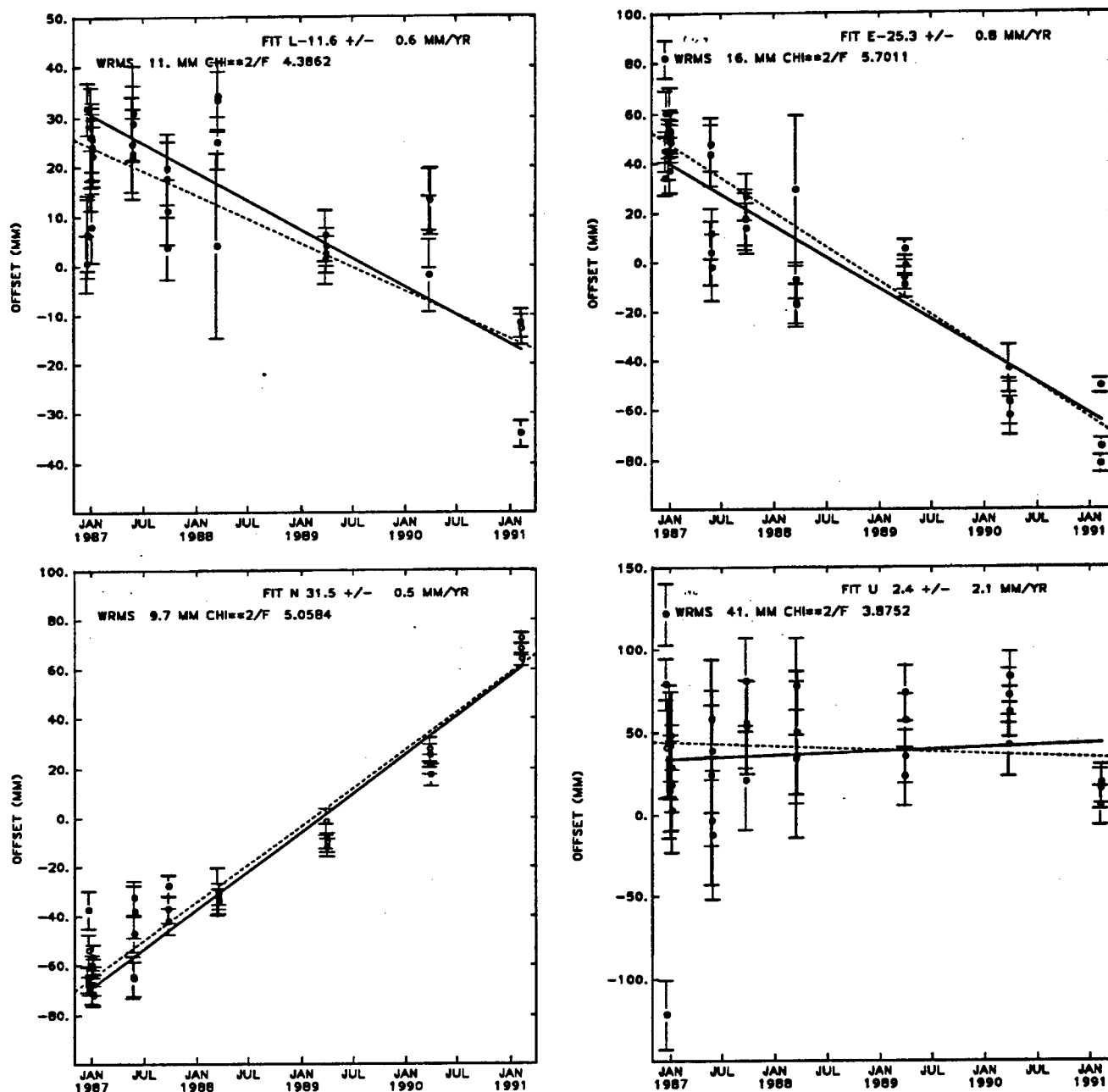


Figure 4.8f. The evolution of Vandenberg's position with respect to Owens Valley Radio Observatory (OVRO). The vector VNDN-OVRO is plotted as a function of time as in Figure 4.8a. The distance between the two stations is 363 km. The measurement made on January 1, 1987 is not shown because it is 300 mm off the line in length and has a similar uncertainty.

Velocities Relative to Vandenberg

We now consider the solution in which station coordinates are parameterized as changing linearly in time (with constant velocity), rather than according to a stochastic process. The estimated velocities relative to VNDN are listed in Table 4.10 and displayed on a map in Figure 4.9. The horizontal velocities of all the stations except GRAS are significantly different from zero at the 95% confidence level.

It is easier to interpret the relative velocities in terms of their compressive and right-lateral components. We can perform such a "tectonic vector decomposition" simply by projecting the velocities onto the structural axes of N30°E and N60°W. These two projections are perpendicular (v_{\perp}) and parallel (v_{\parallel}) to the strike of the fold axes mapped by *Namson and Davis* [1990] and shown in Figure 4.1. For example, if a station moves 10 mm/yr due south with respect to VNDN, its motion may be decomposed into $v_{\perp} = -5$ mm/yr of compressive motion and $v_{\parallel} = 8.6$ mm/yr of right-lateral motion.

These components are listed in Table 4.10, and shown as dashed lines in Figure 4.9. The compressive motion with respect to VNDN is significantly different from zero (at the 95% confidence level) for stations GAVI and MADC, but not for GRAS or LOSP. The right-lateral components are significant at LOSP and MADC, but not at GRAS or GAVI.

Table 4.10. Velocities relative to VNDN

Table 4.10. Velocities relative to VNDN

Station	Rate mm/yr	Azimuth	East mm/yr	North mm/yr	ρ_{EN}	v_L mm/yr	v_{\parallel} mm/yr	vertical mm/yr
TEPW ^a	6.5 ± 1.4	S03°W ± 13°	-0.3 ± 1.5	-6.5 ± 1.4	0.370	6.0 ± 2.0	-3.0 ± 1.0	
TEPW+R ^b	10.0 ± 1.3	S16°E ± 9°	2.8 ± 1.5	-9.6 ± 1.4	0.370	6.9 ± 1.6	-7.2 ± 1.2	
LOSP	2.7 ± 0.3	S48°E ± 8°	2.0 ± 0.4	-1.8 ± 0.3	0.175	0.6 ± 0.4	-2.6 ± 0.4	0.3 ± 2.9
MADC ^c	8.6 ± 1.1	S12°E ± 10°	1.8 ± 1.5	-8.4 ± 1.1		6.4 ± 1.2	-5.8 ± 1.4	
MADC	7.7 ± 0.6	S41°E ± 04°	5.1 ± 0.6	-5.8 ± 0.6	0.065	2.5 ± 0.6	-7.3 ± 0.6	1.8 ± 4.3
GAVI	3.1 ± 0.9	S29°W ± 17°	-1.5 ± 1.0	-2.7 ± 0.7	0.152	3.1 ± 0.8	-0.1 ± 0.9	-4.8 ± 6.7
GRAS	1.5 ± 0.7	S04°W ± 44°	-0.1 ± 1.1	-1.5 ± 0.7	-0.114	1.3 ± 0.8	-0.7 ± 1.1	15.5 ± 5.6

Notes:

Uncertainties are one standard deviation scaled by the $\sqrt{(\chi^2/ff)}$ statistic from the 5 year solution.

^a Calculated by integration of uniform strain rate estimated by *Feigl et al.* [1990].

^b TEPW result plus 0.8×10^{-8} rad/yr clockwise rotation.

^c Estimated from 2.5 years of data by *Larson* [1990].

ρ_{EN} denotes the correlation coefficient between the east and north components.

v_L denotes the projection onto S30°W with compression reckoned positive.

v_{\parallel} denotes the projection onto N60°W with right-lateral motion reckoned negative.

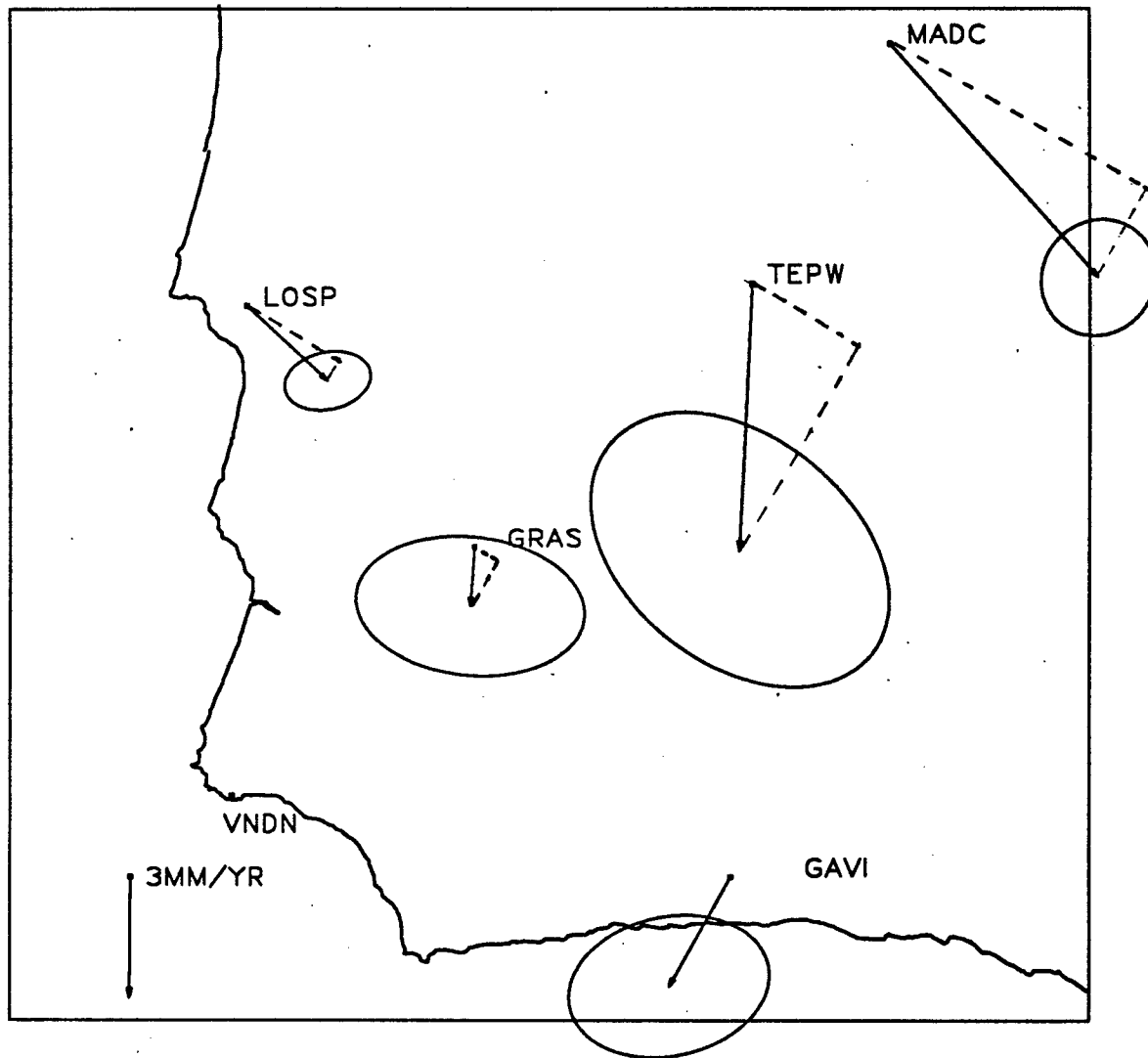


Figure 4.9. Velocity of stations relative to VNDN. Ellipses denote the area of 95% confidence, with two degrees of freedom, scaled by $\sqrt{(\chi^2/f)}$. The velocity shown at TEPW represents the integral of the uniform strain field estimated from the 1879–1987 data set as described in *Feigl et al.* [1990]. The dashed lines indicate the decomposition into the components v_{\perp} and v_{\parallel} perpendicular and parallel to the strike of geologic features.

Graphical Display of Deformation Fields

In contrast to the sophisticated algorithms used for estimating deformation fields, the techniques for displaying them are fairly crude. We briefly describe each technique, give an early example of its use and discuss its advantages.

- A map of displacement. The displacements of stations between two surveys, relative to an origin station are shown as arrows. This type of plot was made as early as 1928 by *Bowie* [1928] and continues to be a useful way to show coseismic displacements e.g., *Clark et al.*, [1990]. Confidence ellipses are a more recent innovation e.g., *Billiris et al.* [1991]. This type of plot has the advantage of displaying the relative station positions, the quantity actually measured by GPS.

- A map of velocity. Instead of displacement, the velocity of each station relative to an origin is shown as an arrow, as in the previous type of plot. Including confidence ellipses, these maps are now standard in the literature e.g., *Prescott* [1981]. They have the advantage of displaying the orientation, magnitude and uncertainty of the estimated deformation field. They have the disadvantage that the differences in velocity between adjacent stations ($\text{grad } v$) is difficult to see, particularly for stations with large arrows, far from the origin e.g., Figure 4 in *Clark et al.*, [1987].

- A map of changes in angle. Used for triangulation studies (e.g., *Chen et al.* [1984]), this type map shows a triangulation network with angular changes annotated at the vertices of the observed triangles. It has the advantage of displaying what is actually measured by triangulation, but is difficult to visualize.

- A map of changes in distance. Used for trilateration studies e.g., *Savage and Burford* [1973], this type of map shows the measured lines annotated with the time rate of change in line length (interstation distance). Like the previous type of plot, it is difficult to visualize.

- A time series. This plot displays interstation distance ("line length") (e.g., *Savage and Burford*, [1973] and Figure 3.10) or the north, east and vertical components of an interstation vector (e.g., *Davis et al.* [1989] and Figure 4.8) as a function of time. Drawn with "error bars", it is excellent for showing how well the estimated model fits the data, but provides no information about the geographical distribution of the deformation.

- A map of principal strain rates. This type of plot shows the principal strain rates as arrows oriented along the principal axis of the strain rate tensor, e.g., *Prescott et al.* [1979]. Usually each set of strain rate parameters is estimated in a subset of stations chosen for their tectonic setting. Unless the arrows are annotated with the standard

deviations of the strain rate parameters, the uncertainty and significance level of the result do not appear on this type of plot. It does have the advantage, however, of displaying the correspondence between rates of deformation and tectonic setting.

- Rate of change in angles as a function of azimuth. Used in triangulation studies (e.g., *Savage and Burford* [1973]; *Snay* [1986]; and Figure 3.9), this type of plot is particularly useful for assessing the consistency of triangulation measurements with a hypothesis of uniform strain because outlier points become prominent.

- Rate of change in lengths as a function of azimuth. This type of plot is similar to the previous one and was first used by *Savage and Lisowski* [1991]. It is particularly useful for testing the hypothesis of uniform strain.

- A grid of relative displacements. This display, first used by *Billiris et al.* [1991], shows the relative displacement between station i and station j as an arrow within a cell in the i th row and j th column of a matrix. When the cells corresponding to statistically significant displacements are shaded, it is possible to see which stations are moving together as a block. It could, of course, be used for velocities as well.

The most powerful display technique would be one which displays the orientation, magnitude, uncertainty and location of the estimated deformation rate. We have developed such a display, and describe it here. It is basically the map of principal strain rates described above, with two extensions. First, the region over which the strain rate is averaged is chosen in a systematic, and uniquely determined way. Second, it graphically displays the uncertainty in the estimates.

As discussed in Chapter 3, the horizontal strain rate tensor is the symmetric part of the gradient of the velocity field, a quantity which is uniquely determined by the relative velocities of three stations. Since the strain rates depend on the triplet of stations chosen, it is convenient to specify the stations uniquely. To do this, we employ an algorithm which divides the network into triangles which are as close to equilateral as possible. These triangles are called Delaunay triangles, which may be formed by the following 2-step process [Davis, 1986]: (1) Form Thiessen polygons such that each polygon encloses one point. A Thiessen polygon is defined such that "every location within the polygon is closer to the enclosed point than to any other point". These polygons are the two-dimensional analogue of Voronoi polyhedra, the classic example of which is soap film spanning a wire frame. (2) Connect each point to its Thiessen neighbors. Points enclosed within adjacent Thiessen polygons are neighbors. The resulting set of triangles constitutes a Delaunay triangulation. An algorithm for producing such a triangulation to contour irregularly spaced data has been developed by *Gold et al.* [1975] and programmed in FORTRAN by *Watson* [1982]. We use this

algorithm to choose triplets of stations from which to estimate the horizontal gradient of the velocity field.

For each triplet of stations, we use the relative velocities estimated from geodetic data to calculate the gradient tensor \mathbf{L} of the velocity field. We then convert these values and their uncertainties into the eigenvalue parameterization, using the formulae in Chapter 3.

Of these parameters, we plot three: the two eigenvalues and the orientation of the eigenvector. The figure resembles a cloverleaf, in which the magnitude of an eigenvalue is given by the length of the corresponding leaf. The radial distance to the edge of the leaf gives the rate of elongation $\dot{\epsilon}$ as a function of azimuth θ

$$\dot{\epsilon}(\theta) = \dot{E}_{11}\sin^2\theta + \dot{E}_{12}\sin 2\theta + \dot{E}_{22}\cos^2\theta \quad (4.1)$$

where \dot{E}_{ij} is the strain rate tensor in the conventional notation of *Prescott et al.* [1979]. (See equation (18) of *Jaeger and Cook* [1979] for a complete derivation). The azimuths of the principal axes of the strain rate tensor are shown by the orientation of the cloverleaf. The uncertainties of the eigenvalues are displayed in three levels of significance. If the eigenvalue is more than 3 times greater than its standard deviation, the leaf has many stripes; between 1 and 3 times greater than its standard deviation, a few stripes; and less than its standard deviation, no stripes. Extension is reckoned as positive and designated by radial stripes. Compression is negative and denoted by transverse stripes. As an example, in Figure 4.10a we plot the strain rates estimated in Chapter 3 from the complete 1879–1987 data set in the SMFTB. This display represents the same information as Figure 3.7, but in a more intuitive way.

Uniform Strain over Subnetworks

For networks of this size, the strain rate tensor is a meaningful quantity. In particular, the orientation of its eigenvectors ("principal axes") can be used for comparison with the trend of geological structures and with the P and T axes of earthquake focal mechanisms. In this section, we address the question: is the strain rate uniform within the SMFTB? We attack the problem by calculating strain rate over several triangular subnetworks as well as estimating it over the entire SMFTB.

Estimating the horizontal strain rate tensor from our estimates of station velocities is straightforward. Given the velocities of at least three stations, we can estimate the horizontal velocity gradient tensor \mathbf{L} [*Malvern*, 1969] by an inverse problem

$$\begin{bmatrix} 1 & 0 & \Delta x_1 & \Delta y_1 & 0 & 0 \\ 0 & 1 & 0 & 0 & \Delta x_1 & \Delta y_1 \\ 1 & 0 & \Delta x_2 & \Delta y_2 & 0 & 0 \\ 0 & 1 & 0 & 0 & \Delta x_2 & \Delta y_2 \\ \vdots & \vdots & \vdots & \vdots & \vdots & \vdots \\ 1 & 0 & \Delta x_n & \Delta y_n & 0 & 0 \\ 0 & 1 & 0 & 0 & \Delta x_n & \Delta y_n \end{bmatrix} \begin{bmatrix} u_0 \\ v_0 \\ L_{11} \\ L_{12} \\ L_{21} \\ L_{22} \end{bmatrix} = \begin{bmatrix} u_1 \\ v_1 \\ u_2 \\ v_2 \\ \vdots \\ u_n \\ v_n \end{bmatrix} \quad (4.2)$$

where Δx_i and Δy_i are the east and north coordinates of the i th station relative to the centroid of the network. The velocities u and v are in the east and north directions, respectively, with the zero subscript denoting the velocity of the centroid. Finally, the four components L_{ij} are the elements of the horizontal velocity gradient tensor L . The eigenvalues and eigenvectors of the strain rate tensor can then be calculated by the formulae in *Feigl et al.* [1990]. The clockwise spin rate $\dot{\omega}$ may also be calculated from the anti-symmetric part of L by equation (3.31).

The problem is uniquely determined for three stations, leading us to estimate the strain rate in triangles chosen by the Delaunay criterion described above. For the five principal stations in our network, there are four such triangles. The strain rates in each of them are qualitatively consistent (Figure 4.10 and Table 4.10) and indicate mostly compressional deformation at rates of $3\text{--}8 \times 10^{-8}$ /yr. The orientation of the compressive eigenvector in the southwest half of the network is significantly different (at 95% confidence) from the value in the northeast half, an observation we interpret in a later section.

It is also possible to "average" the strain rate over the whole of the SMFTB by solving the overdetermined problem for the five stations in our network. The result is shown in Figure 4.10b. The spatially averaged strain rate tensor is qualitatively consistent in orientation with the one estimated from the 1879-1987 data set shown in Figure 4.10c. In magnitude, however, it is several times smaller than our previous estimate.

The spin rates estimated in the four triangular subnetworks all indicate significant clockwise rotation with respect to North America at rates of $2\text{--}8 \times 10^{-8}$ rad/yr ($1\text{--}4^\circ/\text{Myr}$), as shown in Table 4.11. We plot these rotations as fans in Figure 4.11.

TABLE 4.11. Estimated Strain Rates

TABLE 4.11. Estimated Strain Rates

years	data type	subnetwork	half Fig. 4.10	azimuth of compressive eigenvalue θ	least compressive eigenvalue $\dot{\epsilon}_1$	compressive eigenvalue $\dot{\epsilon}_2$	clockwise spin rate \dot{w}
					$10^{-7}/\text{yr}$	$10^{-7}/\text{yr}$	10^{-8} rad/yr
1879-1987	mix	VNDN, GAVI, TEPW, IOSE ^a	a	N17°E \pm 05°	0.6 \pm 0.4	-1.3 \pm 0.3	
1879-1987	mix	VNDN, GAVI, TEPW, IOSE ^b	b	N03°E \pm 10°	0.5 \pm 0.6	-1.2 \pm 0.7	
1986-1991	GPS	VNDN, GAVI, MADC, IOSE, GRAS	c	N11°W \pm 09°	0.1 \pm 0.1	-0.40 \pm 0.09	8.1 \pm 0.8
1986-1991	GPS	GRAS, MADC, IOSE, GAVI	f	N13°W \pm 07°	0.30 \pm 0.1	-0.41 \pm 0.1	8.6 \pm 0.9
1986-1991	GPS	MADC, GAVI, GRAS	d	N03°E \pm 12°	0.51 \pm 0.4	-0.28 \pm 0.1	9.8 \pm 2
1986-1991	GPS	MADC, GRAS, IOSE	d	N21°W \pm 09°	0.26 \pm 0.1	-0.86 \pm 0.3	8.8 \pm 2
1986-1991	GPS	MADC, IOSE, GAVI	e	N16°W \pm 08°	0.27 \pm 0.1	-0.40 \pm 0.1	8.2 \pm 0.9
1986-1991	GPS	GRAS, VNDN, IOSE, GAVI	f	N42°E \pm 30°	-0.26 \pm 0.1	-0.49 \pm 0.2	5.9 \pm 1
1986-1991	GPS	GRAS, IOSE, VNDN	d	S59°E \pm 43°	-0.41 \pm 0.2	-0.71 \pm 0.4	4.1 \pm 2
1986-1991	GPS	GAVI, GRAS, VNDN	d	N61°E \pm 21°	0.06 \pm 0.3	-0.48 \pm 0.2	5.1 \pm 2
1986-1991	GPS	VNDN, IOSE, GAVI	e	N28°E \pm 22°	-0.24 \pm 0.2	-0.56 \pm 0.2	6.7 \pm 1

Notes:

Notation as defined in Chapter 3, with extension reckoned positive. Uncertainties *not* scaled by $\sqrt{\chi^2/\text{df}}$.^a From Feigl *et al.* [1990].^b From Shen [1991].

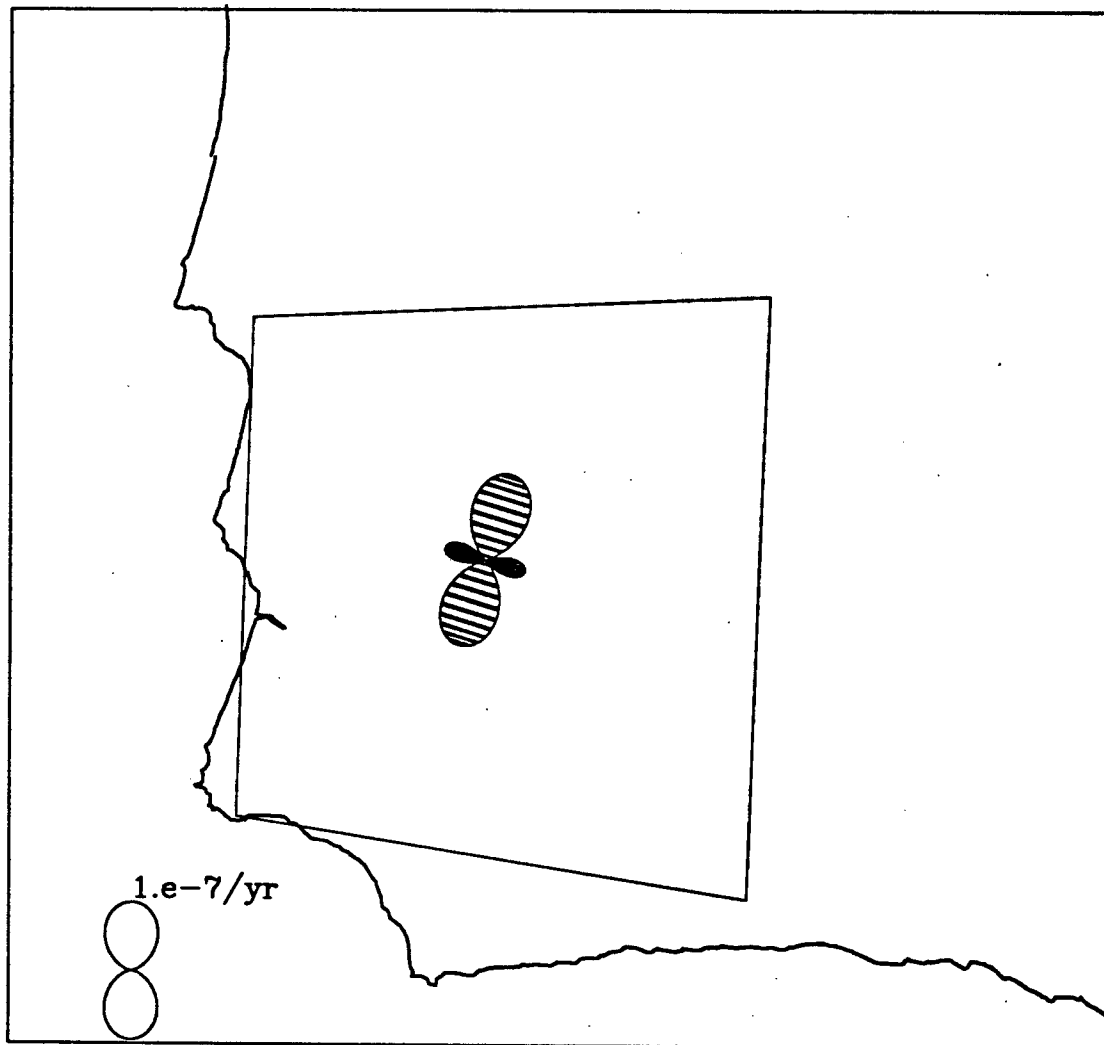


Figure 4.10a. Different estimates of horizontal strain rates displayed as cloverleaves as described in the text. The scale is the same in each figure. Strain rate tensor estimated from the 1879–1987 data set as described in *Feigl et al.* [1990] assuming uniform strain across the network spanned by the outlined quadrilateral formed by stations VNDN, GAVI, LOSP and TEPW.

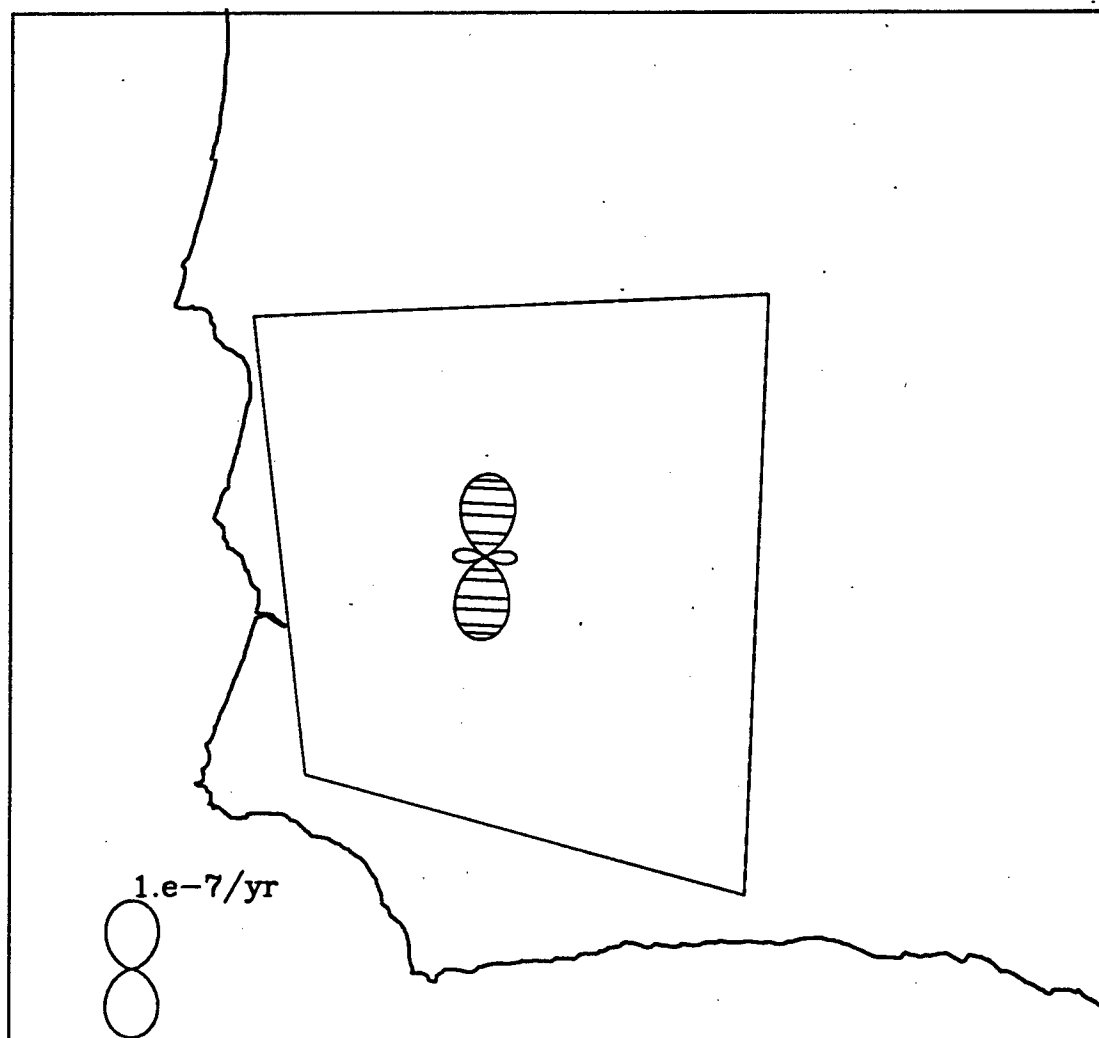


Figure 4.10b. Average strain rate tensor estimated by *Shen* [1991] assuming uniform strain across the network spanned by the quadrilateral formed by stations VNDN, GAVI, LOSP and TEPW.

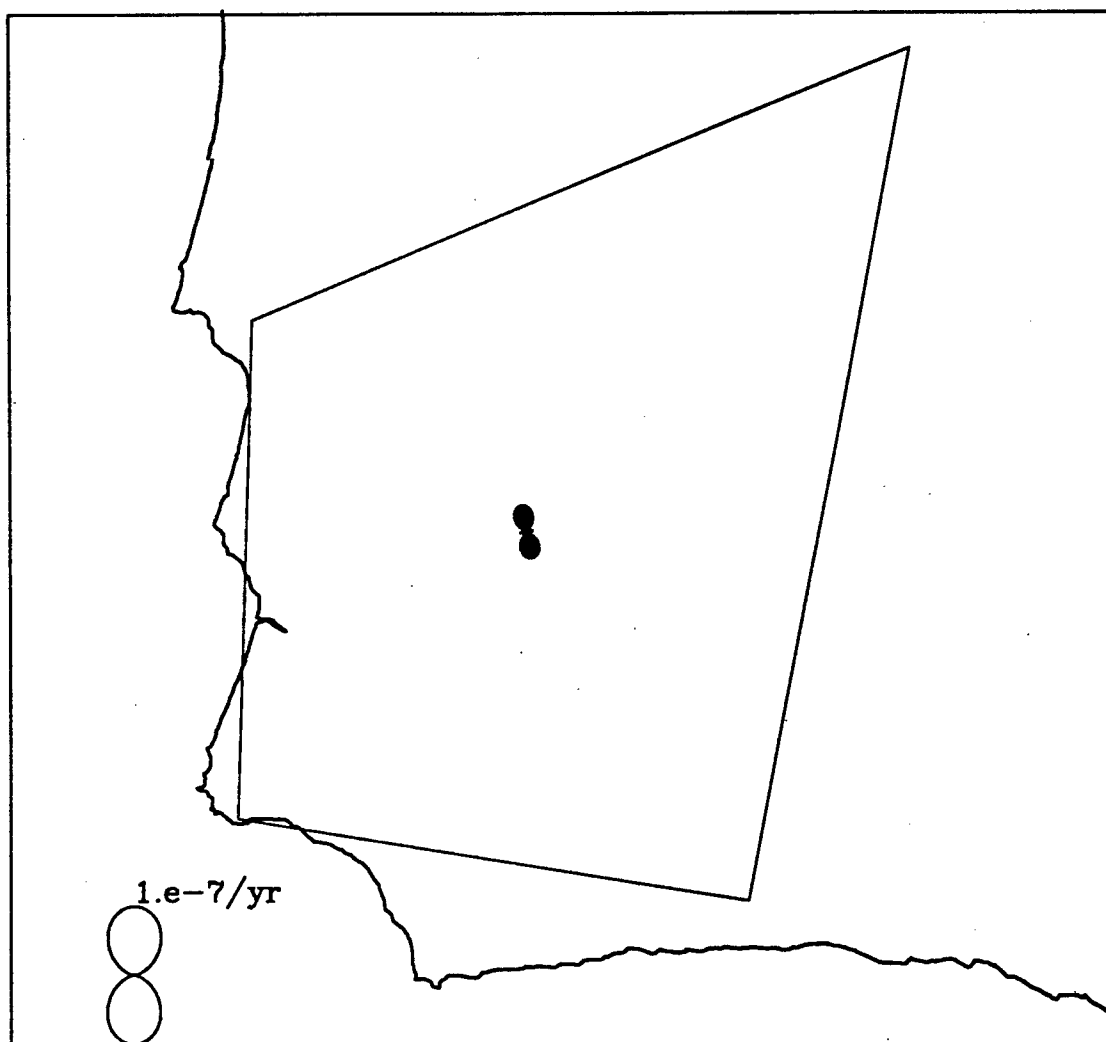


Figure 4.10c. Average strain rate tensor estimated from the 1986–1991 data set. We have assumed the strain to be uniform across the network spanned by the quadrilateral formed by stations VNDN, GAVI, LOSP and MADC. The large quadrants are compressional.

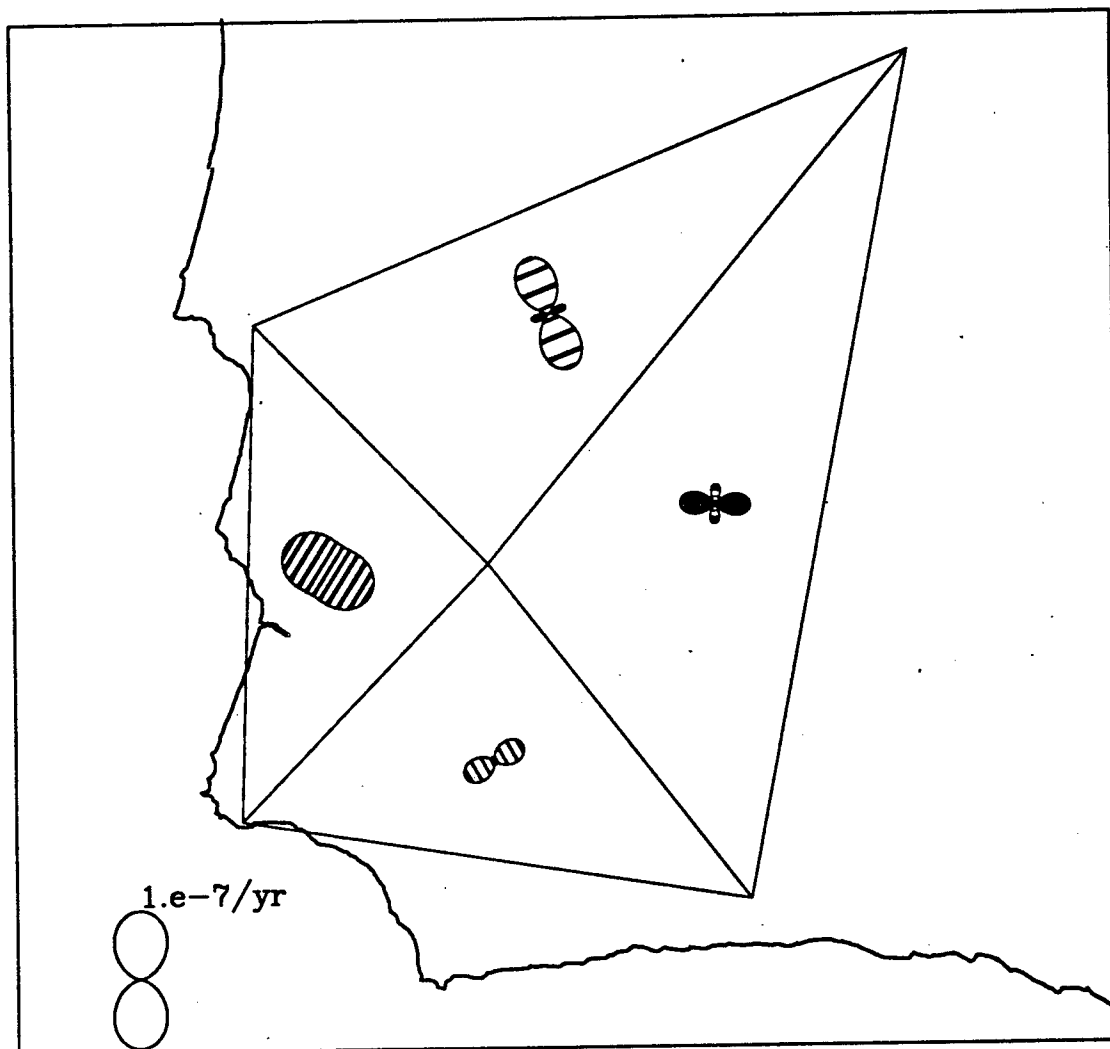


Figure 4.10d. Strain rate tensor estimated from the 1986–1991 data set in four triangular subnetworks. Note from Table 4.11 that the uncertainty in the orientation of the compressive axis is greater than 20° for two of the triangles.

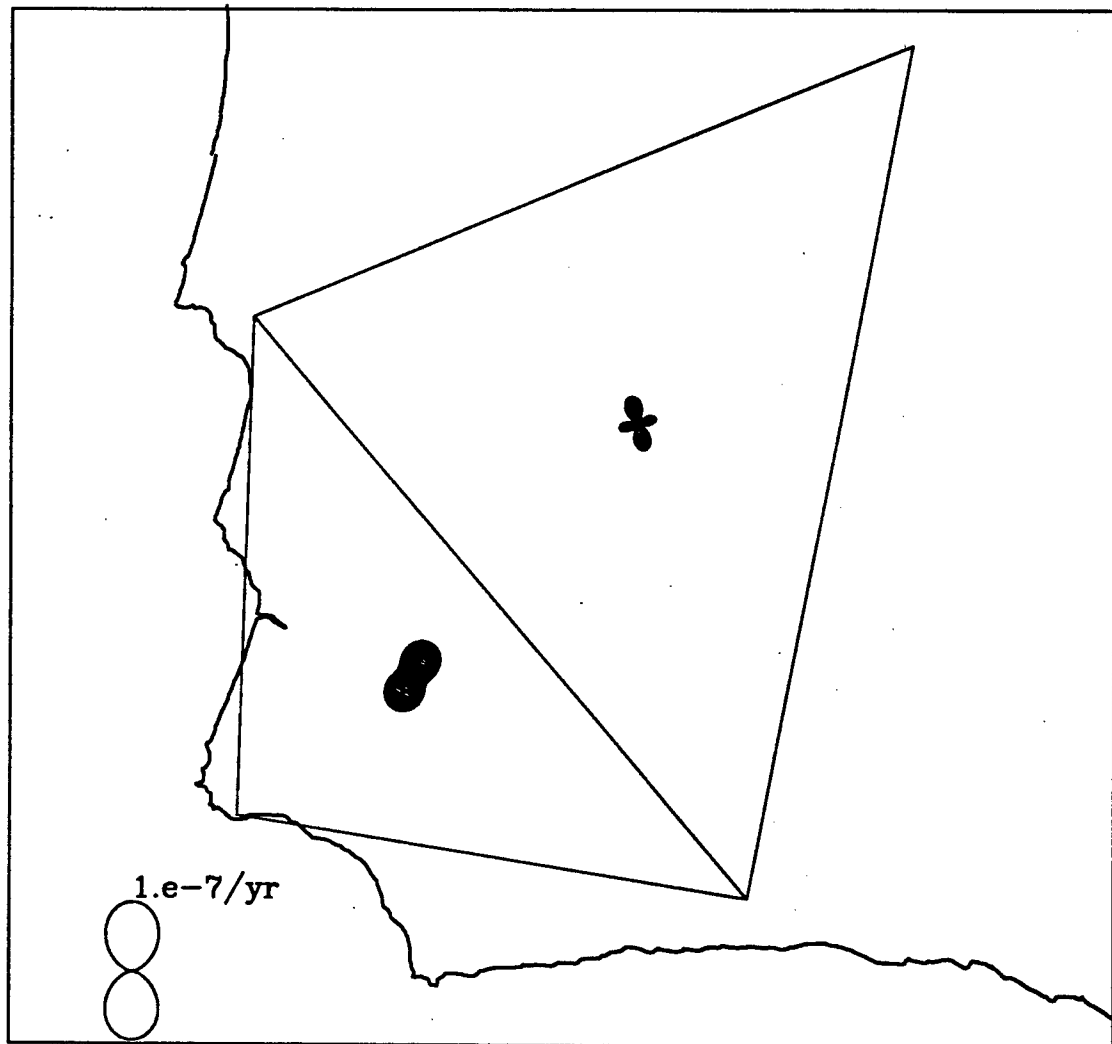


Figure 4.10e. Strain rate tensor estimated from the 1986–1991 data set in two triangular subnetworks which do not include station GRAS.

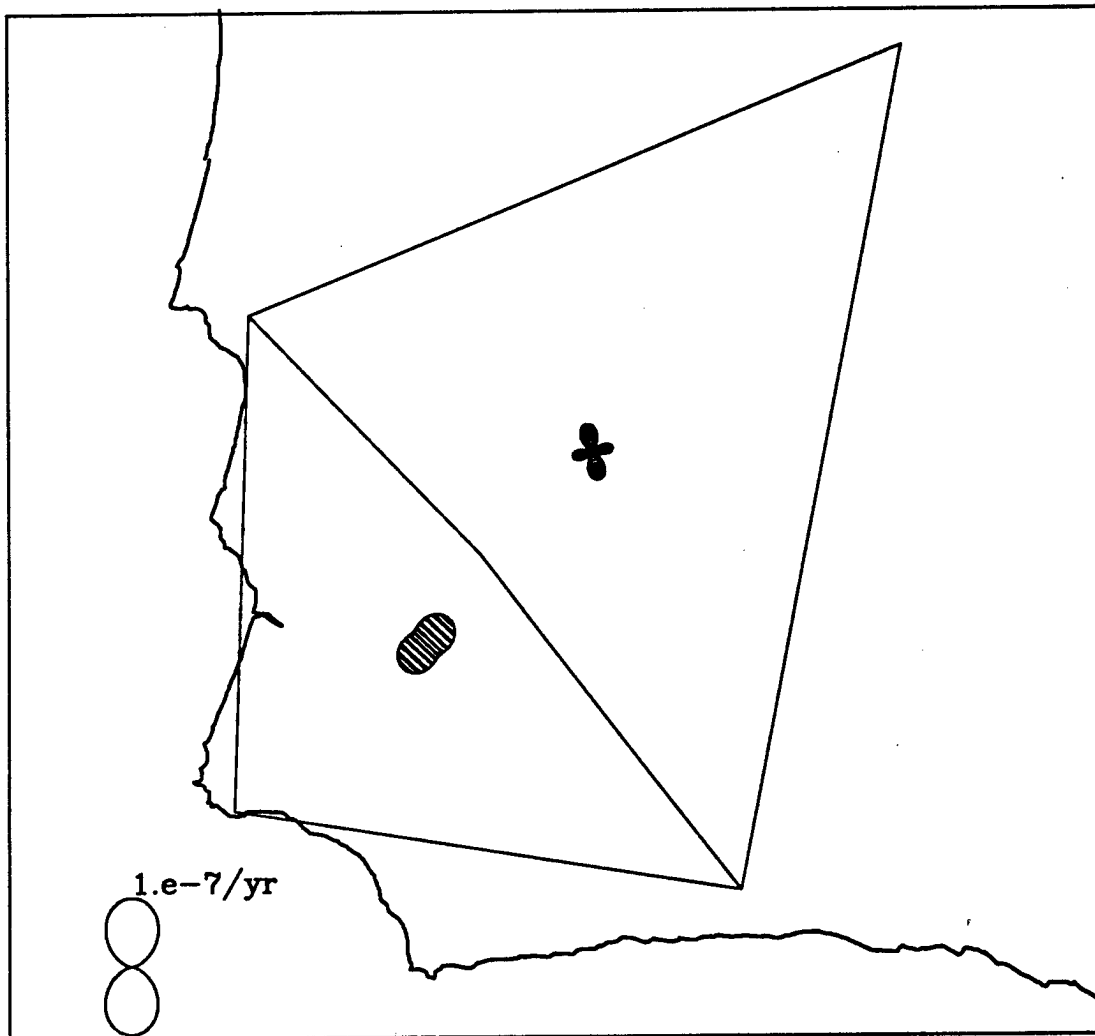


Figure 4.10f. Strain rate tensor estimated from the 1986-1991 data set in two quadrilateral subnetworks which include GRAS.

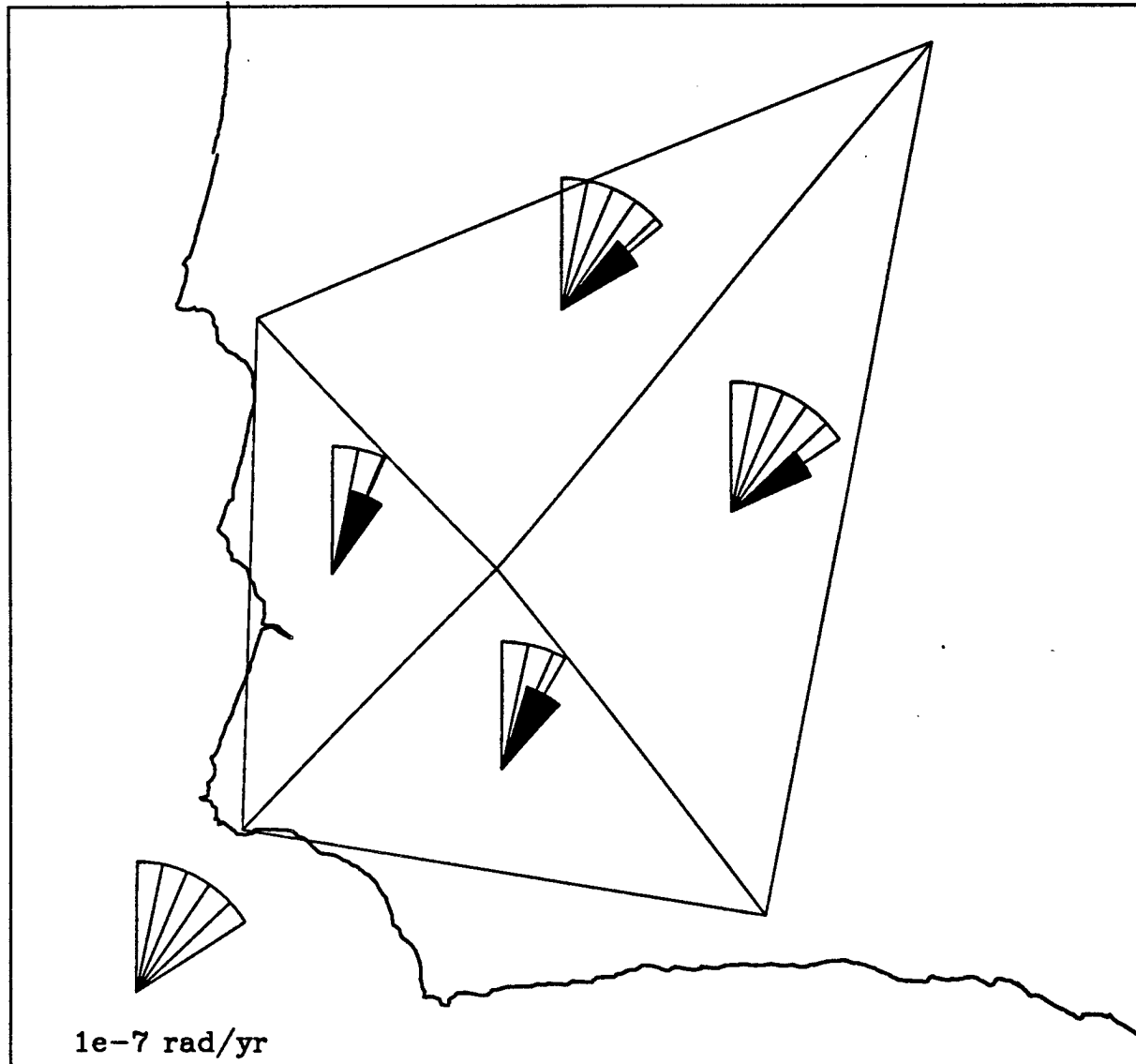


Figure 4.11. Rotation rates inferred from the 1986–1991 data set. The rates are shown as fans, in which each fold denotes 20 nanoradian/yr. The black wedge indicates the 1- σ confidence interval for the rotation rate. The angle subtended by the fan indicates the amount of rotation which would accumulate if our geodetic estimates were constant for 10 Myr. The radius of the fan is arbitrary. All the rotations shown are clockwise with respect to North America.

DISCUSSION

Robustness of the Velocity Estimates

Before interpreting the velocity estimates, we should ensure that they are insensitive to any other part of the analysis, such as reference frame, ambiguity resolution, orbital constraints, or errors in the earth orientation parameters.

A troublesome possibility is that the geometry of the fiducial network changes from year to year, shifting the reference frame in such way as to create the appearance of motion. The magnitude of the inconsistency between two experiments depends on the spatial extent of the fiducial network and the relative accuracy of the station coordinates in it. As an example, *Larson* [1990] found inconsistencies of up to 7 mm between experiments in the first three years of TREX data. If it occurred, this problem would appear as a combination of a dilatation (due to a change in scale in the frame) and a rotation (due to a change in orientation). The dilatation is unlikely because the scale of the SV5 reference frame is demonstrably accurate to several parts in 10^8 [*Murray*, 1991], which implies a dilatational effect of less than 1 mm over the 50 km lines in the SMFTB network.

A rotation in the reference frame is not solely responsible for the motion because we observe strain and changes in length, both of which are invariant to rotation. The changes in distance to VNDN are significant at the level of 95% confidence for all the stations except GRAS (Figure 4.8). Since the strain rate tensor is also invariant to changes in frame [e.g., *Bibby*, 1982], the significance of the strain rates in Table 4.11 and Figure 4.10 increases our confidence in the velocities shown in Figure 4.9.

As seen in other analyses [*Freymuller and Kellog*, 1990; *Larson*, 1990; *Murray*, 1991], the velocity estimates are sensitive to the choice of reference frame. We can evaluate this effect in two ways. First, we vary the constraints themselves. The solution described in Table 4.7 constrains the *a priori* coordinates of Vandenberg, Westford, and Richmond to 10 mm in position and 1 mm/yr in velocity. Keeping the same stations, but loosening the constraints to 50 mm in position and 5 mm/yr has a negligible (0.2 mm/yr) effect on the velocities estimated in the Vandenberg footprint network. Nor does changing the *a priori* values of the station coordinates from the SV5 system to the SV6 system [*Murray*, 1991]. Similarly, changing the *a priori* values of the velocities from the values estimated from the VLBI solution [T. Herring, personal communication] to the SV6 velocities has a negligible (< 0.2 mm/yr) effect on the velocities estimated in the SMFTB.

Our velocity estimates in the SMFTB are also robust to changing the fiducial stations. Constraining Algonquin instead of Westford to 10 mm in position and 1 mm/yr in velocity makes a difference of only 0.2 mm/yr in the east component of MADC-VNDN. Even the extreme test of constraining only Vandenberg or Westford shifts the velocity by only 0.7 mm/yr. We conclude from these tests that our reference frame is accurate to better than 1 part in 10^8 , and therefore makes a millimeter contribution to the error budget of the short (< 80 km) lines in the SMFTB network.

The change which made the biggest difference was correcting an error in the tie between the two antennas used at Westford. The new tie yields a position for the Minimac antenna which is 92 mm to the north, 8 mm to the west, and 24 mm lower than the position obtained from the old tie. Considered with respect to a station ~ 4000 km away in California, the error is about 2 parts in 10^8 . Changing from the old tie (P8X in Figure 4.12) to the new tie shifts the velocity of MADC-VNDN by 1.5 mm/yr to the east and 1.2 mm/yr to the south, outside of the 95% confidence ellipse for our preferred solution, S3X. Such a magnitude is consistent with the roughly 2 mm/yr rate we would expect if the 75 km MADC-VNDN vector incurred a 2×10^{-8} fiducial error between two observations a year apart. It is not immediately clear, however, why a predominantly northward error effects the east component of velocity more than the north.

To verify that the resolution of integer phase ambiguities ("bias fixing") does not create the appearance of motion, we have performed another global analysis, using the "free bias" solutions from GAMIT. In these solutions, we estimate real-valued ambiguities, as described in step (5), above. As expected, the uncertainties in the east components of the estimated velocities are about three times larger for the "free bias" solution than for the "bias-fixed" solution. For example, the rate of change of the east component of the vector between MADC and VNDN (the longest vector in the Vandenberg footprint) is 7.1 ± 1.3 mm/yr in the "free bias" solution, larger than, but consistent with the "bias-fixed" estimate of 5.1 ± 0.6 mm/yr at the 95% confidence level (compare S3R to S3X in Figure 4.12).

As discussed above, our model for non-gravitational forces acting on the satellite is somewhat *ad hoc*, requiring the introduction of stochastic perturbations between days. To evaluate the sensitivity of the velocity estimates to the parameters of this model, we have performed a solution in which we tighten the daily Markov perturbation from 10 m to 1 m. The effect on the MADC-VNDN velocity vector is primarily in the east component, which is reduced by 0.5 mm/yr. Tightening the orbital constraints to 0.1 m reduces it by 1.9 mm/yr (estimates S11X and S10X in Figure 4.12). The

magnitude of the eastward velocity component is important for the tectonic interpretation. When projected onto the structural trend of $N30^{\circ}E$, 1 mm/yr of eastward motion yields 0.86 mm/yr of right-lateral motion and 0.5 mm/yr of compression. Because each of these two components has a very different consequence for the tectonic interpretation, we worry that the eastward components of the velocity estimates are particularly sensitive to the orbital constraints.

The constraints applied to earth orientation parameters have little impact on the velocity estimates. Varying the Markov perturbation by a factor of 10 (tighter or looser) changed the MADC-VNDN velocity by less than 0.1 mm/yr.

We conclude from these tests that our estimates of velocity are robust at the level of about 2 mm/yr to variations in the estimation procedure. In particular, the east component of the velocity seems to be vulnerable to changes in the reference frame, as imposed by the combination of the fiducial and orbital constraints. We are therefore more confident in the compressional components of the velocities in Figure 4.9 than in the right-lateral components.

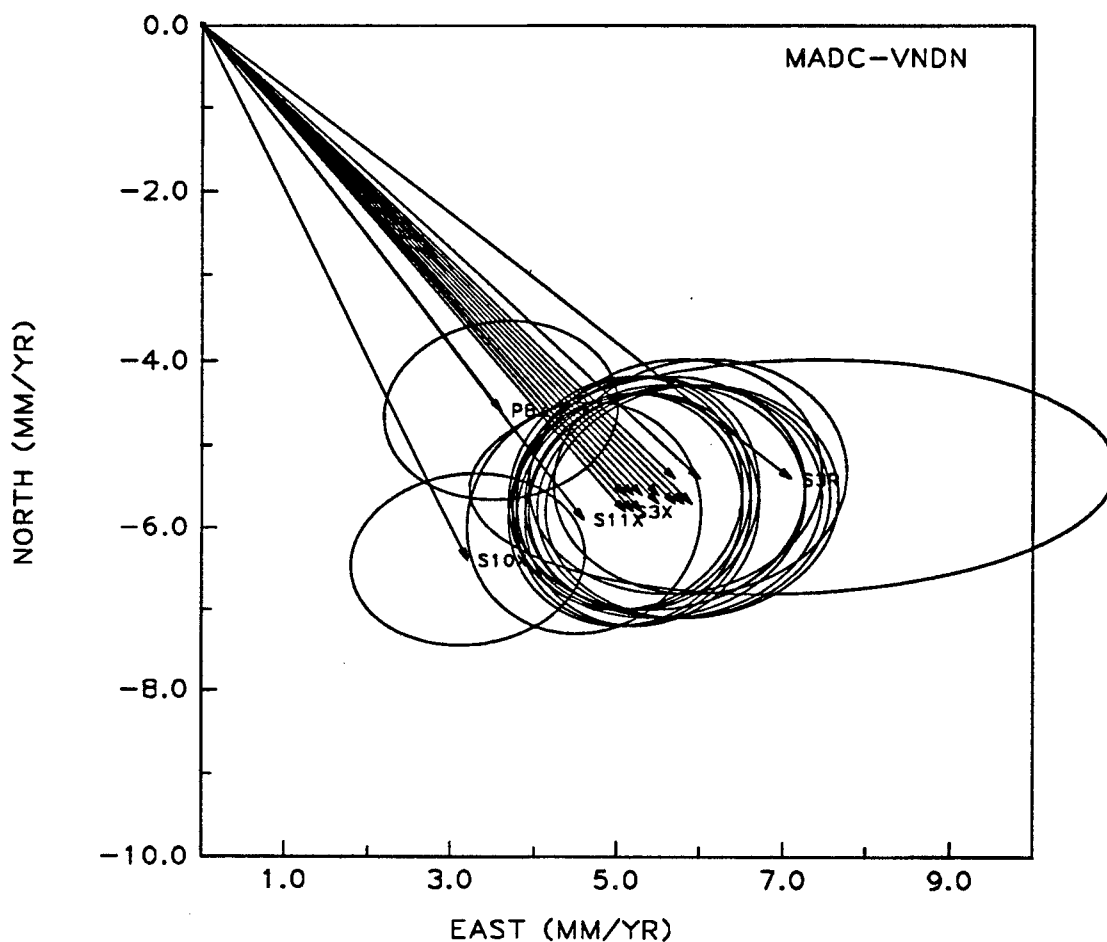


Figure 4.12. Velocity of MADC relative to VNDN as estimated from solutions with different constraints. Our preferred solution (the one we interpret) is labelled S3X. Other solutions include tightening the standard deviation of the random walk process which constrains the daily perturbations of the orbital parameters from the 10 m used in S3X to 1 m (S11X), and 0.1 m (S10X). Solution P8X was estimated using an incorrect value for the tie at Westford. Solution S3R (elongated ellipse) was generated without attempting to resolve integer ambiguities in phase. The ellipses denote the area of 95% confidence scaled by the $\sqrt{(\chi^2/f)}$ statistic for solution S3X.

Comparison with a Previous GPS estimate

We compare our estimate of the velocity of MADC relative to VNDN to a preliminary estimate performed by *Larson* [1990]. Using the GIPSY software package developed at JPL [e.g., *Lichten*, 1990a] to analyze three sets of GPS observations spanning 2.3 years, she estimates the velocity of MADC relative to VNDN to be 9 ± 1 mm/yr oriented at $S12^\circ E \pm 10^\circ$. As shown in Figure 4.13, her estimate is not consistent at the level of 95% confidence with ours, 7.7 ± 0.6 mm/yr at $S41^\circ E \pm 4^\circ$. The difference is more pronounced when expressed in terms of the two components, v_\perp and v_\parallel . Although the right lateral component v_\parallel is similar in the two estimates, (5.8 ± 1.4 mm/yr versus 7.3 ± 0.6 mm/yr), the amount of compression v_\perp is much smaller in our estimate (2.5 ± 0.6 mm/yr) than in *Larson's* (6.4 ± 1.2 mm/yr).

The inconsistency may be due to one of several differences between the analyses. The most obvious difference is that we include more data. Beyond the three surveys analyzed by *Larson* [1990], we include data from three more surveys conducted in March 1990, September 1990, and February, 1991. For comparison, we performed a solution on the 1987-1989 subset of data she analyzed. The estimated MADC-VNDN velocity is consistent with our 1987-1991 estimate, but is still significantly larger than *Larson's* [1990] in the east component. As described above, our estimate of the east component seems to be less robust than the north component.

The second difference between the analyses is that we explicitly estimate station velocities, rather than calculating them from the rate of change of individual vector components. This approach has the advantage of accounting for the (large) correlations between the estimated vector components and also yielding velocity vectors which satisfy the constraint of closure. In the case of the MADC-VNDN vector, however, the approaches yield similar results, as may be seen by comparing the slopes of the dashed and solid lines in Figure 4.8a.

The third difference is that our global solution avoids "fixing" different sets of fiducial stations. Otherwise, the shifting geometry of the fiducial network places the vectors in different reference frames during different experiments, introducing inconsistencies which can reach 7 mm [*Larson*, 1990]. It is possible that such a "fiducial error" and/or the problem with the tie at Westford is responsible for the different results.

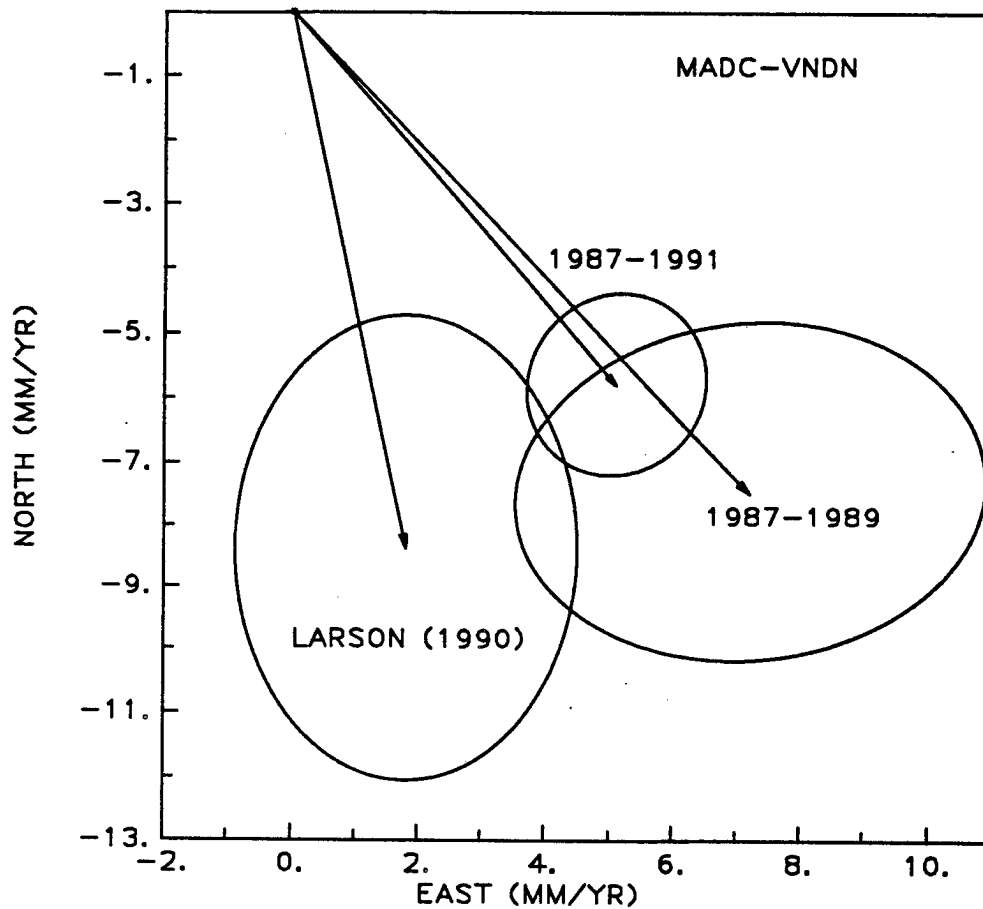


Figure 4.13. Comparison three estimates of the velocity of MADC relative to VNDN. Our preferred solution as discussed in the text (1987–1991), the result of *Larson* [1990] estimated from the GPS observations collected from 1987 through 1989, and our analysis of the same data set (1987–1989). The ellipses denote the area of 95% confidence (with two degrees of freedom) scaled by the $\sqrt{(\chi^2/f)}$ statistic for each solution. The 95% confidence area of *Larson* [1990] has not been scaled by her χ^2/f statistic, which is 0.8 in the east component and 2.0 in the north. Her estimation procedure assumes the east and north components to be uncorrelated.

Comparison with our Previous Result

Our GPS-derived estimate of the strain rate in the SMFTB is smaller than the rates estimated from two different analyses of the historical survey data [Feigl *et al.*, 1990; Shen, 1991]. The compressive eigenvalue $\dot{\epsilon}_2$ of the strain rate tensor estimated from the GPS data is about 3 times smaller than the values estimated from the 1879-1987 data (Figure 4.10a,b,c and Table 4.10). The general N-S orientation of the compressive eigenvector is qualitatively, although not statistically, consistent with the 1879-1987 estimates. The strain rates estimated from the GPS-derived velocities in the triangular subnetworks are larger than the average value for the whole SFMTB, but are still about a factor of 2 smaller than the values estimated from the historical data (Figure 4.10d and Table 4.10).

We can also compare the results from the two data sets in terms of the integrated deformation rate across the SMFTB. In Figure 4.14, we compare the motion of TEPW and MADC with respect to VNDN. The motion of TEPW has been calculated indirectly from the strain rate estimated from the 1879-1987 dataset, assuming that the strain is uniform throughout the SMFTB and that there is no net rotation (Chapter 3). The motion of MADC, however, is a velocity estimated directly from the GPS data. The velocity vectors TEPW-VNDN and MADC-VNDN are not consistent at the level of 95% confidence. The compressive component v_{\perp} estimated for TEPW-VNDN from the 1879-1987 data set is 6 ± 2 mm/yr, much larger than the value of 2.5 ± 0.6 mm/yr estimated from the GPS data. The right-lateral component v_{\parallel} of the motion relative to VNDN is also different between the two estimates. The GPS estimate finds v_{\parallel} at MADC to be 7.3 ± 0.6 mm/yr, while the 1879-1987 data set yields an estimate for TEPW of 3 ± 1 mm/yr, subject to the assumption of no net rotation.

The difference between the two vector velocities could be because (1) the estimation procedures and data sets are not comparable, (2) there is relative motion between TEPW and MADC, (3) the assumption of no net rotation is incorrect, (4) the assumption of uniform strain is not valid, or (5) unmodeled orbital effects introduce an apparent rotation.

We have little reason to doubt the procedure we used to estimate a strain rate from the 1879-1987 data set [Feigl *et al.*, 1990]. The result has been reproduced by Shen [1991]. His data set included the same 1879-1959 triangulation data from the REDEAM project [Snay *et al.*, 1987] and 1986-1987 GPS observations that we use in Chapter 3. He does not, however, include the DMA trilateration measurements from the 1971 and 1985 surveys, which we have found to be important in our analysis.

Applying a rigid block model as prior information, *Shen* [1991] estimates the strain rate in the quadrilateral formed by ARGU (5 km NE of VNDN), GAVI, LOSP and TEPW (Figure 4.10b). His estimate of the strain rate tensor is insignificantly different from ours in magnitude, but slightly (14°) different from ours in orientation (Table 4.8). The similarity of the estimates, despite the differences in inversion techniques and data sets, increases our confidence in them.

The possibility of deformation between stations MADC and TEPW seems unlikely. They are both located in the San Rafael Mountains, about 20 km apart, and do not appear to be separated by any active faults or folds [*Namson and Davis*, 1990]. The difference in their motions with respect to VNDN (Figure 4.14) would suggest extension between TEPW and MADC, a notion which does not seem tectonically reasonable. Local instability at MADC could possibly be a problem, because the benchmark is not set in bedrock, but we have not observed any cracking or slumping of the soil around the concrete monument.

We consider the possibility that the difference in the motions of TEPW and MADC is due to rotation. To calculate the TEPW-VNDN velocity vector from the strain rates estimated from the 1879-1987 data, we assumed that the SMFTB undergoes no net rotation, an assertion which is contradicted by the rotation rates shown in Figure 4.11. As previously noted, however, a clockwise rotation would increase the right-lateral component of the TEPW-VNDN velocity. It would not explain the difference in the compressive components of the TEPW-VNDN and MADC-VNDN velocities. To illustrate this point, we applied the average clockwise rotation rate (8×10^{-8} rad/yr) estimated from the 1986-1991 GPS to TEPW with respect to VNDN. The rotation adds 3.1 mm/yr at $S45E^\circ$ to yield the total vector shown as TEPW + R in Figure 4.14. Including the rotation increases the right-lateral component v_{\parallel} of the TEPW-VNDN velocity from 3 ± 1 mm/yr to 7.2 ± 1.2 mm/yr, in good agreement with the value of 7.3 ± 0.6 mm/yr estimated for MADC-VNDN. In contrast, the rotation adds 0.8 mm/yr of compression, to give a value of $v_{\perp} = 6.9 \pm 1.6$ mm/yr which is larger than the 2.5 ± 0.6 mm/yr rate observed for MADC-VNDN.

The other assumption made in estimating the strain rate from the 1879-1987 data set is that strain is constant in space, *i.e.*, uniform throughout the SMFTB. This assumption may not be appropriate, because the four triangular subnetworks yield different estimates of the strain rate tensor (Figure 4.10d and Table 4.10). In the southwest corner of the network, the compression trends NE and is faster than in the northeast half of the network, where it has a more northerly orientation, near $N10^\circ W$. Since many of the observations in the 1879-1987 data set involve stations on

Vandenberg Air Force Base, in the southwest half of the network, the assumption of uniform strain may have led to an overestimate of the deformation rate across the SFMTB in Chapter 3.

Finally, it is possible that the rotations apparent in the velocity field are due to unmodeled orbital effects. As described above, the eastward component of vectors in the SMFTB seem to be particularly sensitive to the level of constraints applied to the orbital parameters. It may be that a more realistic, tighter constraint on the orbits will yield velocities with smaller eastward velocity components with respect to VNDN. For the stations in the SMFTB, decreasing the east component would shrink the amount of right-lateral motion represented by v_{\parallel} while increasing the amount of compression represented by v_{\perp} .

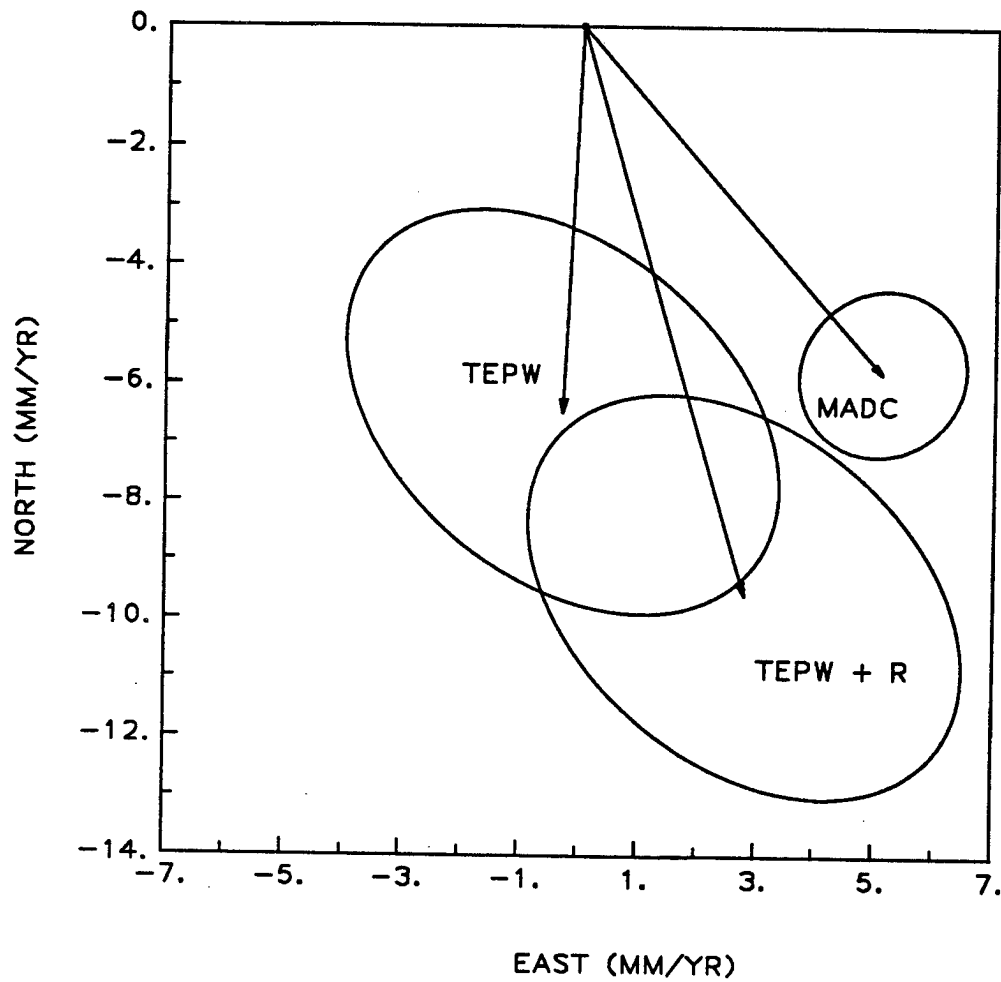


Figure 4.14. Comparison of velocity of TEPW and MADC relative to VNDN. The value for MADC is estimated from the 1986-1991 GPS data. The value for TEPW is based on integrating the average strain rate estimated from the 1879-1987 data set in *Feigl et al.* [1990] under the assumption of no net rotation. Applying the clockwise rotation rate estimated from the 1986-1991 GPS data (81 ± 8 nanoradian/yr) yields a faster velocity (TEPW+R).

Is the Motion Tectonic?

We have argued that the relative motion of the stations is real, but we must now prove that it is tectonic, and not just due to local movement of the benchmarks. Unfortunately, because only the mark at LOSP is anchored to bedrock, our evidence is necessarily circumstantial. We note that the motion of all the stations appears to be consistent with compressive tectonics; no stations are moving away from VNDN, for example.

If local motion were a problem, we would expect it to be aggravated by rainfall, as has been observed for a few monuments at Parkfield [Langbein *et al.*, 1990]. Since the period of our observations coincides with a major drought in California, the measurements were consistently performed under dry conditions. The only exception is the observations performed in the winter of 1986–87, which do not appear to be anomalous (at the level of 5 mm) in Figure 4.8.

Subsidence due to oil withdraw could be a problem at station GRAS, which is located in the Lompoc Oil Field [Crawford, 1971; MacKinnon, 1989]. Quantifying the possible rate of motion must rely on anecdotal experience from surveys in other oil fields. An extreme case occurred in Long Beach, where 5.97 m of subsidence has been documented in the 22 years between 1932 and 1954 [Cline *et al.*, 1984]. The high (270 mm/yr) rate of motion was apparently not confined to the vertical direction, because one station was displaced horizontally by 674 mm in the 28 years between 1933 and 1961, or 24 mm/yr, assuming a constant rate [Cline *et al.*, 1984]. A less severe case has been documented in the Ventura Basin, which is probably similar in size and productivity to the Lompoc field. In the Ventura field, one station underwent 277 mm of differential subsidence between 1934 and 1968 [Buchanan–Banks *et al.*, 1975]. The subsidence was arrested when water was pumped into the wells, to replace the withdrawn oil beginning in 1958. Comparison of the 1960 and 1968 leveling indicates only about 20 mm of subsidence, for a more modest rate of less than 3 mm/yr. Since water is also pumped into the wells in the Lompoc field beneath station GRAS [Greg Yvarra, Unocal geologist, personal communication, 1991], we do not expect large (> 5 mm/yr) horizontal signals due to oil withdrawal.

The observed motion of GRAS with respect to VNDN is 15.5 ± 3.5 mm/yr *upward*. This result cannot be explained by oil withdrawal alone. It might be the result of the volume of water pumped into the well exceeding the volume of oil withdrawn, but uplift due to ongoing anticlinal folding is also a possible explanation.

Strain Accumulation on the Locked San Andreas Fault

The right-lateral motion apparent in Figure 4.9 includes a small amount of motion due to strain accumulation on the San Andreas Fault, which is approximately 30 km NE of MADC, the station in our network nearest to the fault. To estimate the effect of the San Andreas on our network, we use the model of the fault estimated by *Eberhardt-Phillips et al.* [1990]. As parameterized in Table 4.12, it models the San Andreas as three segments locked to 25 km depth, but slipping at 30 mm/yr below that depth. North of the Big Bend, we assume a 750 km segment striking N40°W. South of the bend, in the Western Transverse Ranges, we assume a 100 km segment striking N73°W, turning southward to strike N63°W for 300 km to the Salton Sea. The displacements due to dislocations in this geometry are calculated using the expressions of *Okada* [1985], in a program written by A. Donnellan [personal communications, 1990–1991].

The resulting displacements are small (Table 4.13a). The largest rate is for the longest vector from the station nearest the fault, namely MADC–VNDN, for which the fault model predicts 2 mm/yr east and 1 mm/yr south. Most of this motion is right-lateral shear, shown as $v_{\parallel} = 2.4$ mm/yr, while the compressive component v_{\perp} is only 0.1 mm/yr. These small rates are consistent with our intuition that the most effect of the locked fault dies off beyond about one locking depth (25 km) from the fault.

Table 4.12. Modeled fault geometry

TABLE 4.12. Modeled Fault Geometry

Fault	Latitude of origin	Longitude of origin	Strike d , km	Depth δ	U_1 , mm c	U_2 , mm c	U_3 , mm c	L , km	W , km
Purissima-Solomon thrust ^a	34.70°N	120.70°W	100°	8	25°	0	4	0	30
Point San Luis thrust ^a	34.85°N	120.00°W	310°	13	25°	0	4	0	30
San Andreas N of Big Bend ^b	34.90°N	119.40°W	140°	10000	90°	30	0	0	9975
San Andreas in Big Bend ^b	34.90°N	119.40°W	287°	10000	90°	30	0	0	9975
San Andreas SE of Big Bend ^b	34.70°N	118.40°W	297°	10000	90°	30	0	0	9975

Notes:

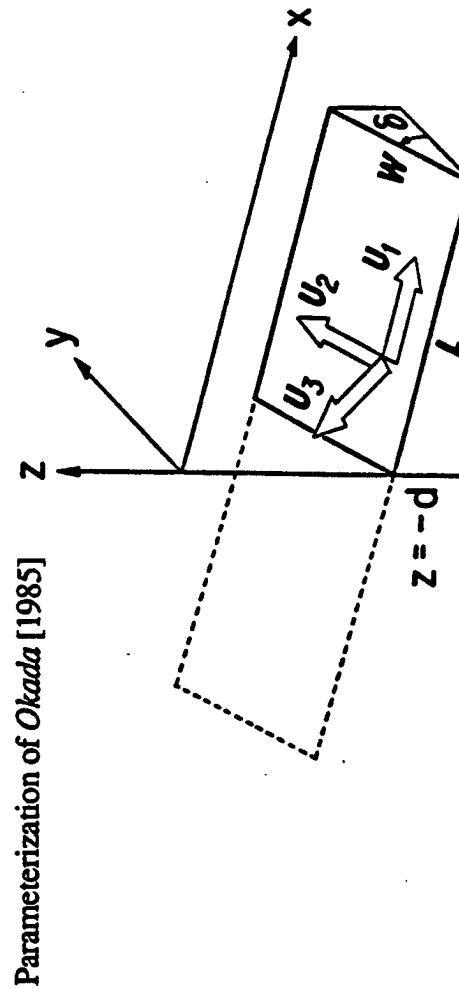
^a After *Namson and Davis* [1990].^b Model D of *Eberhardt-Phillips et al.* [1990].^c Modeled as the displacement of the hanging wall block relative to the foot wall block accumulated in one year.

Table 4.13. Velocities relative to VNDN calculated for modeled faults

a. due to deep slip on the San Andreas fault system

Station	East mm/yr	North mm/yr
GAVI	-0.5	-0.3
GRAS	0.2	0.06
LOSP	0.4	0.2
MADC	2.0	-1.3
TEPW	0.8	-0.3

b. due to slip two thrust faults in the SMFTB

Station	East mm/yr	North mm/yr
GAVI	-0.4	-0.3
GRAS	0.4	1.8
LOSP	-0.4	-2.9
MADC	-1.2	-2.0
TEPW	-1.6	-3.3

c. due to deep slip on San Andreas fault system plus
slip on two thrust faults in SMFTB

Station	East mm/yr	North mm/yr
GAVI	-0.9	-0.6
GRAS	0.6	1.9
LOSP	0.03	-2.8
MADC	0.8	-3.3
TEPW	-0.8	-3.7

TECTONIC INTERPRETATION

Deformation in a Fold and Thrust Belt

The model of *Namson and Davis* [1990] for deformation in the Santa Maria Fold and Thrust Belt predicts the relative motions of our geodetic stations. In particular, several of the stations lie on the axes of anticlines identified as actively deforming in their cross sections. Station GRAS lies on the axis of the Lompoc–Purisima anticline, ALAM on the Orcutt anticline, and LOSP on the Casmalia anticline. Stations GAVI and VNDN are both situated in the Santa Ynez range, which *Nitchman et al.* [1989] have likened to one side of a vise "squeezing" the SMFTB. The other side of the vise is the San Rafael range, containing stations LIND, TEPW, and MADC.

Using the kinematic model sketched in Figure 12 of *Namson and Davis* [1990], we interpret the motion of GRAS with respect to MADC as shortening on the Point San Luis Anticline (Figure 4.15a). Projecting our estimate of the MADC–GRAS velocity vector onto the N30°E trend of their transect, we find 1.1 ± 1.0 mm/yr of convergence, somewhat less than the 2.3–4.6 mm/yr predicted by the balanced cross section, which places 9.2 km of slip on the Point San Luis Thrust in the last 2–4 Myr [Table 1, *Namson and Davis*, 1990]. Most of the observed MADC–GRAS velocity, however, is not convergence, but right-lateral shear along an axis striking S60°E. We estimate 6.6 ± 1.2 mm/yr of such motion, of which about 2.2 mm/yr can be explained by strain accumulation on the San Andreas fault (Table 4.13a).

We interpret the motion between GRAS and VNDN as folding due to slip on the Purisima–Solomon Thrust (Figure 4.15b). This thrust fault lies under the Lompoc–Purisima Anticline on whose crest station GRAS is located. We measure 1.3 ± 0.7 mm/yr of convergence between GRAS and VNDN along the N30°E trend, which agrees quite well with the 1.5–3.2 mm/yr rate estimated from 5.8–6.4 km of slip on the thrust during the last 2–4 Myr [*Namson and Davis*, 1990]. In addition, we measure an insignificant amount (0.7 ± 1.0 mm/yr) of right-lateral motion along a line striking N60°W.

The idea that compression is accommodated in the folds is supported by the orientations of principal stresses inferred from borehole breakout data [*Hansen and Mount*, 1989]. Most of their data indicate that the minimum horizontal stress is parallel to the axes of the Casmalia and Lompoc–Purisima anticlines, (Figure 4.17). We

assume that the folds form in response to compression normal to their axes, or on a NE-SW trend.

Although the seismicity shown in Figure 4.16 suggests a clustering of epicenters near the Casmalia-Orcutt thrust, the small magnitudes ($M_L < 4$) indicate that much of the observed deformation must be occurring aseismically. We have modeled the motions expected from creep on the thrusts described by *Namson and Davis* [1990]. To use the same dislocation theory described above for the San Andreas, [*Okada*, 1985; A. Donnellan, personal communication], we assume the simplest possible geometry of two thrust faults, shown schematically in Figure 4.18.

We approximate the Purisima-Solomon thrust as a rectangular surface striking N80°W, with dimensions 50 km wide by 30 km long, as suggested by the cross-section of *Namson and Davis* [1990] reproduced in Figure 4.15b. We assume the fault slips 4 mm/yr, somewhat faster than the values of 1.6–3.2 mm/yr or 1.5–2.9 mm/yr they estimate. We note, however, that dislocation on a planar fault is a poor model for deformation by folding. For example, although the folding between stations GRAS and VNDN produces convergence between them, our oversimplified fault model places them on the same side of the thrust fault, a geometry which leads to slight extension between the two stations.

The other fault, the Point San Luis Thrust, dips 25° in the opposite direction, toward the northeast. We take it to be a rectangular surface 50 km long by 30 km wide, whose upper edge is 6 km below the crest of the Point San Luis Anticline, as shown in the cross section of *Namson and Davis* [1990] reproduced in Figure 4.15a. We assume a slip rate of 4 mm/yr, at the high end of their estimates of 2.5–4.9 or 2.3–4.6 mm/yr.

In addition, we add the 3-segment model of the San Andreas fault estimated by *Eberhardt-Phillips* [1990] as described above. The final model includes five rectangular fault segments and predicts the station velocities shown in Figure 4.19. The predicted velocities are not in good agreement with the observed velocities in Figure 4.9. Although the observed and predicted velocities lie in the same compass quadrant for three of the four stations, they have different tectonic decompositions. In the following discussion, we consider the components v_{\perp} and v_{\parallel} separately, reckoning all velocities with respect to VNDN.

The observed compressional components v_{\perp} of the observed and modeled velocities are in reasonable agreement. The values are consistent at the 95% confidence level for stations MADC, TEPW and GAVI, supporting our compressive model. The motion of GAVI is S29°W \pm 17°, entirely in the compressive v_{\perp} component. Since GAVI is separated from VNDN by both the north and south branches of the Santa Ynez fault,

one might use the GAVI-VNDN velocity to argue that these faults are active, a notion contradicted by the lack of observed Holocene movements [Sylvester and Darrow, 1979; Clark *et al.*, 1984]. At station LOSP, the observed rate of compression is smaller than the value predicted from the fault model. Contrary to the observed velocity, GRAS is predicted to diverge from VNDN, because the two stations lie on the same side of the modeled Purisima-Solomon fault, as described above. A more complete model for the deformation in the SMFTB would include the effects of folding in addition to faulting.

The observed right-lateral component $v_{||}$ is roughly twice as large as the modeled values at all the stations. This misfit could be due to unmodeled orbital effects corrupting the eastward components of the estimated velocities. It might also be due to unmodeled dextral shear across the SMFTB. At this point, we can only speculate about which of these two competing hypotheses is valid. If the large right-lateral components in the observed velocities are really tectonic, they could arise from unmodeled motion on a strike-slip fault within the SMFTB or strain accumulation on either the San Andreas or Hosgri fault system.

Right-lateral strike slip activity within the SMFTB seems unlikely. The focal mechanisms shown in Figure 3.11 are mostly thrust events, not strike-slip. Most of the right-lateral faults mapped by Hall [1982] are not active in the Quaternary [Clark *et al.*, 1984; Manson, 1985]. If rates of order 5 mm/yr were occurring as strike-slip motion, we would expect to observe some surface expression.

For the effects of the San Andreas to exceed the rates predicted by the simple dislocation model, the fault would have to be locked to a depth greater than 25 km, or perhaps exhibit complex time-dependent behavior as suggested by Li and Rice [1987]. The strike-slip activity of the Hosgri fault in the Quaternary is difficult to quantify because the trace lies offshore [Tuttle, 1985; Clark *et al.*, 1991]. If it is locked like the San Andreas, the accumulating strain will create right lateral shear similar to that in Figure 4.9, especially the increase in $v_{||}$ between LOSP and MADC. We concur with Nitchman *et al.* [1989] that right-lateral motion on the Hosgri is necessarily related to NNE-directed compression in the SMFTB. Without such motion, we would expect the N60°W trend of the onshore folds to continue westward of the Hosgri trace, contradicting the available seismic and bathymetric observations [McIntosh *et al.*, 1991].

Activity on the Hosgri fault has been suggested on the basis of the San Andreas discrepancy argument by Minster and Jordan [1984; 1987]. In their model, at geologic time scales, shear across the transform plate boundary is concentrated on a few,

widely-spaced fault systems, such as the San Andreas and the Hosgri. At geodetic time scales, however, the faults are locked, and we observe broadly distributed "megashear". The uncertainties and possible eastward bias of the GPS-derived velocity estimates do not allow us to place hard constraints on such a model.

Rotations

The rotation rates shown in Figure 4.11 indicate that the SMFTB is rotating clockwise with respect to North America at 2–5°/Myr, comparable to the approximately 5°/Myr rate that from paleomagnetic declinations for the western Santa Ynez range [Hornafius, 1985; Hornafius *et al.*, 1986]. Yet the same geodetic caveats we applied to the right-lateral compression apply to the apparent clockwise rotations. Both are vulnerable to the weakly-determined eastward component of the estimated velocities.

An important observation of the paleomagnetic studies is that the Santa Maria Basin has not undergone significant rotation since the early Miocene, while the Santa Ynez range has been rotating clockwise with respect to magnetic North. The differential rotation has led Hornafius *et al.* [1985] to argue for significant left-lateral strike-slip displacement on the Santa Ynez River fault. Although there is structural evidence for movement in this sense, active faulting in the Holocene has not been established [Sylvester and Darrow, 1979].

If the Santa Ynez River fault is currently accommodating left-lateral motion, it should appear in vectors crossing the fault. The eastward components of the LOSP-VNDN, MADC-VNDN and MADC-GAVI velocities are all positive, indicative of right-lateral motion. We prefer, therefore, a tectonic model in which the Santa Ynez River fault is not active in the Holocene. Such a model has the consequence of pushing the left-lateral strike-slip due to differential rotation further south, into the Santa Barbara Channel. There, a left-lateral sense of motion is required by Sauber's [1989] VLBI estimate of VNDN with respect to JPL in Pasadena, as interpreted by Jackson and Molnar [1990].

CONCLUSIONS

We have used 5 years of GPS measurements to measure the velocities of five stations in the Santa Maria Fold and Thrust Belt. The velocities indicate the importance of N-S compressional deformation in the area, as indicated by geologic cross sections, seismicity, earthquake focal mechanisms and borehole breakout data. The compressional components of four of five of the velocities are grossly consistent with

the deformation predicted by a simple dislocation model involving two thrust faults in the SMFTB, in addition to deep slip on the San Andreas fault. The amount of right-lateral motion is larger than expected from either the fault model or the estimate from the 1879-1987 data set. The right-lateral motions are compatible with clockwise rotation.

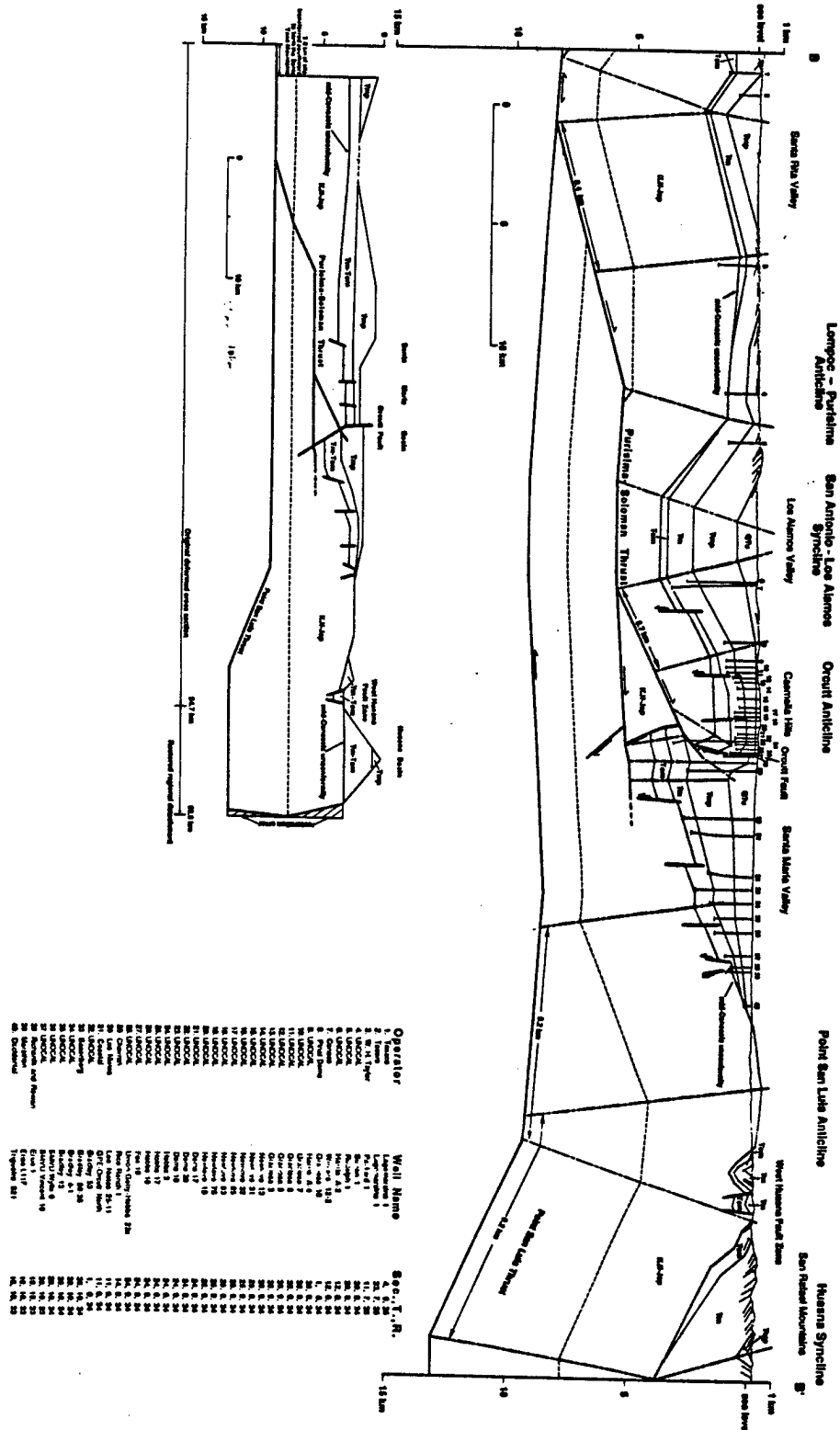


Figure 4.15a. Balanced cross section for the transect between points B and B' shown in Figure 4.1. This section, reproduced from *Namson and Davis* [1990], indicates 2.3–4.6 mm/yr of shortening. Station TEPW is located above the Point San Luis Thrust in the San Rafael Mountains.

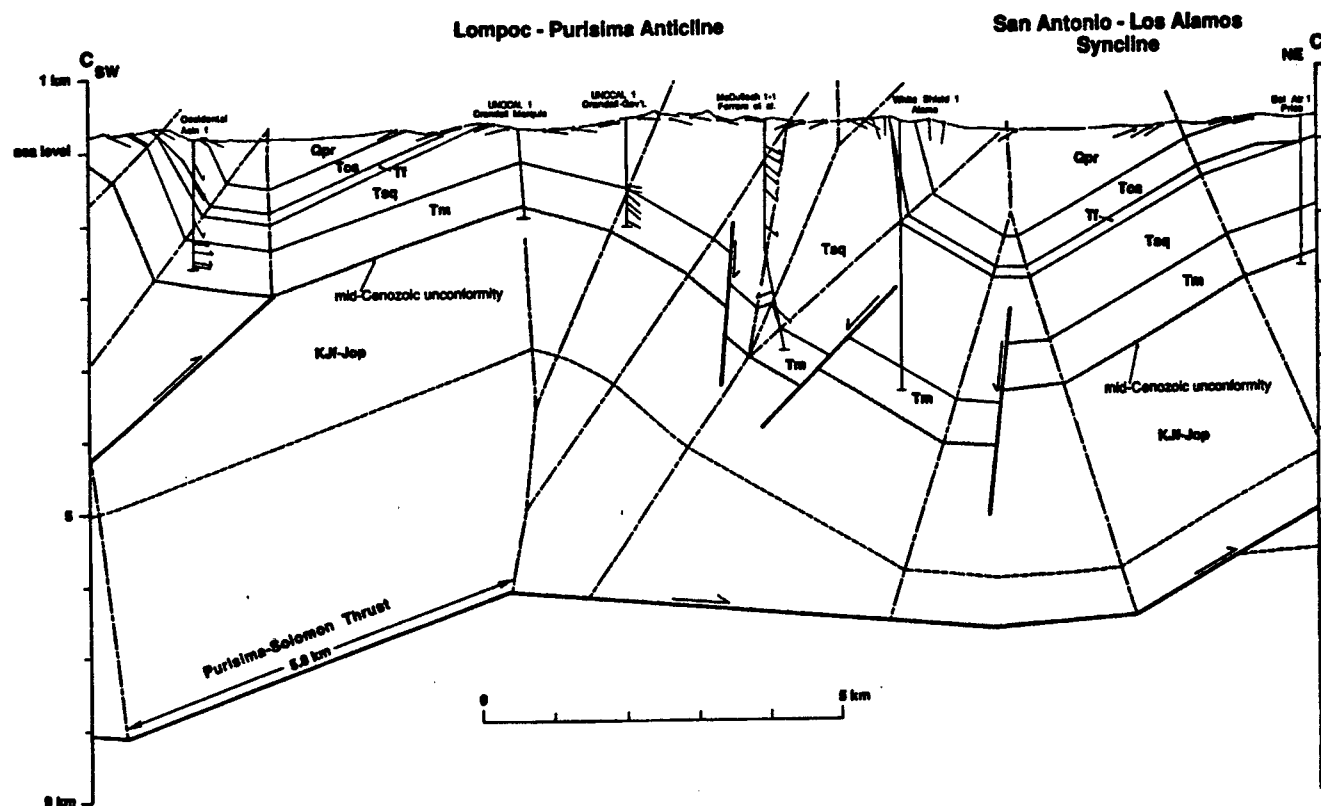


Figure 4.15b. Balanced cross section for the transect between points C and C' shown in Figure 4.1. This section, reproduced from *Namson and Davis* [1990], indicates 1.5–2.9 mm/yr of shortening. Station GRAS is located on the axis of the Lompoc-Purisima Anticline.

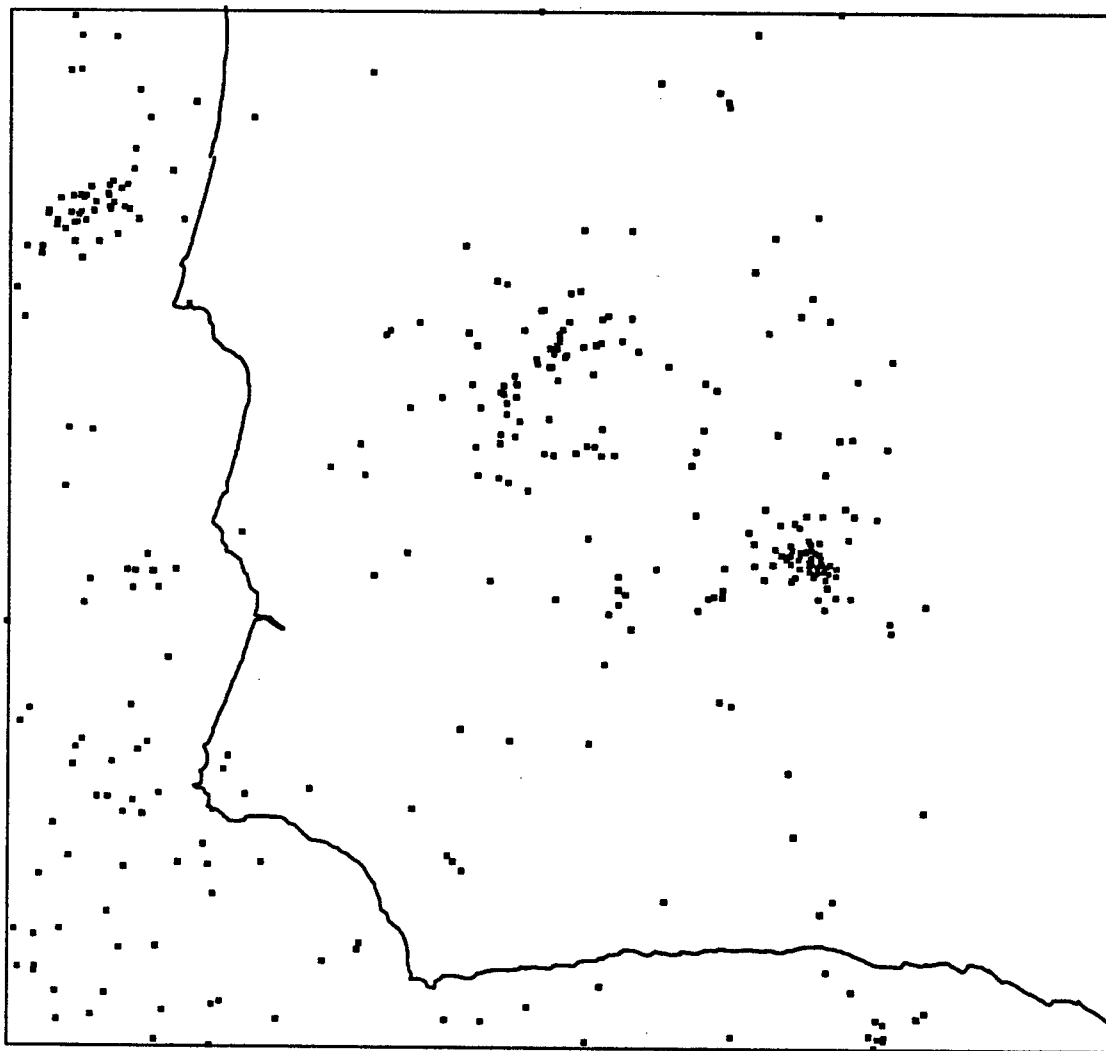


Figure 4.16 Seismicity between 1973 and 1988. Since the nearest station to most of these events is typically 15 km away, these locations are poorly determined. Note the suggestion of a cluster of events near the Orcutt Anticline. The plotted events are a geographic subset of those in Figures 2-26 and 2-27 of *Pacific Gas and Electric* [1988], culled from the USGS and Caltech catalogs by Marcia McLaren [personal communication, 1990]. All of the events have magnitude $M_L < 4$.

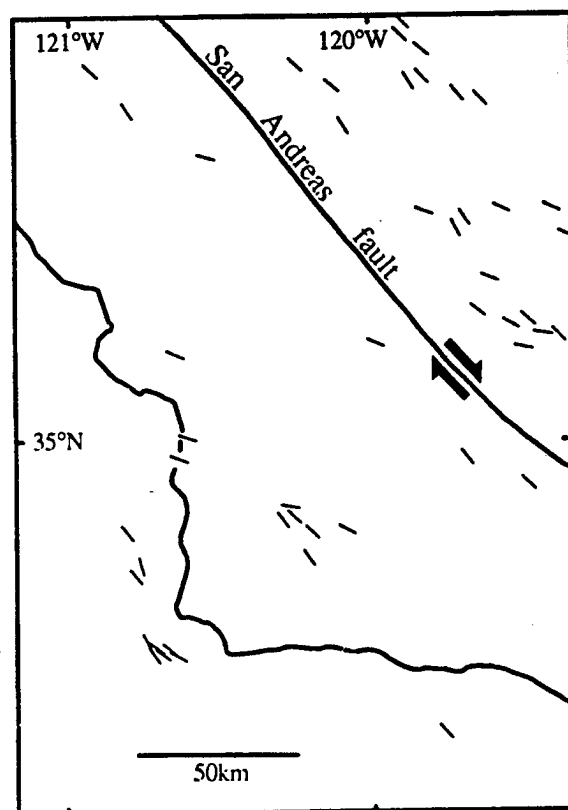


Figure 4.17. Minimum horizontal stress direction inferred from borehole elongation directions. Note that these are perpendicular to the compressive principal axis of strain estimated from the historical geodetic data. Figure published in *Hansen and Mount* [1990], breakout data from V. S. Mount, manuscript in preparation, 1989.

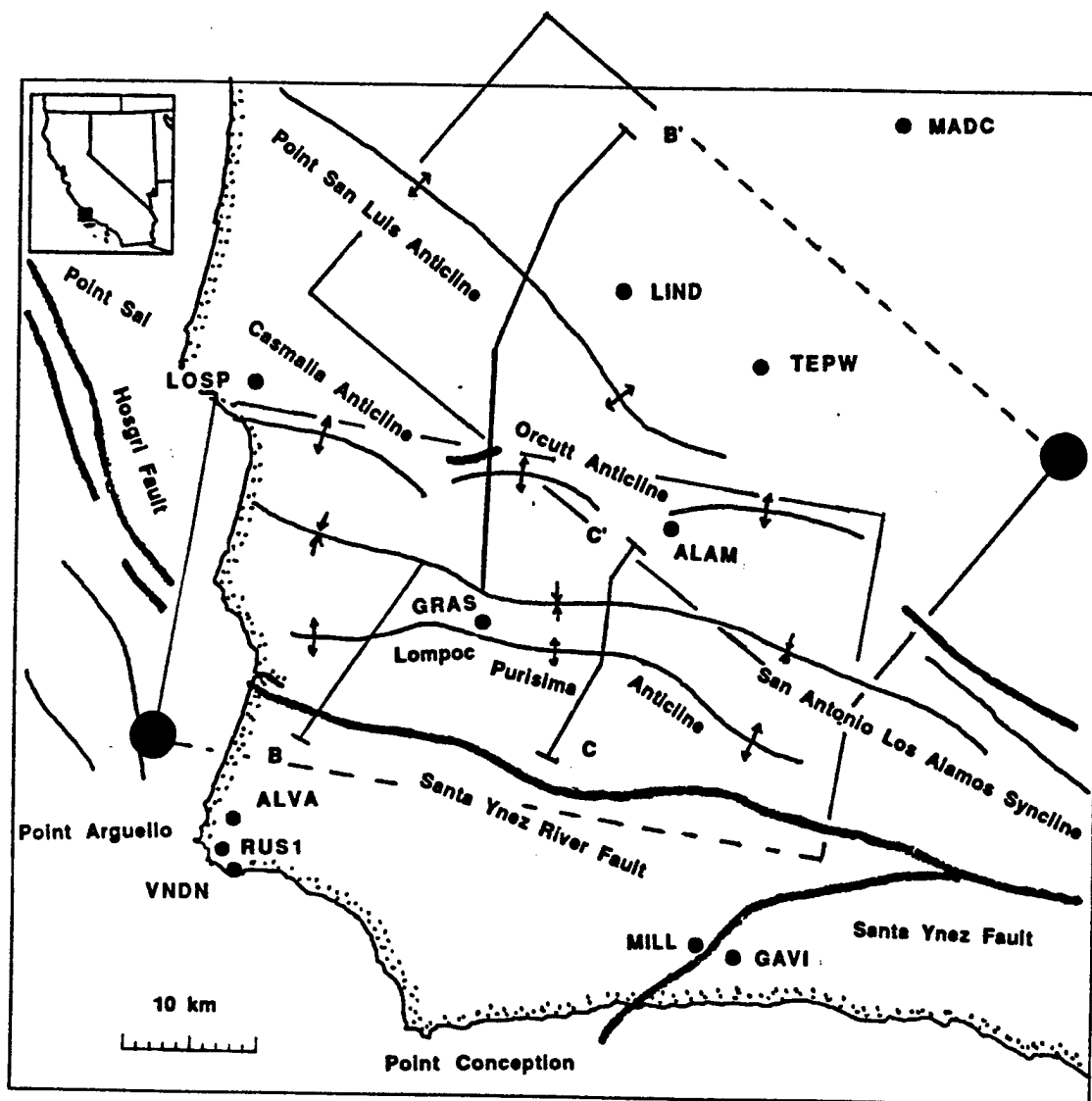


Figure 4.18. Fault geometry for dislocation modeling. The two faults are the Point San Luis thrust (in the north) and the Purisima-Solomon thrust (in the south), after *Namson and Davis* [1990]. The rectangles are the projection fault surfaces onto the Earth's surface, with the large dot denoting the origin in the parameterization of *Okada* [1985]. The dashed lines denote the lower edges of the faults.

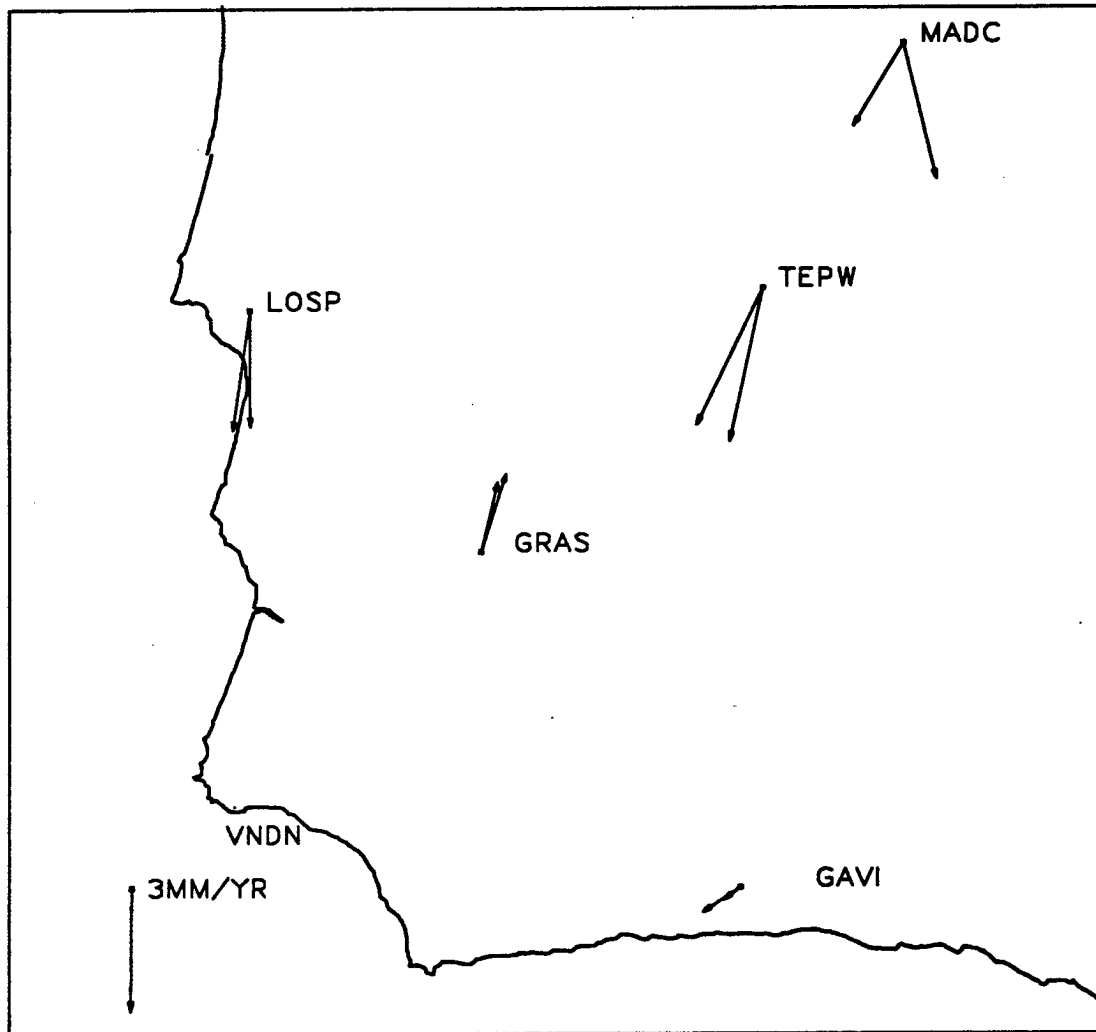


Figure 4.19. Velocities relative to VNDN as predicted by dislocation modeling. The smaller, more westerly arrows are the velocities predicted from slip on the two thrust faults in the SMFTB shown in Figure 4.17. The longer, more easterly arrows include motion due to the two faults in the SMFTB plus the San Andreas fault as modeled by *Eberhardt-Phillips et al.* [1990].

REFERENCES CITED

- Abers, G., and R. McCaffrey, Active deformation in the New Guinea fold-and-thrust belt: seismological evidence for strike-slip faulting and basement-involved thrusting, *J. Geophys. Res.*, **93**, 13,332-13,354, 1988.
- Agnew, D. C., Y. Bock, T. H. Jordan, R. W. King, T. H. Dixon, B. H. Hager, D. D. Jackson, W. H. Prescott, J. L. Stowell, B. E. Schutz, and W. E. Strange, GPS measurements in central and southern California (abstract), *Eos Trans. Amer. Geophys. Un.*, **68**, 282, 1987.
- Aki K., and P. G. Richards, *Quantitative Seismology*, 932 pp., W. H. Freeman, New York, 1980.
- Allan, D. W., Statistics of atomic frequency standards, *Proc. IEEE*, **54**, 221-230, 1966.
- Allan, D. W., Time and frequency (time-domain) characterization, estimation, and prediction of precision clocks and oscillators, in *IEEE Trans. on Ultrasonics, Ferroelectrics and Frequency Control, UFFC-34*, pp. 647-654, 647-654, 1987. Reprinted in D.B., Sullivan et al., *Characterization of Clocks and Oscillators, NIST Tech. Note 1337*, Natl. Inst. Stand., 1990.
- Argus, D. F., and R. G. Gordon, Sierra Nevada-North America motion from VLBI and paleomagnetic data: Implications for the kinematics of the Basin and Range, Colorado Plateau, and California Coast Ranges (abstract), *Eos Trans. Amer. Geophys. Un.*, **69**, 1418, 1988.
- Argus, D. F., and R. G. Gordon, Pacific-North American plate motion from very long baseline interferometry compared with motion inferred from magnetic anomalies, transform faults, and earthquake slip vectors, *J. Geophys. Res.*, **95**, 17,315-17,324, 1990.
- Argus, D. F., and R. G. Gordon, Relation between current Sierra Nevada-North America motion and the direction of maximum Great Basin extension, *Geology*, in press, 1991.
- Atwater, T., Implications of plate tectonics for the Cenozoic evolution of western North America, *Bull. Geol. Soc. Amer.*, **81**, 3513-3536, 1970.
- Barr, T. D., and F. A. Dahlen, Brittle frictional mountain building 2. Thermal structure and heat budget, *J. Geophys. Res.*, **1989**, 3923-3947, 1989.

- Barr, T. D., and F. A. Dahlen, Constraints on friction and stress in the Taiwan fold-and-thrust belt from heat flow and geochronology, *Geology*, 18, 111-115, 1990.
- Barr, T. D., F. A. Dahlen, and D. C. McPhail, Brittle frictional mountain building, 3. Low-grade metamorphism, *J. Geophys. Res.*, 96, 10,319-10,338, 1991.
- Beal, C. H., The earthquake at Los Alamos, Santa Barbara county, California, January 11, 1915, *Bull. Seismol. Soc. Am.*, 5, 14-25, 1915.
- Beck, M. E. Jr., On the mechanism of tectonic transport in zones of oblique subduction, *Tectonophysics*, 93, 1-11, 1983.
- Beck, M. E. Jr., Model for late Mesozoic-Early Tertiary tectonics of coastal California and speculations on the origins of the San Andreas fault, *Tectonics*, 5, 49-64, 1986.
- Bell, L. Preparatory field reconnaissance for site stability surveys around the Vandenberg VLBI site, Vandenberg Air Force Base, Lompoc California, report to the NASA Crustal Dynamics Project, January 22, 1991.
- Bibby, H. M., Unbiased estimate of strain from triangulation data using the method of simultaneous reduction, *Tectonophysics*, 82, 161-174, 1982.
- Bilham, R., Earthquakes and sea level: space and terrestrial metrology on a changing planet, *Rev. Geophys.*, 29, 1-30, 1991.
- Billiris, H., D. Paradissis, G. Veis, P. England, W. Featherstone, B. Parsons, P. Cross, P. Rands, M. Rayson, P. Sellers, V. Ashkenazi, M. Davison, J. Jackson, and N. Ambraseys, Geodetic determination of tectonic deformation in central Greece from 1900 to 1988, *Nature*, 350, 124-129, 1991.
- Bird, P., and R. W. Rosenstock, Kinematics of present crust and mantle flow in southern California, *Geol. Soc. Am. Bull.*, 95, 946-957, 1984.
- Blewitt, G., Carrier phase ambiguity resolution for the Global Positioning System applied to geodetic baselines up to 2000 km, *J. Geophys. Res.*, 94, 10,187-10,203, 1989.
- Blewitt, G., An automatic editing algorithm for GPS data, *Geophys. Res. Lett.*, 17, 199-202, 1990.
- Bock, Y., and S. Shimada, Continuously monitoring GPS networks for deformation measurements, *Global Positioning System: An Overview*, Edinburgh, Scotland, edited by Y. B. a. N. Leppard, Springer -Verlag, 40-56, 1989.

- Bock, Y., R. I. Abbot, C. C. Counselman III, S. A. Gourevitch, and R. W. King, Establishment of three-dimensional geodetic control by interferometry with the Global Positioning System, *J. Geophys. Res.*, **90**, 7689–7703, 1985.
- Bock, Y., S. A. Gourevitch, C. C. Counselman III, R. W. King, and R. I. Abbott, Interferometric analysis of GPS phase observations, *Manuscr. Geod.*, **11**, 282–288, 1986.
- Bomford, G., *Geodesy*, 4th ed., 855 pp., Oxford University Press, New York, 1980.
- Bowie, W., Earth movements in California, *U. S. Coast and Geodetic Survey Spec. Publication No. 106*, 1924. Reprinted in *Reports on Geodetic Measurements of Crustal Movement, 1906–71* U. S. National Geodetic Survey, Rockville, MD, 1973.
- Bowie, W., Comparison of old and new triangulation data in California, *U. S. Coast and Geodetic Survey Spec. Publication No. 151*, 1928. Reprinted in *Reports on Geodetic Measurements of Crustal Movement, 1906–71*, U. S. National Geodetic Survey, Rockville, MD, 1973.
- Buchanan–Banks, L. M., R. O. Castle, and J. I. Ziony, Elevation changes in the central Transverse Ranges near Ventura, California, *Tectonophysics*, **29**, 113–125, 1975.
- Byerly, P., The California earthquake of November 4, 1927, *Bull. Seismol. Soc. Am.*, **68**, 53–66, 1930.
- Caspary, W. F., *Concepts of Network and Deformation Analysis*, 183 pp., University of New South Wales, Kensington, Australia, 1987.
- Chen, Jianming, T. D. Crompton, J. L. W. Walton, and R. Bilham, The survey work of the International Karakoram Project, in *The International Karakoram Project*, edited by K. J. Miller, Cambridge University Press, Cambridge, 1984.
- Clark, D. H., N. T. Hall, D. H. Hamilton, and R. G. Heck, Structural analysis of late Neogene deformation in the central offshore Santa Maria Basin, California, *J. Geophys. Res.*, **96**, 6435–6457, 1991.
- Clark, M. M., K. K. Harms, J. J. Lienkaemper, D. S. Harwood, K. R. Lajoie, J. C. Matti, J. A. Perkins, M. J. Rymer, A. M. Sarna-Wojcicki, R. V. Sharp, J. D. Sims, J. C. T. III, and J. I. Ziony, Preliminary slip-rate table and map of late Quaternary faults of California, *U. S. Geol. Surv., Open file report 84-106*, 1984.

- Clark, T. A., D. Gordon, W. E. Himwich, C. Ma, A. Mallama, and J.W. Ryan, Determination of relative site motions in the western United States using Mark III very long baseline interferometry, *J. Geophys. Res.*, 92, 12,741–12,750, 1987.
- Clark, T. A., C. Ma, J. M. Sauber, J. W. Ryan, D. Gordon, D. B. Shaffer, D. S. Chaprette, and N. R. Vandenberg, Geodetic measurement of deformation in the Loma Prieta, California earthquake with very long baseline interferometry, *Geophys. Res. Lett.*, 17, 1215–1218, 1990.
- Cline, M. W., R. A. Snay, and E. L. Timmerman, Regional deformation of the earth model for the Los Angeles region, California, *Tectonophysics*, 107, 279–314, 1984.
- Clynch, J. R., and D. S. Coco, Error characteristics of high quality geodetic GPS measurements: clocks, orbits, and propagation effects, *Proceedings of the Fourth International Geodetic Symposium on Satellite Positioning*, Austin, 539–556, 1986.
- Cockerham, R. S., and J. P. Eaton, The Point Sal earthquake of May 29, 1980 (abstract), *Earthquake Notes*, 53 (2), 51, 1982.
- Contreras, J., and M. Suter, Kinematic modeling of cross-sectional deformational sequences by computer simulation, *J. Geophys. Res.*, 95, 21,913–21,929, 1990.
- Cox, A., and D. Engebretson, Change in motion of the Pacific plate at 5 Myr. BP, *Nature*, 313, 472–474, 1985.
- Crawford, F. D., Petroleum potential of the Santa Maria Province, California, in *Future petroleum provinces of the United States—their geology and potential*, edited by I. H. Cram, *Memoir 15*, Amer. Assoc. of Petroleum Geologists, Tulsa, OK, 1971.
- Crouch, J. K., S. B. Bachman, and J. T. Shay, Post-Miocene compressional tectonics along the central California margin, in *Tectonics and Sedimentation Along the California Margin*, Publ. 38, edited by J. K. Crouch and S. B. Bachman, pp. 37–54, Pacific Section, Society of Economic Paleontologists and Mineralogists, Bakersfield, Calif., 1984.
- Crustal Dynamics Project Staff, Crustal Dynamics Project: Catalogue of Site Information, *NASA Reference Publication 1198*, March, 1988.
- CSTG (GPS Subcommission under Commission VIII, International Coordination of Space Techniques for Geodesy and Geodynamics of the International Association of Geodesy and International Union of Geodesy and Geophysics) Bulletin, 2, (3), 24, 1989.

- Dahlen, F. A., Noncohesive critical Coulomb wedges: an exact solution, *J. Geophys. Res.*, 89, 10,125-10,133, 1984.
- Dahlen, F. A., J. Suppe, and D. Davis, Mechanics of fold-and-thrust belts and accretionary wedges: cohesive Coulomb theory, *J. Geophys. Res.*, 89, 10087-10101, 1984.
- Davis, D., J. Suppe, and F. A. Dahlen, Mechanics of fold-and-thrust belts and accretionary wedges, *J. Geophys. Res.*, 88, 1153-1172, 1983.
- Davis, J. C., *Statistics and Data Analysis in Geology*, 2nd ed., 646 pp., John Wiley & Sons, New York, 1986.
- Davis, J. L., Atmospheric propagation effects on radio interferometry, Ph.D. thesis, 276 pp., Harvard, Cambridge, MA, 1986.
- Davis, J. L., T. A. Herring, I. I. Shapiro, A. E. E. Rogers, and G. Elgered, Geodesy by radio interferometry: Effects of atmospheric modeling errors on estimates of baseline length, *Radio Science*, 20, 1593-1607, 1985.
- Davis, J. L., W. H. Prescott, J. L. Svarc, and K. J. Wendt, Assessment of Global Positioning System measurements for studies of crustal deformation, *J. Geophys. Res.*, 94, 13,363-13,650, 1989.
- Davis, J. L., T. A. Herring, and I. I. Shapiro, Effects of atmospheric modeling errors on determinations of baseline vectors from very long baseline interferometry, *J. Geophys. Res.*, 96, 643-650, 1991.
- Davis, T. L., M. B. Lagoe, W. J. M. Bazeley, S. Gordon, K. McIntosh, and J. S. Namson, Structure of the Cuyama valley, Caliente Range, and Carrizo plain and its significance to the structural style of the southern Coast Ranges and Western Transverse Ranges, in *Tertiary Tectonics and Sedimentation in the Cuyama Basin, San Luis Obispo, Santa Barbara and Ventura Counties, California*, Publ. 59, pp. 141-158, edited by W. J. M. Bazeley, Pacific Section, Society of Economic Paleontologists and Mineralogists, Bakersfield, Calif., 1988.
- Davis, T. L., J. Namson, and R. F. Yerkes, A cross section of the Los Angeles Area: seismically active fold and thrust belt, the 1987 Whittier Narrows earthquake and earthquake hazard, *J. Geophys. Res.*, 94, 9644-9664, 1989.
- Defense Mapping Agency, Supplement to Department of Defense World Geodetic System 1984 Technical Report: Part II -- Parameters, Formulas and Graphics for the Practical Application of WGS84, DMA TR 8350.2-B, Defense Mapping Agency, 1987.

- Dehlinger, P., and B. A. Bolt, Earthquakes and associated tectonics in a part of coastal central California, *Bull. Seismol. Soc. Am.*, 77, 2056-2073, 1988.
- DeMets, C., R. G. Gordon, S. Stein, and D. F. Argus, A revised estimate of Pacific-North America motion and implications for western North American plate boundary zone tectonics, *Geophys. Res. Lett.*, 14, 911-914, 1987.
- DeMets, C., R. G. Gordon, D. F. Argus, and S. Stein, Current plate motions, *Geophys. J. Intl.*, 101, 425-478, 1990.
- Dibblee, T. W., Jr., The Rinconada and related faults in the southern Coast Ranges, California, and their tectonic significance, *U.S. Geol. Surv. Prof. Pap.* 981, 1977.
- Dixon, T., G. Blewitt, K. Larson, D. Agnew, B. Hager, P. Kroger, L. Skrumeda, and W. Strange, GPS measurements of regional deformation in California: some constraints on performance, *Eos Trans. Amer. Geophys. Un.*, 71, 1051-1056, 1990.
- Dixon, T. H., G. Gonzalez, S. M. Lichten, and E. Katsigris, First epoch geodetic measurements with the Global Positioning System across the northern Caribbean Plate Boundary Zone, *J. Geophys. Res.*, 96, 2397-2415, 1991.
- Dong, D. N., and Y. Bock, GPS network analysis with phase ambiguity resolution applied to crustal deformation studies in California, *J. Geophys. Res.*, 94, 3949-3966, 1989.
- Donnellan, A., B. H. Hager, and S. Larsen, Determination of convergence rates across the Ventura Basin, southern California using GPS and historical triangulation (abstract), *Eos Trans. Amer. Geophys. Un.*, 69, 326, 1988.
- Donnellan, A., B. H. Hager, and R. W. King, Preliminary results from repeat GPS across the Ventura Basin, southern California, manuscript in preparation, 1991.
- Dixon, T. H., An introduction to the Global Positioning System and some geological applications, *Rev. Geophys.*, 29, 249-276, 1991.
- Drew, A. R., and R. A. Snay, DYNAP: The Crustal Dynamics Adjustment Program, software version 1.0, Natl. Geod. Surv., Rockville, MD, 1987.
- Drew, A. R., and R. A. Snay, DYNAP: Software for estimating crustal deformation from geodetic data, *Tectonophysics*, 162, 331-343 1989.
- Eaton, J., Focal mechanisms of near-shore earthquakes between Santa Barbara and Monterey, California, *U.S. Geol. Surv. Open File Rep.*, 84-477, 1984.

- Eberhardt-Phillips, D., M. Lisowski, and M. D. Zoback, Crustal strain near the Big Bend of the San Andreas Fault: Analysis of the Los Padres-Tehachapi trilateration networks, California, *J. Geophys. Res.*, 95, 1139-1153, 1990.
- Feigl, H., The power of positivistic thinking, *Proc. Amer. Phil. Assoc.*, 36, 21-41, 1963. Reprinted in H. Feigl, *Inquiries and Provocations: Selected Writings, 1929-1974*, D. Riedel, Dordrecht, Holland, 1981.
- Feigl, K. L., R. W. King, and T. H. Jordan, Geodetic measurement of tectonic deformation in the Santa Maria fold and thrust belt, California, *J. Geophys. Res.*, 95, 2679-2699, 1990.
- Feigl, K. L., R. W. King, T. A. Herring, and M. Rothacher, A scheme for reducing the effect of Selective Availability on Precise GPS carrier phase measurements, *Geophys. Res. Lett.*, 18, 1289-1292, 1991.
- Fitch, T. J., Plate convergence, transcurrent faults and internal deformation adjacent to southeast Asia and the Western Pacific, *J. Geophys. Res.*, 77, 4432-4460, 1972.
- de La Fontaine, J., Le chêne et le roseau, Fable XXII, 1688. Reprinted in *Œuvres Complètes*, Paris, Gallimard, 1954.
- Fliegel, H. F., W. A. Fees, W. C. Layton, and N. W. Rhodus, The GPS radiation force model, *First International Symposium on Precise Positioning with the Global Positioning System*, Rockville, MD, National Geodetic Information Center, 113-119, 1985.
- Frank, F. C., Deduction of earth strains from survey data, *Bull. Seismol. Soc. Am.*, 56, 35-42, 1966.
- Freymuller, J. T., and J. N. Kellog, The extended tracking network and indications of baseline precision and accuracy in the North Andes, *Geophys. Res. Lett.*, 17, 207-210, 1990.
- Gawthrop, W. H., Seismicity of the central California coastal region *U.S. Geol. Surv. Open File Rep. 75-134*, 1975.
- Gawthrop, W. H., Seismicity and tectonics of the central California coastal region, *Spec. Rep. Calif. Div. Mines and Geol.*, 137, 45-56, 1978a.
- Gawthrop, W. H., The 1927 Lompoc, California, earthquake, *Bull. Seismological Soc. Am.*, 68, 1705-1716, 1978b.
- Georgiadou, Y., and A. Kleusberg, On the effect of ionospheric delay on geodetic relative GPS positioning, *Manus. Geod.*, 13, 1-8, 1988.

- Gergen, J. G., The new adjustment of the North American Datum: The observables, *American Congress on Surveying and Mapping Bull. 51*, Nov., p. 9, 1975.
- Goad, C. C., Gravimetric tidal loading computed from integrated Green's functions, *J. Geophys. Res.*, 85, 2679-2683, 1980.
- Gold, C. M., Automated contour mapping using triangular element data structures and an interpolant over each irregular domain, *Computer Graphics*, 11, 170-175, 1975.
- Guptill, P. D., E. G. Heath, and G. E. Brogan, Surface fault traces and historical earthquake effects near Los Alamos Valley, Santa Barbara County, California, *U.S. Geol. Surv. Open File Rep.*, 81-271, 1981.
- Gurtner, W., TRRINEXO, a DOS program to translate Trimble raw data into RINEX Observation files, Astronomical Institute, University of Berne, 1989.
- Gurtner, W., G. Beutler, and M. Rothacher, Combination of GPS observations made with different receiver types, *Fifth International Geodetic Symposium on Satellite Positioning*, Los Cruces, NM, 362-374, 1989a.
- Gurtner, W., G. Mader, and D. MacArthur, A common exchange format for GPS data, *5th International Geodetic Symposium on Satellite Positioning*, Las Cruces, NM, 920-932, 1989b.
- Hager, B. H., R. W. King, and M. H. Murray, Measurement of crustal deformation using the Global Positioning System, *Ann. Rev. Geophys.*, 19, 351-382 1991.
- Hall, C. A., Jr., Origin and development of the Lompoc-Santa Maria pull apart basin and its relation to the San Simeon-Hosgri strike slip, western California, *Spec. Rep. Calif. Div. Mines and Geol.*, 137, 25-31, 1978.
- Hall, C. A., Jr., San Luis Obispo transform fault and middle Miocene rotation of the western Transverse Ranges, California, *J. Geophys. Res.*, 86, 1015-1031, 1981.
- Hall, C. A., Jr., Pre-Monterey subcrop and structure maps, western San Luis Obispo and Santa Barbara counties, south-central California, *U.S. Geol. Surv. Misc. Field Study*, MF-1384, 1982.
- Hanks, T.C., The Lompoc, California earthquake (November 4, 1927, $M = 7.3$) and its aftershocks, *Bull. Seismol. Soc. Am.*, 69, 451-462, 1979.
- Hansen, K. M., and V. S. Mount, Smoothing and extrapolation of crustal stress orientation measurements, *J. Geophys. Res.*, 95, 1155-1165, 1990.
- Harbert, W., and A. Cox, Late Neogene motion of the Pacific plate, *J. Geophys. Res.*, 94, 3052-3064, 1989.

- Harris, H., Final survey data for NASA VLBI station, report of Defense Mapping Agency, Geodetic Survey Squadron, Detachment 1, August 31, 1984.
- Harris, R. A., and P. Segall, Detection of a locked zone at depth on the Parkfield California segment of the San Andreas Fault, *J. Geophys. Res.*, **92**, 7945-7962, 1987.
- Hartmann, G. K., and R. Leitinger, Range errors due to ionospheric and tropospheric effects for signal frequencies above 100 MHz, *Bull. Geod.*, **58**, 109-136, 1984.
- Hartzell, S. H., and T. H. Heaton, Teleseismic mechanism of the May 2, 1983, Coalinga California earthquake from long-period P waves, The 1983 Coalinga Earthquakes, edited by J. H. Bennett and R. W. Sherburne, *Spec. Publ. Calif. Div. of Mines and Geol.*, **66**, pp. 241-246, Sacramento, 1983.
- Haucksson, E., L. M. Jones, T. L. Davis, L. K. Hutton, A. G. Brady, R. A. Reasenber, A. J. Michael, R. F. Yerkes, P. Williams, G. Reagor, C. W. Stover, A. L. Bent, A. K. Shakal, E. Etheredge, R. L. Porcella, C. G. Bufe, M. J. S. Johnston, and E. Cranswick, The 1987 Whittier Narrows earthquake in the Los Angeles metropolitan area, *Science*, **239**, 1409-1412, 1988.
- Hauksson, E., and L. M. Jones, The 1987 Whittier Narrows earthquake sequence in Los Angeles, southern California: seismological and tectonic analysis, *J. Geophys. Res.*, **94**, 9569-9589, 1989.
- Hearn, T. M., and R. W. Clayton, Lateral velocity variations in southern California I. results for the upper crust from Pg waves, *B. Seism. Soc. Amer.*, **76**, 495-509, 1986a.
- Hearn, T. M., and R. W. Clayton, Lateral velocity variations in southern California II. results for the lower crust from Pn waves, *B. Seism. Soc. Amer.*, **76**, 511-520, 1986b.
- Hellwig, H., Frequency standards and clocks: a tutorial introduction, *616 (revised)*, National Bureau of Standards, 1974.
- Herring, T. A., GLOBK: Global Kalman filter VLBI and GPS analysis program, unpublished documentation, MIT, 1991.
- Herring, T. A., D. Dong, and R. W. King, Sub-milliarcsecond determination of pole position using Global Positioning System data, *Geophys. Res. Lett.*, submitted, 1991.

- Herring, T. A., J. L. Davis, and I. I. Shapiro, Geodesy by radio astronomy: the application of Kalman filtering to very long baseline interferometry, *J. Geophys. Res.*, **95**, 12,561-12,581, 1990.
- Hill, D. P., Contemporary block tectonics: California and Nevada, *J. Geophys. Res.*, **87**, 5433-5450, 1982.
- Hill, D. P., J. P. Eaton, and L. M. Jones, Seismicity of the San Andreas Fault System 1980-1986, The San Andreas Fault System, edited by R. E. Wallace, *U.S. Geol. Surv. Prof. Pap.*, in press, 1989.
- Holton, J. R., *An introduction to dynamic meteorology*, 2nd ed., 391 pp., Academic Press, New York, 1979.
- Hornafius, J. S., Neogene tectonic rotation of the Santa Ynez Range, Western Transverse Ranges, California suggested by paleomagnetic investigation of the Monterey formation, *J. Geophys. Res.*, **90**, 12,503-12,522, 1985.
- Hornafius, J. S., B. P. Luyendyk, R. R. Terres, and M. J. Kamerling, Timing and extent of Neogene tectonic rotation in the western Transverse Ranges, California, *Bull. Geol. Soc. Am.*, **97**, 1476-1487, 1986.
- Humphreys, E. D., and R. W. Clayton, Topographic Image of the southern California mantle, *J. Geophys. Res.*, **95**, 19,725-19,746, 1990.
- Humphreys, E. D., and B. H. Hager, A kinematic model for the late Cenozoic development of southern California crust and upper mantle, *J. Geophys. Res.*, **95**, 19,747-19,762, 1990.
- Humphreys, E. D., and R. J. Weldon II, Kinematic constraints on the rifting of Baja California, *Am. Assoc. Pet. Geol. Mem.* **47**, in press, 1989.
- Humphreys, E., R. W. Clayton, and B. H. Hager, A tomographic image of mantle structure beneath Southern California, *Geophys. Res. Lett.*, **11**, 625-627, 1984.
- Jackson, J. D., *Classical Electrodynamics*, 2nd ed., 848 pp., Wiley, New York, 1975.
- Jackson, J., and P. Molnar, Active faulting and block rotations in the western Transverse Ranges, California, *J. Geophys. Res.*, **95**, 22,073-22,087, 1990. (A correction appears in *J. Geophys. Res.*, **96**, 2203, 1991.)
- Jaeger, J. C., and N. G. W. Cook, *Fundamentals of Rock Mechanics*, 3rd edition, 593 pp., Chapman and Hall, London, 1979.

- Jahns, R. H., Investigations and problems of southern California geology, in *Geology of southern California*, edited by R. H. Jahns, 170, pp. 5-29, California Division of Mines, San Francisco, 5-29, 1954.
- Jennings, C. W., Fault Map of California, Calif. Geol. Map Ser., map 1, Calif. Div. Mines and Geol., 1975.
- Jordan, T. H., and J. B. Minster, Beyond plate tectonics: Looking at plate deformation with space geodesy, in *The Impact of VLBI on Astrophysics and Geophysics, Proceedings of IAU Symposium 129*, edited by M. J. Reid and J. M. Moran, Reidel, 341-350, 1988a.
- Jordan, T. H., and J. B. Minster, Measuring crustal deformation in the American West, *Sci. Am.*, 256, (8), 48-58, 1988b.
- Jordan, T. H., and K. A. Sverdrup, Teleseismic location techniques and their application to earthquake clusters in the south-central Pacific, *Bull. Seismol. Soc. Am.*, 71, 1105-1130, 1981.
- Kamerling, M. J., and B. P. Luyendyk, Paleomagnetism and Neogene tectonics of the Northern Channel Islands, California, *J. Geophys. Res.*, 90, 12,485-12,502, 1985.
- King, N. E., P. Segall, and W. Prescott, Geodetic measurements near Parkfield, California, 1959-1984, *J. Geophys. Res.*, 92, 2727-2766, 1987.
- King, R. W., and Y. Bock, Documentation for the MIT GPS Analysis Software: GAMIT, Massachusetts Institute of Technology, 1991.
- King, R. W., E. G. Masters, C. Rizos, A. Stolz, and J. Collins, *Surveying with GPS*, 128 pp., University of New South Wales, Australia, Kensington, 1985.
- Kleusberg, A., Ionospheric propagation effects in geodetic relative GPS positioning, *Man. Geod.*, 11, 256-261, 1986.
- Klobuchar, J. A., Ionospheric time-delay algorithm for single-frequency GPS receivers, *IEEE Trans. Aerospace and Electronic Systems*, AES-23, 325-331, 1987.
- Lambeck, K., *The Earth's Variable Rotation: Geophysical Causes and Consequences*, 449 pp., Cambridge Univ. Press, Cambridge, 1980.
- Langbein, J. O., R. O. Burford, and L. E. Slater, Variations in fault slip and strain accumulation at Parkfield, California: initial results using two-color geodimeter measurements, *J. Geophys. Res.*, 95, 2533-2552, 1990.

- Larson, K. M., Precision, accuracy and tectonics from the Global Positioning System, Ph.D. thesis, 269 pp., Univ. California, San Diego, San Diego, 1990.
- Lee, W. H. K., R. F. Yerkes, and M. Simirenko, Recent earthquake activity and focal mechanisms in the western Transverse Ranges, California, *U.S. Geol. Survey Circular*, 799A, 1979.
- Leick, A., *GPS Satellite Surveying*, 352 pp., John Wiley & Sons, New York, 1990.
- Li, V. C., and J. R. Rice, Crustal deformation in great Californian earthquake cycles, *J. Geophys. Res.*, 92, 11,533-11,551, 1987.
- Lichten, S. M., High accuracy Global Positioning System orbit determination: progress and prospects, in *Global Positioning System: an overview*, edited by Y. B. and N. Leppard, Springer-Verlag, New York, 146-165, 1989.
- Lichten, S. M., Estimation and filtering for high precision GPS applications, *Man. Geod.*, 15, 159-176, 1990a.
- Lichten, S. M., Towards GPS orbit accuracy of tens of centimeters, *Geophys. Res. Lett.*, 17, 215-218, 1990b.
- Lichten, S. M., and W. J. Bertiger, Demonstration of sub-meter GPS orbit determination and 1.5 parts in 10^8 three dimensional baseline accuracy, *Bull. Geod.*, 63, 167-189, 1989.
- Lin, J., and R. S. Stein, Coseismic folding, earthquake recurrence, and the 1987 source mechanism at Whittier Narrows, Los Angeles basin, California, *J. Geophys. Res.*, 94, 9614-9632, 1989.
- Lisowski, M., W. H. Prescott, J. C. Savage, and J. L. Svarc, A possible geodetic anomaly prior to the Loma Prieta, California, earthquake, *Geophys. Res. Lett.*, 17, 1211-1214, 1990a.
- Lisowski, M., W. H. Prescott, J. C. Savage, and M. L. Johnston, Geodetic estimate of coseismic slip during the 1989 Loma Prieta, California, earthquake, *Geophys. Res. Lett.*, 17, 1437-1440, 1990b.
- Lisowski, M., J. C. Savage, and W. H. Prescott, The velocity field along the San Andreas Fault in central and southern California, *J. Geophys. Res.*, 93, 8369-8389, 1991.
- Luyendyk, B. P., M. J. Kamerling, and R. Terres, Geometric model for Neogene crustal rotations in southern California, *Geol. Soc. Am. Bull.*, 91, 211-217, 1980.

- Luyendyk, B. P., M. J. Kamerling, R. Terres, and J. S. Hornafius, Simple shear of southern California during Neogene time suggested by paleomagnetic declination, *J. Geophys. Res.*, **90**, 12,454–12,466, 1985.
- MacKinnon, T. S., IGC field trip T311: origin of the Miocene Monterey formation in California, in *Oil in the California Monterey Formation: Field Trip Guidebook T311*, edited by T. S. MacKinnon, *28th International Geological Congress*, American Geophysical Union, Washington DC, 1989.
- Malvern, L. E., *Introduction to Mechanics of a Continuous Medium*, 713 pp., Prentice-Hall, Englewood Cliffs, New Jersey, 1969.
- Manson, M. W., Santa Maria Valley faults, Santa Barbara and San Luis Obispo counties, California, 26 pp., *Calif. Div. of Mines and Geol. Fault Eval. Rep. FER-168*, Sacramento, 1985.
- Matsu'ura, M., D. D. Jackson, and A. Cheng, Dislocation model for aseismic crustal deformation at Hollister, California, *J. Geophys. Res.*, **91**, 12,661–12,674, 1986.
- Matz, B., and D. B. Slemmons, Remote sensing study of Pismo syncline and Santa Maria Basin, central coastal California (abstract), *Geol. Soc. Am. Abstr. Programs*, **19**, 429, 1987.
- McCarthy, D. D., editor, IERS Standards (1989), *Technical note 3*, International Earth Rotation Service, 1989.
- McIntosh, K. D., D. L. Reed, E. A. Silver, and A. S. Meltzer, Deep structure and structural inversion along the central California margin from EDGE seismic profile RU-3, *J. Geophys. Res.*, **96**, 6459–6473, 1991.
- McNeff, J. G., Global Positioning System (GPS) policies (abstract), *Eos Trans. Amer. Geophys. Un.*, **71**, 1268, 1990.
- Meltzer, A. S., and A. R. Levander, Deep crustal reflection profiling offshore southern central California, *J. Geophys. Res.*, **96**, 6475–6491, 1991.
- Minster, J. B., and T. H. Jordan, Present-day plate motions, *J. Geophys. Res.*, **83**, 5331–5354, 1978.
- Minster, J. B., and T. H. Jordan, Vector constraints on Quaternary deformation of the western United States east and west of the San Andreas fault, *Tectonics and Sedimentation Along the California Margin*, *Publ. 38*, edited by J. K. Crouch and S. B. Bachman, pp 1–16, Pacific Section, Society of Economic Paleontologists and Mineralogists, Bakersfield, Calif., 1984.

- Minster, J. B., and T. H. Jordan, Vector constraints on western U.S. deformations from space geodesy, neotectonics and plate motions, *J. Geophys. Res.* 92, 4798–4804, 1987.
- Molnar, P., Brace-Goetze strength profiles, the partitioning of strike-slip and thrust faulting at zones of oblique convergence and the stress-heat flow paradox of the San Andreas Fault, in press, 1991.
- Mount, V., and J. Suppe, State of stress near the San Andreas fault: Implications for wrench tectonics, *Geology*, 15, 1143–1146, 1987.
- Murray, M. H., Global Positioning System measurements of crustal deformation in central California, Ph.D. thesis, 273 pp., MIT, Cambridge, MA, 1991.
- Murray, M. H., Y. Bock, D. N. Dong, K. L. Feigl, and R. W. King, Assessing the long term repeatability and accuracy of three GPS campaigns in California (abstract), *Eos Trans. Amer. Geophys. Un.*, 69, 323, 1988.
- Murray, M. H., R. W. King, and P. J. Morgan, SV5: a terrestrial reference frame for monitoring crustal deformation with the Global Positioning System (abstract), *Eos, Trans. Amer. Geophys. Un.*, 71, 1274, 1990.
- Namson, J. S., and T. L. Davis, Seismically active fold and thrust belt in the San Joaquin Valley, central California, *Geol. Soc. Am. Bull.*, 100, 257–273, 1988a.
- Namson, J., and T. Davis, Structural transect of the western Transverse Ranges, California: implications for lithospheric kinematics and seismic risk evaluation, *Geology*, 16, 675–679, 1988b.
- Namson, J., and T. Davis, Late Cenozoic fold and thrust belt of the southern Coast Ranges and Santa Maria Basin, California, *AAPG Bull.*, 74, 467–492, 1990.
- Nitchman, S. P., Tectonic geomorphology and neotectonics of the San Luis range, San Luis Obispo County, California, M. S. thesis, Univ. of Nevada at Reno, 120 pp., 1988.
- Nitchman, S., M. A. Ellis, B. Matz, D. B. Slemmons, and E. Vittori An active fold and thrust belt in the San Luis Obispo/Santa Maria region of coastal central California, *Geol. Soc. Amer. Spec. Pap.*, in press, 1989.
- Okada, Y., Surface deformation to shear and tensile faults in a half-space, *Bull. Seism. Assoc. Amer.*, 75, 1135–1154, 1985.
- Pacific Gas and Electric Company, Final Report of the Diablo Canyon Long-Term Safety Program for the Diablo Canyon Power Plant, *Docket numbers 50-275 and 50-323*, submitted to the Nuclear Regulatory Commission, 1988.

- Page, B. M., Geology of the Coast Range of California, *California Div. Mines and Geology Bull.*, 90, 255-276, 1966.
- Page, B. M., The southern Coast Ranges, in *The Geotectonic Development of California*, edited by W. G. Ernst, pp. 329-417, Prentice Hall, Englewood Cliffs N.J., 1981.
- Prescott, W.H., An extension of Frank's method for obtaining crustal shear strain from survey data, *Bull. Seismol. Soc. Am.*, 66, 1847-1853, 1976.
- Prescott, W. H., The determination of displacement fields from geodetic data along a strike-slip fault, *J. Geophys. Res.*, 86, 6067-6072, 1981.
- Prescott, W. H., J. C. Savage, and W. T. Kinoshita, Strain accumulation in the western United States between 1970 and 1978, *J. Geophys. Res.*, 84, 5423-5435, 1979.
- Press, W. H., B. P. Flannery, S. A. Teukolsky, and W. T. Vetterling, *Numerical Recipes: The Art of Scientific Computing*, 818 pp., Cambridge University Press, Cambridge, 1986.
- Reed, R. D., and J. S. Hollister, *Structural Evolution of Southern California*, 157 pp., Amer. Assoc. Petrol. Geol., Tulsa, OK, 1936, reprinted 1958.
- Remondi, B. W., Using the Global Positioning System (GPS) phase observable for relative geodesy: modeling, processing, and results, Ph. D. Thesis, 360 pp., University of Texas, Austin, May 1984.
- Rocken, C., The Global Positioning System: a new tool for tectonic studies, Ph.D., 265 pp., Univ. of Colorado, Boulder, 1988.
- Rocken, C., and C. M. Meertens, GPS antenna and receiver tests: multipath reduction and mixed receiver baselines, *Fifth International Geodetic Symposium on Satellite Positioning*, Los Cruces, NM, 375-385, 1989.
- Rocken, C., and C. Meertens, Monitoring Selective Availability dither frequencies and their effect on GPS data, *Manus. Geod.*, submitted, 1991.
- Rockwell International Corporation, Navstar GPS Space Segment Navigation User Interfaces, *ICD-GPS-200*, 1984.
- Rockwell, T. K., E. A. Keller, M. N. Clark, and D. L. Johnson, Chronology and rates of faulting of Ventura River terraces, California, *Geol. Soc. Amer. Bull.*, 95, 1466-1474, 1984.

- Rockwell, T. K., E. A. Keller and G. R. Dembroff, Quaternary rate of folding of the Ventura Avenue anticline, western Transverse Ranges, southern California, *Geol. Soc. Am. Bull.*, 100, 850-858, 1988.
- Saastamoinen, J., Atmospheric correction for the troposphere and stratosphere in radio ranging of satellites, in *The Use of Artificial Satellites for Geodesy*, edited by S. W. Henriksen et al., *Geophys. Monogr. Ser.*, 15, pp. 247-251, AGU, Washington, D. C., 247-251, 1972.
- Sauber, J. M., Geodetic measurement of deformation in California, Ph.D. thesis, 219 pp., Mass. Inst. Technol., Cambridge, Nov. 1988 (available as *NASA Tech. Memo. 100732*).
- Savage, J. C., A possible bias in the California state Geodimeter data, *J. Geophys. Res.*, 80, 4078-4088, 1975.
- Savage, J. C., Strain accumulation in the western United States, *Annu. Rev. Earth Planet. Sci.*, 11, 11-43, 1983.
- Savage, J. C., and R. O. Burford, Geodetic determination of relative plate motion in central California, *J. Geophys. Res.*, 832-845, 1973.
- Savage, J. C., and M. Lisowski, Strain measurements and the potential for a great subduction earthquake of the coast of Washington, *Science*, 252, 101-103, 1991.
- Savage, J. C., and W. H. Prescott, Geodetic control and the 1927 Lompoc, California Earthquake, *Bull. Seismol. Soc. Am.*, 68, 1699-1703, 1978.
- Savage, J. C., M. Lisowski, and W. H. Prescott, An apparent shear zone trending North-Northwest across the Mojave Desert into Owens Valley, Eastern California, *Geophys. Res. Lett.*, 17, 2113-2116, 1990.
- Schaffrin, B., and Y. Bock, A unified scheme for processing GPS phase observations, *Bull. Géod.*, 62, 142-160, 1988.
- Schutz, B. E., C. S. Ho, P. A. M. Abusali, and B. D. Tapley, CASA UNO orbit and baseline experiments, *Geophys. Res. Lett.*, 17, 643-646, 1990.
- Sedlock, R. L., and D. H. Hamilton, Late Cenozoic tectonic evolution of southwestern California, *J. Geophys. Res.*, 96, 2325-2351, 1991.
- Segall, P., and M. V. Matthews, Displacement calculations from geodetic data and the testing of geophysical deformation models, *J. Geophys. Res.*, 93, 14,954-14,966, 1988.

- Sheffels, B., and M. McNutt, Role of subsurface loads and regional compensation in the isostatic balance of the Transverse Ranges California: evidence for intracontinental subduction, *J. Geophys. Res.*, 91, 6419-6431, 1986.
- Shen, Z., Regional tectonic deformation in southern California, inferred from terrestrial geodesy and the Global Positioning System, Ph.D, 163 pp., University of California, Los Angeles, 1991.
- Sieh, K. E., and R. H. Jahns, Holocene activity of the San Andreas fault at Wallace Creek, *Geol. Soc. Am. Bull.*, 95, 8832-896, 1984.
- Smith, L. E., The United States western test range traverse measurements, paper presented to the International Symposium on Terrestrial Electromagnetic Distance Measurements and Atmospheric Effects on Angular Measurements, Royal Institute of Technology, Stockholm, Sweden, 1974.
- Snay, R. A., Horizontal deformation in New York and Connecticut: Examining contradictory results from the geodetic evidence, *J. Geophys. Res.* 91, 12,695-12,702, 1986.
- Snay, R. A., M. W. Cline, and E. L. Timmerman, Regional deformation of the earth model for the San Diego Region, California, *J. Geophys. Res.* 88, 5009-5024, 1983.
- Snay, R. A., M. W. Cline, and E. L. Timmerman, Project REDEAM: models for historical horizontal deformation, *NOAA Tech. Report. NOS 125 NGS 42*, 1987.
- Soffel, M. H., *Relativity in Astrometry, Celestial Mechanics and Geodesy*, 208 pp., Springer-Verlag, Berlin, 1989.
- Sonder, L. J., Effects of density contrasts on the orientation of stresses in the lithosphere: relation to principal stress directions in the Transverse Ranges, California, *Tectonics*, 9, 761-771, 1990.
- Spilker, J. J. Jr., GPS signal structure and performance characteristics, *Navigation*, 25, 121-146, 1978. Reprinted in *Global Positioning Papers*, pp. 55-73, Institute of Navigation, Washington, D. C., 29-54 1980.
- Stacey, F. D., *Physics of the Earth*, 414 pp., Wiley, New York, 1977.
- Stein, R. S., and G. C. P. King, Seismic potential revealed by surface folding: 1983 Coalinga, California, earthquake, *Science*, 224, 869-872, 1984.
- Stein, R. S., and R. S. Yeats, Hidden earthquakes, *Sci. Am.*, 260 (6), 48-57, 1989.

- Steritz, J. W., and P. B. Luyendyk, Southern termination of the Hosgri fault zone, offshore California (abstract), *Eos Trans. Amer. Geophys. Un.*, 67, 1214, 1986.
- Strange, W. E., Results of the southern California GPS crustal motion network (abstract), *Eos Trans. Amer. Geophys. Un.*, 68, 283, 1987.
- Suppe, J., Mechanics of mountain building and metamorphism in Taiwan, *Mem. Geol. Soc. China*, 4, 67-89, 1981.
- Suppe, J., Geometry and kinematics of fault-bend folding, *Amer. J. Sci.*, 283, 684-721, 1983.
- Suppe, J., and D. A. Medwedeff, Geometry and kinematics of fault-propagation folding, *Eclogae geol. Helv.*, 83, 409-454, 1990.
- Sylvester A. G., and A. C. Darrow, Structure and neotectonics of the western Santa Ynez fault system in southern California, *Tectonophysics*, 52, 389-405, 1979.
- Terres, R. R., and B. P. Luyendyk, Neogene tectonic rotation of the San Gabriel region, California, suggested by paleomagnetic vectors, *J. Geophys. Res.*, 90, 12,467-12,484, 1985.
- Tralli, D. M., T. H. Dixon, and S. A. Stephens, Effect of wet tropospheric path delays on estimation of geodetic baselines in the Gulf of California using the Global Positioning System, *J. Geophys. Res.*, 93, 6545-6557, 1988.
- Tuttle, M. P., Earthquake potential of the San Gregorio-Hosgri Fault Zone, California, M.S. thesis, U. California, Santa Cruz, 1985.
- U. S. Dept. of Transportation, 1990 *Federal Radionavigation Plan*, Report number DOT-VNTSC-RSPA-90-3/DOD-4650.4, 1990. Supposedly available through the National Technical Information Service, tel. 703 487-4600, Springfield, VA, 22161. Actually obtained from the library of the Transportation Systems Center, tel. 617 494-2306, Cambridge, MA 02139.
- U. S. Geological Survey Staff, The Loma Prieta, California, earthquake: an anticipated event, *Science*, 247, 286-293, 1990.
- Up De Graff, J. E., and B. P. Luyendyk, Gravity study of the boundary between the western Transverse Ranges and the Santa Maria Basin, California, *J. Geophys. Res.*, 93, 1817-1826, 1989.
- Van Dierendonck, A. J., S. S. Russell, E. R. Kopitzke, and M. Birnbaum, The GPS Navigation Message. Originally published in volume 25, no. 2 of *Navigation*, 1978. Reprinted in *Global Positioning Papers*, pp. 55-73, Institute of Navigation, Washington, D. C., 55-73, 1980.

- Vessot, R. F. C., Frequency and time standards, in *Methods of Experimental Physics*, edited by M. L. Meeks, *I2C*, pp. 198-227, Academic Press, New York, 198-227, 1976.
- Walcott, R. I., Present tectonics and Late Cenozoic evolution of New Zealand, *Geophys. J. R. Astr. Soc.*, *52*, 137-164, 1978a.
- Walcott, R. I., Geodetic strains and large earthquakes in the axial tectonic belt of North Island, New Zealand, *J. Geophys. Res.*, *83*, 4419-4429, 1978b.
- Ward, S. N., Pacific-North America plate motions: new results from very long baseline interferometry, *J. Geophys. Res.*, *95*, 21,965-21,981, 1990.
- Watson, D. F., ACORD: Automatic contouring of raw data, *Computers and Geosciences*, *8*, 97-101, 1982.
- Webb, F. H., Geodetic measurement of deformation in the offshore of southern California, Ph. D. thesis, 211 pp., California Inst. Tech., Pasadena, CA, June, 1990.
- Weldon, R., and E. Humphreys, A kinematic model of southern California, *Tectonics*, *5*, 33-48, 1986.
- Wells, D., N. Beck, D. Delikaraoglou, E. J. Krakiwsky, G. Lachapelle, R. B. Langley, M. Nakboglu, K.-P. Schwarz, J. M. Tranquilla, and P. Vanicek, *Guide to GPS Positioning*, 2nd ed, Fredrickton, NB, Canadian GPS Associates, 1986.
- Welsch, W., A review of the adjustment of free networks, *Gt. Brit. Surv. Rev.*, *25* (194), 167-180, 1979.
- Wild, U., G. Beutler, W. Gurtner, and M. Rothacher, Estimating the ionosphere using one or more dual frequency GPS receivers, *5th International Geodetic Symposium on Satellite Positioning*, Las Cruces, NM, 724-736, 1989.
- Wu, S. C., W. I. Bertiger, and J. T. Wu, Minimizing selective availability error on Topex GPS measurements, *American Institute of Aeronautics and Astronautics*, Astrodynamics Conference, Portland, OR, Paper 90-2942, 1990.
- Yeats, R. S., Quaternary flake tectonics of the California Transverse Ranges, *Geology*, *9*, 16-20, 1981.
- Yeats, R. S., Large-scale Quaternary detachments in Ventura Basin, California, *J. Geophys. Res.*, *88*, 569-583, 1983.

- Yeats, R. S., Late Quaternary slip rate on the Oak Ridge Fault, Transverse Ranges, California: implications for seismic risk, *J. Geophys. Res.*, **93**, 12,137-12,149, 1988.
- Yeats, R. S., G. J. Huftile, and F. B. Grigsby, Oak Ridge fault, Ventura fold belt, and the Sisar decollement, Ventura basin, California, *Geology*, **16**, 1112-1116, 1988.
- Yeats, R. S., Late Quaternary slip rate on the Oak Ridge fault, Transverse Ranges, California: Implications for seismic risk, *J. Geophys. Res.*, **93**, 12,137-12,149, 1988.
- Yerkes, R. F., and W. H. K. Lee, Late Quaternary deformation in the Western Transverse Ranges, California, *U.S. Geol. Surv. Circ.*, **799B**, 1979.
- Zoback, M. D., M. L. Zoback, V. S. Mount, J. Suppe, J. P. Eaton, J. H. Healy, D. Oppenheimer, P. Reasenber, L. Jones, C. B. Raleigh, I. G. Wong, O. Scotti, and C. Wentworth, New evidence on the state of stress of the San Andreas fault system, *Science*, **238**, 1105-1111, 1987.